



University
of Glasgow

Giuni, Michea (2013) *Formation and early development of wingtip vortices*. PhD thesis.

<http://theses.gla.ac.uk/3871/>

Copyright and moral rights for this thesis are retained by the author

A copy can be downloaded for personal non-commercial research or study, without prior permission or charge

This thesis cannot be reproduced or quoted extensively from without first obtaining permission in writing from the Author

The content must not be changed in any way or sold commercially in any format or medium without the formal permission of the Author

When referring to this work, full bibliographic details including the author, title, awarding institution and date of the thesis must be given.



Department of Aerospace Engineering
School of Engineering

Formation and early development of wingtip vortices

MICHEA GIUNI

A thesis submitted in partial fulfillment of the requirements for the
degree of Doctor of Philosophy

Declaration of authorship

I herewith declare that I have produced this paper without the prohibited assistance of third parties and without making use of aids other than those specified; notions taken over directly or indirectly from other sources have been identified as such. This work has not previously been presented in identical or similar form to any other Scottish or foreign examination board.

The thesis work was conducted from January 2009 to June 2012 under the supervision of Dr. Emmanuel Bénard and of Dr. Richard B. Green at the University of Glasgow, United Kingdom.

5th October 2012, Glasgow

Formation and early development of wingtip vortices

Abstract: wingtip vortices are extremely important phenomena in fluid dynamics for their negative effects in many applications. Despite the many studies on this particular flow, the current understanding is still poor in providing a firm base for the design of effective tip geometry modifications and vortex control devices. A rectangular wing with squared and rounded wingtips was tested in order to identify the main mechanisms involved in the formation of the vortex on the wing and in its early development in the wake. The complementarity of a number of experimental techniques adopted, such as surface flow visualizations, wall pressure measurements, smoke visualizations and stereoscopic particle image velocimetry (SPIV), gave a richer insight of the physics and the basic mechanisms of the vortex development. Furthermore, a large number of configurations were tested exploring the effects of several parameters such as wing chord, aspect ratio, wingtip geometry, angle of attack and Reynolds number.

The development of the vortex along the wing showed the formation of several secondary vortices which interacted with the primary vortex generating low frequency fluctuations. The structure of the flow at this stage was analysed introducing a compact description through characteristic lines of the vortex system defined from the velocity vector field in the vicinity of the wing surface. The high spatial resolution achieved by the SPIV arrangement allowed a deeper understanding of the vortex structure in the early wake and the turbulence production and dissipation within the vortex core. The relaminarization process of the vortex core promoted by centrifugal motion was observed. The relation between vortex meandering, turbulence, secondary vortices and wake sheet was discussed. A comparison of different methods for the averaging of instantaneous planar vector fields was performed showing the effects and importance of the meandering. An axial acceleration of the flow within the vortex was observed and the formation of different axial flow distributions was discussed. A minimum wake-like flow of 0.62 and a maximum jet-like flow of 1.7 times the freestream velocity were measured and a linear relation between a vortex circulation parameter and the axial velocity peak was found.

Keywords: wingtip vortex, wake, SPIV, relaminarization.

*to Rugiada
and her inspiring faith*

*to Dario
and his exemplary strength*

Acknowledgments

THIS dissertation is actually not the fruit of just my efforts and time but it is more a fruit of the guidance, support, patience and encouragement of other people, to whom I am thankful.

I sincerely thank Dr. Emmanuel Bénard for providing me with this opportunity to enjoy a research in Fluid Dynamics, for believing in my abilities and for his guidance in the experimental analysis. I also would like to thank with the same sincerity Dr. Richard B. Green for his invaluable assistance and guidance in shaping this work and helping me in bringing it to a closure.

I will certainly thank also all the technical support staff involved in this research, particularly Mr. Tony Smedley, Mr. Robert Gilmour, Mr. John Kitching and Mr. Ian Scouller.

Special thanks to my girlfriend who accepted to become my wife during this journey and to move to Glasgow for me, to my parents and my brothers. Thanks also to my friends and “brothers”, old and far, new and near, who encouraged me and made me laugh and grow during these years so that I could enjoy them.

List of publications

The contents of this dissertation have been partially published, or in the process of being published, in highly rated journal papers and presented in related conferences.

Journal publications

- GIUNI, M., GREEN, R. B. & BENARD, E. 2012 Unsteady flow in wingtip vortex formation. Under preparation for submission, *Journal of Fluid Mechanics*.
- GIUNI, M. & GREEN, R. B. 2012 Vortex formation on squared and rounded tip. Under review, *Aerospace Science and Technology*.

Conference publications

- GIUNI, M. & BENARD, E. 2011 Analytical/Experimental comparison of the axial velocity in trailing vortices. *49th AIAA Aerospace Science Meeting, 4-7 January*. Orlando, Florida.
- GIUNI, M., BENARD, E. & GREEN, R. B. 2011 Investigation of a trailing vortex near field by stereoscopic particle image velocimetry. *49th AIAA Aerospace Science Meeting, 4-7 January*. Orlando, Florida.
- GIUNI, M., BENARD, E. & GREEN, R. B. 2010 Near field structure of wing tip vortices. *Experimental Fluid Mechanics Conference, 24-26 November*. Liberec, Czech Republic.

Presentations

- GIUNI, M., BENARD, E. & GREEN, R. B. 2010 SPIV Experiments on wing trailing vortices. *University of Glasgow: Engineering Graduate School Conference, 17-18 August*. Glasgow, UK.
- GIUNI, M., BENARD, E. & GREEN, R. B. 2010 Wing trailing vortex axial velocity. *University of Dundee: 23rd Scottish Fluid Mechanics Meeting, 19 May*. Dundee, UK.

Table of contents

| | |
|----------------------------------|------|
| <i>Declaration of authorship</i> | ii |
| <i>Abstract</i> | iii |
| <i>Acknowledgments</i> | v |
| <i>List of publications</i> | vi |
| <i>List of figures</i> | xiii |
| <i>List of tables</i> | xx |
| <i>Nomenclature</i> | xxi |

| | | |
|----------|--|-----------|
| 1 | <i>Introduction</i> | 1 |
| 1 | Why are wingtip vortices so important? | 2 |
| 2 | Theoretical background: why do wingtip vortices form? | 8 |
| 3 | Literature review: what is the current understanding of wingtip vortices? 13 | |
| | (a) Far and mid field | 15 |
| | (b) Formation and near field | 19 |
| 4 | What are the scope and contributions of this work to the unresolved issues? 24 | |
| 5 | Structure of the thesis | 26 |
| | | |
| 2 | <i>Experimental apparatus and procedure</i> | 27 |
| 1 | Wind tunnels | 28 |
| | (a) Argyll wind tunnel | 28 |
| | (b) Smoke visualization wind tunnel | 29 |
| 2 | Wing models | 30 |
| | (a) M1 : high aspect ratio wing | 31 |
| | (b) M2 : low aspect ratio wing | 31 |
| 3 | Experimental techniques | 33 |
| | (a) Surface oil flow visualizations | 33 |
| | (b) Pressure measurements | 34 |
| | (c) Smoke visualizations | 39 |
| | (d) Hot film anemometry | 40 |
| | (e) Stereoscopic particle image velocimetry | 41 |
| 4 | Reference systems | 50 |
| | (a) Wake reference system | 50 |
| | (b) Vortex reference system | 52 |
| | (c) Wing chord reference system | 52 |
| | (d) Wing surface reference system | 53 |

| | | |
|----------|---|-----------|
| 3 | <i>Wingtip vortex formation</i> | 54 |
| 1 | Surface oil flow visualization | 56 |
| 2 | Pressure on the wing surface | 59 |
| | (a) Average pressure distribution | 60 |
| | (b) Pressure fluctuation at the wingtip | 64 |
| 3 | Smoke visualization on the rolling up | 67 |
| | (a) Rolling up on squared and rounded wingtip | 67 |
| | (b) Angle of attack and Reynolds number effects | 71 |
| 4 | Vortex characteristic lines via SPIV | 75 |
| | (a) Characteristic lines definition | 76 |
| | (b) Effects of the distance of the laser plane from the surface | 82 |
| | (c) Reynolds number and tip geometry effects | 84 |
| | (d) Angle of attack effects | 85 |
| 5 | Unsteadiness of the vortex formation via hot film | 86 |
| | (a) Unsteadiness and intermittency | 88 |
| | (b) Signal spectra on squared tip | 89 |
| | (c) Signal spectra on rounded tip | 91 |
| 6 | Unsteadiness of the vortex in the early wake | 92 |
| | (a) Reynolds number effects | 94 |
| | (b) Angle of attack effects | 95 |
| | (c) Downstream distance effects | 96 |
| 7 | Summary | 97 |

| | | |
|----------|--|------------|
| 4 | <i>Wingtip vortex early wake</i> | 100 |
| 1 | Localization of the vortex centre and averaging of velocity vector fields . | 102 |
| | (a) Swirl velocity distribution | 111 |
| | (b) Axial velocity distribution | 113 |
| | (c) Turbulent quantities | 115 |
| | (d) Convergence of averages | 121 |
| 2 | Shape of the vortex core | 127 |
| | (a) Vortex core shape definition | 127 |
| | (b) Vortex core shape fluctuation | 130 |
| | (c) Rotation of the core | 131 |
| | (d) Vortex core shape for different tip geometries | 135 |
| 3 | Axial flow | 136 |
| | (a) Shape of the axial flow | 139 |
| | (b) Axial velocity at the centre of the vortex | 144 |
| 4 | Turbulence in the vortex core | 149 |
| | (a) Turbulent kinetic energy evolution | 150 |
| | (b) Reynolds shear stress and shear strain | 153 |
| | (c) Turbulence production | 157 |
| 5 | Early wake behind squared and rounded wingtips | 162 |
| | (a) Development of averaged properties | 162 |
| | (b) Meandering and instantaneous behaviour of the vortex structure | 167 |
| | (c) Turbulence and shear strain evolution | 169 |
| | (d) Vortex pair formation without generation of lift | 173 |
| 6 | Summary | 174 |
| 5 | <i>Measurement accuracy and error</i> | 177 |
| 1 | Pressure, frequency and meandering | 177 |
| 2 | SPIV | 178 |
| 6 | <i>Conclusions and recommendations for future work</i> | 181 |
| 1 | Conclusions | 181 |
| 2 | Recommendations for future work | 184 |

| | |
|--|------------|
| <i>Bibliography</i> | 186 |
| <i>Appendices</i> | 201 |
| <i>A PIV: laser pulse separation and image processing</i> | 202 |
| 1 Laser pulse separation tests | 202 |
| (a) Calculation of the pulse separation | 203 |
| (b) Pulse separation comparison | 204 |
| 2 Image processing procedure tests | 207 |
| (a) Interrogation window size | 210 |
| (b) Number of iterations | 211 |
| (c) Interrogation window overlap | 213 |
| (d) Processing time and memory | 214 |
| (e) Conclusive remarks | 216 |
| <i>B Vortex centre identification on grayscale pictures</i> | 218 |
| 1 GRAY and BW methods | 218 |
| (a) BW method | 219 |
| (b) GRAY method | 219 |
| 2 Position distribution and movement frequency | 220 |
| <i>C Some equations relevant to vortices</i> | 226 |
| 1 Governing equations | 226 |
| 2 Vorticity form of the Navier–Stokes equation (or vorticity equation) | 229 |
| 3 Reynolds–averaged Navier–Stokes equations | 230 |
| 4 Conversion between cartesian and cylindrical coordinate systems | 232 |

List of figures

| | | |
|------|--|----|
| 1.1 | Examples of wingtip vortices 1. | 3 |
| 1.2 | Examples of wingtip vortices 2. | 6 |
| 1.3 | Examples of wingtip vortices 3. | 7 |
| 1.4 | Vortex systems replacing the lifting wing and its wake (Houghton & Carpenter, 2003). | 10 |
| 1.5 | Early stage of the roll up of the wake sheet. The vortex sheet element positions are plotted on the left and an interpolating curve is plotted on the right (Krasny, 1987). | 11 |
| 1.6 | Pressure field interpretation of the wingtip vortex formation. | 12 |
| 1.7 | Shear layer interpretation of wingtip vortex formation. | 13 |
| 1.8 | Vortex life schematics: the approximate length scale is taken from Albano <i>et al.</i> (2003) for a typical airplane although they may drastically vary depending on the case (see for example Dieterle <i>et al.</i> (1999) for a different length scale). | 14 |
| 2.1 | Argyll wind tunnel: top view. | 29 |
| 2.2 | Experimental arrangement of smoke visualizations on the vortex formation: wing M2 mounted in the flow visualization wind tunnel. | 30 |
| 2.3 | M1 wing mounted in the Argyll wind tunnel (without fixing cables). . . | 31 |
| 2.4 | M2 wing mounted in the Argyll wind tunnel and SPIV calibration plate. . . | 32 |
| 2.5 | Pressure tappings map and names. | 34 |
| 2.6 | Pressure measurements arrangement. | 38 |
| 2.7 | Typical response of a pressure measurement system at an equivalent altitude of 2300 ft as function of the tube length and internal diameter (Whitmore <i>et al.</i> , 1990). | 39 |
| 2.8 | Camera mounting and laser delivery for SPIV experiments. | 45 |
| 2.9 | Vector field computation flow chart of a two pulses two frames SPIV. . . | 49 |
| 2.10 | Reference systems. | 51 |

| | | |
|------|--|----|
| 3.1 | Surface flow visualizations: suction surface. | 57 |
| 3.2 | Surface flow visualizations: tip surface (freestream from left to right). | 58 |
| 3.3 | Pressure coefficient distribution and pressure tappings at $Re = 5 \cdot 10^5$ and $\alpha = 12^\circ$: suction and pressure surface. | 61 |
| 3.4 | Pressure coefficient distribution and pressure tappings at $Re = 5 \cdot 10^5$ and $\alpha = 12^\circ$: tip surface. The circles correspond to the pressure tapping positions. | 62 |
| 3.5 | Pressure coefficient distribution on the suction surface at $Re = 5 \cdot 10^5$ | 63 |
| 3.6 | Pressure coefficient distribution along tappings row T1 at $Re = 5 \cdot 10^5$ | 63 |
| 3.7 | McAlister & Takahashi (1991) experiments: pressure coefficient distribution at $Re = 1 \cdot 10^6$ and $\alpha = 12^\circ$ | 64 |
| 3.8 | Pressure coefficient distribution at $Re = 5 \cdot 10^5$ and $\alpha = 12^\circ$ | 65 |
| 3.9 | Pressure standard deviation. | 65 |
| 3.10 | Pressure signal for $\alpha = 12^\circ$ | 66 |
| 3.11 | Vortex at $Re = 3000$, $x_c = 0.75$ and $\alpha = 12^\circ$ on rounded tip; wing section in gray. | 68 |
| 3.12 | Vortex evolution at $Re = 3000$ and $\alpha = 12^\circ$ on rounded tip; wing section in gray. | 69 |
| 3.13 | Vortex evolution at $Re = 3000$ and $\alpha = 12^\circ$ on squared tip; wing section in gray. | 70 |
| 3.14 | Snapshots at $f = 30$ Hz, $Re = 3000$, $\alpha = 12^\circ$ and $x_c = 0.7$ on squared tip. | 72 |
| 3.15 | Vortex evolution at $Re = 3000$ and $\alpha = 12^\circ$ on rounded tip; wing section in gray. | 73 |
| 3.16 | Experimental arrangement and field of view of the SPIV cameras. | 75 |
| 3.17 | SPIV laser sheet positions. | 76 |
| 3.18 | Mean flow plane streamlines for squared tip at $\alpha = 12^\circ$, $Re = 10^5$ and $d = 3$ mm. | 77 |
| 3.19 | Characteristic lines legend for squared tip at $\alpha = 12^\circ$, $Re = 10^5$ and $d = 3$ mm. | 78 |
| 3.20 | Mean flow and characteristic lines for squared tip at $\alpha = 12^\circ$, $Re = 10^5$ and $d = 3$ mm (characteristic lines legend from the most inboard to the nearest to the wingtip: L1 continuous line, L2 dashed–dotted line, L3 dashed line, L4 dotted line). | 79 |

| | | |
|------|--|-----|
| 3.21 | Mean flow and characteristic lines for squared tip at $\alpha = 12^\circ$, $Re = 10^5$ and $d = 3$ mm (characteristic lines legend from the most inboard to the nearest to the wingtip: L1 continuous line, L2 dashed-dotted line, L3 dashed line, L4 dotted line). | 80 |
| 3.22 | Smoke visualizations at $x_c = 0.7$, $\alpha = 12^\circ$ and $Re = 3000$ | 81 |
| 3.23 | Vortex formation diagram on a rectangular wing with rounded tip. | 82 |
| 3.24 | Schematics of the primary vortex streamlines and the evaluated reattachment points positions for measurement planes at different distances from the surface. | 83 |
| 3.25 | Characteristic lines for squared tip at $\alpha = 12^\circ$ | 83 |
| 3.26 | Characteristic lines at $d = 5$ mm and $\alpha = 12^\circ$ | 84 |
| 3.27 | Velocity components contours for a rounded tip at $Re = 10^6$ | 85 |
| 3.28 | In-plane vorticity contours for a rounded tip at $Re = 10^6$ | 86 |
| 3.29 | Characteristic lines and hot film positions. | 87 |
| 3.30 | Hot film signals standard deviations. | 89 |
| 3.31 | Square tip power spectra: $Re = 10^5$, $\alpha = 12^\circ$, $x_s = -0.20$ | 90 |
| 3.32 | Square tip power spectra: $Re = 10^6$, $\alpha = 12^\circ$, $x_s = -0.20$ | 91 |
| 3.33 | Rounded tip power spectra: $Re = 10^6$, $\alpha = 12^\circ$, $x_s = -0.20$ | 92 |
| 3.34 | Rounded tip power spectra: $Re = 10^6$, $\alpha = 4^\circ$, $x_s = -0.20$ | 93 |
| 3.35 | Signal spectra at $x_w = 1$ and $\alpha = 12^\circ$ | 94 |
| 3.36 | Signal spectra at $x_w = 1$ and $Re = 10 \cdot 10^5$ | 96 |
| 3.37 | Signal spectra at $\alpha = 15^\circ$ and $Re = 5 \cdot 10^5$ | 97 |
| 4.1 | Instantaneous velocity vectors and vorticity at $x_w = 1$, $Re = 5 \cdot 10^5$ and $\alpha = 12^\circ$; projection of the trailing edge in dashed line. | 103 |
| 4.2 | Instantaneous seeding distribution at $x_w = 1$, $Re = 5 \cdot 10^5$ and $\alpha = 12^\circ$ | 104 |
| 4.3 | Centering methods for an instantaneous realization at $x_w = 1$, $Re = 5 \cdot 10^5$ and $\alpha = 12^\circ$ | 108 |
| 4.4 | Instantaneous vortex centre positions calculated with different centering methods at $x_w = 1$, $Re = 5 \cdot 10^5$ and $\alpha = 12^\circ$ | 110 |
| 4.5 | Simple averaged flow field at $x_w = 1$, $Re = 5 \cdot 10^5$ and $\alpha = 12^\circ$; in-plane velocity minimum (black cross), axial velocity maximum (white cross). | 112 |
| 4.6 | Average swirl velocity profiles and mean values (red line) calculated with different centering methods at $x_w = 1$, $Re = 5 \cdot 10^5$ and $\alpha = 12^\circ$ | 113 |

| | | |
|------|---|-----|
| 4.7 | Average axial velocity profiles and mean values (red line) calculated with different centering methods at $x_w = 1$, $Re = 5 \cdot 10^5$ and $\alpha = 12^\circ$ | 114 |
| 4.8 | Velocity fluctuations at $x_w = 1$, $Re = 5 \cdot 10^5$ and $\alpha = 12^\circ$; part 1 of 2. | 117 |
| 4.9 | Velocity fluctuations at $x_w = 1$, $Re = 5 \cdot 10^5$ and $\alpha = 12^\circ$; part 2 of 2. | 118 |
| 4.10 | Instantaneous axial velocity peaks at $x_w = 1$, $Re = 5 \cdot 10^5$ and $\alpha = 12^\circ$ | 118 |
| 4.11 | Turbulence at $x_w = 1$, $Re = 5 \cdot 10^5$ and $\alpha = 12^\circ$; part 1 of 2. | 119 |
| 4.12 | Turbulence at $x_w = 1$, $Re = 5 \cdot 10^5$ and $\alpha = 12^\circ$; part 2 of 2. | 120 |
| 4.13 | Swirl velocity at $x_w = 1$, $Re = 5 \cdot 10^5$ and $\alpha = 12^\circ$ | 122 |
| 4.14 | Axial velocity at $x_w = 1$, $Re = 5 \cdot 10^5$ and $\alpha = 12^\circ$ | 122 |
| 4.15 | Convergence and errors of velocity and core radius at $x_w = 1$, $Re = 5 \cdot 10^5$ and $\alpha = 12^\circ$ | 123 |
| 4.16 | Vorticity at $x_w = 1$, $Re = 5 \cdot 10^5$ and $\alpha = 12^\circ$ | 123 |
| 4.17 | Convergence and errors of vorticity, helicity and swirling strength at $x_w = 1$, $Re = 5 \cdot 10^5$ and $\alpha = 12^\circ$ | 124 |
| 4.18 | In-plane velocity fluctuation σ_v at $x_w = 1$, $Re = 5 \cdot 10^5$ and $\alpha = 12^\circ$ | 124 |
| 4.19 | Reynolds shear stress $\overline{v'w'}$ at $x_w = 1$, $Re = 5 \cdot 10^5$ and $\alpha = 12^\circ$ | 125 |
| 4.20 | Shear strain ε_{yz} at $x_w = 1$, $Re = 5 \cdot 10^5$ and $\alpha = 12^\circ$ | 125 |
| 4.21 | Convergence and errors of velocity fluctuation, Reynolds stress and shear strain at $x_w = 1$, $Re = 5 \cdot 10^5$ and $\alpha = 12^\circ$ | 126 |
| 4.22 | Swirl velocity and slicing cuts at $\alpha = 8^\circ$, $x_w = 1$ and $Re = 5 \cdot 10^5$ | 128 |
| 4.23 | Vortex core shape at $Re = 1 \cdot 10^5$ and $\alpha = 12^\circ$ | 129 |
| 4.24 | Vortex core shape at $Re = 5 \cdot 10^5$ and $\alpha = 8^\circ$ | 129 |
| 4.25 | Vortex core shape at $\alpha = 12^\circ$ and $x_w = 1$ | 130 |
| 4.26 | Core shape fluctuation. | 131 |
| 4.27 | Vortex core shape for different averaging methods at $\alpha = 8^\circ$, $x_w = 0.5$ and $Re = 5 \cdot 10^5$ | 132 |
| 4.28 | Axial velocity profiles. | 133 |
| 4.29 | Core rotation estimation as function of the angle of attack at $Re = 1 \cdot 10^5$ | 134 |
| 4.30 | Vortex core shape for different tip geometries at $x_w = 0.25$ and $\alpha = 12^\circ$ | 135 |
| 4.31 | Estimation of the vortex core structure at the trailing edge. | 136 |
| 4.32 | Axial velocity contours and planar streamlines at $x_w = 1$ and $Re = 1 \cdot 10^5$ (M1 model). | 140 |
| 4.33 | Schematic of generic profiles of the axial velocity across the vortex in the early wake for different angles of attack. | 141 |

| | | |
|------|--|-----|
| 4.34 | Average axial velocity contours and planar streamlines at $x_w = 1$ and $Re = 1 \cdot 10^5$ (M1 model). | 142 |
| 4.35 | Axial velocity, vorticity and planar streamlines at $\alpha = 15^\circ$ and $Re = 5 \cdot 10^5$ (M1 model). | 143 |
| 4.36 | Axial velocity at the centre of the vortex as function of the circulation parameter. | 146 |
| 4.37 | Trendlines of the present work compared with other experimental data. | 148 |
| 4.38 | Velocity fluctuations in cartesian and cylindrical coordinates and turbulent kinetic energy in the wake of the M1 wing at $\alpha = 12^\circ$, $x_w = 1$ and $Re = 5 \cdot 10^5$ | 150 |
| 4.39 | Evolution in the wake of the velocity fluctuations and turbulent kinetic energy for $\alpha = 12^\circ$ and $Re = 5 \cdot 10^5$ | 152 |
| 4.40 | Turbulent kinetic energy at the centre of the vortex. | 153 |
| 4.41 | Evolution of the shear stress $\overline{v'w'}$ in cartesian coordinate for different angles of attack at $Re = 5 \cdot 10^5$ | 154 |
| 4.42 | Evolution of the shear strain ε_{yz} in cartesian coordinate for different angles of attack at $Re = 5 \cdot 10^5$ | 155 |
| 4.43 | Reynolds stresses in cartesian and cylindrical coordinates at $x_w = 1$, $\alpha = 12^\circ$, $Re = 1 \cdot 10^5$ | 156 |
| 4.44 | Evolution of the axial velocity in the wake for different angles of attack and $Re = 5 \cdot 10^5$ | 158 |
| 4.45 | Radial gradient of the axial velocity at $Re = 5 \cdot 10^5$ | 159 |
| 4.46 | Evolution of the shear stress $\overline{u'_x u'_r}$ in cylindrical coordinate for different angles of attack at $Re = 5 \cdot 10^5$ | 160 |
| 4.47 | Evolution of the average of the absolute value of the minimum and maximum peak of shear stresses in cylindrical coordinate for different angles of attack at $Re = 5 \cdot 10^5$ | 160 |
| 4.48 | Evolution of the normal stress $\overline{u'_r{}^2}$ in cylindrical coordinate for different angles of attack at $Re = 5 \cdot 10^5$ | 161 |
| 4.49 | Evolution of the stresses in cylindrical coordinate for different angles of attack at $Re = 5 \cdot 10^5$ | 161 |
| 4.50 | Axial velocity at $Re = 12.7 \cdot 10^5$ and $\alpha = 12^\circ$ | 163 |
| 4.51 | Vorticity at $Re = 12.7 \cdot 10^5$ and $\alpha = 12^\circ$ | 164 |
| 4.52 | Vorticity profiles and mean value (red line) at $x_w = 0.25$, $Re = 12.7 \cdot 10^5$ and $\alpha = 12^\circ$ | 165 |

| | | |
|------|--|-----|
| 4.53 | Swirl velocity profiles and mean value (continuous red line) at $x_w = 0.25$, $Re = 12.7 \cdot 10^5$ and $\alpha = 12^\circ$. Location of local maximum and minimum in dashed vertical red lines; velocity profile of the Lamb–Oseen vortex in blue. | 166 |
| 4.54 | Circulation profiles and location of local maximum and minimum of swirl velocity (vertical red lines) at $x_w = 0.25$, $Re = 12.7 \cdot 10^5$ and $\alpha = 12^\circ$ | 167 |
| 4.55 | Instantaneous vorticity at $x_w = 0.25$, $Re = 12.7 \cdot 10^5$ and $\alpha = 12^\circ$ for squared wingtip. | 168 |
| 4.56 | Vortex meandering for squared and rounded tips as function of the angle of attack at $Re = 7.4 \cdot 10^5$ | 168 |
| 4.57 | Evolution of the shear strain ε_{yz} for squared and rounded tip at $\alpha = 12^\circ$ and $Re = 12.7 \cdot 10^5$ | 170 |
| 4.58 | Evolution of the Reynolds shear stress $\overline{v'w'}$ for squared and rounded tip at $\alpha = 12^\circ$ and $Re = 12.7 \cdot 10^5$ | 171 |
| 4.59 | Turbulent kinetic energy at the centre of the vortex generated by rounded and squared tips. | 171 |
| 4.60 | Axial velocity at $\alpha = 0^\circ$, $x_w = 0.25$ and $Re = 7.4 \cdot 10^5$ | 173 |
| 4.61 | Vorticity at $\alpha = 0^\circ$, $x_w = 0.25$ and $Re = 7.4 \cdot 10^5$ | 174 |
| A.1 | Swirl velocity profiles for different laser pulse separations. | 205 |
| A.2 | Axial velocity profiles for different laser pulse separations. | 205 |
| A.3 | Vorticity contours for different laser pulse separations. | 206 |
| A.4 | Velocity fluctuations for different laser pulse separations. | 206 |
| A.5 | Cross-correlation procedure scheme (DaVis, 2007). | 208 |
| A.6 | Example of 50% interrogation window overlap (DaVis, 2007). | 208 |
| A.7 | Swirl velocity profiles for different interrogation window sizes. | 211 |
| A.8 | Axial velocity profiles for different interrogation window sizes. | 212 |
| A.9 | Swirl velocity profiles for different numbers of iterations. | 213 |
| A.10 | Axial velocity profiles for different numbers of iterations. | 214 |
| A.11 | Swirl velocity profiles for different interrogation window overlaps. | 215 |
| A.12 | Axial velocity profiles for different interrogation window overlaps. | 216 |
| B.1 | Common steps. | 220 |
| B.2 | BW steps. | 221 |
| B.3 | GRAY steps. | 222 |
| B.4 | Histogram of the light intensity for steps 1, 2 and 3. | 222 |

| | | |
|-----|--|-----|
| B.5 | BW method: instantaneous vortex positions (rounded tip, $x_w = 1$, $\alpha = 12^\circ$, $Re = 10^6$). | 223 |
| B.6 | GRAY method: instantaneous vortex positions (rounded tip, $x_w = 1$, $\alpha = 12^\circ$, $Re = 10^6$). | 223 |
| B.7 | BW method: vortex movement power spectra (rounded tip, $x_w = 1$, $\alpha = 12^\circ$, $Re = 10^6$). | 224 |
| B.8 | GRAY method: vortex movement power spectra (rounded tip, $x_w = 1$, $\alpha = 12^\circ$, $Re = 10^6$). | 225 |

List of tables

| | | |
|-----|--|-----|
| 2.1 | Summary of wing models characteristics and experiments. | 32 |
| 2.2 | Pressure tappings coordinates. | 37 |
| 2.3 | Summary of SPIV experiments (79 independent tests). | 44 |
| 4.1 | Core rotation estimate: $Re = 1 \cdot 10^5$, $\alpha = 12^\circ$ | 133 |
| 4.2 | Core rotation estimate: $Re = 5 \cdot 10^5$, $\alpha = 8^\circ$ | 133 |
| 4.3 | Wing models characteristics and experiments of references in Figure 4.37. | 148 |
| 4.4 | Important production terms of the Reynolds stresses. | 158 |
| 4.5 | Enstrophy dispersion radius in the wake of squared and rounded wingtips; $Re = 12.7 \cdot 10^5$ and $\alpha = 12^\circ$ | 164 |
| A.1 | Summarizing table of the processing procedures tested. | 210 |
| A.2 | Processing procedures: time and memory required. | 217 |

Nomenclature

List of symbols

Latin symbols

| | |
|-----------------------|--|
| A | anemometer constant, [V] |
| AR | aspect ratio of the wing, $= \frac{b}{c}$ |
| b | span of the wing, [m] |
| c | chord of the wing, [m] |
| c_P | pressure coefficient, $= \frac{P - P_\infty}{\frac{1}{2} \rho U_\infty^2}$ |
| d | distance of the SPIV plane from the wing surface, [mm] |
| D | diameter of the tube for the pressure measurement, [mm] |
| E | anemometer output voltage, [V] |
| f | frequency, [Hz] |
| \bar{f} | dimensionless frequency, $= \frac{f c}{U_\infty}$ |
| F_S | sampling frequency, [Hz] |
| H_x | streamwise helicity |
| k | turbulent kinetic energy |
| L1, L2, L3, L4 | vortex characteristic lines |
| M1 | high aspect ratio wing model |
| M2 | low aspect ratio wing model |
| N | number of measurements |
| N_{px} | interrogation window size, [number of pixels] |
| P | pressure, [Pa] |
| \bar{P} | averaged pressure, [Pa] |
| P_∞ | freestream stagnation pressure, [Pa] |

| | |
|--|--|
| $ P(f) $ | signal power spectral density |
| $ P_{yy}(f) $ | power spectral density of the displacements along the y axis |
| $ P_{zy}(f) $ | cross spectral density of the displacements along the z and y axes |
| $ P_{zz}(f) $ | power spectral density of the displacements along the z axis |
| Q | discriminant of the characteristic equation of the velocity gradient |
| r_{EN} | enstrophy dispersion radius, [m] |
| R | vortex core radius |
| $R(\theta)$ | directional vortex core radius |
| S | generic surface, [m ²] |
| r, θ, x | cylindrical coordinates |
| Re | Reynolds number, $= \frac{U_\infty c}{\nu}$ |
| u, v, w | velocity in cartesian coordinates |
| u_r, u_θ, u_x | velocity in cylindrical coordinates |
| u_{core} | core axial velocity |
| \mathbf{u} | velocity vector, [m/s] |
| $\bar{\mathbf{u}}$ | velocity vector mean, $= \mathbf{u} - \mathbf{u}'$, [m/s] |
| \mathbf{u}' | velocity vector fluctuation, $= \mathbf{u} - \bar{\mathbf{u}}$, [m/s] |
| U_∞ | freestream velocity, [m/s] |
| $\overline{u'^2}, \overline{v'^2}, \overline{w'^2}$ | turbulent normal stresses in cartesian coordinates |
| $\overline{u'^2}, \overline{u_r'^2}, \overline{u_\theta'^2}$ | turbulent normal stresses in cylindrical coordinates |
| $\overline{v'w'}, \overline{u'v'}, \overline{u'w'}$ | Reynolds stresses in cartesian coordinates |
| $\overline{u'_r u'_\theta}, \overline{u'_x u'_r}, \overline{u'_x u'_\theta}$ | Reynolds stresses in cylindrical coordinates |
| $\tilde{x}, \tilde{y}, \tilde{z}$ | dimensional cartesian coordinates |
| x, y, z | dimensionless cartesian coordinates |
| \mathbf{x} | generic coordinate vector |

Greek symbols

| | |
|-------------|--|
| α | angle of attack, [deg] |
| Γ | vortex circulation, [m ² /s] |
| $\Gamma(r)$ | vortex circulation distribution, [m ² /s] |

| | |
|--------------------------------------|--|
| ΔH | dissipation function, [m ² /s ²] |
| $\Delta \mathbf{x}$ | marker displacement, [m] |
| Δx_w | scaled distance along the streamwise direction |
| Δt | time interval, [s] |
| ε_{xx} | normal strain |
| $\varepsilon_{yy}, \varepsilon_{zz}$ | elongational strains |
| $\varepsilon_{yz}, \varepsilon_{zy}$ | shear strains |
| Θ | rotation of the vortex core, [deg] |
| λ_2 | eigenvalue of the tensor $\Sigma^2 + \Omega^2$ |
| ν | freestream kinematic viscosity, [m ² /s] |
| ρ | freestream density, [kg/m ³] |
| σ_m | scaled standard deviation of the vortex meandering |
| σ_r, σ_θ | scaled root mean square of the in-plane components of the velocity fluctuation in cylindrical coordinates |
| σ_R | scaled fluctuation of the vortex core shape |
| σ_u | scaled root mean square of the axial velocity fluctuation |
| σ_v, σ_w | scaled root mean square of the in-plane components of the velocity fluctuation in cartesian coordinates |
| Σ | strain tensor |
| τ_w | wall shear stress, [Pa] |
| ϕ | rotation rate of the vortex, [rps] |
| ω_x | scaled streamwise vorticity |
| $\boldsymbol{\omega}$ | vorticity vector |
| Ω | vorticity tensor |

Subscripts

| | |
|--------|-------------------------------|
| $()_c$ | wing chord reference system |
| $()_i$ | relative to measurement i |
| $()_s$ | wing surface reference system |
| $()_v$ | vortex reference system |
| $()_w$ | wake reference system |
| $()_0$ | relative to the vortex centre |

List of acronyms

| | |
|------|---|
| BVI | Blade Vortex Interaction |
| CCD | Charge Coupled Device |
| CSD | Cross Spectral Density |
| DNS | Direct Numerical Simulation |
| FFT | Fast Fourier Transform |
| LDV | Laser Doppler Velocimetry |
| LES | Large Eddy Simulation |
| PDV | Particle Displacement Velocimetry |
| PIV | Particle Image Velocimetry |
| PLV | Pulsed Light Velocimetry |
| POD | Proper Orthogonal Decomposition |
| PSD | Power Spectral Density |
| RANS | Reynolds–Averaged Navier–Stokes equations |
| RMS | Root Mean Square |
| RSM | Reynolds Stress Model |
| SPIV | Stereoscopic Particle Image Velocimetry |
| 2D2C | Two–Dimensional Two–Components |
| 2D3C | Two–Dimensional Three–Components |

Introduction

Can a mortal ask questions which God finds unanswerable? Quite easily, I should think. All nonsense questions are unanswerable. How many hours are there in a mile? Is yellow square or round? Probably half the questions we ask - half our great theological and metaphysical problems - are like that.

CLIVE STAPLES LEWIS

The greatest challenge to any thinker is stating the problem in a way that will allow a solution.

BERTRAND ARTHUR WILLIAM RUSSELL

When an aerodynamic surface of finite span, such as an airplane wing or a helicopter blade, moving relatively to the fluid produces lift, circular patterns of rotating fluid, namely vortices, are formed. These vortices generally develop near the tips of the lifting surface and they are found in the literature with different names such as wing vortices, tip vortices or trailing vortices. They are characterized by high vorticity levels, large regions of highly rotating fluid and a great persistence downstream of the surface. The big interest in these vortices comes from their great importance and the large number of applications where they can be found. An overview of the most common fields where wingtip vortices are observed and the main problems related to them is presented in Section 1.1. A discussion on the physical explanation of the presence of the tip vortex is given in Section 1.2 where different and complementary approaches are presented. The present state of the understanding of this important vortical flow is discussed in Section 1.3 where past experimental, numerical and theoretical studies are presented. Despite the wide range and large amount of studies on wingtip vortices, the literature review

reveals key points on the formation and early development of the vortex which are still unclear and need more attention. The position of this work in relation to the unresolved issues is expressly addressed in Section 1.4. It is anticipated that complementary views from different experimental techniques and a wide range of parametric and detailed experiments make of this research a fresh and deep contribution to the understanding of the complexity of the wingtip vortex flow. The guideline of the presentation of the results in the following chapters is described in Section 1.5.

SECTION 1

Why are wingtip vortices so important?

Wingtip vortices are most commonly related to vortices formed at the tip of airplane wings but they similarly occur in a variety of other situations. Moreover, the implications and effects that these vortices bring may considerably vary depending on the situation. For aircraft, a common mean of visualization of these vortical flows is by condensation of water vapour in the air. In the vicinity of the centre of the vortex the high centrifugal forces are balanced by strong radial pressure gradients. At the vortex centre the pressure reaches a minimum value which, for certain atmospheric conditions, causes the condensation of the water vapour. A collection of situations where the effects of wingtip vortices are particularly important is depicted in Figures 1.1, 1.2 and 1.3 which include vortices in the vicinity of airports and contrails in the sky; winglet devices for high aspect ratio wings and delta wing vortices; vortices from tips of airplane propellers, helicopter blades, wind turbine blades and marine propellers; vortices from wings of cars and the effects of vortices in the V -formation.

One of the major challenges in today's aeronautics is the problem of improving flight safety and the airspace in the vicinity of airports is particularly challenging (Vyshinsky, 2001; Hünecke, 2001). In particular, the encounter of an aeroplane during take-off or landing with the wake generated by a preceding aircraft can pose a serious hazard which is particularly dangerous because it occurs near the ground. Imposed roll, loss of altitude and strong structural loads are some of the dangers that the following aeroplane will suffer. Chigier (1974) has reported that over 100 serious injuries and deaths have occurred as a result of such encounters. To avoid such wake encounters, regulations require aircraft to maintain set distances behind each other and set time intervals between landings and take-offs. As a result of this, the operating costs to airlines and



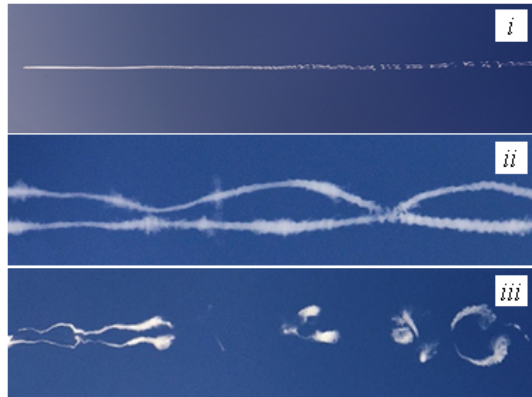
(a) Wingtip vortices from an Airbus A300 during take off (D. Umaña, jetphotos.net).



(b) Spiroid winglets mounted on the Aviation Partners Falcon 50 (planephotoman, flickr.com).



(c) Contrails behind a Boeing 747 engines entrained by wingtip vortices (J. P. Willems, airliners.net).



(d) *i* Crow instability forming in a contrail of a passing Boeing 747; *ii* and *iii* are zoomed pictures at different stages of the instability (herbraab, flickr.com).



(e) Bursting of delta wing vortices on Concorde wings during landing (Federation of Aeronautical Engineers blogspot).



(f) Vortices from the tips of the propeller blades of a Thunder Mustang (D. Cannon, Thunder Mustang blogspot).

Figure 1.1: Examples of wingtip vortices 1.

passengers are also severely impacted. Chambers (2003) presents the current regulation and research on this problem in the chapter on wake–vortex hazard. The goal of many researches on this aspect is to be able to create real–time automated systems that could measure and predict wake vortex conditions at airports so that planes may fly closer, airport congestion may be reduced and runway service rate increased.

An accurate understanding of the trailing of the tip vortex from a lifting wing is crucial also because the flow in the tip region has a great influence on the performance of the wing. The trailing vortex system is responsible for the downwash and consequently for the induced drag of the wing. During take–off, when the aeroplane is flying at high lift coefficients, the induced drag may contribute up to 60% to the total drag (Anderson, 2001). Understanding the physics of the vortex formation is therefore a key factor for the improvement of the wing efficiency. In the present economic and ecological scenario, a strong interest from aircraft companies on wing efficiency is drawn also towards its contribution to fuel burn saving and atmospheric carbon emission reduction (Lockney *et al.*, 2010). The study of the wingtip flow is very important also in the design of gliders where the efficiency of the wing plays a dominant role.

In the past decades, several solutions have been proposed either to alleviate or to benefit from the effects of the wingtip vortices on an aeroplane’s wing. Wing end–plates, wingtip tanks, vertical winglets, spiroid winglets, wingtip–mounted propellers (Snyder & Zumwalt, 1969), oscillating flaps (Gupta, 2011) and blowing devices (Gursul *et al.*, 2007) are just some of the many devices presented in the past years. The idea behind most of the wingtip devices is to diffuse the strong vortices released at the tip and to optimise the lift distribution, while maintaining the additional moments on the wing within certain limits (Arora *et al.*, 2005). Nevertheless, very few of the many wingtip concepts are actually adopted on wings. The difficulties in parametrically describing all those designs and in computationally testing them are still influencing designers of modern aircraft towards more known, corroborated and simple choices. A deeper understanding of the physics of the formation and evolution of the vortex is essential in improving predictions and research on wingtip devices. NASA research in the 1980s (Yates & Donaldson, 1986) assessed a number of winglets and other drag reduction devices, and they found that wingtip devices (such as winglets, feathers and sails) could reduce drag due to lift by 10 to 15% if they are designed as an integral part of the wing. The most recent winglet variants adopted on commercial airplanes, called raked wingtips, are the result of an integrated design of wing and wingtip, and they are represented by a tip region with a higher degree of sweep than the rest of the wing. The

Boeing 787 Dreamliner and Airbus A350 are among the aeroplanes which have adopted this solution.

The study of the wingtip geometry does not stop at the effects on the aeroplane but it extends to the vortex development behind the wing. In particular, the mechanisms causing the breakdown and decay of a counter rotating vortex pair is of great importance. As discussed earlier, vortices which dissipate quicker would enhance airport capacity. Jacquin *et al.* (2005) presented a short but complete overview of the important factors in the stability of trailing vortices and a comprehensive review of the studies undertaken over the past five decades on the types of vortex breakdown was provided by Lucca-Negro & O'Doherty (2001). One of the most common patterns that we see forming in the sky due to the passage of aeroplanes is called Crow instability (Crow, 1970), generated by the interaction of the two vortices so that symmetric sinusoidal oscillations with long wavelength develop. Also, recent studies on the prediction and limitation of such contrails aim to limit their influence on the global warming (Naiman *et al.*, 2009).

The inclusion of the vortices observed over delta wings as wingtip vortices is not strictly appropriate. Delta wing vortices, generated by the sharp and swept leading edges, are a major source of lift for this type of wing. These vortices develop all along the wing and they create a strong suction on the top surface near the leading edge, hence producing lift (Anderson, 2001). However, some of the mechanisms in the vortex formation are similar to those that can be observed in high aspect ratio wings such as the formation of secondary and tertiary vortices, the separation of the flow from a sharp edge and the reattachment of the flow on the wing surface. Because more resources and data can be found on delta wing vortices than on wingtip vortices, particularly on the vortex structure and unsteadiness, it is useful to relate the two phenomena.

A particular attention in the literature is also given to trailing vortices behind rotating blades such as aircraft propellers, helicopter rotors, wind turbines and marine propellers. The interaction between the wake of an aircraft propeller and the wing induces a considerable variation in the lift and drag distribution compared to wing encountering a clean flow. An optimal integration of the propeller and the airframe is a matter of recent researches (Thom, 2011). Also, unlike aeroplane wings and depending on the intensity of the flow parallel to the rotation axis, rotating blades may operate in the wake trailed from the preceding blades. This is often the case for helicopters where the interaction of the wake with the blade, commonly known as blade–vortex interaction (BVI), has profound effects on the aerodynamics and structural dynamics



(a) Tip vortices from the main rotor of an AH-1 Cobra in hovering flight (J. Diaz, gizmodo.com.au). (b) Smoke visualization of wingtip vortices from a wind turbine experiment (Chattot, 2007).



(c) Cavitating tip vortices and cavitation behind the shaft in an experiment on a marine propeller (National Research Council of Canada). (d) Tip vortices formed over the rear wing of an F1 car (G. McCabe, McCabism blogspot).

Figure 1.2: *Examples of wingtip vortices 2.*

of the rotor system. The velocity induced by the unsteady wake results in impulsive changes in the flow encountered by the rotor blades which significantly contribute to noise and vibration (Duraisamy, 2005). Wingtip vortices are also a major source of unsteadiness, noise and vibrations in wind turbines and the study of the structure of wind turbine wakes is the aim of many researches (e.g. Vermeer *et al.*, 2003; Massouh & Dobrev, 2007; Yang *et al.*, 2012).

Cavitation in marine propellers due to tip vortices is a very common phenomenon and it is an important factor in propeller design. Cavitation occurs as a consequence of the rapid growth of small bubbles that have become unstable owing to a change in the pressure. These bubbles either can be imbedded in the flow or come from small crevices at the bounding surfaces of the flow (Arndt, 2002). Cavitation is a significant cause of damage to components, of noise and vibration. Also, the extent of cavitation erosion

can range from a minor amount of pitting after years of service to catastrophic failure in a relatively short period of time.



(a) Pelicans flying in V-formation (fotosds, flickr.com). (b) Delta wing type vortices generated by a spoon moving vertically in a cup of coffee.

Figure 1.3: *Examples of wingtip vortices 3.*

Moreover, the control of wingtip vortices can be quite relevant in cars or sailing competitions where the high efficiency of wings, or in general aerodynamic surfaces, is demanded. However, it must be remembered that there are also instances where the effects of wingtip vortices are desired and favourable. An example is the use of vortex generators to avoid or delay flow separation, to enhance the lift of a wing or to reduce the drag of aircraft fuselage (Lin, 2002).

Also, migrating birds are commonly seen flying in V-formation. Such formation allows birds to fly in the upwash region of the wingtip vortex of the bird ahead (Hummel, 1983). The upwash assists each bird in supporting its own weight achieving a considerable reduction of induced drag. An extension of this concept was explored by NASA in the Autonomous Formation Flight Project when an F/A-18 flew in the upwash of the wingtip vortex of a DC-8 experiencing a 29% fuel savings and 14% of fuel savings was found for an F/A-18 flying in formation with another F/A-18. For a particular fleet configuration and wing spanload, Iglesias & Mason (2002) even predicted a negative induced drag (which is thrust) for the following aircraft.

Lastly, the same process of formation of tip vortices from lifting surfaces can be observed also in instances where generation of a lift force is unintentional. For example, the author found that the vertical movement of a spoon in a cup of coffee is one of these instances. The spoon, moving vertically at an angle with respect to the coffee surface, generates a lift force and two counter rotating delta wing-like vortices are observed in the cup.

SECTION 2

Theoretical background: why do wingtip vortices form?

The main and basic concepts of the existence of wingtip vortices are presented in this section. The case of a rectangular fixed wing is used as a reference but these concepts can be easily transferred to other instances. After a descriptive overview of the trailing vortex formation and development based on established observations, different models and mechanisms which explain the presence of the vortex will be presented. These different approaches can be viewed as the same phenomenon described from different perspectives.

Looking at the visualization of the flow in the vicinity of the surface of a rectangular wing at an incidence, in a region near the tip the streamlines on the suction surface are bent towards the root of the wing whereas the flow on the pressure surface are bent towards the tip (Green & Acosta, 1991; Chow *et al.*, 1997a). The roll up process is observed to originate near the leading edge when the flow is accelerated from the pressure side to the suction side and it wraps around the tip (Francis & Kennedy, 1979). In detail, with the development of this process along the tip, the flow coming from the pressure surface encounters a strong adverse pressure gradient which eventually forces the boundary layer to a separation (Duraisamy, 2005). The lifting off of fluid by the crossflow velocity in conjunction with the flow in the streamwise direction form a vortical structure with a strong helical motion. The vortex so formed grows in size and strength along the wing and secondary vortices are detected in the region of separated flow (Chow *et al.*, 1997a). The physics of this flow for aeronautical applications is extremely complex since the process is largely turbulent, highly three-dimensional and involves high velocity gradient regions with multiple flow separations (Chow *et al.*, 1997b). This vortical flow is convected downstream of the trailing edge and it eventually forms the trailing vortex (Devenport *et al.*, 1996). The flow embedded in the boundary layer grown over the surfaces of the wing is shed downstream of the trailing edge in the form of a thin sheet with a high level of vorticity. This wake is also entrained into the tip vortex and, at a distance of few chords from the trailing edge, a pair of counter-rotating axisymmetric trailing vortices is observed (Devenport *et al.*, 1996). This system of two parallel trailing vortices is unstable and a number of interaction mechanisms may appear as it moves downstream of the wing (see Widnall, 1975; Devenport *et al.*, 1997; Fabre

et al., 2002).

Looking at the complicated nature of the trailing vortex life, the requirement for simple models and elementary mechanisms which are able to shed light on the key physical factors is essential. Wu *et al.* (2006) explained the gap which is often found in fluid dynamics between the formulas and the local dynamics as follows.

“Suppose one is given a set of finite-domain data for a viscous flow over a body. One can then calculate the stress on the wall and [...] get the force. Then one may look at various fields in the domain: streamlines, velocity vectors, the contours of pressure and vorticity, etc. These together form a quite complete physical picture of the flow. However, if one wishes to identify the physical mechanisms that result in that force status, only some qualitative assessments can be drawn from these plots. They are still insufficient to pinpoint what flow structures have net contribution to the force, in what way, how, and why.

[...]

Modern aerodynamics is not merely a simple combination of the flow data and standard formulas [...]. The more complicated the flow is, the more important role will the key physical factors play. “Bypassing flow details as much as possible” (Wu, 2005) so as to reveal the key physical factors to force and moment is actually the most valuable legacy of the pioneering aerodynamicists, which should be continued and further enriched.” (Wu *et al.*, 2006, pp. 590-593)

A great and fundamental step forward in aeronautics came with the Lanchester-Prandtl *finite wing theory*¹ which showed how data from a two-dimensional aerofoil could be used to predict the aerodynamic characteristics of a wing of finite span. Such a model was also very important in understanding the role of trailing vortices in the generation of the lift and the reason for their formation.

Within this model, the lifting wing and its wake are replaced by a system of vortices that imparts to the surrounding air a motion similar to the actual flow and generates a force equivalent to the lift. The vortex system can be divided into three main parts which together form a vortex ring: the starting vortex, the trailing vortex system and the bound vortex system (Houghton & Carpenter, 2003). Whereas the first two are observable physical entities, the bound vortex system is a hypothetical arrangement of

¹For an historical account of the development of the finite wing theory see Anderson (2001, p. 408).

a number of vortices which replace the real physical wing and where the vorticity of each vortex filament is associated with the spanwise gradient of the wing circulation distribution. This upstream segment of the vortex ring represents the boundary layer of the upper and lower surfaces of the wing and it is the source of the lift and drag through pressure and shear stress distributions. The distribution of vortex filaments eventually merge into the trailing vortex system downstream of the wing. Moreover, the starting vortex is soon left behind and for practical purposes the trailing vortices are often modeled as stretching to infinity. Because of its shape, the resulting system, which models the wing and its wake, is known as *horseshoe vortex* and it is sketched in Figure 1.4(a).

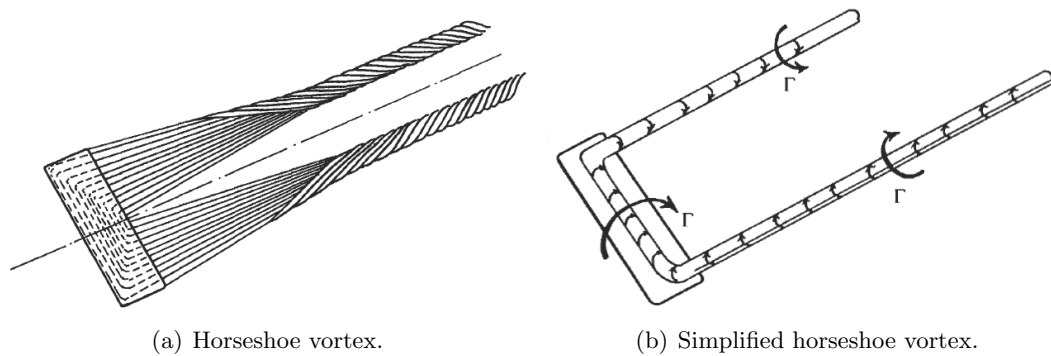


Figure 1.4: Vortex systems replacing the lifting wing and its wake (Houghton & Carpenter, 2003).

The horseshoe vortex is an important representation of the lifting wing and the lattice method derived from this representation is a powerful numerical tool for the investigation of the global effects of the wing configuration and geometry. For estimation of distant phenomena such as vortex effects on flight formation (Iglesias & Mason, 2002), a *simplified horseshoe vortex* model is adopted which is formed by a single bound vortex and two trailing vortices as sketched in Figure 1.4(b). Based on Helmholtz theorems² valid for inviscid and incompressible flows, the vortex filament replacing the wing will continue in the wake as two infinitely long free trailing vortices and the strength of the bound vortex is equal to the strength of the trailing vortices. Although the viscosity

²Helmholtz theorems establish basic principles on the vortex behaviour (Anderson, 2001; Wu *et al.*, 2006):

1. the strength of a vortex filament is constant along its length;
2. a vortex filaments can not end in a fluid; it must extend to the boundaries of the fluid or form a closed path;
3. in the absence of rotational external forces, a fluid that is initially irrotational remains irrotational which is to say that the strength of a vortex filament does not vary with time.

plays a crucial role in the interaction of the fluid with the wing, during the vortex formation, roll up, evolution in the wake and final dissipation, this model is able to give accurate results on the lift generated by the wing. Furthermore, the horseshoe vortex model explains and justifies the formation and existence of wingtip vortices with conservation laws.

The self-induced motion of the wake sheet shed from the wing generates a rolling of the sheet around its ends which eventually forms two separated vortices (see Figure 1.4(a)). The study of the shape that the wake assumes during this process is known as *Kaden problem*. Kaden (1931) was the first to derive a similarity law of the geometry of a tightly rolled semi-infinite vortex sheet for an elliptical load distribution on the wing. The evolution with the time of a typical vortex sheet is represented in Figure 1.5. Moore & Saffman (1973) also obtained the Kaden law by a dimensional analysis.

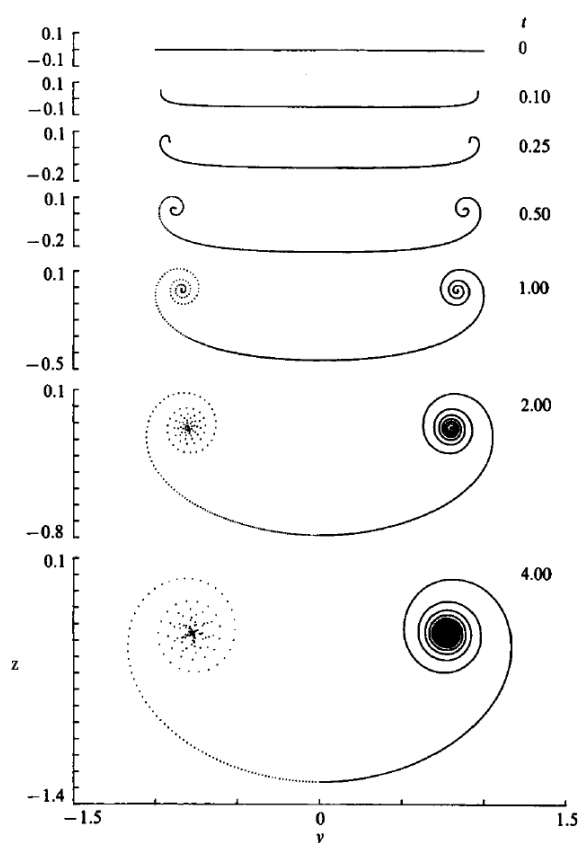


Figure 1.5: Early stage of the roll up of the wake sheet. The vortex sheet element positions are plotted on the left and an interpolating curve is plotted on the right (Krasny, 1987).

The mechanism of the formation of the tip vortex on the wing can be explained also by other complementary approaches than the finite wing theory and the Kaden problem. One of these views, probably the one which is most commonly used for its simplicity

and immediacy, is the *pressure field interpretation*, represented in the sketch of Figure 1.6. The physical mechanism for generating lift of the wing is the existence of a higher pressure on the bottom surface than on the top surface (the contribution to the lift of the shear stress is usually negligible). The net imbalance of the pressure distribution creates the lift (Anderson, 2001). The flow near the wingtips, forced by the difference of pressure between the two surfaces, curls from the bottom to the top side of the wing. As a result, the flow on the lower surface of the wing presents a spanwise component directed from the root to the tip causing the streamlines to bend, and vice versa for the upper surface. The crossing flow cannot move indefinitely in the spanwise direction along the upper surface because of the gradual equalization of the pressure which, combined with the streamwise velocity component, produces a convection of the flow in the direction of the trailing edge in a vortical motion (Duraismy, 2005). Moreover, the difference of directions of the flow from the pressure and the suction surfaces results in a thin vorticity layer which represents the wake sheet.

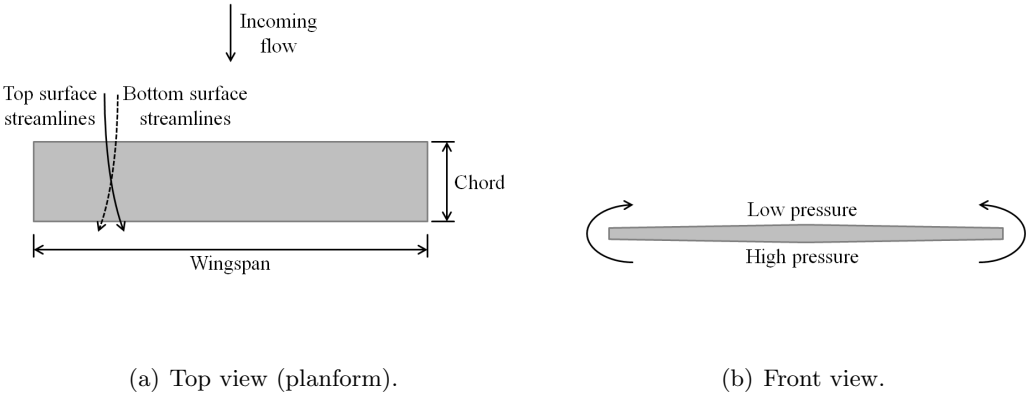


Figure 1.6: *Pressure field interpretation of the wingtip vortex formation.*

Another way to explain tip vortices is based on the *shear layer* that exists near the wingtip (Green, 1995). The undisturbed flow on a plane some spanwise distance away from the wing, parallel to the wing incoming flow, is sketched in Figure 1.7 along with the projection of the flow over the wing surface (assuming no separation). The non-parallelism of the wing surface and the freestream velocity vectors implies the existence of vorticity approaching the wingtip. This mechanism is important because it explains the existence of two vortices of opposite sign and same magnitude behind a wingtip also when there is no generation of lift.

As presented, several approaches can be taken to describe the reasons of the generation of wingtip vortices and each one underlines different and complimentary physical

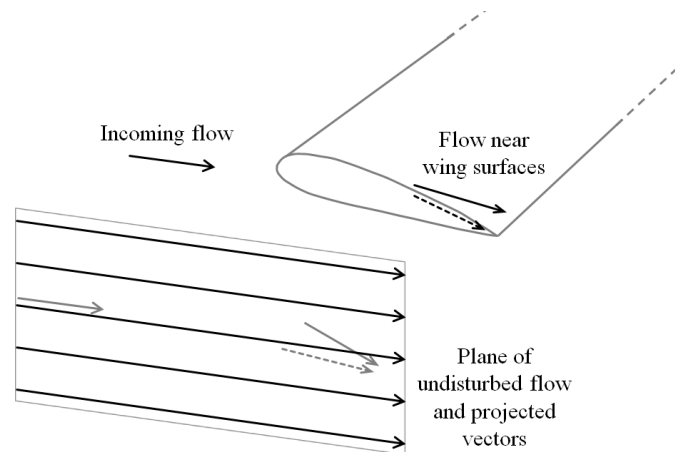


Figure 1.7: *Shear layer interpretation of wingtip vortex formation.*

factors of the trailing vortex life. However, much of the real flow in the early development and formation is still hidden and in particular the role of boundary layer, viscosity and turbulence is not described by these approaches. This lack can be justified by the complexity needed by more comprehensive approaches and the good overall accuracy of the present models. However, this lack of more sophisticated models comes also from a still unsatisfactory understanding of this flow.

SECTION 3

Literature review: what is the current understanding of wingtip vortices?

Looking at the importance of tip vortices, the number of applications where they are found and the complexity of the flow field, it is not surprising to find a wide scientific literature and several intensive research programs on this flow. Since the beginning of the 1960s, the aerospace industry started to understand the importance and the implications that wingtip vortices have. Hundreds of scientists have faced the challenges of this flow and have contributed to a deeper and clearer understanding through analytical, experimental and numerical studies.

The experiments of the present research focus on a single vortex trailed from the tip of a fixed wing mounted on the wall of a wind tunnel. Although this choice limits the study to a specific field, the subjects which are addressed are general and most of the observations and conclusions are true also for a wider range of applications, especially

when they regard the physics of the early formation of the vortex. In fact, the roll up mechanism of the flow around the tip of a lifting surface is similar for many of the applications. Also, the vast majority of the studies found in the literature focuses on fixed wings although in the recent years many studies are found also on the wake of helicopter blades (e.g. Ramasamy *et al.*, 2009c, and related works).

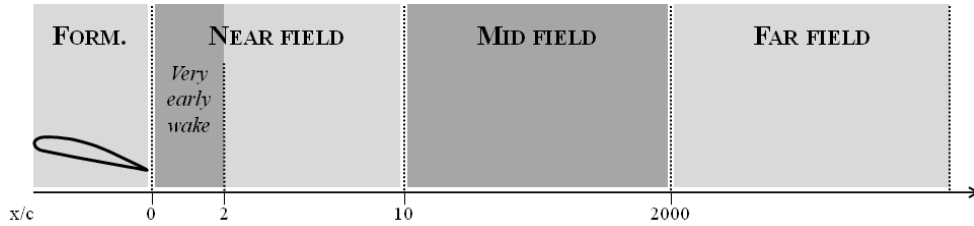


Figure 1.8: *Vortex life schematics: the approximate length scale is taken from Albano et al. (2003) for a typical airplane although they may drastically vary depending on the case (see for example Dieterle et al. (1999) for a different length scale).*

One of the possible classifications of the studies on fixed wings is based on the distinction of the vortex life into different zones as sketched in Figure 1.8, each one characterized by different phenomena and different life times (Francis, 1976; Albano *et al.*, 2003). The *formation* of the vortex begins on the wingtip. The flow moves from the pressure to the suction surface and generates a vortical structure which develops along the wing. The *near field* or *near wake* extends from the trailing edge to some chords behind the aircraft where a complete roll up of the wake is observed and all the circulation is contained in the vortices. In this range, secondary flow structures interact and merge with the trailing vortices (e.g. wake sheet, secondary tip vortices, vortices from flaps and tail, vortex sheet from nacelles, wing–fuselage junction). The number of vortical structures observed in this region depends on wing configuration and the airplane geometry (Gerz *et al.*, 2001). The resulting trailing vortex appears as an axisymmetric line vortex with smooth velocity profiles. A sub–region, namely *very early wake*, confined in few chords behind the trailing edge of the wing, can be also defined. In this region, the influence of the wing geometry is of great importance and the primary vortex shows a remarkable asymmetry³. The *mid field* region is characterized by the development of a number of axisymmetric line vortices and it can extend up to few hundreds chords from the wing. In this region, the vortex circulation decays at a relatively small rate, defined as the *diffusion regime* (Gerz *et al.*, 2001). Lastly, the *far field* region is the phase where vortices show instability mechanisms which remarkably

³The notation of *extended near wake* can also be found in the literature and it corresponds to the present definition of *near wake*.

change their shape. The vortex circulation presents a rapid decay and breakdown; vortex interaction and dissipation are observed in this region.

Because of the different nature of the phenomena observed in each region, studies do not usually focus on the whole vortex life but only on a limited range. Moreover, the dual requirement of high resolution for detailed studies in the formation and near field regions, and the large domain needed for the development of instabilities and the observation of the decay, is usually too demanding for either experimental or numerical studies.

(a) Far and mid field The study of far field and mid field is very important especially for problems related to the wake encountering following airplanes. Gerz *et al.* (2001) present two possible strategies for the generation of less harmful wakes, both based on the reduction of roll moments on follower aircrafts by specific modifications during the vortex system formation. The *quickly decaying vortex* strategy aims at anticipating the onset of instabilities, hence the occurrence of the far field, which lead to an early decay of the vortex system; the *low vorticity vortex* strategy aims at producing weaker vortices when observed in the mid field. These two strategies can be seen also as two different views of the long term behaviour of trailing vortices: predictable decay and stochastic collapse (Spalart, 1998).

A common and effective way to accelerate the dissipation of trailing vortices is to force three-dimensional instabilities. The time required to break up the vortices under natural conditions depends on several factors such as the strength of the atmospheric turbulence, the number of trailing vortices, the dominant instability mechanism and the growth rate of that particular instability. Many numerical studies and instability criteria can be found for the far field and experimental works in this region are usually based on flow visualizations (e.g. smoke injected in the trailing vortex). Rossow (1999) presented an extensive review of studies on trailing vortex instabilities and several mechanisms of interaction between pairs of vortices. Wavelengths and amplitudes of such instabilities are shown to be strongly affected by initial disturbances. For instance, a typical value of the most amplified wavelength of the Crow instability behind an aircraft (Crow, 1970) with an elliptically loaded wing is of about 8 times the vortex spacing. Leweke & Williamson (1998) presented a well balanced theoretical and experimental work on the interaction between short wavelength and long wavelength instabilities in the breakdown of a vortex pair. However, more realistic airplane wakes present multiple vortex pairs (Jacquin *et al.*, 2001) generated for instance by flaps, ailerons and

horizontal tail, which can reduce the time required for safe wake encounters of following airplanes by a factor of 4 or more (Rossow, 1999) and increase the complexity in the evolution and in the parametrization of the phenomenon. Crouch (1997) derived a set of stability equations describing the growth of disturbances in a system composed of two vortex pairs modeling respectively the wing tip vortices and the flap vortices. Two instability mechanisms, with wavelengths spanning between 1.5 and 6 of the vorticity centroid spacing, which influence the final break up of the vortices are described for this configuration. Rennich & Lele (1999) and Fabre & Jacquin (2000), adopting Direct Numerical Simulation (DNS) and a vortex filament method, also observed these mechanisms and they showed the beneficial effects on the instability growth rate which can be obtained by introducing long wavelength perturbations in the vortex system. Holzäpfel *et al.* (2001) performed a large eddy simulation (LES) of a vortex pair superimposed with aircraft induced turbulence and atmospheric turbulence. They observed that the short wavelength instability is triggered by atmospheric and wake turbulence and leads to a quicker decay of the vortex circulation. Moreover, Billant *et al.* (1998) and Jacquin & Pantano (2002) showed that the stability of a single vortex is strongly affected by the swirl parameter, proportional to the ratio between the maximum swirl velocity and the axial velocity at the centre of the vortex. Duraisamy & Lele (2008) described the mechanism of angular and axial momentum transport of an isolated turbulent trailing vortex in terms of secondary turbulent structures moving radially from the vortex core to the external flow. Moreover, Khorrami (1991) described an axisymmetric viscous mode of trailing vortex instability which presents successive and sudden expansions (*bursting*) of the vortex.

The mid field is particularly important because most of the vortex models and analytical studies refer to assumptions and approximations to the Navier–Stokes equations which are satisfied only in this region. Axisymmetry, stationarity, incompressibility, boundary layer–type approximation, small axial perturbation (light loading) are some of the assumptions commonly adopted (see Hoffmann & Joubert, 1963; Batchelor, 1964; Moore & Saffman, 1973; Phillips, 1981) and they lead to self–similar solutions of trailing vortices (Birch, 2012). The fundamental governing equations of laminar and turbulent isolated vortices are reported in Appendix C. Experimental studies confirmed these assumptions to be reasonably valid (e.g. Devenport *et al.*, 1996; Ramasamy, 2004). However, measurements in the mid and near field are complicated by the phenomenon of meandering (Green & Acosta, 1991; Devenport *et al.*, 1996; Heyes *et al.*, 2004). Meandering, also known as wandering, is attributed to a variety of reasons (Jacquin *et al.*,

2001) including freestream turbulence, intermittency, interference with wind tunnel unsteadiness, amplification of vortex instabilities, perturbation due to the rolling up shear layer and propagation of unsteadiness originating on the model. As a result, time-averaged point measurements become weighted averages in both space and time (Green & Acosta, 1991) so that the measured data needs to be corrected. Depending on the measurement technique, different correction models have been suggested (e.g. Devenport *et al.*, 1996; Leishman, 1998; Heyes *et al.*, 2004; Ramasamy *et al.*, 2011). Use of uncorrected data gives an apparent “smeared-out” version of the actual flow field and may contribute to large errors, especially in the vortex dimensions and swirls and axial velocity peaks. Most experimental measurements prior to the 1990s do not account for the effect of wandering and should therefore be interpreted with caution (Duraisamy, 2005).

A variety of analytical descriptions of vortices can be found although they may correspond to real flows only in a local region or for a finite period of time (Wu *et al.*, 2006, chapter 6.2). Assuming laminar flow, Batchelor (1964) derived an axisymmetric similarity solution for a steady incompressible isolated vortex, which has been often used as a viscous solution suitable to describe a wake vortex in the mid field. Further, assuming that axial gradients were much smaller than radial gradients (boundary layer-type approximation), Batchelor described the inviscid driving mechanism for the development of the axial flow in terms of low pressure and importance of viscous effects within the vortex core. Moore & Saffman (1973) extended the above analysis taking into account also the roll up process of the wake and they were able to relate the mid field vortex velocity field from a rectangular wing to the Reynolds number and the angle of attack.

Since the trailing vortex flow of most of the applications presents turbulence, a considerable number of authors studied the Reynolds-averaged momentum equations (presented in Appendix C) analytically and numerically. Hoffmann & Joubert (1963) introduced isotropic eddy viscosity assumption to represent the turbulence inside a trailing vortex. Iversen (1976) used the mixing length analogy and derived a similarity solution using empirical inputs and he predicted the structure of a turbulent vortex as a function of the Reynolds number for both laminar and turbulent cases. Phillips (1981) studied the turbulent roll up of a vortex sheet and predicted in detail the structure of the swirl velocity and the Reynolds stresses profiles. Specifically, he divided the vortex region in three concentric regions.

1. The innermost part presents predominantly viscous effects and the swirl velocity decreases linearly to zero in correspondence to the vortex centre. In addition,

approaching the centre, the rotation is close to a solid body rotation and the Reynolds shear stress goes to zero with the square of the distance from the centre. In this region, the stabilizing effects of the rotation of the flow are believed to promote relaminarization.

2. The second region is located around the point of maximum swirl velocity (vortex core radius). The viscous effects are small and in this highly strained turbulent region a logarithmic law for the circulation applies (Hoffmann & Joubert, 1963).
3. In the outer region the flow is turbulent, the swirl velocity decays as a potential vortex (which is as $1/r$) and the Reynolds stress goes to zero as $1/r^2$.

Different investigations (e.g. Ramaprian & Zheng, 1997; Birch & Lee, 2005) demonstrated that the circulation distribution in the first two regions shows a universal behaviour already in the very near field, which is described by semi-empirical laws. However, Birch (2012) demonstrated also that the wandering of the vortex, if is not correctly removed, can give a strong contribution in converging the circulation profile upon the universal profile.

The effects of turbulence in the diffusion and decay of trailing vortices are still in an area of disagreement (Spalart, 1998), also because different sources of turbulence can be identified such as boundary layer, viscous wake, vortex sheet rolling up and atmosphere. Moreover, the behaviour of the turbulence within the vortex core is also a matter of many studies. Cotel & Breidenthal (1999) used Bradshaw's analogy (Bradshaw, 1969) between streamline curvature and stratification to explain the possible relaminarization process in the vortex core. Ramasamy & Leishman (2004) extended the similarity proposed by Iversen (1976) to account for the relaminarization and they found a good correlation of the swirl velocity profiles between the theory and the experiments. A region of transition between laminar and turbulent flow within the vortex was predicted. Bandyopadhyay (1990) explained a mechanism of relaminarization by centrifugal motions of patches of turbulent flow moving from an outer annulus into the vortex core. This mechanism is consistent with the existence of secondary structures convected along the vortex.

Whereas a number of analytical studies can be found on the evolution of vortex properties in the far wake, the interaction between wing and flow and the complex structure in the near wake strongly limit an analytical description. The importance of studying the formation and early wake of a trailing vortex lies in the framework of finding a link between the early stage and the development in the far wake. The question on if it is possible to infer from the near field data (e.g. vortex topology,

spacing, circulation distribution) the behaviour in the far field is still open (Gerz *et al.*, 2001) and a proven method to characterize and control wake vortices is not available yet.

(b) Formation and near field The assumptions adopted in the far field are violated in the near field: the velocity field during the formation on the wing and in the early wake is not axisymmetric; multiple vortices and interactions with the wake sheet generate an unsteady flow; strong gradients and axial perturbations can be observed in the vortex core; turbulence intensity is large. Moreover, the wing geometry and the formation process strongly affect development and characteristics of the vortex and the identification and understanding of the dominant phenomena taking place in this region is still poor. For these reasons, a vast literature covering the last 4 decades is found regarding the early life of wingtip vortices where wind tunnel experiments and Computational Fluid Dynamics (CFD) have been the main approaches⁴. Furthermore, the investigation techniques have greatly changed over the years resulting in a great improvement of the accuracy of the results.

The first important investigation of the near field of tip vortices was made by Grow (1969) using a five-hole pressure probe and a vorticity meter. He studied the effect that the wing geometry and the boundary layer have on the trailing vortex. An increase of vortex circulation and maximum swirl velocity was found with the increase of aspect ratio, taper ratio and angle of attack.

Chigier & Corsiglia (1971) measured the tip flow generated by a NACA 0015 wing with squared tip at different distances from the trailing edge and during its formation on the surface. This investigation was based on triple-sensor hot wire velocimetry and surface pressure measurements. A maximum axial velocity of 1.4 times the freestream velocity was found during the formation at three quarters of chord. The axial velocity reduced to $1.1U_\infty$ at the trailing edge and a positive gradient in the axial direction

⁴Actually, the reasons of such a big number of studies on this topic can be more complex as explained by Conlisk & Komerath (2001):

“The reasons are three-fold. The first is the omnipresence of vortices in fluid dynamics, complicated by the sheer variety of phenomena encountered when vortices interact with their environment, and the potential benefits in reliably controlling vortex-dominated flows. The second is the limited opportunity (and willingness in some cases) of researchers to go beyond their application area to look for answers to problems by tying together the clues observed by others. The third is that information is not readily available in integrated form on the actual formation process of a vortex. As we demand more detailed prediction of vortex behavior, we see that it depends strongly on the formation process: the textbook model of solid-body-rotation in the core, and $1/r$ dropoff in tangential velocity outside, is not enough.”

was observed up to 3.75 chords downstream of the trailing edge with a final axial velocity of $1.2U_\infty$. This behaviour might be related to the vorticity intensification by the mechanism of *vortex stretching* as presented in Appendix C.2. Moreover, from integration of the wall pressure, generation of lift was observed in the tip region. On a later study (Chigier & Corsiglia, 1972), they showed increasing level of turbulence at the vortex centre line when the angle of attack was increased.

Orloff (1974) measured the mean velocity field at two chords downstream of a NACA 0015 wing with rounded tip using a two-dimensional laser velocimeter. Defect and excess of axial velocity at the centre of the vortex with respect to the freestream velocity was observed respectively for an angle of attack of 8° and 12° . He also demonstrated the usefulness of laser velocimetry in quantitatively assessing the relative effectiveness of vortex alleviation devices (specifically of dissipator panels).

Thompson (1983) performed visualizations with hydrogen bubbles and dye in a water channel to study the vortex formation for different wingtip geometries. The squared tip produced flow separation from the sharp edges and two distinct vortices were observed for the rounded tip. The secondary vortex, located outboard of the primary vortex, is induced by the primary one and presents opposite sense of rotation. When the secondary vortex rolled up and wrapped in the primary vortex, a rapid change of direction of the primary vortex core was observed.

Francis & Katz (1988) presented the development of the tip vortex on a rectangular wing at different Reynolds numbers and angles of attack. Illumination with a thin laser sheet together with distribution of dye were utilized as means of observation and several dimensions were measured off the video recordings. The flow at the squared tip was dominated by multiple vortex structures including the main counter rotating vortex, shear layer eddies and several other secondary structures.

A notable work was presented by McAlister & Takahashi (1991) who carried out an extended experimental campaign on a rectangular wing as function of a number of parameters: chord length, aspect ratio, wingtip geometry, Reynolds number and angle of attack. They adopted pressure measurements on the wing and two-component laser velocimetry for the evaluation of the mean flow. Trends of the main features with the variation of the above parameters were given such as wing circulation; lift, drag and moment coefficients and peaks and distributions of the swirl and axial velocity. The presence of the vortex system generates regions of suction near the wingtip on the upper surface which has the effect of producing an increase in the lift distribution over the end part of the wing. On planes near the trailing edge, the swirl velocity profiles of a vortex

from a high angle of attack showed inflections which were attributed to the presence of secondary vortices, and the initial shape of the axial velocity presented simultaneous regions of deficit and excess compared to the freestream velocity.

Shekarriz *et al.* (1993) also observed that the circulation and swirl velocity profiles in the near field are dominated by the presence of secondary vortices. They implemented particle displacement velocimetry (PDV) to measure the global instantaneous velocity distribution within a tip vortex. An axisymmetric vortical structure was observed at less than 1 chord downstream of the trailing edge of the wing and a constant overall circulation was measured in the whole range studied (up to 6.7 chords from the trailing edge).

Another important study is the work by Chow *et al.* (1997a) (see also Chow *et al.*, 1992, 1997b) which represented a benchmark for several following numerical studies (e.g. Dacles-Mariani *et al.*, 1993; Dacles-Mariani & Kwak, 1996; Dacles-Mariani *et al.*, 1997; Kim & Rhee, 2005; Duraisamy & Iaccarino, 2005; Craft *et al.*, 2006; Churchfield & Blaisdell, 2009). The accuracy of the measurement technique and the detailed description of the wingtip in its formation and evolution in the near wake is still now hardly matched. Several experimental techniques were adopted for qualitative and quantitative measurements such as laser-illuminated smoke visualizations, surface oil flow visualizations, surface pressure measurements, 7-hole pressure probe measurements and triple-wire probe velocimetry. The correlation of the results from these different techniques allowed an accurate description of the process of formation and initial roll up of the wingtip vortex generated by a low aspect ratio wing with symmetric profile and rounded wingtip at a fixed angle of attack and Reynolds number. Highly three-dimensional flow was observed on the wing surface near the tip. Crossing of flow from the pressure to the suction surface was observed as early as 30% of the chord from the leading edge. The presence of a secondary and a tertiary vortex was indicated by convergence lines in the surface visualizations between the main vortex separation line and the wingtip. The pressure coefficient on the surface was minimum in correspondence to the core of the main vortex. A maximum axial velocity of $1.77U_\infty$ was found at the vortex centre just downstream of the trailing edge followed by a slow decrease, differently from the experiments by Chigier & Corsiglia (1971), to a value of $1.69U_\infty$ at 0.69 chord from the trailing edge. An important achievement was the measurement of the Reynolds stresses in the near field. The evolution and distribution of the turbulent stresses and a discussion of the importance of the different terms in the Reynolds stresses transport equations was presented. They found that the production of the tur-

bulence within the vortex in the early wake is associated with the high axial velocity gradients in the vicinity of the vortex centre. However, relaminarization had a much larger effect which resulted in a high decay rate of the overall turbulence within the vortex core. Misalignment of the distributions of the shear stress and the mean strain rate were measured within the vortex, which makes isotropic eddy viscosity models for the turbulence closure of Reynolds-averaged Navier-Stokes simulations (RANS) deficient in accurately representing the turbulence field (Dacles-Mariani *et al.*, 1997). For this reason, more recent numerical simulations adopt different models (e.g. Duraisamy & Iaccarino, 2005; Craft *et al.*, 2006) which better predict the early wake of a wingtip vortex. However, simulations still find difficulties when predicting the turbulence and the diffusion of the vortex core. Only in recent years, LES on wingtip vortices have become feasible and they showed a better agreement with the experimental results than RANS simulations. For instance, Jiang *et al.* (2007) described a primary tip vortex originally turbulent which then rapidly relaminarized after shedding in the near field. Moreover, Cai (2006) observed that the turbulence inside the primary vortex is caused by the turbulent shear layer and the interaction between the primary and the secondary vortices.

A considerable work on the vortex meandering and turbulence was presented by Devenport *et al.* (1996) who studied the wingtip vortex in the wake of a rectangular wing at a distance between 5 and 30 chords from the trailing edge. They noted that the meander creates a smoothing effect that can make the vortex appear with a larger diameter and reduced swirl and axial velocity peaks compared to the instantaneous vortex. Moreover, artificially large values of turbulent stresses may result from experiments that do not correct for vortex meandering. They also showed a complex structure of the turbulence within the vortex core and in the spiral layer around it. Velocity spectra measured at the vortex centre indicated that the vortex core was laminar and that velocity fluctuations in this region were a consequence of “inactive motions” produced by turbulence in the surrounding spiral wake. Some of the profiles, especially those measured at upstream locations, showed a two-layered structure formed by an outer core affected by a secondary vortex formed during the roll up process and an inner core growing within it. These results were compared with RANS simulations by Lockard & Morris (1998) and Spall (2001) who presented considerable discrepancies on the diffusion of the vortex moving downstream (respectively overpredicting and underpredicting the diffusion).

Stereoscopic particle image velocimetry (SPIV) on wingtip vortices was first adopted

by Zuhai (2001) (see also Zuhai & Gharib, 2001) who measured the three-dimensional velocity field in the near field of a rectangular wing with squared tip. The wing generated multiple vortices of opposite signs. Farther downstream, the vortices with opposite direction of rotation broke up into smaller vortices which orbited around the tip vortex. This study confirmed that the interaction of the tip vortex with satellite vortices is a main cause of meandering generating unsteady motions of the primary vortex.

Birch *et al.* (2003) (see also Birch *et al.*, 2004) presented measurements on the wing and on the trailing vortex using PIV, a 7-hole pressure probe and a balance for force measurements. They allowed variations of the tip geometry to establish its influence on the growth of the main structures. Multiple vortices were observed around the main vortical structure. The core radius, the maximum swirl velocity and the axial velocity peak of the vortex significantly increased with the angle of attack. Also, depending on the angle of attack, the axial velocity in the core was directed either towards the wing or away from it.

Bailey *et al.* (2006) (see also Bailey & Tavoularis, 2008) studied the vortex formation and development around a squared tip up to 9 chords downstream of the wing using a four-sensor hot-wire probe. From the analysis of the velocity fluctuations, two kinetic energy peaks were found, one above the suction surface and another near the tip surface. Approaching the trailing edge, the two peaks merged together and a new smaller peak appeared on the tip surface. These three peaks were associated with respectively primary, secondary and tertiary vortices and they were confirmed by flow visualizations through dye injection. An attentive comparison of the wingtip vortex formation for different freestream turbulence levels showed that, although the amplitude of the wandering depended on freestream conditions, its wavelength is insensitive to changes in the freestream turbulence. Recent works on the meandering were presented by Del Pino *et al.* (2009) and Del Pino *et al.* (2010) who observed elliptical distributions of the instantaneous vortex centre positions. They also performed proper orthogonal decompositions (POD) of the vortex movement identifying the main frequency of the most energetic mode (axisymmetric base vortex flow) as the frequency characterizing the vortex meandering.

Due to its increased reliability and accuracy, PIV technique has gained the reputation of a powerful and time effective flow diagnostic method for the quantitative whole-field study of complex fluid flows (Scarano, 2002). In addition to the studies mentioned above, several other experiments on wingtip vortices based on PIV measurements can be found in the recent years. These works focus on different aspects such as effects of

the wing geometry, formation process, meandering structure and shape of the rolled up vortex (e.g. Dieterle *et al.*, 1999; Albano *et al.*, 2003; Troolin *et al.*, 2006; Karakus *et al.*, 2008; Igarashi *et al.*, 2010; Sohn & Chang, 2011; Del Pino *et al.*, 2011). Dieterle *et al.* (1999) applied PIV on a catapult facility in order to study the far field behaviour of trailing vortices in the wake of an aircraft model. Karakus *et al.* (2008) performed a PIV on a rectangular wing with 151 mm of chord and squared tip. At a Reynolds number of 32000 they observed the formation of three vortical structures around the tip which merged together at around 60% of the chord. The tip region was dominated by the stronger interaction between the multiple secondary vortices and the primary vortex. Del Pino *et al.* (2011) found a good correlation between experimental data of the swirl velocity profile and vorticity in the near field with the analytical vortex presented by Moore & Saffman (1973).

SECTION 4

What are the scope and contributions of this work to the unresolved issues?

As shown in the literature review, a great number of authors studied the wingtip vortex. However, this flow still presents many questions. The key points that have not been successfully answered by previous studies and that have been addressed in the present work are presented as follows.

- Although the work done by Chow *et al.* (1997a) represented an important step forward in the understanding of the formation and early wake of wingtip vortices, such tests were performed only at one condition (on one wing model, angle of attack and freestream velocity). A parametric study for a range of angles of attack, Reynolds numbers, wingtip shapes would greatly improve the understanding of the basic mechanisms of the initial roll up, of the formation of the axial flow and of the origin and effects of secondary vortical structures.
- In order to put the design of effective tip modifications on a firm basis and to develop trustworthy prediction methods, more work is needed in the understanding of the fundamental flow physics and in the characterization of the vortex formation on the wing. Even the formation of the tip vortex on simple geometries, such as rectangular wings with squared and rounded tips, reveals a number of peculiar and

very challenging phenomena which are hardly predicted by numerical simulations. The study of the unsteadiness of the vortex system during the formation is also very important in understanding more about meandering sources and in suggesting tip modifications which excite instability mechanisms on particular wavelength and so quicken the decay of the vortex in the far field.

- Whether and when the vortex core is turbulence or laminar is a matter of controversy and the role of the turbulent and its effects on the early development of wingtip vortices is not clear (Birch, 2012). Two main answers have been proposed: the first is that the turbulence plays only a passive role in the development of the vortex core which is subjected to a rapid relaminarization process; the second claims the existence of convected secondary structures within the vortex core producing high levels of turbulent stresses. More studies are needed for this question to be better addressed and answered.
- Nowadays, CFD methods have reached a state of reliability and resources which can give detailed descriptions of complex flows; in particular it is now common to find RANS simulations on wings or even full aircraft. However, the approach on the closure problem is still posing serious questions on the accuracy of such results which is particularly true for trailing vortices. Moreover, an accurate representation of the formation and the near wake is extremely important if the aim is the prediction of the development and decay of the trailing system or its interaction with other bodies. Detailed experimental results on the early development of the vortex are therefore very important not only as benchmarks for numerical simulations but also for a deeper understanding of the physics and vortex dynamics in this range so that more faithful models for the Reynolds stresses can be developed.

This research is based on an experimental study focused on the formation and very early wake of a wingtip vortex from a rectangular wing. The effects of a number of parameters on the development of the tip vortex are addressed and a deeper understanding of the physics involved in this flow is reached. Surface oil flow visualizations, surface pressure measurements, laser-illuminated smoke visualizations, surface-mounted hot film investigations and stereoscopic particle image velocimetry have been completed for several configurations. The choice of adopting SPIV as the main experimental technique was dictated by the need of a non intrusive, instantaneous, global and highly spatial resolved measurement technique for the investigation of this complex flow field. These qualities are necessary to adequately describe the mean flow structure of the vortex

core, the turbulent activity and secondary structure dynamics. The detail reached on these measurements represents a unique contribution of this research to wingtip vortex studies.

SECTION 5

Structure of the thesis

The presentation of the results of this research follows the classification of the wingtip vortex life proposed in Section 1.3. The experimental apparatus used during this work is described in Chapter 2 where the wind tunnels used, the characteristics of the wing models tested and the components of the experimental techniques adopted are presented.

In Chapter 3, a description of the formation of the wingtip vortex is presented with the cooperating contribution of several experimental techniques. A model and a characterization of the formation is proposed. Unsteadiness measurements on the formation and in the very early wake are correlated giving insights into the effects of secondary structures on the meandering of the vortex. Chapter 4 presents several aspects of the early wake of the wingtip vortex such as the vortex core shape, the axial flow development and the turbulence behaviour within the core. Due to the number of different phenomena presented and in order to keep a general and short literature review in this chapter, individual short introductions and specific literature reviews on the particular topics are given at the beginning of each section. Chapter 5 presents a discussion on the accuracy and error of the measurements with particular emphasis on the SPIV.

Finally, Chapter 6 concludes this dissertation with a summary of the main contributions and results from this research on the various aspects of the vortex formation and early wake. Recommendations for future work are suggested based on these conclusions.

Experimental apparatus and procedure

When you can measure what you are speaking about, and express it in numbers, you know something about it; but when you cannot measure it, when you cannot express it in numbers, your knowledge is of a meager and unsatisfactory kind: it may be the beginning of knowledge, but you have scarcely, in your thoughts, advanced to the stage of science.

LORD KELVIN (WILLIAM THOMSON)

A series of experiments adopting different experimental techniques were conducted with the objective of qualitatively and quantitatively describing the initial roll up of the tip vortex on the wing and in the early wake. Surface oil flow visualizations and pressure measurements on the wing were performed in order to gather global and panoramic information of the flow on the wing at different configurations. Due to its relative simplicity in the implementation, surface flow visualizations served as a preliminary tool for providing qualitative information of the surface flow when complex structures are present. Moreover, smoke visualizations on the tip region were conducted to give a deeper understanding on the structure and dynamics of the vortex development on the wing.

A study of the unsteadiness in the formation of the trailing vortex system was accomplished using surface hot film anemometry and stereoscopic particle image velocimetry (SPIV) on the flow parallel to the wing surface. Lastly, the major part of the research was carried out performing parametric SPIV measurements in the early wake changing a number of parameters such as wing and tip geometry, angle of attack and Reynolds number.

The research was entirely conducted within the University of Glasgow and the ex-

periments carried out during this study were based on two wind tunnels and two wing models. Details of experimental facilities, wing models, experimental techniques and apparatus used during each experiment are provided in this chapter. Particular attention is drawn toward the description of the stereoscopic particle image velocimetry technique. Lastly, the reference systems adopted in the presentation of the results is described in Section 2.4.

SECTION 1

Wind tunnels

(a) Argyll wind tunnel All the experiments were carried out in the Argyll wind tunnel with the exception of the smoke flow visualizations of the formation of the wingtip vortex. An overview of this facility is shown in Figure 2.1.

The Argyll wind tunnel is a large facility for subsonic experiments. This is a closed-return facility with an octagonal test section of 2.65 m width, 2.04 m height and 5.60 m length. The diameter of the fan is 3 m and it is located on the opposite side of the circuit with respect to the test section which is vented to the atmosphere by gaps of around 0.05 m on the walls respectively at the leading edge and at the trailing edge. The vents keep the test section static pressure equal approximately to the atmospheric pressure. The nominal maximum operating wind condition that the flow in the test section can reach is 76 m/s. A Pitot tube and a thermocouple for the measurement of the freestream speed are positioned at the test section inlet and connected to a dedicated computer. The turbulence level, evaluated from hot wire anemometry in the centre of the test section, is of around 0.4% in the velocity range between 10 and 25 m/s, which corresponds to the range of the experiments presented in this study. A 3.75 m long by 1.9 m wide moving ground, designed to operate independently from the flow at a maximum of 60 m/s, is placed on the ground. One of the two wing models tested in this research was mounted vertically on the floor. In order to allow this model to be mounted on the floor, a board covering the rolling road was mounted at 0.1 m of height from the moving ground. A rounded leading edge was adopted. The test section is equipped with several windows allowing a wide optical access from both the sides and from the roof.

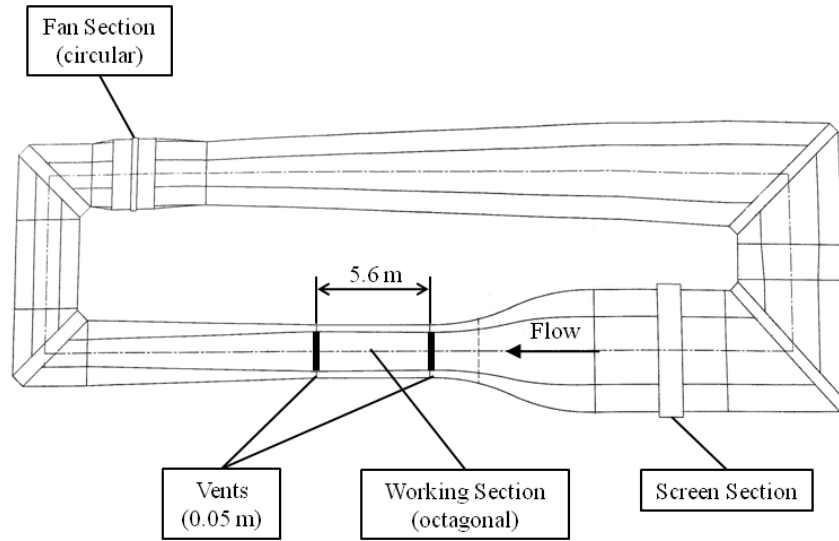


Figure 2.1: *Argyll wind tunnel: top view.*

(b) Smoke visualization wind tunnel Smoke flow visualizations of the formation of the wingtip vortex were carried out in a wind tunnel dedicated to this kind of experiments.

The smoke visualization wind tunnel is a purpose built facility with cross section of 0.91 m by 0.91 m and maximum operating speed of 5 m/s. The working section is 4 m long with a 9:1 contraction at the upstream end and a fan at the downstream end. A schematic of the experimental arrangement is shown in Figure 2.2.

Flow visualization is achieved by injecting smoke through uniformly distributed orifices of 1 mm of diameter and 6.35 mm pitch, drilled into a pipe of 12 mm diameter positioned vertically at the test section inlet. A range of horizontal positions of the pipe allows the smoke filaments to be released at different planes. The pressure, density and velocity of the smoke at the orifices can be adjusted so that smoke filaments are aligned with the freestream. Smoke tracer is generated by heating Shell Ondina EL oil which is injected in the test section using high pressure carbon dioxide as a propellant.

The smoke lines are illuminated with a continuous laser sheet of 2 mm of thickness from a diode laser (5 W power at 532 nm) which is shone from the top of the test section and perpendicularly to the freestream flow. The laser is mounted on a rail so that the laser sheet can be moved along the wind tunnel longitudinal axis.

A high resolution camera (DALSA 2M30 of 1600 by 1200 pixels) with 50 mm focal length lens and f -number equal to 4, is used to capture instantaneous smoke realizations with a maximum frame rate of 30 Hz. The camera is controlled by an in-built LabView

code which permits adjustments on the exposure time in a range between 1 and 400 ms. The camera is mounted downstream of the wing at a distance of 1.5 chords from the trailing edge. The comparison of the vortex structure with and without the camera showed that the flow on the wing was not sensibly affected by the presence of the camera.

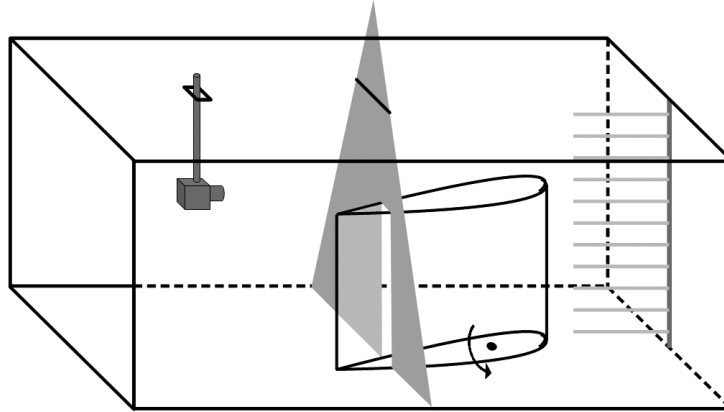


Figure 2.2: *Experimental arrangement of smoke visualizations on the vortex formation: wing M2 mounted in the flow visualization wind tunnel.*

SECTION 2

Wing models

The determination of the wing size of the model was based on the minimization of the blockage effects while keeping a size which still allowed a detailed description of the flow around the tip based on the resolution of the present measurement instrumentation. The length of the test section did not limit the size of the model being only the early wake (up to 2–3 chords) the region of interest. Two wings with different chord lengths and aspect ratios were studied, namely **M1** and **M2**. For both the models, a blockage effect in the Argyll wind tunnel of less than 3% is calculated for the wing at 15° . As described by Igarashi *et al.* (2011), a small blockage reduces the interferences of the walls in the wandering of the trailing vortex. The value calculated in the current investigations ensures minimum walls effect on the tip vortex behaviour.

The interest in a better understanding of the basic physics behind wingtip vortices leads to the choice of a widely tested and known geometry. A rectangular wing with

symmetric NACA profile is adopted and squared and rounded tip geometry are studied.

(a) M1: high aspect ratio wing A rectangular wing model with NACA 0015 profile, 0.42 m chord, 1.3 m span (corresponding to an aspect ratio of $AR = 3.1$) and rectangular wingtip was tested. The model, slid through the test chamber side wall of the Argyll wind tunnel, was mounted on an adjustable plate which allowed the angle of attack and the model height to be adjusted. The angle of attack of the wing was measured with a digital inclinometer positioned on the mounting plate and it was confirmed by zero lift measurement from surface pressure integration at an indicated angle of attack equal to zero. The wing was positioned at the mid height of the test section and the tip was approximately along the centerline (see Figure 2.3).

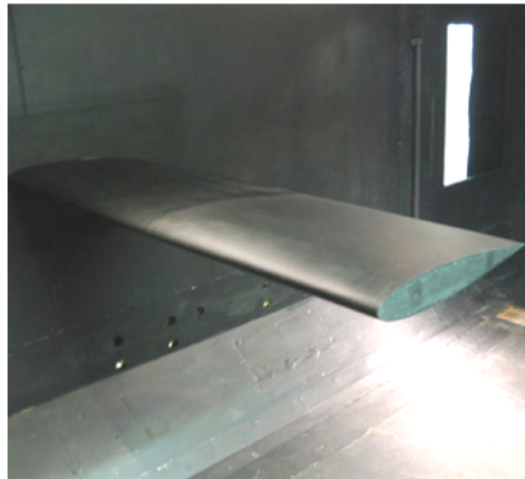


Figure 2.3: *M1 wing mounted in the Argyll wind tunnel (without fixing cables).*

In order to limit bending of the wing and to avoid flutter during the experiments, two cables of adjustable length were fixed at the test section wall and at the wing shaft from the upper and the lower surfaces. The fixing point was at 1.5 chord from the tip so that the effect of the cables on the tip region was negligible.

(b) M2: low aspect ratio wing A low aspect ratio wing ($AR = 0.75$) was also tested. The **M2** model is a rectangular planform with NACA 0012 profile, 0.76 m chord and 0.57 m span. Squared and rounded wingtips were tested by attaching a rounded cap. The wing area with the round cap was around 7% greater than the wing area with squared tip. The model was mounted vertically on a circular plate on the floor allowing the angle of attack to be adjusted by a rotation about the quarter chord which laid on the middle plane of the test

section. The zero angle of attack was identified by integration of the surface pressure along a pressure tapping array on both sides of the wing and placed at a distance of 0.10 m from the ground. A picture of the wing model and the calibration plate used for the stereoscopic particle image velocimetry is illustrated in Figure 2.4.

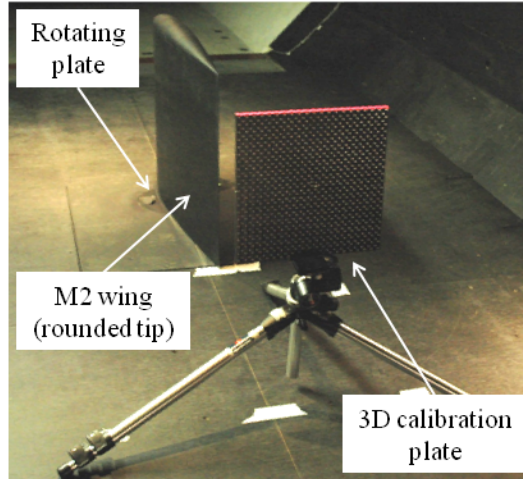


Figure 2.4: *M2 wing mounted in the Argyll wind tunnel and SPIV calibration plate.*

A summary of the main characteristics of the two models and the experimental techniques adopted for each wing is given in Table 2.1.

| | M1 | M2 |
|----------------------------------|-----------|------------------|
| Aerofoil | NACA 0015 | NACA 0012 |
| Chord, c [m] | 0.42 | 0.76 |
| Span, b [m] | 1.3 | 0.57, 0.62 |
| Aspect ratio, AR | 3.1 | 0.75, 0.81 |
| Tip geometry | squared | squared, rounded |
| Pressure measurements | ✓ | |
| Surface flow visualizations | ✓ | |
| Smoke visualizations, formation | | ✓ |
| Smoke visualizations, early wake | | ✓ |
| Hot film anemometry | | ✓ |
| SPIV, limiting flow | | ✓ |
| SPIV, early wake | ✓ | ✓ |

Table 2.1: *Summary of wing models characteristics and experiments.*

SECTION 3

Experimental techniques

(a) Surface oil flow visualizations Oil with a fluorescent agent is used to visualize the characteristics of the flow near the surface. Due to frictional forces the air stream carries the oil with it. From the pattern of oil accumulation on the surface, qualitative conclusions can be drawn with respect to the location of flow separation lines, reattachment lines and the local magnitude of skin friction (Merzkirch, 1987; Yang, 1989). The wall shear stress is defined as the spatial derivative normal to the surface of the velocity field at the surface. Integral curves of the velocity in this vector field are sometimes referred to as limiting streamlines, wall shear stress trajectories or skin friction lines. It is this vector field which produces oil flow patterns in wind tunnel experiments (Kenwright, 1998). Whether the oil film follows the surface streamlines and whether the motion indicates the skin friction lines is discussed by Lu (2010). The interpretation and reliability of these observations relies on the small effects that the oil film has on the boundary conditions of the air flow near the wall. Squire (1961) theoretically studied the motion of a thin oil sheet on a surface under a boundary layer and he showed that the oil follows the boundary layer surface streamlines except near flow separations where it tends to form an envelope upstream to the true separation envelope. This effect is less marked for turbulent than for laminar boundary layers and the displacement increases for thicker oil layers and smaller Reynolds numbers.

Surface oil flow visualizations were performed on the wing model **M1** using a mixture of Ondina oil and fluorescent powder and photographed using a Nikon D70 still camera with a 28–105 mm zoom lens. A smooth black adhesive film was applied on the model in order to cover the pressure tappings and to create a uniform and suitable surface for the paint. An ultraviolet lamp was used to illuminate the mixture which gave more contrast with the background surfaces than with normal lighting. A thin layer of mixture was uniformly brushed onto the wing surface near the tip with the wind tunnel off. The wind tunnel was then turned on and, once the pigment was stably distributed on the wing surface, pictures of the oil distribution were taken.

(b) Pressure measurements Pressure measurements from the wing surface were conducted as a preliminary study of the vortex formation and its effects of the lift distribution. Wall pressure was measured at 159 stations on the wing model **M1** as sketched in Figure 2.5, with particular attention to measurements in the tip region and the suction surface. The choice of the pressure tappings distribution was oriented by the work of McAlister & Takahashi (1991) who described the pressure distortion due to the tip vortex on the surface of a rectangular wing with NACA 0015 profile and aspect ratio of 6.6. They found that the pressure in the outer 4% of the span (corresponding to around 13% of the chord length) was affected by the vortex. The pressure tappings, arranged as rows, are named as shown in the sketch of Figure 2.5(d) and the corresponding dimensional coordinates are presented in Table 2.2 (with origins as in the related sketches).

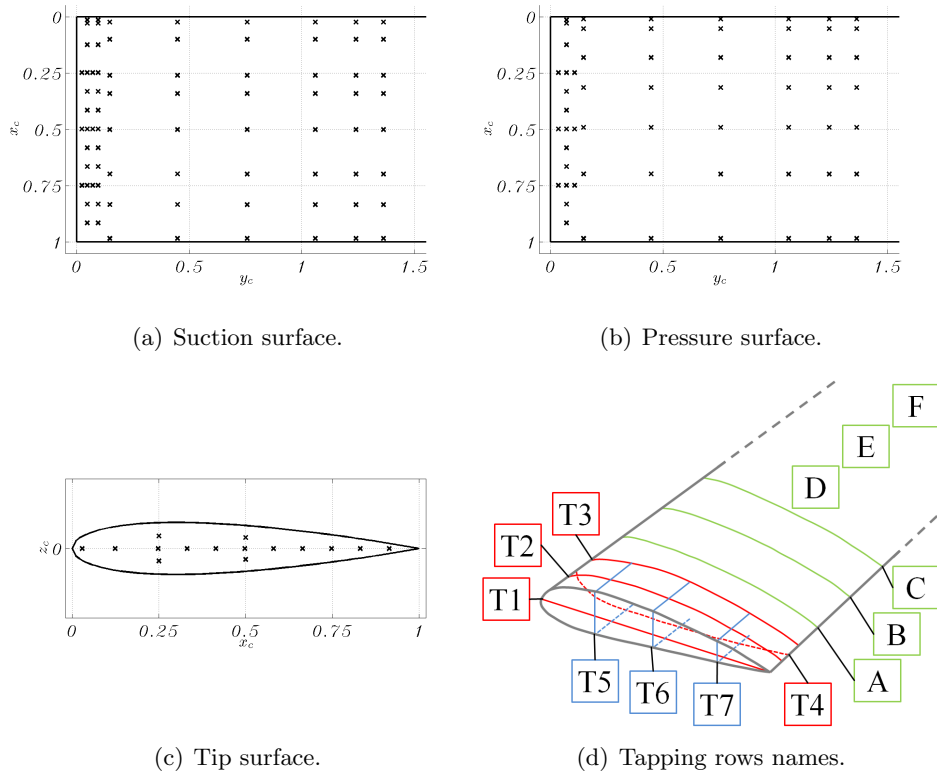


Figure 2.5: Pressure tappings map and names.

| Row | \tilde{x}_c [mm] | \tilde{y}_c [mm] | Surface | Row | \tilde{x}_c [mm] | \tilde{y}_c [mm] | Surface |
|-----|--------------------|--------------------|---------|-----|--------------------|--------------------|---------|
| T1 | 384 | 0 | T | A | 413 | 62 | S |
| | 349 | 0 | T | | 350 | 62 | S |
| | 314 | 0 | T | | 293 | 62 | S |
| | 279 | 0 | T | | 210 | 62 | S |
| | 244 | 0 | T | | 143 | 62 | S |
| | 209 | 0 | T | | 109 | 62 | S |
| | 174 | 0 | T | | 42 | 62 | S |
| | 139 | 0 | T | | 10 | 62 | S |
| | 104 | 0 | T | | 0 | 62 | S |
| | 52 | 0 | T | | 4 | 62 | S |
| | 12 | 0 | T | | 22 | 62 | S |
| T2 | 76 | 20 | S | 350 | 62 | S | |
| | 349 | 20 | S | 132 | 62 | S | |
| | 314 | 20 | S | 206 | 62 | S | |
| | 279 | 20 | S | 293 | 62 | S | |
| | 244 | 20 | S | 413 | 62 | S | |
| | 209 | 20 | S | B | 413 | 188 | S |
| | 174 | 20 | S | | 350 | 188 | S |
| | 139 | 20 | S | | 293 | 188 | S |
| | 104 | 20 | S | | 210 | 188 | S |
| | 52 | 20 | S | | 143 | 188 | S |
| | 12 | 20 | S | | 109 | 188 | S |
| 6 | 20 | S | 42 | | 188 | S | |
| T3 | 384 | 40 | S | | 10 | 188 | S |
| | 349 | 40 | S | | 0 | 188 | LE |
| | 314 | 40 | S | | 4 | 188 | P |
| | 279 | 40 | S | | 22 | 188 | P |
| | 244 | 40 | S | 76 | 188 | P | |
| | 209 | 40 | S | 132 | 188 | P | |
| | 174 | 40 | S | 206 | 188 | P | |
| | 139 | 40 | S | 293 | 188 | P | |
| | 104 | 40 | S | 413 | 188 | P | |

Table 2.2: Pressure tapings coordinates (multipage table).

| Row | \tilde{x}_c [mm] | \tilde{y}_c [mm] | Surface | Row | \tilde{x}_c [mm] | \tilde{y}_c [mm] | Surface |
|-----|--------------------|--------------------|---------|-----|--------------------|--------------------|---------|
| | 52 | 40 | S | | 413 | 318 | S |
| | 12 | 40 | S | | 350 | 318 | S |
| | 6 | 40 | S | | 293 | 318 | S |
| T4 | 384 | 30 | P | C | 210 | 318 | S |
| | 349 | 30 | P | | 143 | 318 | S |
| | 314 | 30 | P | | 109 | 318 | S |
| | 279 | 30 | P | | 42 | 318 | S |
| | 244 | 30 | P | | 10 | 318 | S |
| | 209 | 30 | P | | 0 | 318 | LE |
| | 174 | 30 | P | | 4 | 318 | P |
| | 139 | 30 | P | | 22 | 318 | P |
| | 104 | 30 | P | | 76 | 318 | P |
| | 52 | 30 | P | | 132 | 318 | P |
| | 12 | 30 | P | | 206 | 318 | P |
| | 6 | 30 | P | | 293 | 318 | P |
| T5 | 104 | 40 | S | | 413 | 318 | P |
| | 104 | 30 | S | D | 413 | 445 | S |
| | 104 | 20 | S | | 350 | 445 | S |
| | 104 | 10 | S | | 293 | 445 | S |
| | 104 | 0 | Ts | | 210 | 445 | S |
| | 104 | 0 | T | | 143 | 445 | S |
| | 104 | 0 | Tp | | 109 | 445 | S |
| | 104 | 15 | P | | 42 | 445 | S |
| | 104 | 30 | P | | 10 | 445 | S |
| | 104 | 45 | P | | 0 | 445 | LE |
| | | | | | 4 | 445 | P |
| T6 | 209 | 40 | S | | 22 | 445 | P |
| | 209 | 30 | S | | 76 | 445 | P |
| | 209 | 20 | S | | 132 | 445 | P |
| | 209 | 10 | S | | 206 | 445 | P |
| | 209 | 0 | Ts | | 293 | 445 | P |
| | 209 | 0 | T | | 413 | 445 | P |
| | 209 | 0 | Tp | | | | |
| | 209 | 15 | P | | 413 | 521 | S |

Table 2.2: Pressure tapings coordinates (multipage table).

| Row | \tilde{x}_c [mm] | \tilde{y}_c [mm] | Surface | Row | \tilde{x}_c [mm] | \tilde{y}_c [mm] | Surface |
|-----|--------------------|--------------------|---------|-----|--------------------|--------------------|---------|
| | 209 | 30 | P | | 350 | 521 | S |
| | 209 | 45 | P | | 293 | 521 | S |
| | 314 | 40 | S | | 210 | 521 | S |
| | 314 | 30 | S | | 143 | 521 | S |
| | 314 | 20 | S | | 109 | 521 | S |
| T7 | 314 | 10 | S | | 42 | 521 | S |
| | 314 | 0 | T | | 10 | 521 | S |
| | 314 | 15 | P | E | 0 | 521 | LE |
| | 314 | 30 | P | | 4 | 521 | P |
| | 314 | 45 | P | | 22 | 521 | P |
| | | | | | 76 | 521 | P |
| | | | | | 132 | 521 | P |
| | | | | | 206 | 521 | P |
| | | | | | 293 | 521 | P |
| | | | | | 413 | 521 | P |
| | | | | | 413 | 572 | S |
| | | | | | 350 | 572 | S |
| | | | | | 293 | 572 | S |
| | | | | | 210 | 572 | S |
| | | | | | 143 | 572 | S |
| | | | | | 109 | 572 | S |
| | | | | | 42 | 572 | S |
| | | | | | 10 | 572 | S |
| | | | | F | 0 | 572 | LE |
| | | | | | 4 | 572 | P |
| | | | | | 22 | 572 | P |
| | | | | | 76 | 572 | P |
| | | | | | 132 | 572 | P |
| | | | | | 206 | 572 | P |
| | | | | | 293 | 572 | P |
| | | | | | 413 | 572 | P |

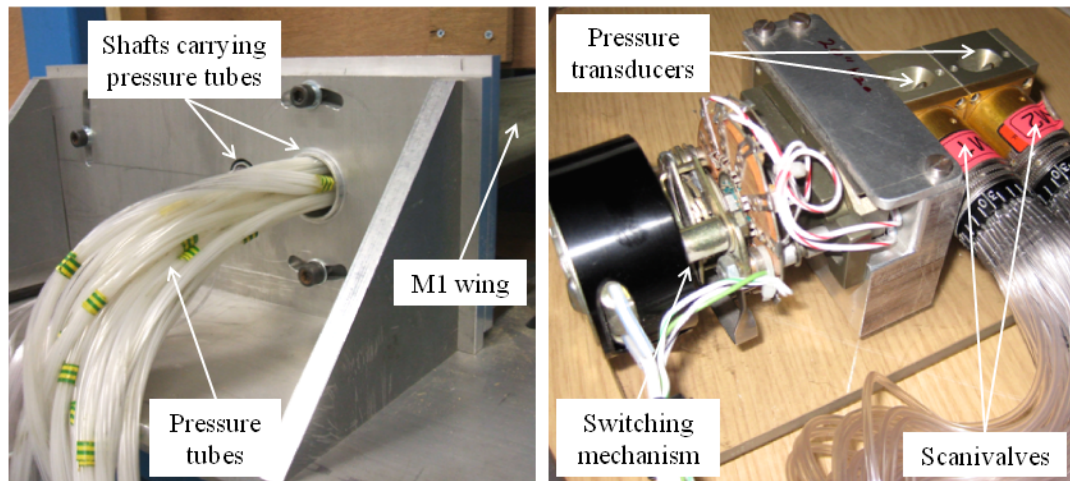
(P) Pressure surface. (S) Suction surface. (T) Tip mean line.

(Ts) Tip surface: upper half. (Tp) Tip surface: lower half. (LE) Leading edge.

Table 2.2: Pressure tapings coordinates.

The tubes, of 1 mm of internal diameter D , were routed from each pressure tapping to the outside of the test section through two shafts along the wing and then connected to 2 scanivalves. Each scanivalve contained a 20 inches of water (4977 Pa) differential–pressure transducer and the two voltage outputs were recorded simultaneously by a dedicated LabView code through a NI USB–6229 card. The opposite side of each transducer was vented to ambient conditions outside the wind tunnel (since the Argyll wind tunnel presents a vented test section). A calibration was carried out with a portable pressure calibrator Druck dpi 615 and a linear relationship between pressure and output voltage was found with sensitivity of 0.001 V/Pa. The regression coefficient, also known as correlation coefficient, was greater than 0.99998 in the whole range of the instrument and a resolution lower than 1 Pa could be inferred. The total distance between each tapping and the scanivalve was approximately 3 m. The LabView code controlled also the scanivalve switchings, the sampling frequency and the sampling time of each recording. A delay of a tenth of a second between two successive acquisitions was set in order to allow the switching of the scanivalve and the equalization of the pressure along the tube.

Pictures of the pressure tubes coming from the M1 wing, the mounting plate outside the test section, the pressure transducers and the scanivalves are presented in Figure 2.6.



(a) M1 mounting plate and tubes from pressure tapplings.

(b) Pressure transducers and scanivalve.

Figure 2.6: *Pressure measurements arrangement.*

The response of the pressure measurement system installed as described can be inferred from the work of Whitmore *et al.* (1990) and can be modeled as a second–order

dynamic system. The authors studied the dynamic response of tubes with different length and diameter at a range of pressure which simulated the change of flight altitude. The typical response of the pressure measurement system they found is reported in Figure 2.7 as a function of the tube geometry. As the tubing length approaches zero, the damping ratio of the system also approaches zero and the natural frequency grows rapidly. Moreover, as the diameter of the tube is increased, the damping ratio decreases whereas only a slight change on the natural frequency is observed so that the natural vibration is primarily a function of the length only. With the present arrangement, a damping ratio of around 0.6 and a natural frequency of the system at around 30 Hz is estimated.

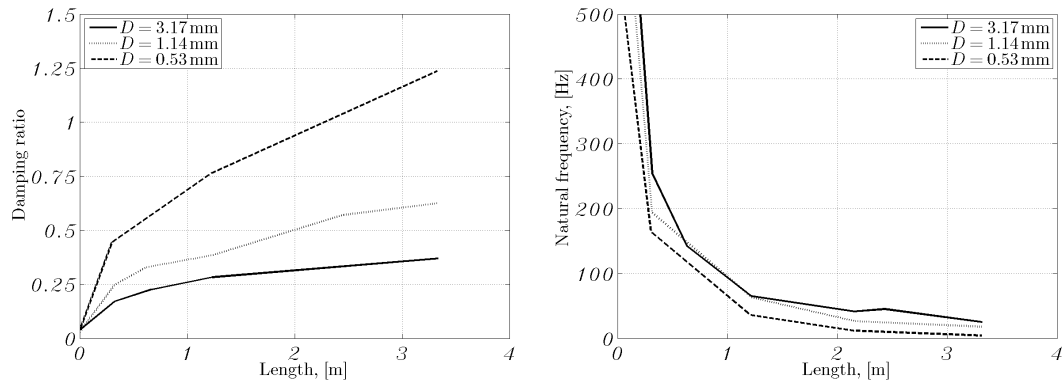


Figure 2.7: Typical response of a pressure measurement system at an equivalent altitude of 2300 ft as function of the tube length and internal diameter (Whitmore et al., 1990).

(c) **Smoke visualizations** Two types of smoke visualizations were adopted on the **M1** wing. The first aimed to explore the flow structure of the vortex during its formation on the model whereas the second was used in the study of the meandering of the vortex in the wake.

On the model Visualizations of the vortex formation on the model **M1** with squared and rounded tip were conducted in the smoke visualization wind tunnel. The wing was mounted vertically on the tunnel floor at approximately 0.8 m from the inlet section and pictures of instantaneous realization of the tip vortex structure were taken at several planes perpendicular to the freestream. Details of the experimental arrangement and procedure were given in Section 2.(b) and a sketch is shown in Figure 2.2.

In the wake The high resolution camera (Dalsa 2M30) with a 300 mm focal length lens and f -number equal to 4, was mounted on the side of the test section of the Argyll

wind tunnel and it was used to study the unsteadiness of the trailing vortex in the near wake of the wing through smoke visualizations. The flow was completely seeded with olive oil particles by an Aerosol Generator PivPart40 series through a pipe installed at the end of the test section. The peak in the probability density function of the olive oil particles size distribution was at $1 \mu\text{m}$. The model was mounted on the floor of the Argyll wind tunnel and a continuous laser sheet was shone from the top of the test section and perpendicular to the freestream flow at a distance from the trailing edge. A picture of a calibration plate with a cartesian grid of dots located on the laser plane was used for the reconstruction of the images as described by Raffel *et al.* (2007).

Commonly for experiments in air of trailing vortices, oil particles drift away from the vortex core due to centrifugal forces (Marshall, 2005; Grant, 1997). Hence, the smoke density is lower in the vortex core and a darker region (i.e. less laser light scattering) can be observed in the image. Vortex centre positions are calculated on the basis of the assumption that the centroid of the dark hole is a good approximation of the vortex centre. The bespoke method adopted to locate the centroid of the darker region (discussed in Appendix B) lead to an accuracy of the order of 1 pixel. With the present arrangement, the oscillation of the vortex centre was of the order of 200 pixels at the magnification used, equivalent to about 2.5% of the chord.

Frame rates of 10 Hz and 30 Hz were adopted for this study. The exposure time of the frames was set in a range between $250 \mu\text{s}$ and $500 \mu\text{s}$ so that the darker region at the vortex core was still visible and the error from the movement of the particles during the exposure was minimum.

(d) Hot film anemometry The wall shear stress measurement using an electrically heated element positioned on the surface is a well established technique introduced by Bellhouse & Schultz (1966) and it relies upon the similarity between the velocity profile adjacent to the wall and the temperature profile of the thermal boundary layer that is generated by the element.

The relationship between the rate of heat transfer from a hot film, which is proportional to the square of the anemometer output voltage E , and the wall shear stress τ_w takes the following form:

$$(\tau_w)^{1/3} \propto (E^2 - A^2) \quad (2.1)$$

where A is a constant. Calibration of hot films is a difficult and time consuming process (Hodson, 1985). However, as long as only unsteady flow phenomena are investigated and quantitative information on the velocity and skin friction are not required, a calibration

of the sensors is not necessary and surface mounted hot films can be satisfactorily used to provide qualitative or semi-quantitative data (Haselback & Nitsche, 1996). In the present work, signal frequency spectra and comparative analysis of the signal fluctuations are presented.

Surface hot films (Dantec 55R47 glue-on probe) were deployed for the determination of the degree of unsteadiness of the surface flow in the wingtip region. The sensors were oriented perpendicular to the freestream direction and positioned near the wingtip. They were operated with Dantec mini constant temperature anemometer (at a film temperature of approximately 125°C) and recorded at 1 KHz, with sampling time of 100 s and low-pass filter cutting frequency of 1 KHz. These studies focused on a frequency range below 15 Hz and a high-pass filter cutting frequency of 0.1 Hz was employed as a post-processing step. The film was glued for the duration of the experiment directly onto the surface at the point of interest and the cables leading to the anemometer were taped on the wing oriented as the freestream down to the trailing edge and then along the trailing edge to the floor. The film was moved after each test to the next position.

(e) Stereoscopic particle image velocimetry In fluid dynamics history, an important evolution in the investigation of flows was the replacement of passive observations of nature by experiments carefully planned to extract information about a targeted phenomenon. One of the pioneers was Ludwig Prandtl (1875–1953), who designed and utilized flow visualization techniques in a water tunnel to study steady and unsteady separated flows behind wings and other objects. At that time, only a qualitative description of the flow field was possible. With the scientific and technical progress achieved in the last 30 years in optics, lasers, electronics, imaging technology and computer hardware, it is now possible to extract quantitative information on the instantaneous velocity fields exactly from the same kind of images available more than a century ago to Prandtl (Raffel *et al.*, 2007).

Particle image velocimetry (PIV) is part of a broader class of velocity measurement techniques called pulsed-light velocimetry (PLV) which measures the motion of small, marked regions of a fluid by comparing the locations of the images of the markers at two or more times (Adrian, 1991). Such techniques can differ in many ways such as in type, dimension and density of markers; duration and number of light pulses; type and number of light sources; type, framing rate and number of recording devices; processing technique of the images. The estimation of the local velocity vector \mathbf{u} is based on the

(first order of the) fundamental definition of velocity

$$\mathbf{u}(\mathbf{x}, t) \doteq \frac{\Delta \mathbf{x}(\mathbf{x}, t)}{\Delta t} \quad (2.2)$$

where $\Delta \mathbf{x}$ is the displacement of a marker, located in \mathbf{x} at time t , and Δt is the time interval separating two observations of the marker. As Δt approaches to zero, the limit of \mathbf{u} is the instantaneous local velocity.

With recording and laser devices outside the tunnel, particle image velocimetry is a non intrusive method for instantaneous velocity measurements. In contrast to more traditional single point measurement techniques (such as with hot wires or pressure probes), the PIV technique provides an analysis of a flow field without disturbing the flow with probes. Furthermore, PIV is a whole field technique that allows the recording of images of an extended region of the flow field and the extraction of the instantaneous velocity vector information out of these images. The majority of all the other techniques for velocity measurements only allows the measurement of the velocity of the flow at a single point, in most cases at a high temporal resolution. The spatial resolution of PIV can be very large, whereas the temporal resolution (frame rate of image recording) may be limited due to current technological restrictions on laser frequency, camera architecture or data transfer speed.

Nowadays, the PIV technique is commonly based on a planar laser light sheet, which is pulsed twice on a wide portion of the flow. The flow is seeded with fine markers and images of these particles lying in the light sheet are recorded on a video camera. The displacement of the particle between the two laser pulses is measured on the image plane and is used to determine the displacement of the particles in the flow. The most common way to measure the particles shift is to divide the first image into small interrogation windows and to cross-correlate each one of them with the respective interrogation window on the second image. The cross-correlation produces a peak corresponding to the average displacement vector of the particles inside the interrogation cell. The velocity associated with each interrogation spot is simply the displacement divided by the time delay between the two laser pulses. Despite the recognized maturity of the cross-correlation based methods, PIV image processing algorithms have continuously been improved during the past decades. Comprehensive overviews of the situation were presented by Keane & Adrian (1992), Grant (1997) and Raffel *et al.* (2007).

If the flow is highly three-dimensional, the velocity component perpendicular to the laser sheet can be a source of error in the measured velocity up to more than 15% of

the mean flow velocity (Raffel *et al.*, 2007). The error is due to the dependence of the in-plane projection of the velocity vector on the viewing direction and on the out-of-plane component. A variety of approaches capable of recovering the complete set of velocity components have been described in the literature (Hinsch, 1995). Stereoscopic particle image velocimetry (SPIV) is based on the same fundamental concepts of PIV but it is capable to evaluate all the three components of the velocity vector from a two-dimensional slice of the flow field. This method generally employs at least two imaging systems to record simultaneous but distinct off-axis views of the same region of interest. Two pairs of images are recorded at the same time by the two cameras. Each pair is analysed independently to derive two in-plane velocity fields. Knowing the perspective angles between the imaging systems and the measuring plane, the cross flow velocity component can also be derived (see for example Lawson & Wu, 1997; Prasad, 2000). Moreover, SPIV is known to produce more accurate measurements also of the in-plane velocity components in the flow field than the PIV.

A commercial PIV system (LaVision) was used for experiments on model **M1** and **M2** in the Argyll wind tunnel. A variety of configurations of the wings were tested and several planes in the wake and close to the surface of the model were studied for a detailed quantitative understanding of the evolution of the vortex system from the model to the early wake. A summary of all the SPIV experiments is presented in Table 2.3. In the present dissertation, not all these configurations are discussed, although all of them were analysed and compared during this study.

The general experimental setup of SPIV tests is presented here following the sub-system sectioning proposed by Raffel *et al.* (2007). Some of the elements of the SPIV system can be seen in the pictures of Figure 2.8.

Laser A Litron double cavity, Nd:YAG laser, Q-switched to produce 0.5 J pulses of 8 ns duration and 532 nm wavelength was used. The laser frequency, corresponding to the acquisition frequency of the recorded images, was kept constant at 2 Hz.

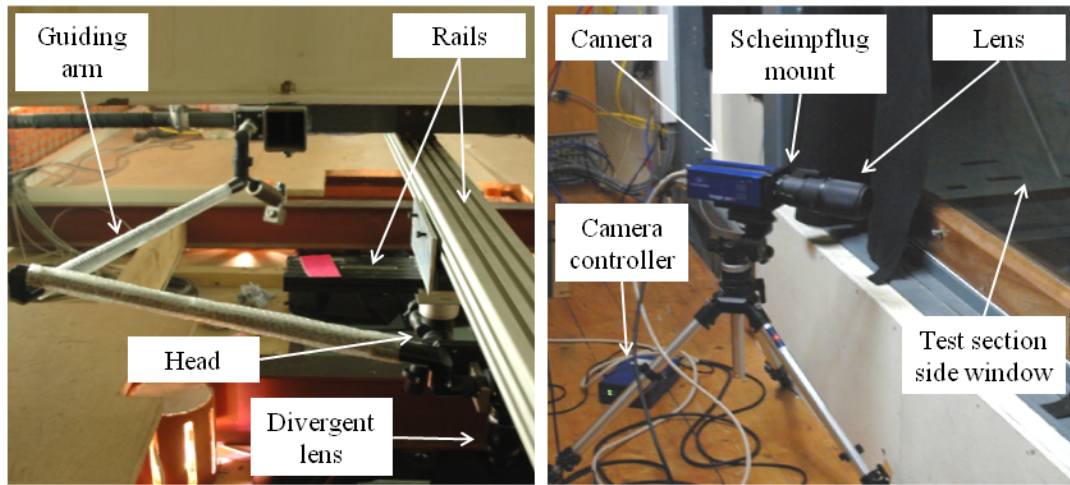
A number of mirrors and a laser guiding arm were used for delivering the laser beam to the divergent lens which was mounted on a camera head installed on a system of two rails above the test section. This arrangement allows two-dimensional translations and three-axes rotations of the laser sheet covering a wide range of the test section. Depending on the field of view required, a divergent lens with focal length of -20 mm or -10 mm was installed which generated a 3 mm thick lens sheet.

| Wing | Tip | Laser plane position | α [°] | Re [$\cdot 10^5$] | | | | |
|---------|----------------|----------------------|--------------|---------------------|----------------|----------------|----|----------------|
| M1 | squared | In the wake | $x_w = 0.25$ | 4 | 1, 5 | | | |
| | | | | 8 | 1, 5 | | | |
| | | | | 12 | 1, 5 | | | |
| | | | $x_w = 0.5$ | 15 | 1, 5 | | | |
| | | | | 4 | 1, 5 | | | |
| | | | | 8 | 1, 5 | | | |
| | | | $x_w = 1$ | 12 | 1, 5 | | | |
| | | | | 15 | 1, 5 | | | |
| | | | | 4 | 1, 5, 10 | | | |
| | | | M2 | squared | In the wake | $x_w = 0.25$ | 0 | 2.6, 7.4, 12.7 |
| | | | | | | | 4 | 2.6, 7.4, 12.7 |
| | | | | | | | 12 | 2.6, 7.4, 12.7 |
| | | | | | | $x_w = 1$ | 0 | 2.6, 7.4, 12.7 |
| | | | | | | | 4 | 2.6, 7.4, 12.7 |
| | | | | | | | 12 | 2.6, 7.4, 12.7 |
| rounded | $x_w = 0.25$ | 0 | | | | 2.6, 7.4, 12.7 | | |
| | | 4 | | | | 2.6, 7.4, 12.7 | | |
| | | 12 | | | | 2.6, 7.4, 12.7 | | |
| | | 20 | | 2.6, 7.4, 12.7 | | | | |
| | | $x_w = 1$ | | 0 | 2.6, 7.4, 12.7 | | | |
| | | | | 4 | 2.6, 7.4, 12.7 | | | |
| 12 | 2.6, 7.4, 12.7 | | | | | | | |
| M2 | squared | On the model | | $d = 3$ | 12 | 1, 5, 10 | | |
| | | | | $d = 5$ | 12 | 1, 5, 10 | | |
| | | | $d = 7$ | 12 | 1, 5, 10 | | | |
| | rounded | | $d = 5$ | 4 | 1, 10 | | | |
| | | | $d = 5$ | 12 | 1, 10 | | | |

Table 2.3: Summary of SPIV experiments (79 independent tests).

Glare problems are one of the overriding difficulties encountered when undertaking PIV experiments close to a wall and they can limit the accuracy of the results in the vicinity of objects. Glare is caused by laser reflection off the wall surface that may exceed the scattering signal of the seeding particles and it depends on several factors such as laser intensity, laser incident direction, camera sensitivity, viewing angle and surface roughness (R. A. Humble, 2007; Adrian & Westerweel, 2010).

In order to reduce the intensity of the reflection, a matt black paint was used on the surface of the model and the whole test section, although this did not completely remove the glare especially on the sharp corners (trailing edge and squared tip). SPIV experiments were also conducted on planes parallel to the wing surface at a small dis-



(a) Imager pro X camera mounted outside the test section.

(b) Laser beam delivery system.

Figure 2.8: Camera mounting and laser delivery for SPIV experiments.

tance from it. For this arrangement, the laser sheet was accurately positioned so that it did not generate glare with the exception of some spots near the trailing edge. However, the effect of the glare on the results is minimum and it is discussed in Section 3.4.

Tracer The PIV technique measures flow velocity indirectly, that is from the tracer displacements. Therefore, the dynamics of the seeding particles has to be studied to avoid significant errors in the velocity evaluation and the assumption that the tracer particles suspended in the flow faithfully follow the fluid motion has to be valid (Melling, 1997). Moreover, the light scattering property of the particles is another important aspect in the selection of the tracer. Raffel *et al.* (2007) treat these topics remarking the compromise that has to be found between a very small particle which ensures good tracking of the fluid motion and a particle which is big enough to ensure a good light scattering. They also present the most common solutions for several experimental conditions and flow features.

In the current investigation, the entire flow was seeded through a pipe mounted downstream of the test section with olive oil particles generated by the Laskin Nozzle Aerosol Generator PivPart40 series. The nominal peak in the probability density function of the olive oil particles size distribution is at $1 \mu\text{m}$ (PIVTEC, 2007). However, as explained by Adrian (1991), the effective particle diameter on the image plane is a function of the physical particle diameter and the point response function of the lens. For a reference case of the present experiments, it is found that the particle size on the

image plane is approximately independent of the physical particle size and it is equal to a value around $90\ \mu\text{m}$ which corresponds to a value between one and two pixels on the object plane. This choice of seeding leads to a satisfactory behaviour of the tracer and a good quality of the results.

Another important aspect about the seeding is the particle density. The probability of a correct displacement evaluation is increasing with the number of particles present in both the interrogation windows during the correlation. This number depends on the overall particle density, the amount of in-plane displacement, the amount of out-of-plane displacement and the image processing procedure (Keane & Adrian, 1992). A higher number of particle pairs increases the signal strength of the correlation peak. However, the particle density is limited to a maximum by the contrast of the PIV recording system. In general, a densely seeded flow ensures high valid detection rate and low measurement uncertainty. Additionally, it allows the use of smaller interrogation windows which ensures higher spatial resolution.

Cameras Two Imager pro X, 11 Megapixel cameras (CCD chip of 4008 by 2672 pixels) with $9\ \mu\text{m}$ pixel size were used and DaVis 7.2, the software accompanying the LaVision system, was used to synchronize laser and cameras. A range of Nikon lenses (200 mm and 300 mm focal length with f -number equal to 4) were used to obtain the required field of view during each test.

The cameras were mounted outside the test section and arranged in angular displacement arrangement (Prasad, 2000) for greater measurement accuracy of the velocity components (Lawson & Wu, 1997). Depending on the orientation and positioning of the laser plane, the cameras were installed on the two sides of the test section or on the same side. Camera perspective angles were determined by DaVis 7.2 software during the calibration procedure and the angles between cameras and the object plane were in a range which ensures low errors in the evaluation of both the in-plane and out-of-plane velocity components, based on Lawson & Wu (1997) analysis.

The focusing of the PIV cameras on the required region of interest was performed manually; manual Scheimpflug adaptors were used to ensure uniform magnification gradients across the image obtaining images in good focus over the entire image plane (Prasad & Jensen, 1995).

Calibration of the cameras Calibration of PIV systems is accomplished to relate the camera chip coordinate with the physical coordinates of the flow field and to pro-

vide transfer functions which are necessary to convert the derived pixel displacements to physical particle displacements. LaVision FlowMaster software was used to perform the SPIV calibration based on a three-dimensional calibration-based (pinhole) reconstruction (Prasad, 2000; DaVis, 2007). This approach uses a spotted board (calibration plate) with known geometrical properties. The board presents a cartesian grid of dots positioned on two levels (three-dimensional calibration plate) in known positions and it is located on the object plane (i.e. laser plane). With the system in the experiment configuration (usually just before the measurements), a number of images is taken from each camera. The accuracy of this calibration is improved by taking more than one image in a neighborhood of the laser plane by slightly rotating or translating the calibration plate. The average deviation of the dewarped marker position to the ideal regular grid was around 0.5 pixels which is below the suggested limit for a good calibration process (DaVis, 2007). Focal length of camera lenses, distance from cameras to calibration plate and camera viewing angles of the calibration plate are all calculated during the calibration process.

Laser pulses separation Time separation between successive laser pulses is an important parameter that has to be optimized during PIV measurements. Prior knowledge of the flow field (i.e. maximum and minimum velocities, velocity gradients and flow direction), interrogation window size, laser sheet thickness, correlation process are the most important factors among the many involved in the calculation of the optimum pulse separation (Raffel *et al.*, 2007).

As described by Boillot & Prasad (1996), the restrictions change if the correlation is an auto-correlation (two pulses on the same frame) or a cross-correlation (two pulses on two different frames). In cross-correlations the delay time is less dependent on the interrogation spot size because the correlation can involve interrogation window shifting and deformation (Scarano, 2002). Furthermore Keane & Adrian (1990) showed that generally, to achieve a valid detection probability of at least 90%, the image density (defined as the mean number of particles per interrogation window) must be greater than 15 and the average particle displacement must be limited to less than 30% of the interrogation window size (Boillot & Prasad, 1996).

Although several calculation methods of the pulse separation can be found in the literature (Adrian, 1988; Keane & Adrian, 1990; Boillot & Prasad, 1996; Raffel *et al.*, 2007), *“it is advisable to apply a quick-look evaluation during recording for the optimization of the experimental parameters”* (Raffel *et al.*, 2007, p. 95). In the current

study, a simple calculation method was used for a preliminary estimation of the pulse separation which was then adjusted by observations of the resulting vector fields. In Appendix A.1, the pulses delay calculation and optimization is applied on a reference case of a wingtip vortex.

Image processing procedure The analysis of the recorded image is one of the most important steps in the entire process, as it couples with the acquisition process to determine the accuracy, reliability, and spatial resolution of the measurement; usually, it is also the most time-consuming part of the process (Adrian, 1991). A typical procedure for the vector field computation of a SPIV is reported in Figure 2.9. For a the stereo cross-correlation, each acquisition consists of four images: two single-exposed frames with a time interval Δt from each of the two cameras. Each frame is then dewarped through the mapping function and segmented into interrogation windows with set initial size, weight and overlapping values. Each interrogation window is cross-correlated with the corresponding region, shifting based on a reference vector field, on the second frame from the same camera. The highest peak in the cross-correlation image is the most likely displacement vector and it is used to calculate the velocity vector of that interrogation window. After this operation, a pair of two-dimensional two-components vector fields (2D2C) is obtained. From the two planar vector fields, the stereoscopic reconstruction of a two-dimensional three-components vector field (2D3C) is accomplished. The vectors, after a validation process, are then projected into planar vector fields which are used as references for a new cross-correlation with different interrogation window size and overlapping values. This loop is repeated accordingly to the multi-pass processing procedure adopted. No need for vector post-processing was seen on the final vector fields. A median filter with vector removal and iterative replacement, a fill-up process by interpolation and a 3x3 smoothing filter on the vector field was applied only between each step of the multi-pass iterations. This implies a good quality of the seeding and of the images giving a high level of reliability to these experiments.

DaVis 7.2 was used for the processing of the images and the calculation of the vector fields, whereas Matlab codes were written for the analysis of the results. The compromise between results accuracy, spatial resolution, processing time and memory requirement was found with a stereo cross-correlation of the image pairs composed of a double step process on an interrogation window of 64 by 64 pixels with 25% of overlap followed by other two steps with interrogation window of 32 by 32 pixels with 50% of overlap. Tests on the image processing parameters (i.e. overlapping, interrogation

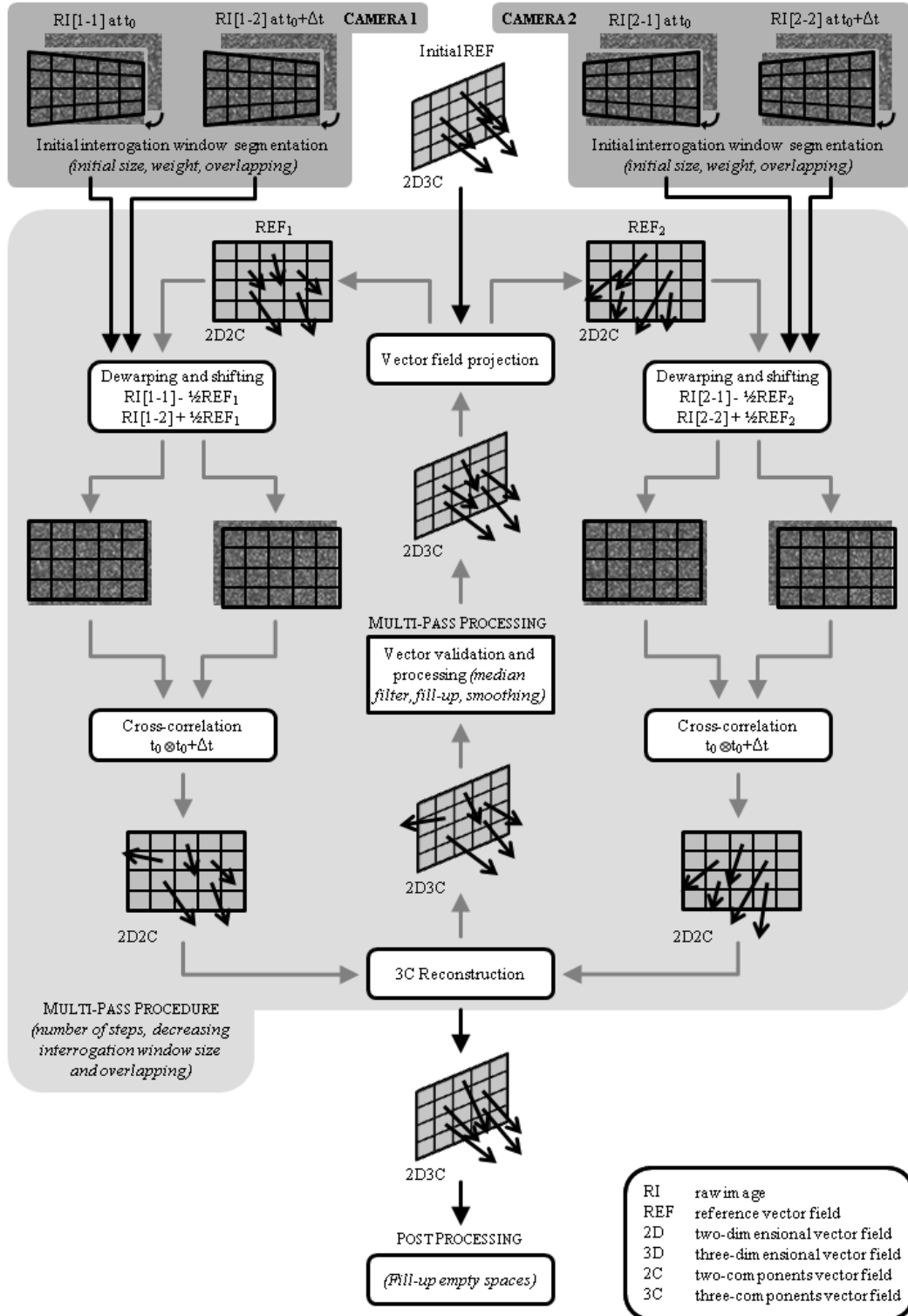


Figure 2.9: Vector field computation flow chart of a two pulses two frames SPIV.

window size, number of iterations) which led to the optimum compromise are reported in Appendix A.2. A standard cyclic FFT-based cross-correlation algorithm was used

which assures a fast computation and very good results when combined with adaptive multi pass processes. More details on the functions involved in the image processing (e.g. image dewarping and shifting, correlation function, peak validation, median filter, fill-up of empty spaces, smoothing filter) can be found in the LaVision manual (DaVis, 2007) and references therein.

The PIV hardware used during this investigation limits the maximum acquisition frequency of image pairs to a value around 2.2 Hz. Also, the internal memory of the cameras limits the number of image pairs that each camera can record for each run at a constant frequency to 121. In order to keep the acquisition frequency constant and to reach satisfactory statistical convergence, tests were typically composed of 121 image pairs for each camera (equivalent to 121 vector fields) at sampling frequency of 2 Hz. Studies on the statistical convergence of different quantities (e.g. velocity, vorticity, turbulent quantities) are described in Section 4.1.(d) and considerations on the memory required to store the images are made in Appendix 2. Final considerations on the errors encountered adopting this experimental technique are presented in Section 5.2.

SECTION 4

Reference systems

Because of the different nature of the experiments, the natural reference system for each experiment was preferred and several reference systems are therefore adopted during the discussion of the results. Sketches of the different reference systems adopted in this study are shown in Figure 2.10. All the coordinates, with the exception of the angular coordinate, are normalised by the wing chord.

(a) Wake reference system The natural reference system for wing wake measurements is with the x_w axis aligned with the freestream velocity, the y_w axis aligned with the wing span and directed inboard (from tip to root) and the z_w axis in the direction of the lift force (see Figure 2.10(a)). This is the reference system which is commonly seen for trailing vortex measurements. However, the vortex axis in general is not aligned with the freestream and in particular the vortex moves upward (in the direction of the lift) and inboard when shed from the wing. That is to say that the vortex axis can not be assumed to be perpendicular to the PIV plane in the wake of the wing.

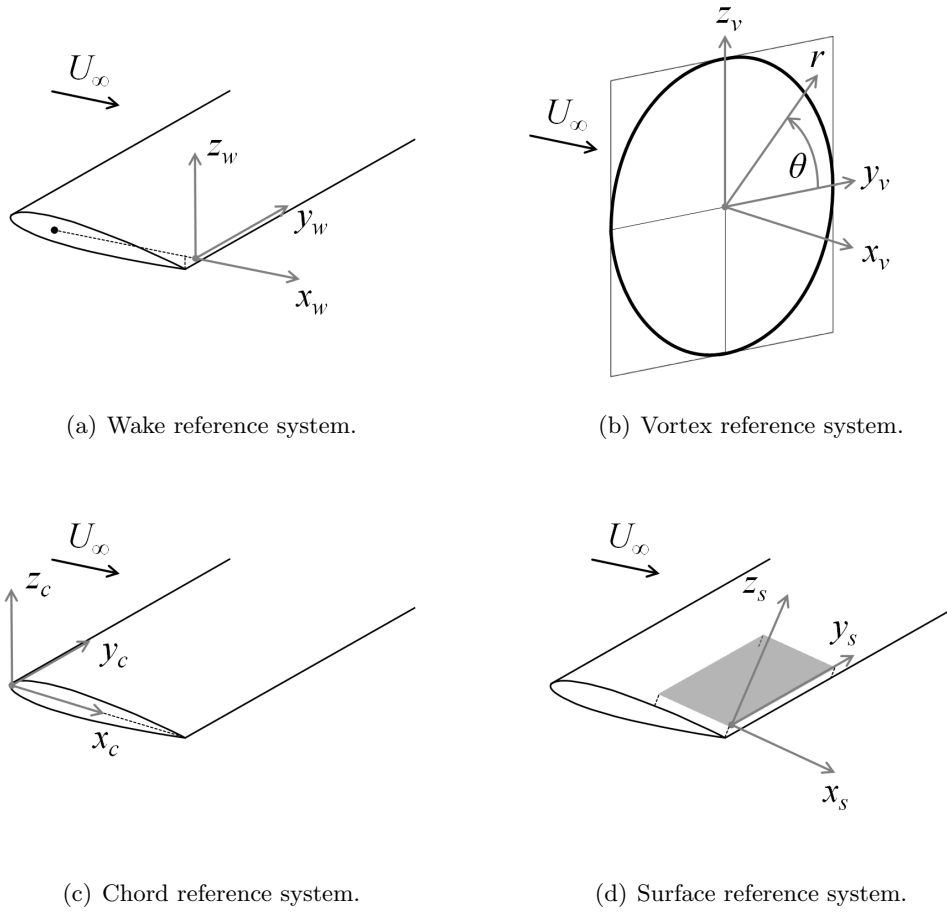


Figure 2.10: Reference systems.

Devenport *et al.* (1996) described the inboard movement of the vortex axis, in the range $x_w = 5-30$ and produced by a blunt wingtip with NACA 0012 profile, with the trend $y_0 \propto x_w^{0.5}$. Experiments in the near field, $x_w = 0.1-3.33$, of a square tip of a horizontal wing with NACA 0015 profile carried by Ramaprian & Zheng (1997) revealed inboard and vertical movement following respectively the trends $y_0 \propto x_w^{0.75}$ and $z_0 \propto x_w^{0.5}$. The difference between the two different trends may be attributed to the different range of streamwise locations they describe and to the different tip geometry which largely affects the vortex formation and development.

Taking the trends suggested by Ramaprian & Zheng (1997) and assuming, as a first approximation, the virtual origin of the vortex at the trailing edge of the tip, the misalignment between the vortex axis and the x_w axis in the range $x_w = 0.25-4$ is between 2.7° and 5.5° for the spanwise movement and between 1.3° and 5.1° for the rise movement. On vortex measurements on planes perpendicular to the freestream, this leads to an estimation of the maximum plane misalignment error of 3.7% of the chord.

This error corresponds to the maximum displacement between the measurement plane and the vortex plane (plane perpendicular to the vortex axis) found at a distance of 0.25 chords from the vortex centre at $x_w = 0.25$.

Assuming an axisymmetric vortex which axis follows the analytical trends, this misalignment corresponds to assume velocity vectors which are at 0.074 chords of distance along the freestream direction as they were on the same plane (this distance rapidly decreases moving downstream). This distance is small compared to the length scales of the axial evolution of the vortex and therefore the misalignment error is negligible.

The origin of this reference system is at the trailing edge of the tip at an angle of attack of $\alpha = 0^\circ$ so that the actual distance from the trailing edge changes as $0.75c \cdot (1 - \cos \alpha)$, which corresponds to 1.6% of the chord for an angle of attack of 12° .

(b) Vortex reference system A vortex can be described either with a cartesian coordinate system or a cylindrical system (see Figure 2.10(b)). The first shows x_v on the vortex axis and the y_v and z_v axes on the vortex plane, the first directed as the wing span and the latter perpendicular to the two and directed as the lift. The cylindrical coordinate r is the radial coordinate with origin at the centre of the vortex and θ the angular coordinate which is 0 on the y_v axis. The relation between the two reference systems and the relations of velocity vectors and Reynolds stresses expressed in the two reference frames are given in Appendix C.4.

The misalignment error between the freestream and the vortex axis is discussed in the previous section and the assumption of local alignment of vortex axis and freestream is used throughout, that is $x_w \equiv x_v$, $y_w \equiv y_v$ and $z_w \equiv z_v$.

(c) Wing chord reference system For point measurements on the wing (i.e. hot film and pressure tappings) and for measurements on planes on the wing and perpendicular to the freestream (i.e. flow visualizations), the reference system adopted has the origin at the leading edge of the tip, the x_c axis aligned with the chord, y_c aligned with the span and pointing towards the root and z_c perpendicular to the two (see Figure 2.10(c)). This is not a fixed reference system but is rotates with the angle of attack. The x_c coordinate is 0 at the leading edge and 1 at the trailing edge; y_c is 0 at the tip and equal to the aspect ratio at the root. Negative values of y_c occur at the tip region when it is not squared.

(d) Wing surface reference system For measurements on planes parallel to the wing surface, x_s is the curvilinear coordinate which follows the surface and has origin at the tip trailing edge (see Figure 2.10(d)). The y_s axis is aligned with the span and z_s is directed perpendicular to the wing surface and away from it. Because the surface curvature of the last 40% of a symmetric NACA profile is small and the tangent angle is also small, the difference between x_s and x_c is below 1% in that region. Therefore, the comparison of measurements on these two reference systems without a conversion can be done without incurring significant errors.

Wingtip vortex formation

The human mind is generally far more eager to praise and dispraise than to describe and define.

CLIVE STAPLES LEWIS

The trailing vortex forms along the tip of the wing and the behaviour and characteristics of the trailing vortex in the wake are strongly affected by the initial process. In particular, the wing layout, wingtip geometry, wing load distribution, Reynolds number and boundary layer on the wing are important factors in the formation of a trailing vortex.

Moreover, changes in the vortex structure and decay characteristics are usually accomplished by changes on the wing. All the wingtip vortex control devices are related to the vortex during its formation and development on the wing. Therefore, the effectiveness of such devices depends upon a correct understanding of the physics of the flow at the wingtip.

The wing configuration and the tip geometry have a big impact on the initial process, particularly on the swirl and axial velocity distribution of the vortex in the very early wake (Green, 1995). Baker *et al.* (1974) and Devenport *et al.* (1996) believe that the vortex wandering is due to the freestream turbulence which has a beneficial effect as it enhances the vortex rate of decay (Sharpkaya & Daly, 1987). Bailey & Tavoularis (2008) tested several turbulence grids for the incoming flow over an airfoil and they showed that an increase of the freestream turbulence resulted in an increase of the amplitude of vortex wandering. Also, they observed that for the no-grid case there could be multiple sources of the wandering, each with a different range of dominant frequency including frequencies lower than 2 Hz. Jacquin *et al.* (2001) presented the meandering as a consequence of several phenomena such as line vortex instabilities, entrained turbulence from the rolling up or propagation of unsteadiness originated by

the model. Green & Acosta (1991) considered also the possibility of several vortex core instabilities. Beresh & Henfling (2010) indicated that the meandering can be induced by an external source to the vortex itself suggesting that the meandering is already present on the surface, prior to vortex shedding.

Whereas several studies on the meandering of the vortex in the wake can be found, there is obviously a lot missing on the unsteadiness of the vortex when forming on the model and also on the possible links between the two stages. Common methods for disturbing the vortex flow in its early stage are based on changes in the tip geometry which result in complicated flowfields which are often too challenging for a detailed computational study. Therefore, the study and evaluation of these devices are mainly experimental and go usually through several adjustments based on the experience and intuitions of the designer. A characterization method of the flow is needed for the description of the mechanism of the formation of a tip vortex.

Moreover, understanding the relationship between meandering and unsteadiness of the vortex in the wake with the unsteadiness of the flow on the wing is one of the key steps of vortex control. Beside passive (static) vortex control methods based mainly on changes in the wing configuration (vortex generators, winglets, wingtip-mounted propellers, different tip geometries), several active (dynamic) methods have been recently deployed where continuous or periodic controls are adopted such as blowing (Heyes & Smith, 2004; Gursul *et al.*, 2007), oscillating flaps (Haverkamp *et al.*, 2005; Gupta, 2011; Breitsamter & Allen, 2009), dynamic Gurney flaps (Greenblatt & Meyer, 2009), boundary layer separation control (Greenblatt, 2005) and surface-mounted actuators (Quackenbush *et al.*, 1999). The often poor efficiency of control techniques can be in great part attributed to insufficient knowledge of breakdown. Mitchell & Delery (2001) pointed out that the difficulty in adopting periodic control devices is to identify characteristic frequencies in the vortical structure in order to adjust the position and intensity of such control actions. Information on those frequencies, which play a big role in the excitation of vortex instabilities, is still lacking.

The aim of this chapter is to enlighten on the mechanisms that lead to the formation of a wingtip vortex. The link between the unsteadiness of the vortex formation on the wing and its development in the early wake is also addressed. Different experimental techniques are applied on the wingtip vortex formation on a rectangular wing with squared and rounded tip. A number of techniques have been adopted for these studies in the past decades and information from each of these methods revealed different aspects of the tip vortex flow. The combined description of different flow features provides a

greater insight into the interaction phenomena (Pagendarm & Walter, 1994) because each technique gives a compact and meaningful representation of a selected feature in the data.

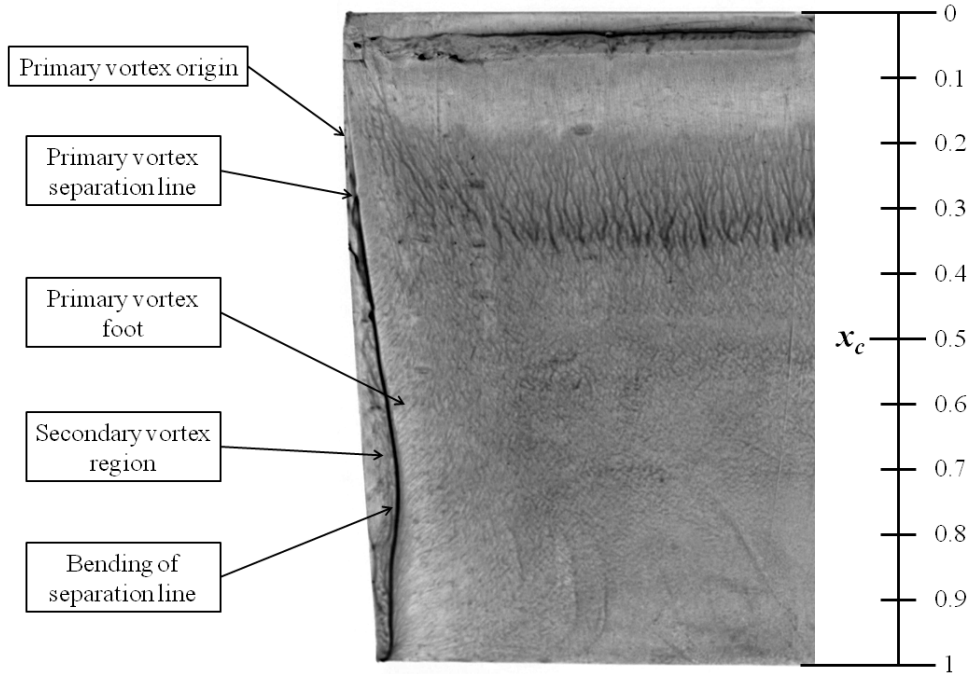
An initial study of the vortex footprint on the wing surface is accomplished by surface oil flow visualizations and presented in Section 3.1. In Section 3.2, pressure measurements on the wing surface give a quantitative description of the vortex footprint and analysis on the unsteadiness of the pressure measurements near the wingtip reveal the unsteady nature of the vortex system. After an overview of the vortex main features, a bigger scale model is adopted in order to highlight the rolling up mechanism and the dynamics of the multi-vortex structure through smoke visualizations presented in Section 3.3. In Section 3.4 stereoscopic particle image velocimetry on planes parallel to the wing surface are presented with a new method for the identification of the vortex structure. Section 3.5 discusses the unsteadiness of the vortical structure on the wing surface which is measured by wall-mounted hot film probes. Analysis of signal spectra show intense contributes on the vortex movement at low frequencies. Low frequencies, calculated from video recordings of smoke visualizations, are found also in the unsteadiness of the vortex in the early wake and presented in Section 3.6.

SECTION 1

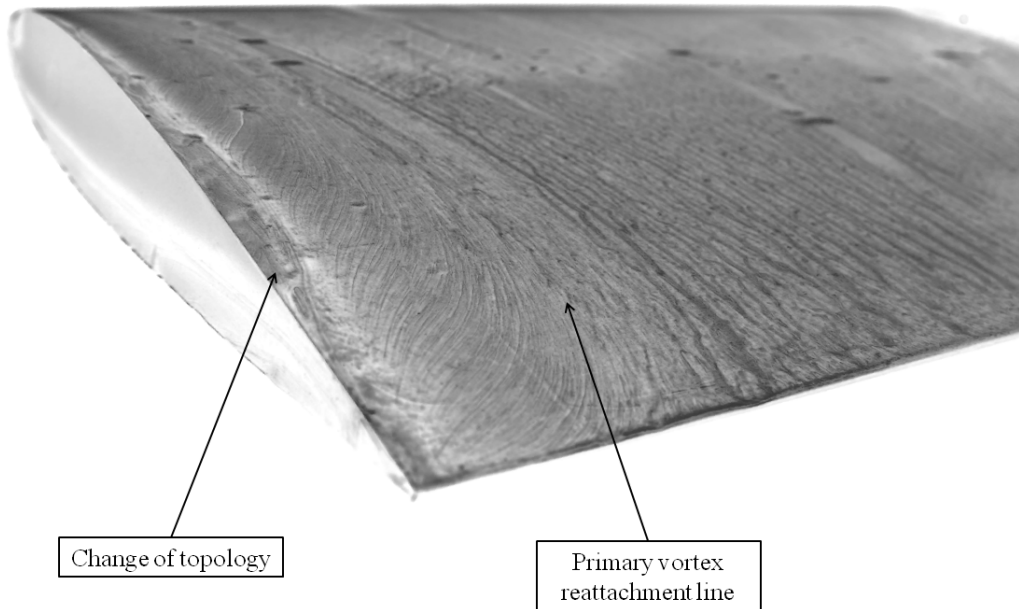
Surface oil flow visualization

In order to gather general information on the limiting streamlines of a typical wingtip vortex during its formation on the wing, surface oil flow visualizations are presented for model **M1** installed in the Argyll wind tunnel at Reynolds number of $5 \cdot 10^5$ and angle of attack of 12° in Figures 3.1 and 3.2. Pictures show a darker colour where the oil is accumulated. The assumption of oil film pattern well representing the actual wall streamlines is valid when the pressure gradient is small compared with the skin friction (Merzkirch, 1987). Therefore, this kind of visualization is a very good tool for a visual understanding of the structure of the surface flow but might become not very accurate in determining the position of separation and reattachment lines. Also, differently from patterns observed for delta wings where convergence and divergence of wall shear stress lines clearly show separation and reattachment lines (Taylor & Gursul, 2004), rectangular wingtip vortices are less intense than delta wing vortices and the flow in the tip region is dominated by the streamwise component of the velocity vector. For

this reason the definitions of separation and reattachment lines of the vortex need to be based also on considerations other than convergence or divergence of skin friction lines.



(a) Top view (freestream from top to bottom).



(b) Trailing edge.

Figure 3.1: Surface flow visualizations: suction surface.

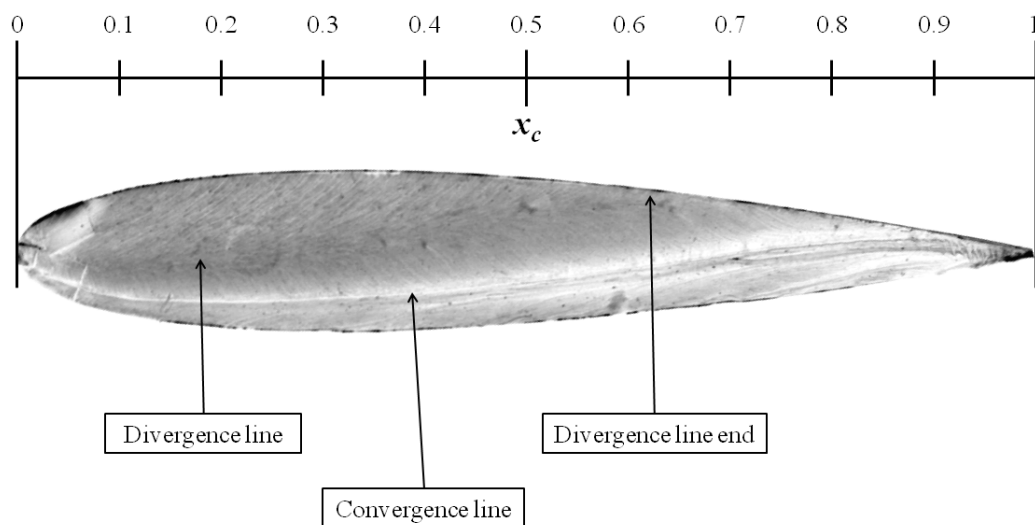


Figure 3.2: *Surface flow visualizations: tip surface (freestream from left to right).*

A strongly three-dimensional flow is observed near the tip region. The primary vortex originates at around $x_c = 0.2$ (from the top view in Figure 3.1(a)) which is where the flow crosses over the sharp edge of the tip and moves inboard. The primary vortex separation line is indicated by an accumulation of pigment (convergence line) and its distance from the tip grows linearly until $x_c = 0.75$ where it bends toward the tip suggesting a change of vortex structure topology. Unlike typical two-dimensional separations, the skin friction magnitude is not zero along this line (due to the presence of a streamwise component of the velocity). Tobak & Peake (1982) referred to this type of line as indicative of local separations (or open separations). The peculiar characteristic of this kind of separation is that there are no singular points in the skin friction line topology. Additionally, there is no zone of stagnant fluid or reversed flow in the x_c direction which typically occurs in flows which are globally separated (for more details, see for example Zilliac (1988) and Delery (2001)). The region between the primary vortex separation line and the tip is occupied by a counter-rotating secondary vortex. It is the combination of the primary and secondary vortices induced flow on the surface that produces the accumulation of pigment. The foot of the primary vortex (where the vortex streamlines on the vortex plane are parallel to the surface) is identified by a region of maximum chordwise gradient of the skin friction lines on the right of the separation line. The primary vortex reattachment line can be identified, as a first approximation,

by the region where limiting streamlines bend toward the tip as shown in Figure 3.1(b).

Despite the simple geometry, vortices from squared tips reveal a complicated flow structure due to the two sharp edges which induce separations of the flow. From the tip side (Figure 3.2), the presence of a divergent and a convergent line suggests the presence of another system of vortices which interacts with the primary and secondary vortices on the suction surface. Both these lines start from the leading edge: the divergent line ends on the top edge at around $x_c = 0.6$; the convergent line ends at the trailing edge. The region between the two lines is occupied by a vortex which grows along the chord and, interacting with the vortices on the suction surface, contributes to the change of topology of the vortex structure.

SECTION 2

Pressure on the wing surface

Results on the effect of the angle of attack on the pressure distribution in the vicinity of the squared wingtip of the **M1** model are presented. In this section, the high aspect ratio guarantees a vortex structure which is not influenced by the presence of the wall. The wing is tested at angles of incidence of 0° , 4° , 8° , 12° and 15° and Reynolds number of $5 \cdot 10^5$.

Signals from the pressure tappings are recorded on a sampling window of 2 seconds which was observed to satisfy the convergence of the average pressure. A sampling frequency of 1 KHz was adopted and a moving average is applied as low-pass filter with cutting frequency of 30 Hz accordingly to the estimated bandwidth of the pressure measurement system (see Section 2.(b)). The averaged surface pressure coefficients are calculated as follows:

$$c_P = \frac{P - P_\infty}{\frac{1}{2}\rho U_\infty^2} \quad (3.1)$$

Frequency studies from pressure measurements through long pipes are also presented although they can be affected by several errors and generally they are not very reliable. However, indications on the wall pressure unsteadiness are useful in drawing preliminary observations on the phenomenon. The fluctuation of the signal from selected pressure tappings indicates the unsteady nature of the vortex flow on the wing surface at low frequencies.

(a) Average pressure distribution Averaged pressure coefficients contours from the pressure, suction and tip surfaces are plotted respectively in Figures 3.3(a), 3.3(b) and 3.4 for the wing at $\alpha = 12^\circ$. Cubic interpolation of the data is applied for such contours.

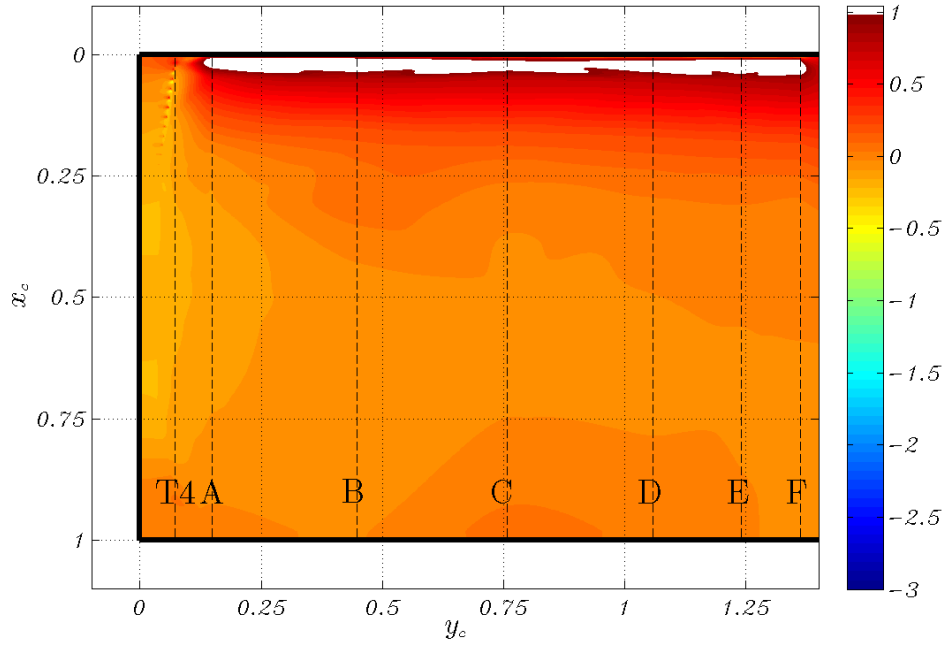
The pressure coefficient on the pressure side of the wing shows a stagnation line (white region) nearly straight across most of the wing at an average distance from the leading edge of 3% of the chord. The flow approaches two-dimensional behaviour from $y_c > 0.5$. Near the tip of the wing, the flow becomes three-dimensional; the flow in the direction of the tip is induced by the favorable pressure gradient in the y_c direction. The sharp edge of the squared tip geometry forces the flow to separate at the tip and to form the tip side vortex structure observed in the surface flow visualizations.

Similarly, on the suction side of the wing (Figure 3.3(b)), the pressure coefficient contour is two-dimensional for $y_c > 0.5$. At the leading edge, a suction peak is observed and the minimum surface pressure coefficient is -3.11 which is found at the tapping row F (the most inboard array). The footprint of the wingtip vortex on the wing surface appears as a suction region which is shaped as a vertical region at around $y_c = 0.07$. This region widens moving toward the trailing edge and it includes pressure tapping rows T2 and T3. The integrated effect of the vortex is to produce an increase in the lift distribution over the region near the wingtip (McAlister & Takahashi, 1991). The spatial resolution limitations of these measurements can not clearly confirm a secondary suction peak due to the secondary vortex.

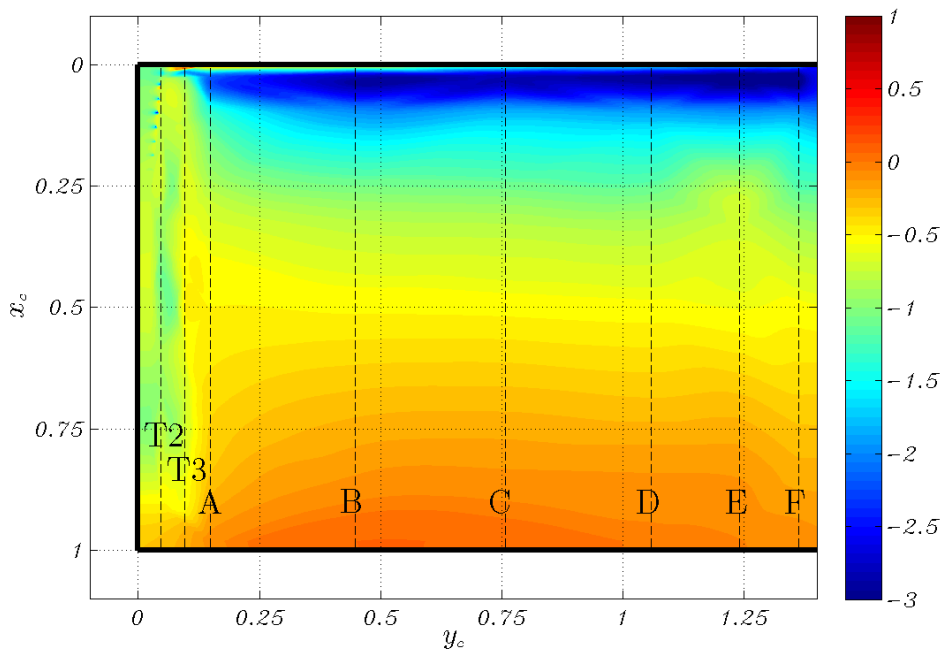
Because the vortex flow over a squared tip encounters abrupt separations at the sharp edges, the resulting surface pressure distribution is not smooth when crossing from the pressure to the tip surface and from the tip to the suction surface. Chow *et al.* (1997a) described the pressure distribution over a wing with rounded tip. A very different distribution of the pressure on the tip surface is found. The rounded tip geometry generates a tip vortex which does not separate abruptly and the pressure on the suction surface shows a smoother distribution.

On the tip surface (Figure 3.4) the pressure information is limited by the pressure tappings position to a region around the symmetry plane. The low pressure region developing from around $x_c = 0.3$ (green colour) might indicate the growing of the tip vortex system observed also in the surface oil flow visualization of Figure 3.2.

The effect of the angle of attack on the surface pressure is observed in Figure 3.5 where the suction surface pressure distribution is reported for angles of attack of 4° , 8° , 12° and 15° . The increase of the suction peak at the trailing edge with the angle of



(a) Pressure surface.



(b) Suction surface.

Figure 3.3: Pressure coefficient distribution and pressure tapings at $Re = 5 \cdot 10^5$ and $\alpha = 12^\circ$: suction and pressure surface.

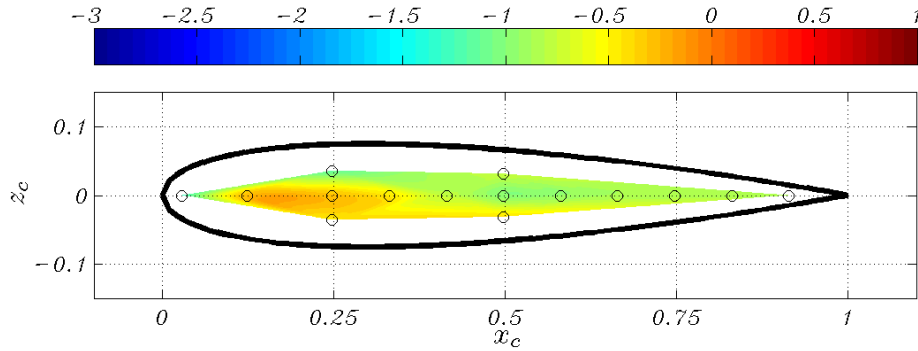


Figure 3.4: Pressure coefficient distribution and pressure tapings at $Re = 5 \cdot 10^5$ and $\alpha = 12^\circ$: tip surface. The circles correspond to the pressure tapping positions.

attack is clearly observed. Although the region affected by the presence of the tip vortex shows a similar size in the y_c direction at all the angles of attack, the suction peak due to the vortex (and therefore the vortex intensity) increases from around $c_P = -0.5$ for $\alpha = 4^\circ$ to $c_P = -1.5$ at $\alpha = 15^\circ$. Also, the extension in the x_c direction grows with the angle of incidence and it indicates an earlier initial rolling up of fluid for higher angles. The apparent suction around the origin of the reference system is believed to be a result of the interpolation.

The earlier initial rolling up at higher angles of attack is confirmed by the behaviour of the pressure distribution along the pressure tapings row T1 on the mid plane of the tip surface (Figure 3.6). Peaks are observed between $x_c = 0.4$ and 0.6 and they grow and move toward the leading edge as the angle of attack increases. This peak is attributed to the suction caused by the vortex growing on the tip surface and originated by the separation of the lower sharp edge. The peak on the pressure tapping near the leading edge might be caused by a local separation of the flow.

McAlister & Takahashi (1991) presented a large parametric study of wing pressure distributions for a rectangular wing with NACA 0015 profile. The pressure distribution on a wing with aspect ratio of 3.3, chord of 0.52 m and squared tip is presented in Figure 3.7. A gradual reduction in the suction peak as the tip of the wing is approached is observed. A distortion over the suction surface is also observed for $y_c < 0.1$ which generates an increase in the lift over the region near the wingtip. In Figure 3.7(f), the pressure curve exhibits two strong undulations which were linked to the presence of the secondary vortex. The Reynolds number appeared to have a smaller effect on the pressure undulations in the squared tip case than in the rounded tip case. This apparent insensitivity is believed to be due to the transition fixing nature of the sharp edge.

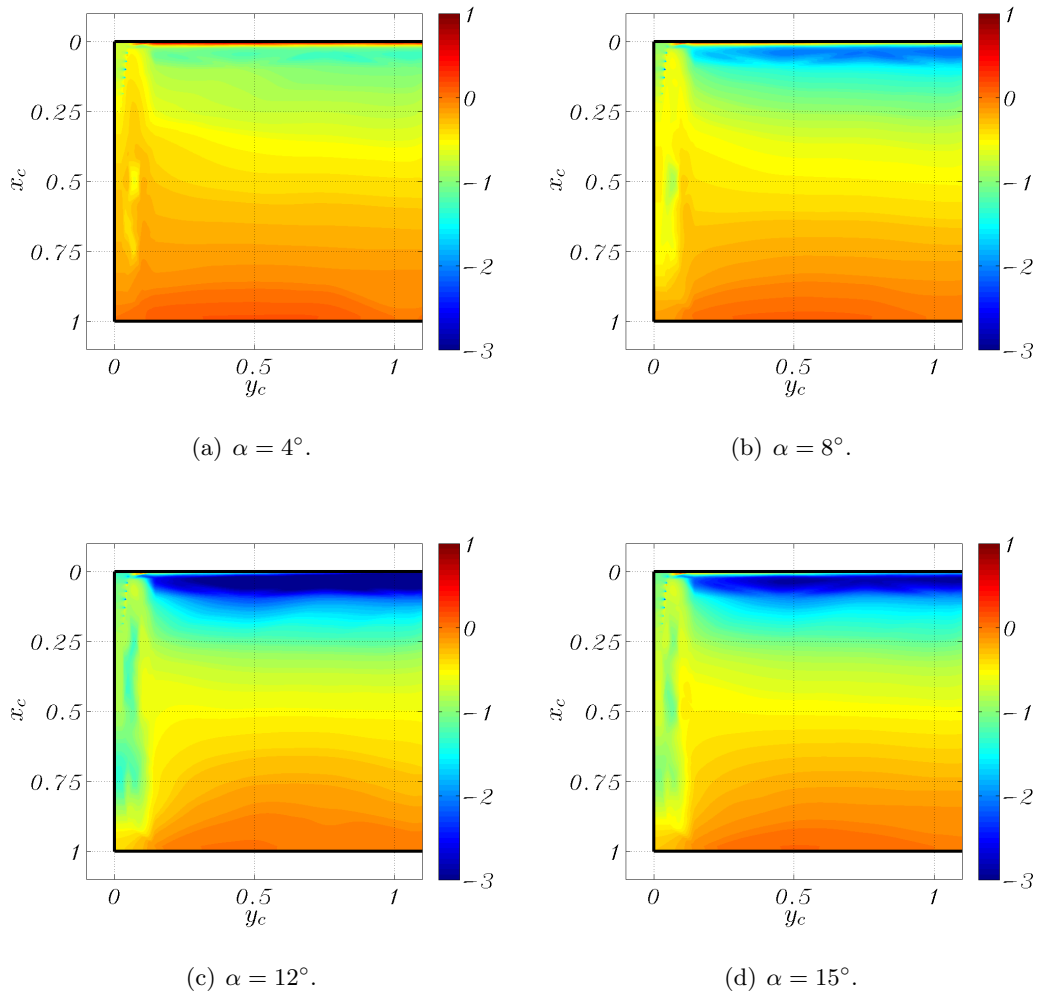


Figure 3.5: Pressure coefficient distribution on the suction surface at $Re = 5 \cdot 10^5$.

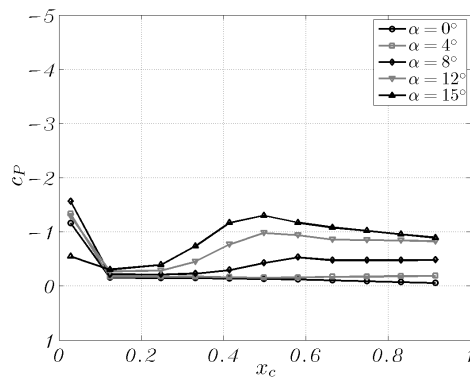


Figure 3.6: Pressure coefficient distribution along tapping row T1 at $Re = 5 \cdot 10^5$.

The present experiment is similar to the one presented by McAlister & Takahashi (1991) and reported in Figure 3.7, and the relative pressure coefficient distributions are

shown in Figure 3.8. Less intense undulations and lower values of the suction peaks are observed and they might be caused by the lower spatial resolution of the pressure tappings. However, the double undulation on the suction surface near the tip is observed and similar distributions are found for $y_c > 0.15$. The undulation at around $x_c = 0.4$ in Figure 3.8(f) and the undulation in Figure 3.8(e) at $x_c = 0.75$ are believed to be related to the suction generated by the primary vortex which moves inboard as the trailing edge is approached. Instead, the second undulation in Figure 3.8(f) at around $x_c = 0.7$ is generated by the secondary vortex which does not grow and move inboard enough to affect the pressure on the tapping row T3.

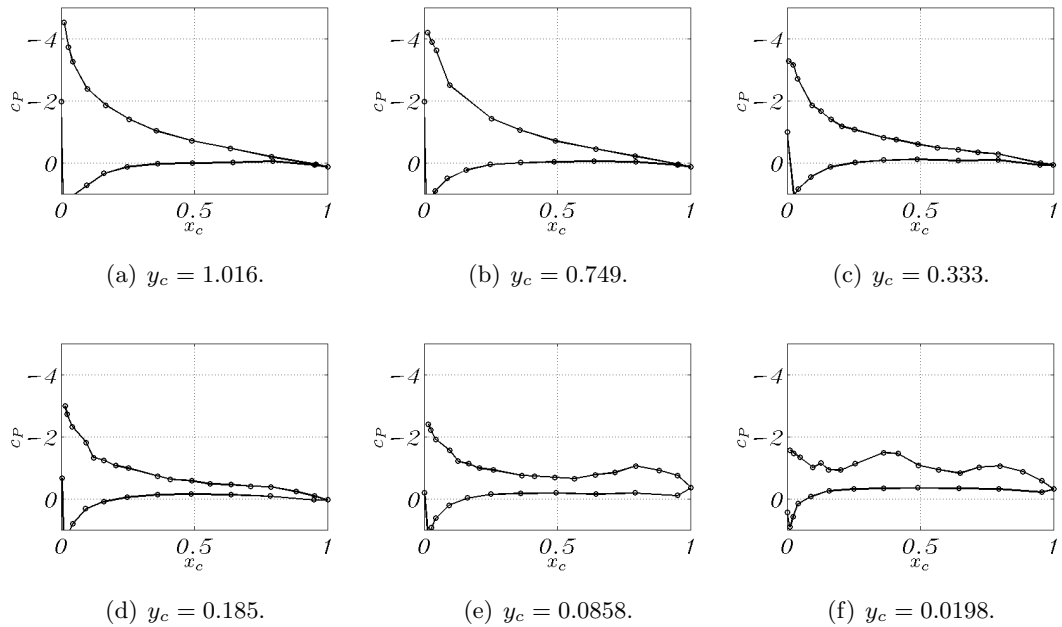


Figure 3.7: *McAlister & Takahashi (1991) experiments: pressure coefficient distribution at $Re = 1 \cdot 10^6$ and $\alpha = 12^\circ$.*

(b) Pressure fluctuation at the wingtip

Recordings at 1KHz and sampling window of 10 seconds were also accomplished for the evaluation of fluctuations and the same low pass filter with cutting frequency of 30 Hz was applied. The unsteadiness of the pressure signals is presented in terms of standard deviation normalised by the reference static pressure outside the test section.

Pressure fluctuations on measurements from some of the tappings of row T2 (chordwise row near the tip) are reported in Figure 3.9 for different angles of attack. At $\alpha = 0^\circ$, the signal standard deviation does not change moving along the chordwise

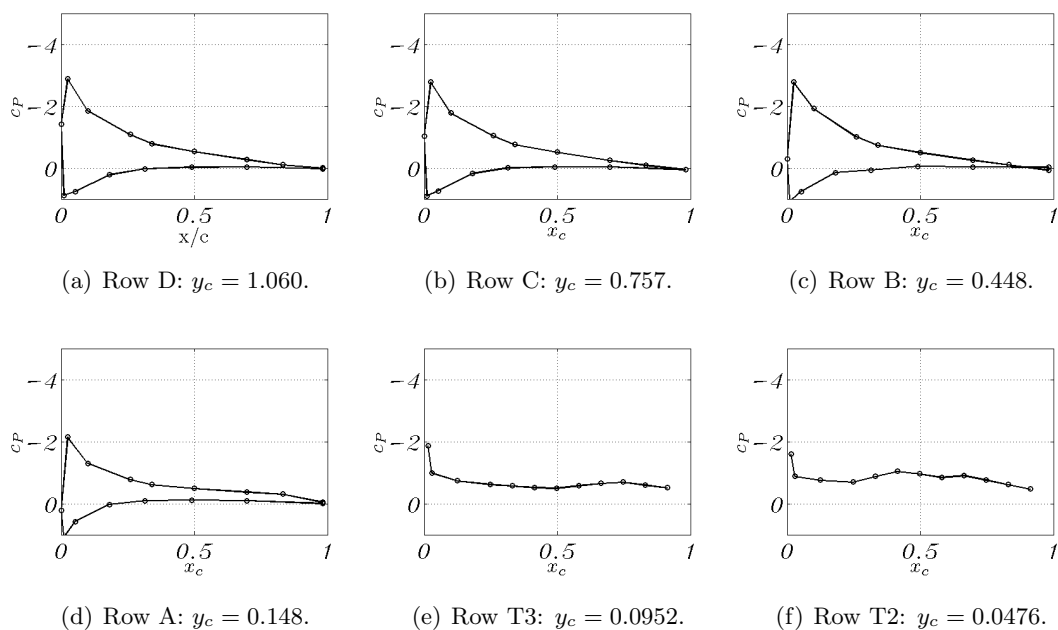


Figure 3.8: Pressure coefficient distribution at $Re = 5 \cdot 10^5$ and $\alpha = 12^\circ$.

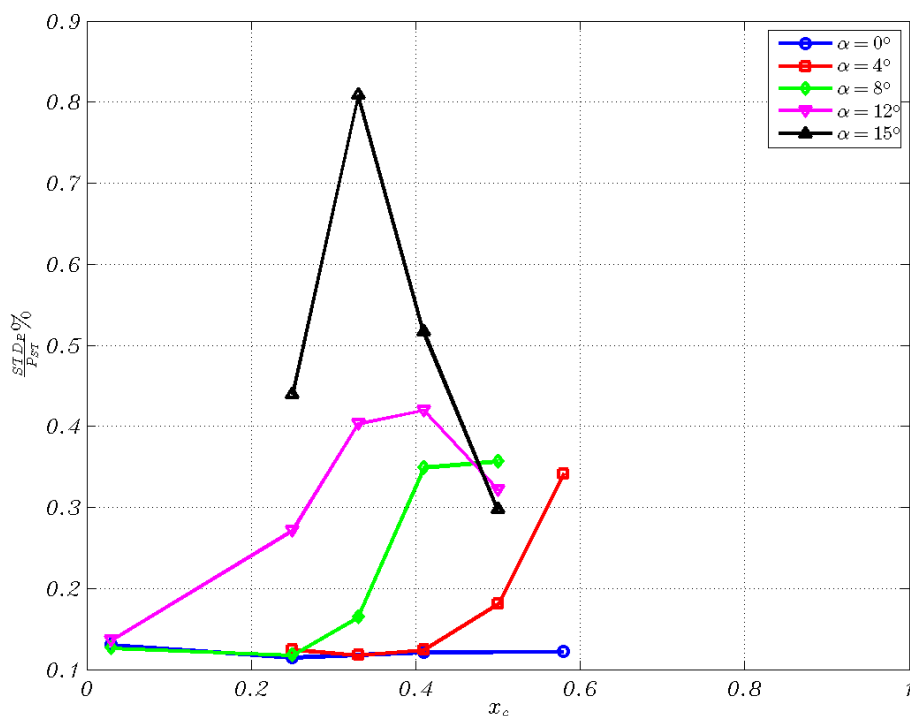


Figure 3.9: Pressure standard deviation.

direction. For the wing at an angle, the standard deviation trend shows a peak which moves toward the leading edge when α is increased: at $\alpha = 4^\circ$ the peak is observed at

the most downstream station ($x_c = 0.58$) whereas at $\alpha = 15^\circ$ the peak is at $x_c = 0.33$. Also, fluctuations are higher for higher angles of attack. The fluctuations at the pressure tapping near the leading edge ($x_c = 0.029$) is the same for all the angles. Looking at the pressure contours in Figure 3.5, the maximum fluctuation is observed in the early stage of the rolling up of the vortical flow. Downstream of the peak, the value of the fluctuation decreases and it is believed that the position of maximum unsteadiness moves inboard due to the growing of the primary vortex and therefore is not seen anymore by the pressure tappings from row T2.

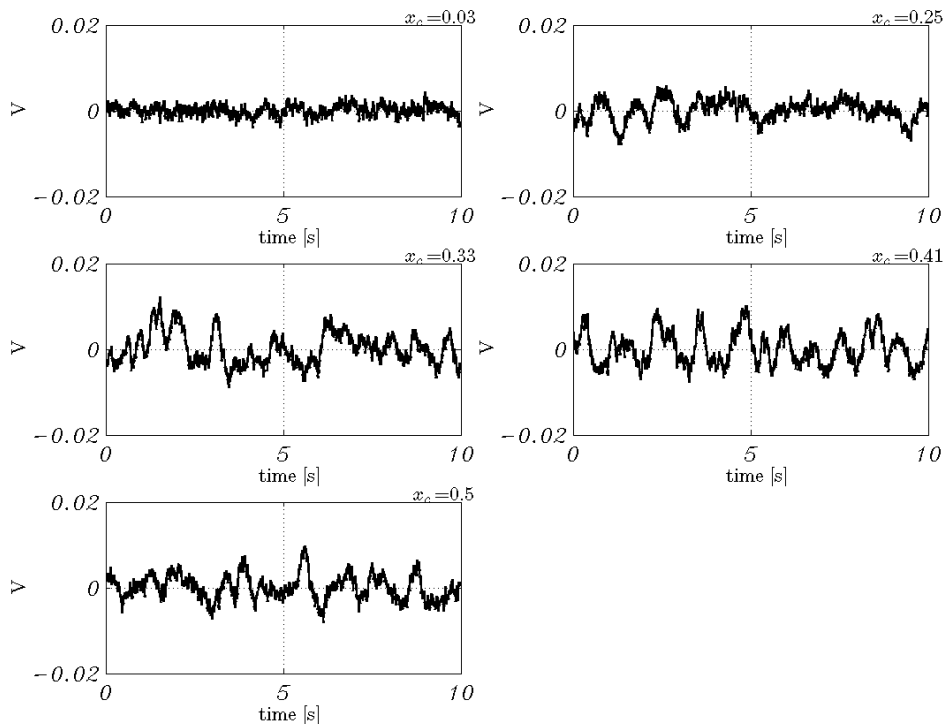


Figure 3.10: Pressure signal for $\alpha = 12^\circ$.

The signal as function of the time for $\alpha = 12^\circ$ is presented in Figure 3.10. The increasing of the pressure unsteadiness moving toward the trailing edge comes primarily from a low frequency signal of period of around 1 Hz observed for $x_c = 0.33$, 0.41 and 0.5. At $x_c = 0.03$, the signal does not show this low frequency disturbance and at $x_c = 0.25$ that disturbance is observed only for the first 5 seconds of sampling. These observations suggest a low frequency and intermittent behaviour of the initial roll up of fluid around the tip.

SECTION 3

Smoke visualization on the rolling up

Smoke visualizations of the wingtip vortex formation were performed in the smoke visualization wind tunnel on the **M2** model with squared and rounded tip. Pictures on laser planes perpendicular to the freestream and at different chordwise positions were taken. The test was carried out at a low Reynolds number of 3000, corresponding to a wind speed of 0.057 m/s, so that a laminar rolling up was observed. The wing sections on the following pictures are added during the post-processing of the images.

(a) Rolling up on squared and rounded wingtip A typical smoke visualization of a wingtip vortex system on the rounded tip is shown in Figure 3.11. The dominant flow is perpendicular to the laser sheet and it generates discontinuous smoke lines which are more evident where the ratio between the cross-plane velocity and the in-plane velocity is high. The thick smoke lines coming from the top edge of the picture are traces of the curved smoke filaments that have left the smoke pipe upstream of the wing. If the smoke filaments did not bend, they would appear as discrete dots on the laser plane. The primary vortex is fed by the tip-crossing flow which moves from the pressure surface (left) to the suction surface (right) and forms a spiral structure around the primary vortex centre. A counter-rotating secondary vortex is formed at the foot of the primary vortex and a tertiary vortex is also observed between the secondary vortex and the tip-crossing flow.

From the evolution of the vortex along the tip in Figure 3.12, the tip-crossing flow from the wing pressure surface can be observed as early as $x_c = 0.30$ (Figure 3.12(a)). However, the adverse pressure gradient is not strong enough and the tip radius is not small enough to induce the separation of the flow from the surface (Duraismy, 2005). The vortex system is remarkably different at $x_c = 0.40$ (Figure 3.12(b)), where the separation of the crossing flow generates a vortical structure squeezed on the surface. At $x_c = 0.60$ (Figure 3.12(d)), the tip vortex system is composed of three vortical structures. Along with the primary vortex, a counter-rotating second vortex and a third vortex are formed. This vortex system is clearly seen at $x_c = 0.80$ (Figure 3.12(f)) where the secondary and tertiary vortices are enclosed by a bigger primary vortex and the plane streamlines of the separated flow from the pressure side of the wing. At $x_c = 0.90$ (Figure 3.12(g)), the reduction in the thickness of the wing and the enlargement of the primary vortex pushes the secondary and tertiary vortices outboard. Finally, at the

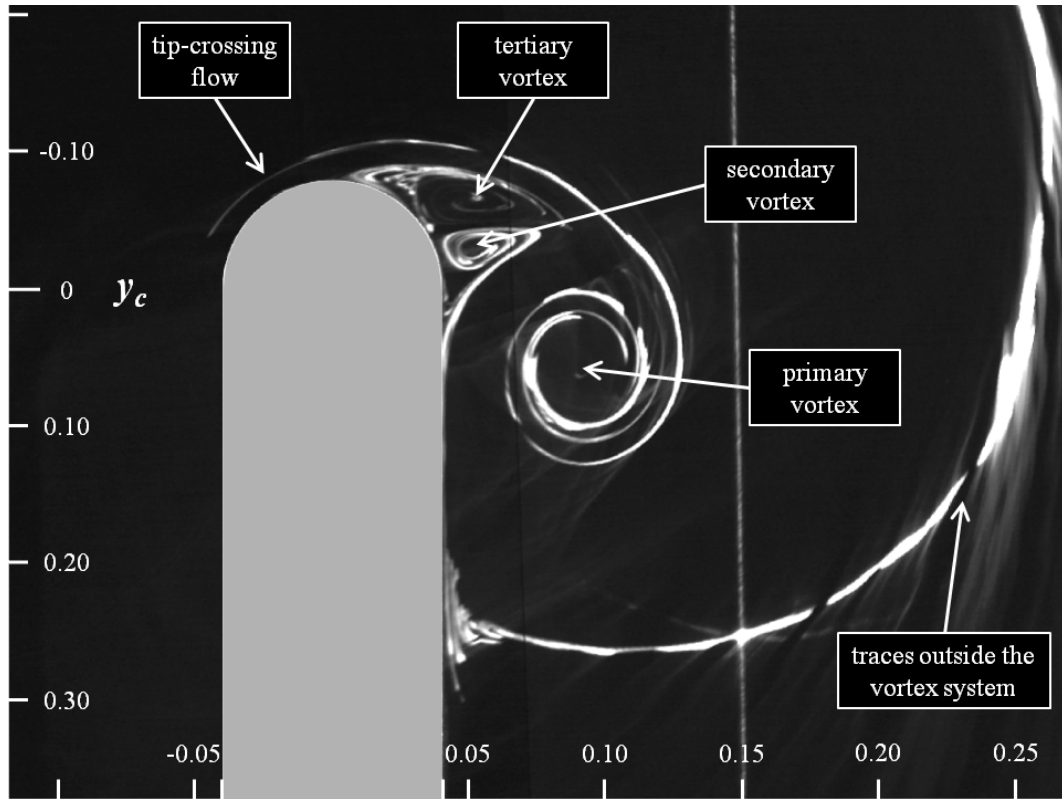


Figure 3.11: *Vortex at $Re = 3000$, $x_c = 0.75$ and $\alpha = 12^\circ$ on rounded tip; wing section in gray.*

trailing edge (Figure 3.12(h)), the secondary and tertiary vortex are not bounded by the surface anymore but they wrap around the primary vortex with the flow from the pressure surface.

At Reynolds number of 3000, the tip vortex system on rounded tip is weakly time-dependent and the primary, secondary and tertiary vortices are well identifiable. At a fixed plane they do not move around but they form a stable multi-vortex system and the spiral shape is very clear.

On squared tip, the separation of the crossing flow from the pressure surface to the suction surface does not happen smoothly but it is forced by the sharp edges of the tip. Therefore the number of vortices due to separations increases and their interaction generates a time-dependent vortex system which enhances the merging of the vortices with the spiral layers and the diffusion of the smoke, as also observed by Sohn & Chang (2011). In Figure 3.13, the evolution of the tip vortex system over the squared tip is presented. At $x_c = 0.20$ (Figure 3.13(a)), several vortices can be already identified. A first set of three vortices formed by the pressure surface-tip edge appears in a similar form of the vortex system on the rounded tip in Figure 3.11. A squared tip was tested

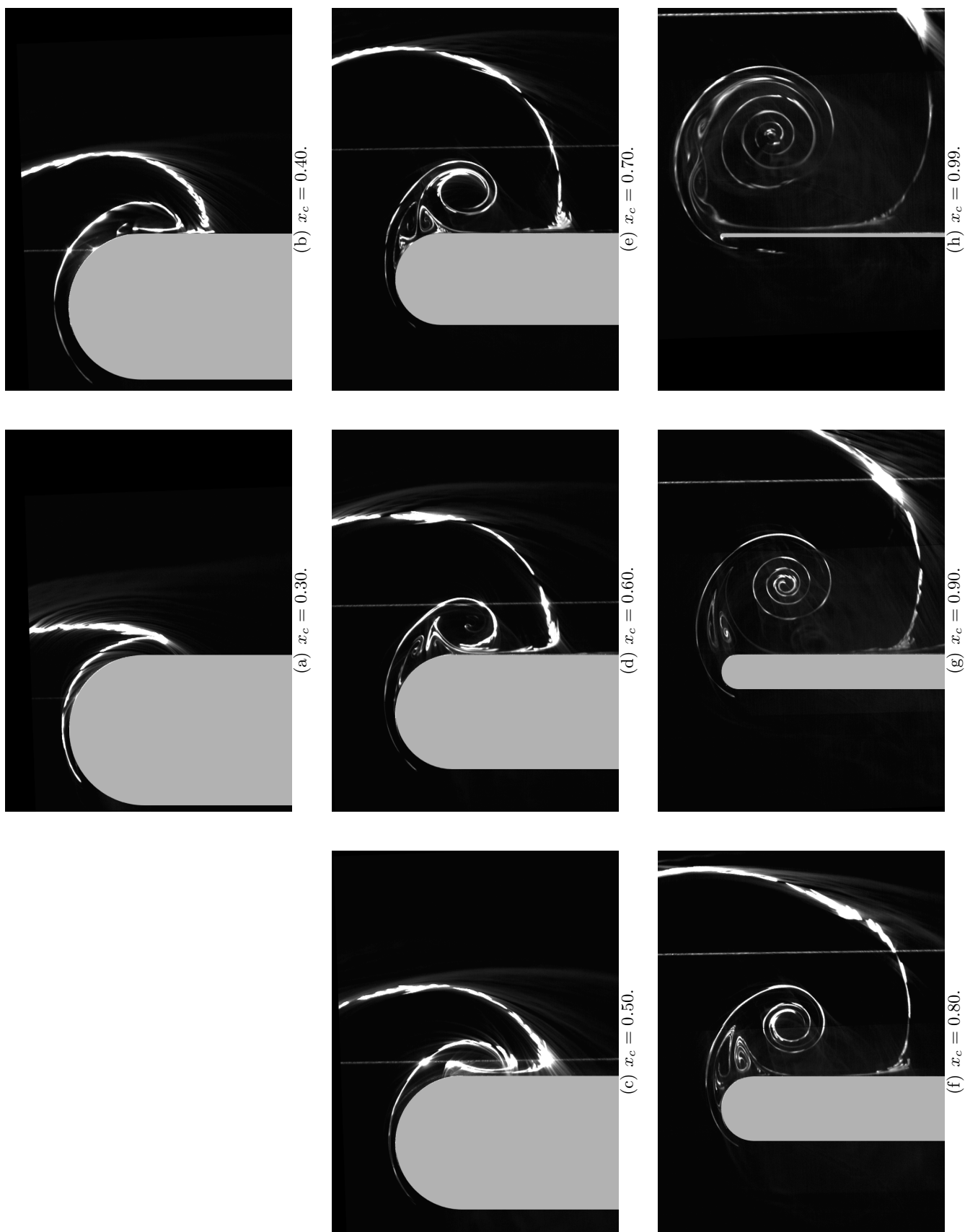


Figure 3.12: Vortex evolution at $Re = 3000$ and $\alpha = 12^\circ$ on rounded tip; wing section in gray.

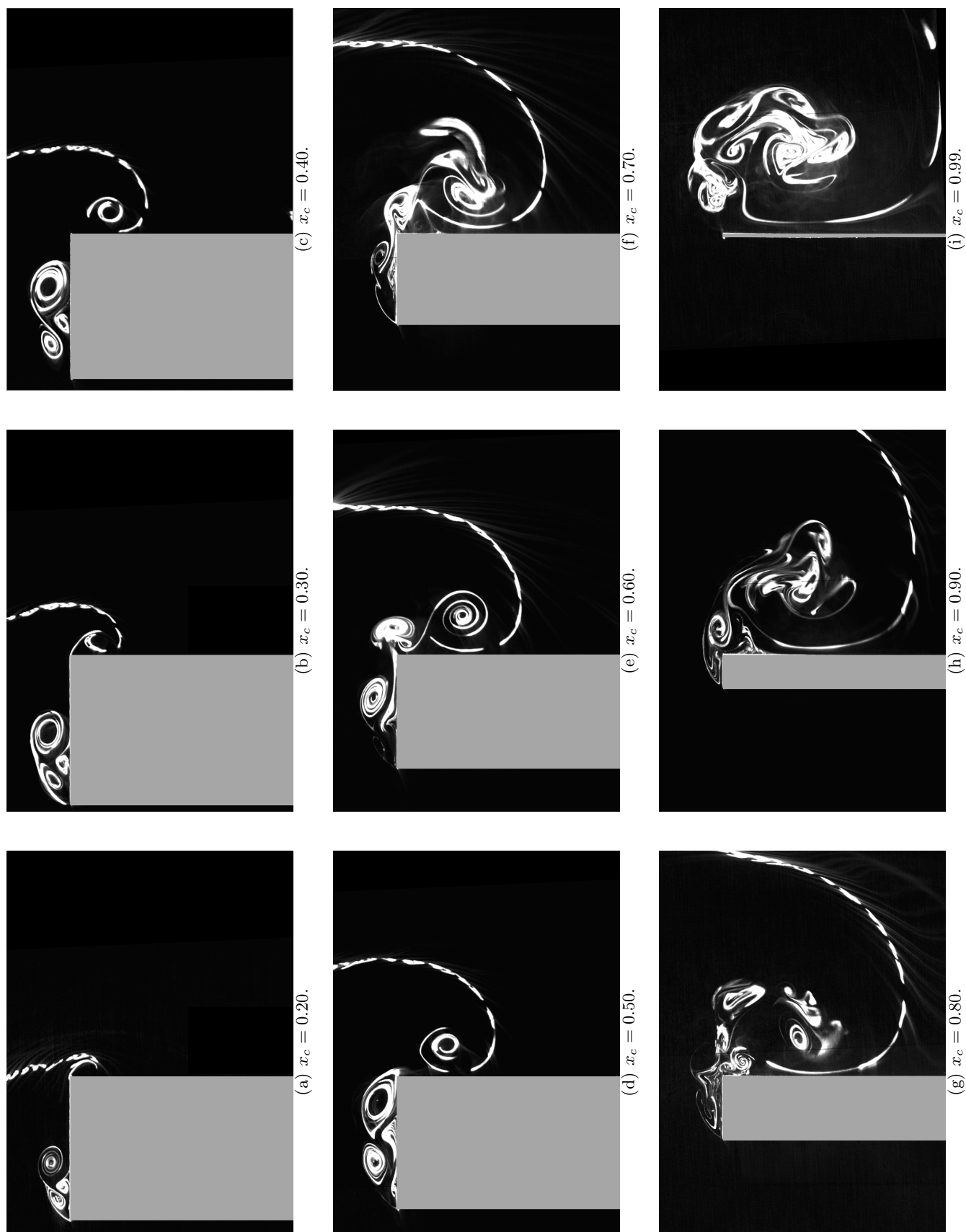


Figure 3.13: Vortex evolution at $Re = 3000$ and $\alpha = 12^\circ$ on squared tip; wing section in gray.

also by Francis & Kennedy (1979) who found similar secondary structures originating close to the leading edge at a Reynolds number of $3.85 \cdot 10^5$. Another set of vortices is formed from the suction surface–tip edge which will become the main vortex system. Initially the two sets of vortices evolve independently of each other and no sign of strong time–dependency is observed. From $x_c = 0.20$ to $x_c = 0.50$ (Figures 3.13(a) to 3.13(d)) these vortices grow and the first vortex system moves towards the suction surface–tip edge stretching over the whole tip area. At $x_c = 0.60$ (Figure 3.13(e)) the two vortex systems start to interact. In particular, the vortices from the first system move to the suction surface and they interact with the primary vortex modifying its shape and increasing the mixing of the spiral layers. At this plane, the vortices fluctuate from the tip surface to the suction surface generating high level of unsteadiness on the primary vortex. In Figure 3.14, a collection of snapshots is reported in order to highlight the unsteadiness when the two vortex systems interact; position, size and shape of the secondary vortices vary greatly with time. However, the shape and velocity field of the inner part of the primary vortex is very little affected by secondary structures as noted by the almost identical smoke pattern of the primary vortex core. From $x_c = 0.70$ (Figure 3.13(f)), the primary vortex is surrounded by vortices coming from the tip which mix with the spiral layers. At this stage there is not a stable secondary vortex between the primary vortex and the tip edge. Several secondary structures are observed away from the surface so that the definition of the accumulation line as the primary vortex separation point on surface flow visualizations may not be strictly valid anymore. This is not true for a rounded tip where the secondary vortex remains on the wing surface. The bending of the accumulation line in Figure 3.1(a) indicates this change of topology in the tip vortex structure. Several vortices can be counted at $x_c = 0.80$ and $x_c = 0.90$ (Figures 3.13(g) and 3.13(h)) and they wrap around the primary vortex. The shape of the spiral structure is dominated by the interaction with secondary vortices. At the trailing edge (Figure 3.13(i)), the tip vortex is shed from the wing as a strongly unsteady vortex system which includes secondary vortices and shear layer eddies (Francis & Katz, 1988).

(b) Angle of attack and Reynolds number effects The effect of a change in the angle of attack ($\alpha = 4^\circ, 12^\circ$) and in the Reynolds number ($Re = 3000, 7000$) on the wingtip vortex formation on the rounded tip is shown in Figure 3.15 at 3 plane locations ($x_c = 0.50, 0.75$ and 0.99).

As also observed in the pressure distribution, a lower angle of attack produces a

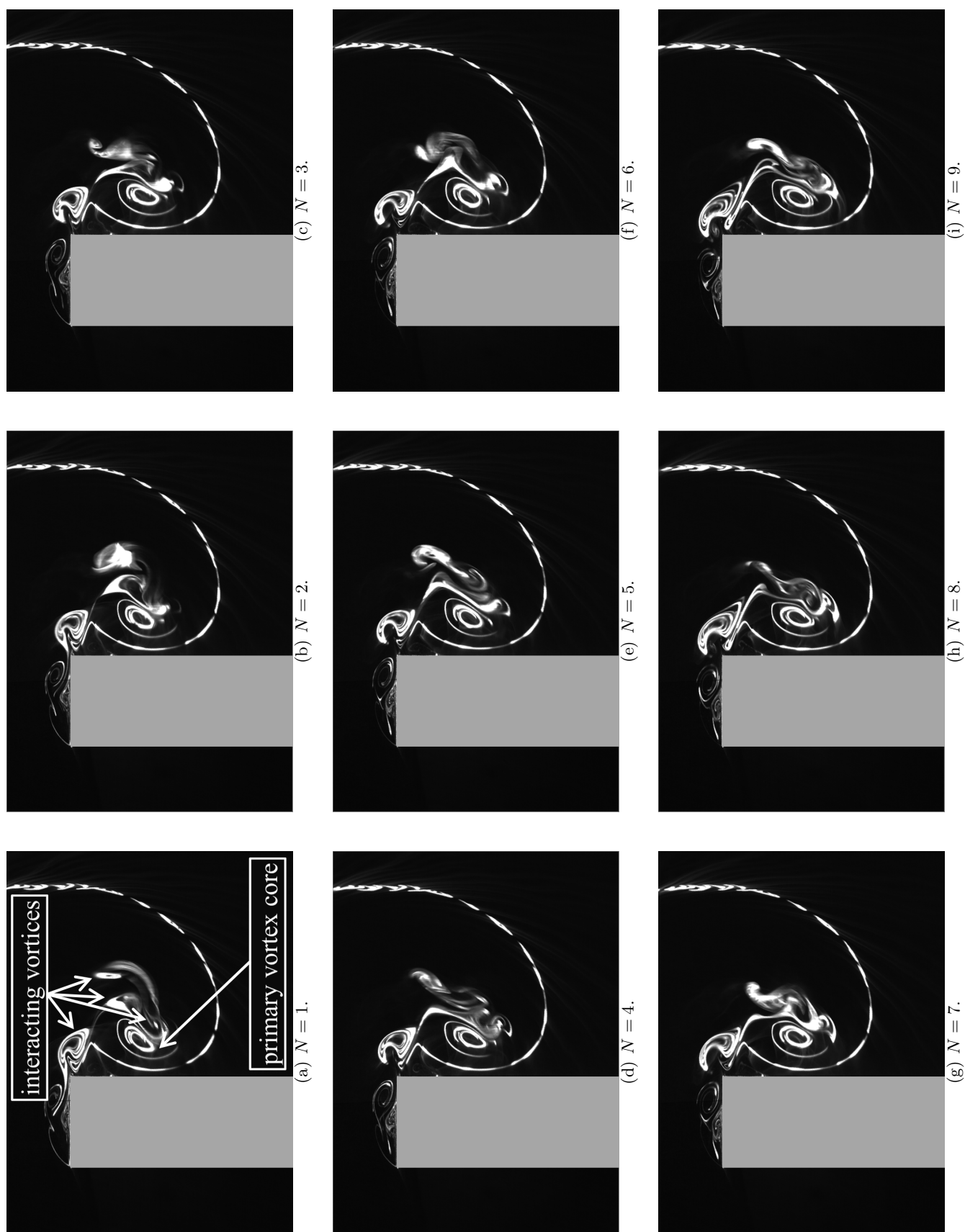


Figure 3.14: Snapshots at $f = 30$ Hz, $Re = 3000$, $\alpha = 12^\circ$ and $x_c = 0.7$ on squared tip.

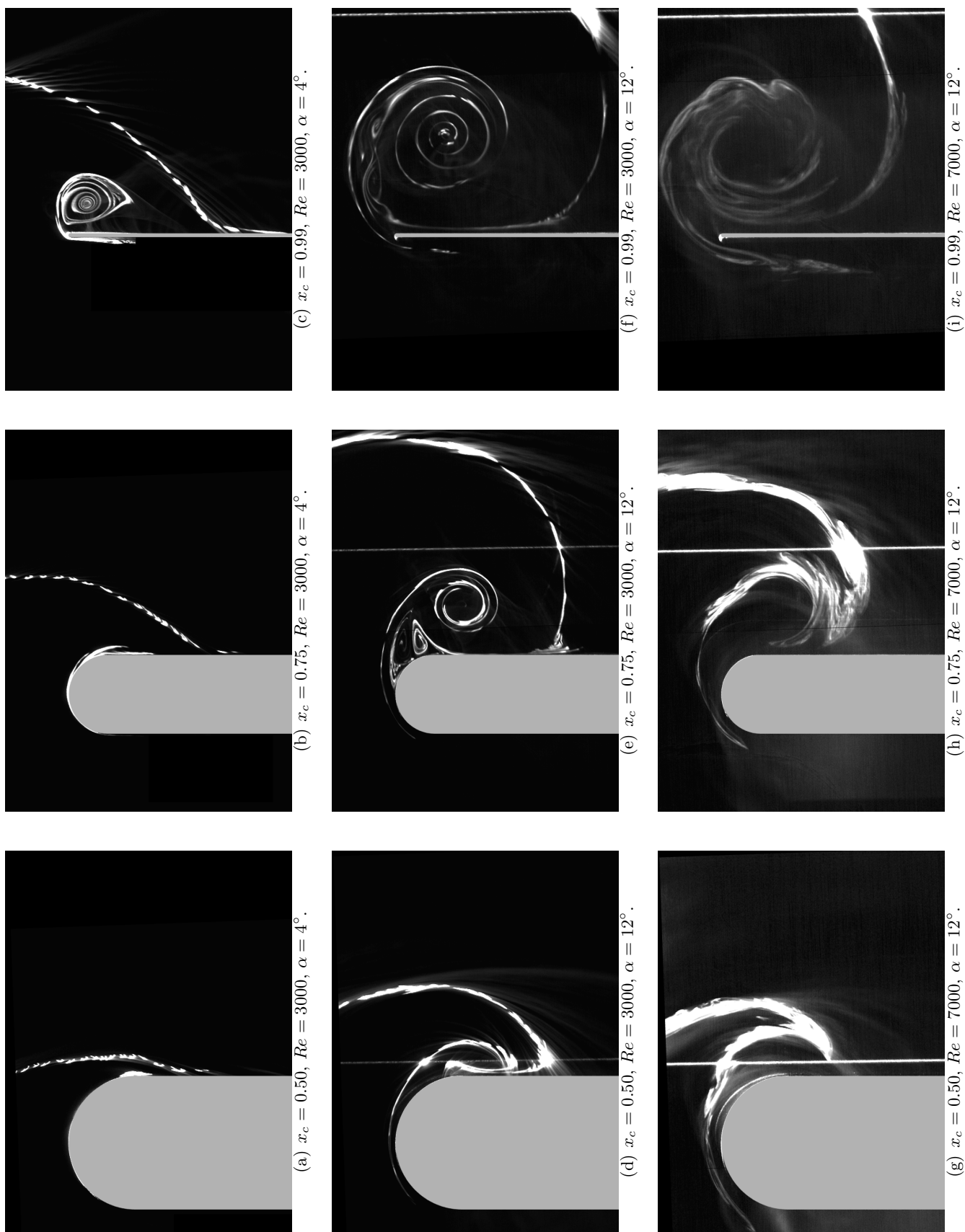


Figure 3.15: Vortex evolution at $Re = 3000$ and $\alpha = 12^\circ$ on rounded tip; wing section in gray.

lower lift and generates a smaller vortex with a delayed starting point. At $x_c = 0.75$ the wing at high angle of attack already shows a clear multi-vortex structure (Figure 3.15(e)) whereas the flow visualization of the wing at low angle of attack does not show a vortical structure (Figure 3.15(b)). An intermittent separation of the tip-crossing flow was observed at this stage and a resulting small vortex could be only occasionally detected. The average pressure gradient across the tip surface is not strong enough to separate the flow and maintain a steady vortical structure. Compared to delta wing vortices where the vortex starts from the apex of the wing, on rectangular wings the wingtip vortex does not have a clearly defined chordwise starting point. Computational studies by Duraisamy (2005) showed that for an early stage of a wingtip flow from a rounded tip, the adverse pressure gradient is mild enough for the cross flow boundary layer to remain attached on the surface without wrapping the flow around the tip. At $x_c = 0.99$, the vortex for the low angle of attack is observed (Figure 3.15(c)) but it is remarkably smaller than for the high angle of attack (Figure 3.15(f)). However, the number of turns of the spiral structure at the trailing edge of the smoke filament coming from the pressure side is approximately the same. Assuming that the two angles of attack generate vortices with similar swirl velocity profiles with the exception of a scaling factor, the number of turns are directly proportional to a reference value of the swirl velocity and the development length of the vortex, and inversely proportional to the axial velocity within the vortex core. Also, the swirl velocity is proportional to the pressure difference between the suction and the pressure surfaces of the wing or, in other terms, to the circulation of the wing. This results in the following relation:

$$\text{number of turns} \propto \frac{\text{swirl velocity} \cdot \text{development length}}{(\text{wing circulation}) \cdot \text{on the wing}} \cdot \frac{1}{\text{core axial velocity}} \quad (3.2)$$

Hence, at high angle of attack, the longer and more intense vortex (high swirl velocity) has to generate a vortex axial velocity considerably higher than the wing at low angle of attack so that the number of turns might result similar.

At a higher Reynolds number (comparing Figures 3.15(d) to 3.15(f) with Figures 3.15(g) to 3.15(i)), the vortex appears with similar sizes at all the laser planes which indicates a similar structure to the lower Reynolds number case. Also, the traces outside the vortex system bend more around the vortex which indicates a sensibly higher intensity of the vortex (higher swirl velocity). At this Reynolds number, the blurred pictures are generated by the higher turbulence of the incoming flow and the more intense mixing of the smoke filaments.

SECTION 4

Vortex characteristic lines via SPIV

The vortex flow topology over wing surfaces (from rectangular to delta wings) is often extracted from wall shear stress patterns by surface flow visualizations or from convergence or divergence of limiting streamlines (Taylor & Gursul, 2004). Moreover, several methods have been presented for automatic detection of the flow topology over a surface (e.g. Kenwright, 1998; Surana *et al.*, 2006). The literature on the description and characterization of delta wings vortices is more vast than on rectangular wings. Recent PIV experiments on planes parallel to delta wing surfaces have been presented by Taylor & Gursul (2004), Yavuz *et al.* (2004) and Gursul (2004). They described the near surface topology and flow structure in terms of streamlines, vorticity and velocity fluctuations which gave a more detailed insight of the vortex structure than surface flow or smoke visualizations.

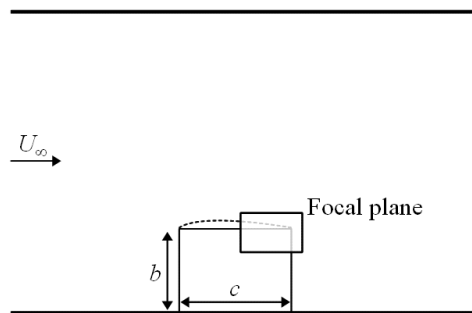


Figure 3.16: *Experimental arrangement and field of view of the SPIV cameras.*

The wing **M2** was mounted on the floor of the Argyll wind tunnel (Figure 3.16) and stereoscopic particle image velocimetry was performed on planes parallel to the wing surface near the trailing edge where the curvature is almost zero as shown in Figure 3.17(a). For the case of rounded tip, the laser sheet was parallel to the suction surface and therefore at a different distance from the tip surface as sketched in Figure 3.17(b). Although glare was reduced to tolerable levels by black paint on the model and by a high quality surface finish, wrong vectors were found in correspondence to the trailing edge and to the sharp edge on the squared tip. However, this problem did not influence much the measurements because of the good quality of the correlation in the surrounding regions.

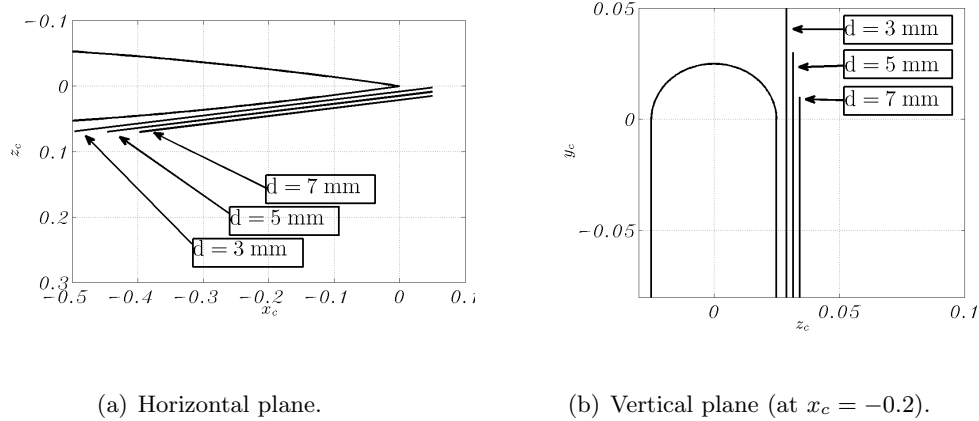


Figure 3.17: SPIV laser sheet positions.

Results are presented for the tip vortex formation on squared and rounded tip, at Reynolds numbers of $1 \cdot 10^5$, $5 \cdot 10^5$ and $10 \cdot 10^5$, angles of attack of 4° and 12° , at planes parallel to the model surface at a distance of 3, 5 and 7 mm. Each test consisted in taking the time average of 121 two-dimensional three-components velocity vector fields recorded at a constant frequency of 2 Hz. The flowfield is appropriately scaled: the scaling parameter for the velocities is the freestream velocity; for the turbulent quantities and the turbulent kinetic energy is the square of the freestream velocity. The vorticity was calculated from the scaled velocity field adopting the 8 points circulation method as described by Raffel *et al.* (2007). The mean flow and the fluctuations are presented in this section.

(a) Characteristic lines definition With the large volume of quantitative data that the SPIV generates, methods for the identification of meaningful and compact information on the vortex development along the wing can be defined giving more insight into the phenomenon than the limiting streamlines from a surface flow visualization. In Figure 3.18 the streamlines computed from one SPIV test are reported. The pattern is very similar to the surface oil flow visualization in Figure 3.1 which was at same Reynolds number and angle of attack but for the wing model **M1** and similar observations can be made. Near the tip, for $y_s < 0.02$, the region occupied by the secondary vortex is identified by an accumulation of streamlines. The region of maximum chordwise gradient of the streamlines (indication of the primary vortex foot) is also clearly visible between $y_s = 0.05$ and $y_s = 0.1$. More inboard, the curvature of the streamlines indicates the reattachment line of the primary vortex.

Plane streamlines are computed from the SPIV data using only the plane component

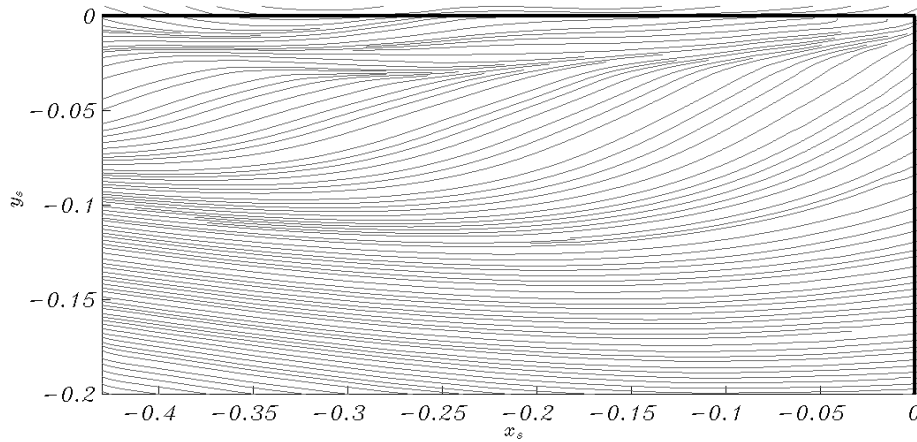


Figure 3.18: Mean flow plane streamlines for squared tip at $\alpha = 12^\circ$, $Re = 10^5$ and $d = 3$ mm.

of the velocity vectors: u and v . The resulting patterns for a plane close to the surface does not show much more information than the surface flow visualization. However, having access to the whole velocity vector gives the possibility for a wider understanding and a quantitative description of the wingtip vortex system. Moreover it is worthy of reminder that the SPIV technique, differently from the surface flow visualization with oil, is a non-intrusive method and it is not affected by the process of interpretation of the oil streaks.

Looking at the velocity components and the vorticity contours, four characteristic lines can be defined. The identification of these lines gives insights into the flow topology and vortex system characteristic also when the limiting streamlines do not generate a distinctive pattern. A similar approach is described by Helman & Husselink (1989) who presented a method to reduce the information from a vector field to a set of characteristic points describing the flow topology and also by Okada & Lane (1997) who used colours, based on velocity vectors magnitude and orientations, to enhance the separation and reattachment lines detection. Francis & Katz (1988) introduced similar characteristic lines but based on smoke visualizations.

In Figure 3.19, the legend of the characteristic lines, which are introduced and

defined in this section, is reported. In Figure 3.20 the three components of the mean velocity vector and their turbulent fluctuations (RMS) contours are reported for the case at angle of attack of 12° , Reynolds number of 10^5 , squared tip and distance between wing surface and laser sheet of $d = 3$ mm. In Figure 3.21 the in-plane vorticity (out-of-plane component of the vorticity vector) and the turbulent kinetic energy k (which is an indication of the overall fluctuation) are also reported. The wingtip vortex characteristic lines are plotted on all these contours.

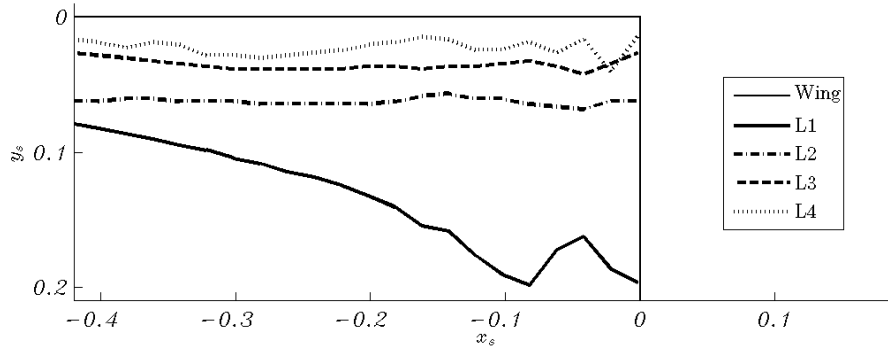


Figure 3.19: Characteristic lines legend for squared tip at $\alpha = 12^\circ$, $Re = 10^5$ and $d = 3$ mm.

Referring to Figures 3.20 and 3.21, the four characteristic lines introduced in this study are defined as follows, from the most inboard to the closest to the tip:

- **L1** is the most inboard line where the v -component of the velocity is equal to zero (from Figure 3.20(c)). This line separates the flow directed towards the wingtip from the flow directed towards the root of the wing and it is therefore an indication of the dimension of the primary vortex. It initially grows almost linearly in the chord direction showing an increase of the vortical system dimension (i.e. diameter) with the streamwise coordinate. The bump observed in the proximity to the trailing edge is related to measurement errors due to glare and it can be easily eliminated adopting a more sophisticated identification method.
- **L2** is the line where the w -component of the velocity is equal to zero (from Figure 3.20(e)) and it corresponds to the foot of the primary vortex (where the vortex streamlines on the vortex plane are parallel to the surface). It can be seen as a first indication of the vortex centre position. This line lies on the region of maximum velocity magnitude and the wall shear stress is also maximum which explains the lighter colour at this region on the oil visualization of Figure 3.1(a). Between **L1** and **L2** the out-of-plane velocity component w is negative which corresponds to flow going in the direction of the wing surface.

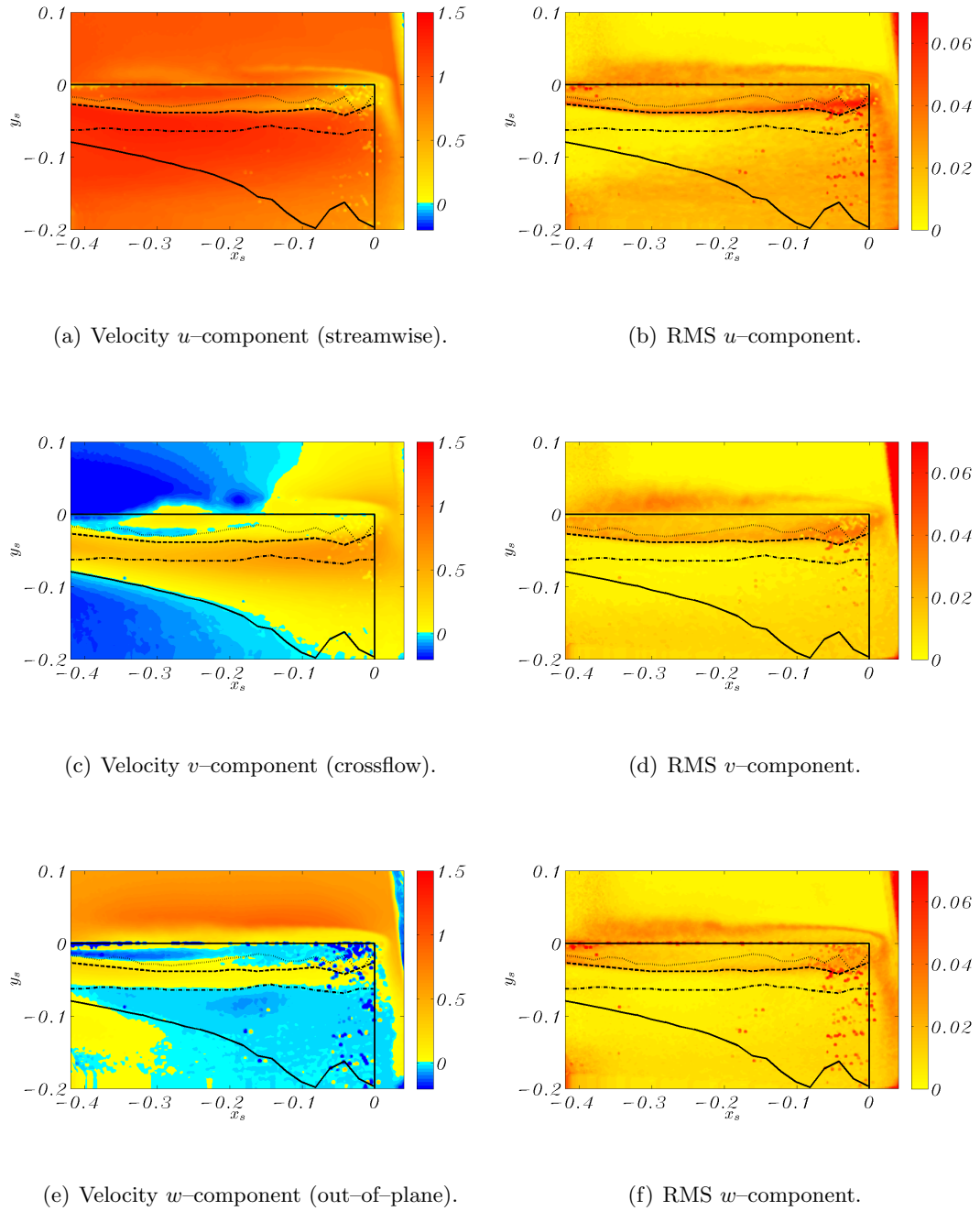


Figure 3.20: Mean flow and characteristic lines for squared tip at $\alpha = 12^\circ$, $Re = 10^5$ and $d = 3$ mm (characteristic lines legend from the most inboard to the nearest to the wingtip: **L1** continuous line, **L2** dashed-dotted line, **L3** dashed line, **L4** dotted line).

- **L3** is the line where the in-plane vorticity is maximum (from Figure 3.21(a)) and it identifies the separation line of the primary vortex. Between **L2** and **L3** the out-of-plane velocity component is positive which is flow moving away from the surface. Maximum turbulent kinetic energy is also observed along this line (Figure

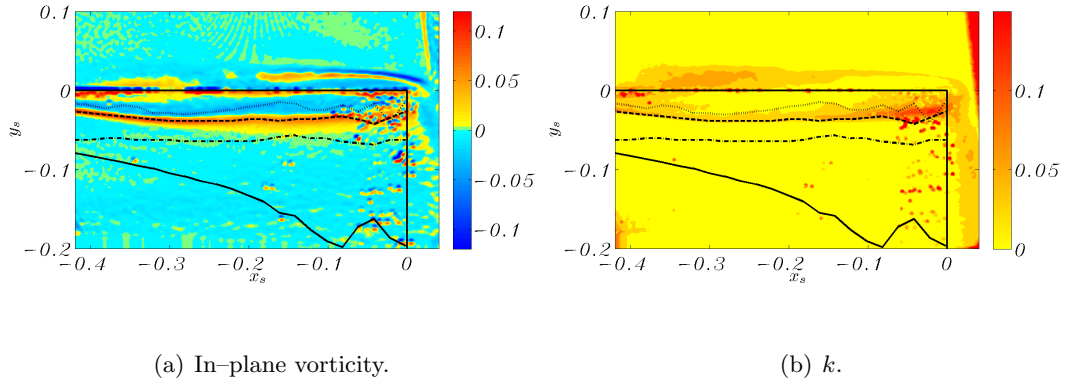


Figure 3.21: Mean flow and characteristic lines for squared tip at $\alpha = 12^\circ$, $Re = 10^5$ and $d = 3$ mm (characteristic lines legend from the most inboard to the nearest to the wingtip: **L1** continuous line, **L2** dashed-dotted line, **L3** dashed line, **L4** dotted line).

3.21(b)) and in particular the u -component of the fluctuations is maximum. The region between **L3** and the tip is a region of higher fluctuation of the v -component compared to the rest of the wing surface. This indicates that the main source of the unsteady spanwise motion of the primary vortex comes from the region occupied by secondary vortices.

- **L4** is the line where the in-plane vorticity is minimum (from Figure 3.21(a)) and it corresponds to the separation line of the secondary vortex. The sign of the vorticity on **L3** and **L4**, respectively positive and negative, is due to the local minimum of the velocity u -component between the two lines. In fact, the vorticity out-of-plane component is calculated as

$$\omega_z = \frac{\partial v}{\partial x} - \frac{\partial u}{\partial y} \quad (3.3)$$

where the gradient along the x -coordinate is much smaller than the spanwise gradient ($\partial/\partial y$) which is negative on **L3** and positive on **L4**. As observed in the smoke visualization of Figure 3.13, moving toward the trailing edge secondary vortices lift up from the wing surface around $x_c > 0.8$ ($\simeq x_s > -0.2$) and the wing tip vortex system becomes more unsteady. Therefore, for $x_s > -0.2$, **L4** does not give anymore an accurate description of the secondary vortex structure. However, for $x_s < -0.2$, the presence of the secondary vortex is also seen in the negative values of the w and v component of the velocity in the region near the tip edge. The bending of **L4**, which indicates the lifting up of the secondary vortex and the

change of vortex structure topology, is observed around $x_s = -0.3$, similarly to the surface flow visualization of Figure 3.1(a).

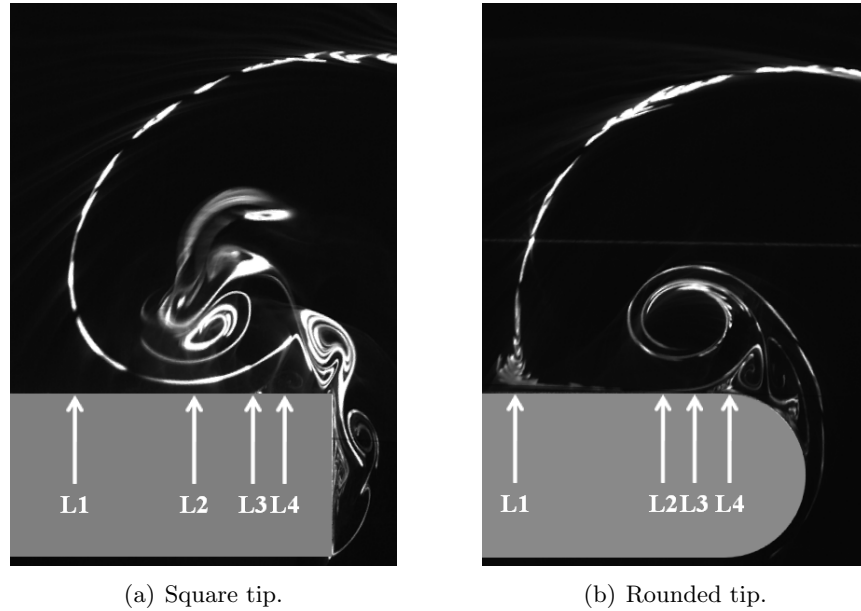


Figure 3.22: *Smoke visualizations at $x_c = 0.7$, $\alpha = 12^\circ$ and $Re = 3000$.*

In Figure 3.22(a), the position of the lines are sketched with respect to the smoke visualizations of Section 3.3. The smoke visualizations refer to the position $x_c = 0.7$, Reynolds number of 3000 and angle of attack of 12° . It is believed that the kinematics of the tip vortex formation does not change radically for a wide range of Reynolds numbers, especially on sharp edges where the separation points are fixed. Karakus *et al.* (2008) and Bailey *et al.* (2006) studied a similar geometry at Reynolds numbers respectively of $3.2 \cdot 10^4$ and $2.4 \cdot 10^5$ and they showed the same multiple vortex structures of Figure 3.22(a). Dye visualizations in a water tank were presented by Francis & Katz (1988) for a hydrofoil with squared tip at Reynolds number in a range between $3 \cdot 10^4$ and $1.3 \cdot 10^6$; the same multiple vortex structure and interaction was observed.

In Figure 3.22(b), the vortex characteristic lines are positioned with reference to a typical vortex system formed over the same wing but with rounded tip. For a Reynolds number of $4.6 \cdot 10^6$ on a low aspect ratio NACA 0012 rectangular wing with rounded tip, Chow *et al.* (1992) showed a similar vortex structure confirming that also on rounded tip geometries the vortex structure does not topologically change with the Reynolds number.

In Figure 3.23 a diagram of a typical formation of the primary vortex over a rectangular wing with rounded tip is sketched based on the information gathered during

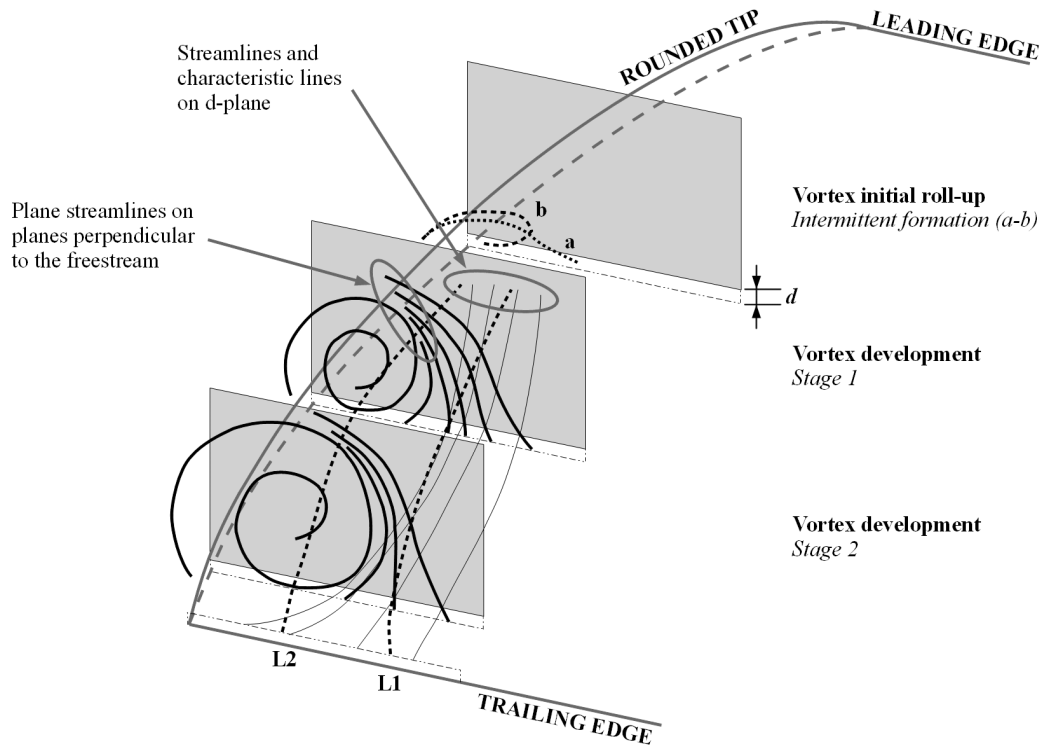


Figure 3.23: Vortex formation diagram on a rectangular wing with rounded tip.

these experiments. The streamlines over the plane parallel to the wing surface at a small distance (SPIV plane) are also reported along with the characteristic lines **L1** and **L2**. The development of the vortex on the wing is highlighted by plane streamlines on planes perpendicular to the freestream at different chordwise positions. Also, as it will be described in Section 3.5, the initial roll up of the vortex over a rounded tip is an intermittent process and the two phases of the intermittency are sketched. It is also important to remark that because of the highly three-dimensional nature of the flow, plane streamlines (on the wing surface and on perpendicular planes) are not the actual streamlines but they are streamlines based on the projection of the velocity vectors on those planes.

(b) Effects of the distance of the laser plane from the surface The sketch in Figure 3.24 illustrates the effects of the distance of the laser plane from the wing surface regarding the location where the vertical component of the velocity is equal to zero (which is how **L1** is defined). A shift toward the tip is observed when the plane is moved away from the surface. This behaviour is confirmed by Figure 3.25 where the characteristic lines for different distances between the laser plane and the wing surface are plotted for a squared

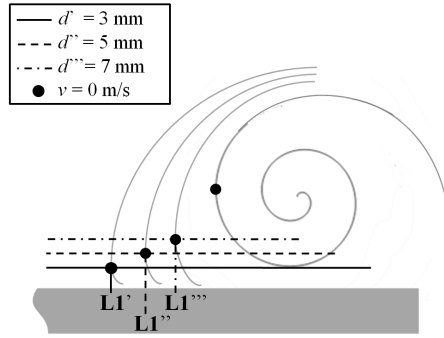


Figure 3.24: Schematics of the primary vortex streamlines and the evaluated reattachment points positions for measurement planes at different distances from the surface.

tip at two Reynolds numbers. The three planes are at a distance from the wing surface corresponding to 0.4%, 0.65% and 0.9% of the chord and they cut the primary vortex below the vortex centre. No particular differences on the positions of the lines are observed with the exception of a shifting of **L1** for $x_s > -0.2$. The closer the cutting plane is to the surface, the more accurate is the description of the shape of **L1** as the distinctive line on the surface that divides the flow directed towards the root from the flow directed towards the tip of the wing. It is expected therefore that the primary vortex reattachment line on the surface is shifted more towards the wing root than what observed on these near surface streamlines. For instance, assuming a linear shifting of **L1** when the plane moves closer to the surface, at $x_s = -0.1$ the reattachment lines of the primary vortex for Reynolds numbers of 10^5 and 10^6 are respectively at $y_s = 0.22$ and $y_s = 0.17$ with an error below 3% compared to the estimation on the plane at $d = 3$ mm.

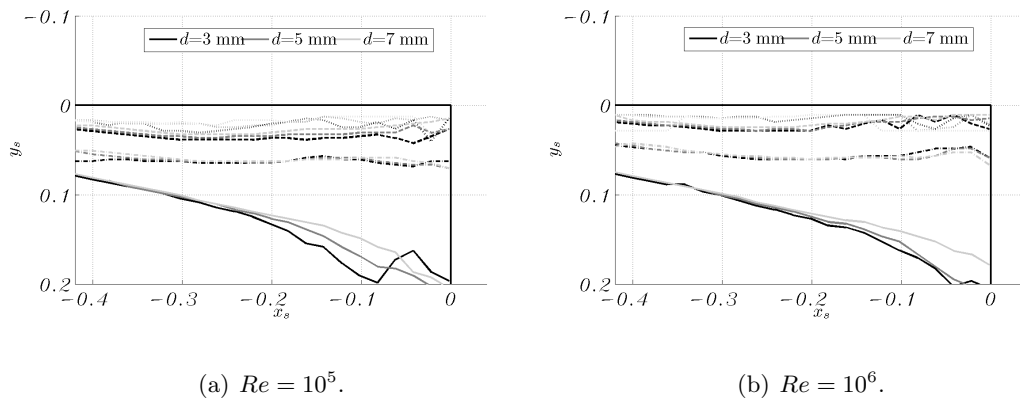


Figure 3.25: Characteristic lines for squared tip at $\alpha = 12^\circ$.

(c) Reynolds number and tip geometry effects The characteristic lines for the two different wing tip geometries (squared and rounded tip) at two Reynolds numbers (10^5 and 10^6) are shown in Figure 3.26. It is observed that the sharp geometry of the squared tip fixes the separation point of the crossing flow and, as a consequence, the overall dimension of the primary vortex, as indicated by **L1**, is the same for the two Reynolds numbers. On the squared tip, small variations in the position of the other lines are observed which indicates the invariance of the primary vortex position to the Reynolds number. On the rounded tip, a shift of all the characteristic lines is detected when the Reynolds number is changed. **L1**, **L2** and **L3** move in the direction of the tip when the Reynolds number is increased, indicating a primary vortex around 20% smaller than the vortex formed at the low Reynolds number (estimated as distance between the wingtip edge and **L1**). **L4** lies outside of the wing geometry because the secondary vortex is partially situated on the rounded edge and, as observed in Figure 3.17(b), for $y_s > 0$ the laser plane is not parallel to the surface. Even though the unsteadiness, the number of vortices, the formation and the initial roll up process are different between the squared and the rounded wingtips, the four characteristic lines are clearly found in both cases.

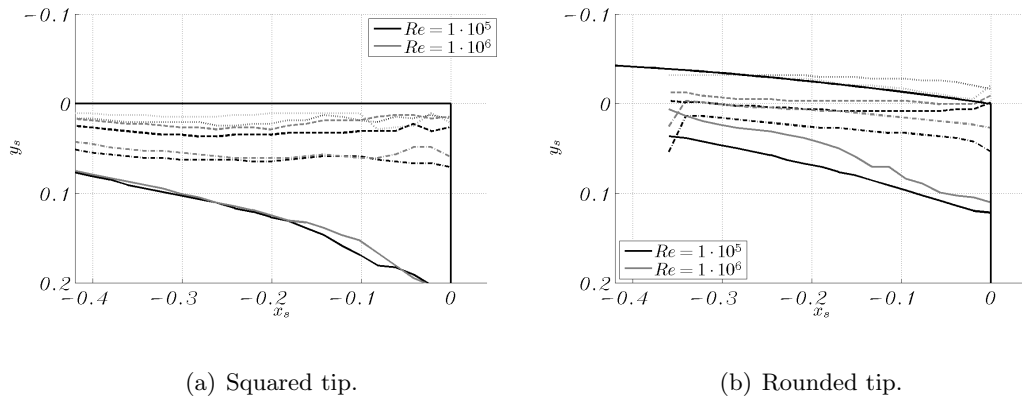


Figure 3.26: Characteristic lines at $d = 5$ mm and $\alpha = 12^\circ$.

What also appears in Figure 3.26 when comparing the characteristic lines from the vortex systems formed on the two wingtip geometries, is that **L2** lies parallel to the tip edge (i.e. horizontal for squared tip and diagonal for rounded tip) so that the distance between this line and the tip edge remains constant along at least the last 35 percent of the wing ($x_s > -0.35$). This behaviour was observed also by Yavuz *et al.* (2004) and it indicates that the vortex centre moves parallel to the edge of the wing.

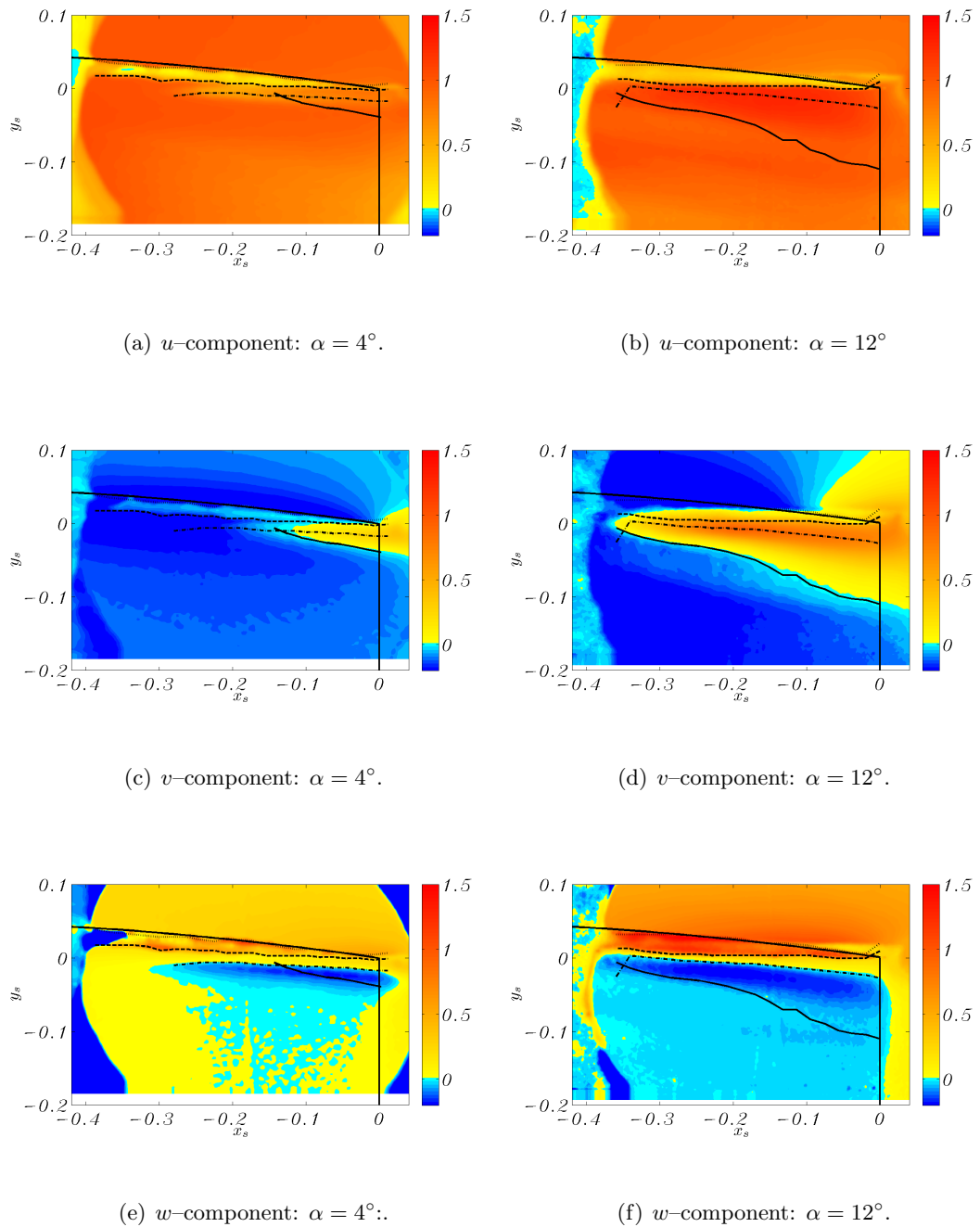


Figure 3.27: Velocity components contours for a rounded tip at $Re = 10^6$.

(d) Angle of attack effects The vortex systems on a rounded tip wing at the two angles of attack 4° and 12° are compared in this section for the Reynolds number of 10^6 . The three velocity components (Figure 3.27) and the vorticity (Figure 3.28) are reported. At this angle, the region at the left and right edges of the contours is not in the field of view of the cameras and presents a wrong velocity

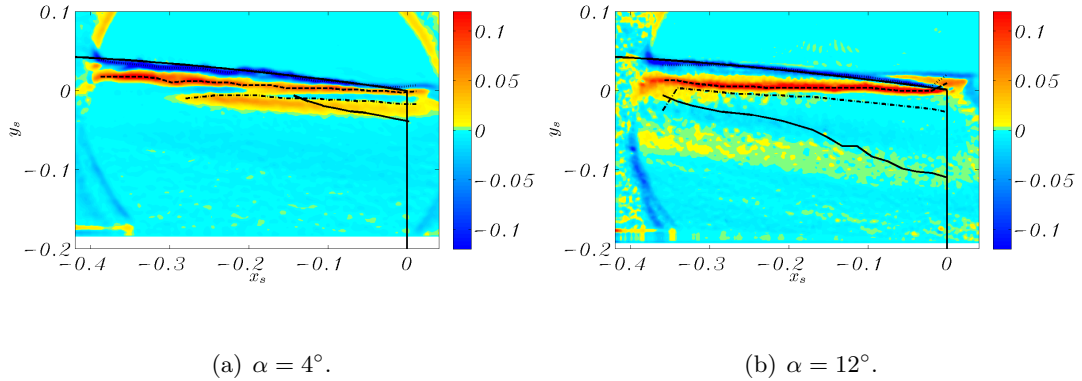


Figure 3.28: *In-plane vorticity contours for a rounded tip at $Re = 10^6$.*

field (particularly clear in Figure 3.27(e)). However, this region is included for the sake of immediacy in comparing with previous results.

At a lower angle of attack, the pressure difference between the two surfaces of the wing is smaller and the circulation generated by the wing is consequently smaller. As also observed on the smoke visualizations of Figure 3.15, the vortex at lower angle of attack is smaller and the rolling up of the vorticity sheet begins at a later stage along the wing. As a consequence, the characteristic lines on the low angle of attack case are not as evident as in the high angle of attack case and they are shorter. The primary vortex reattachment line **L1** appears only for $x_s > -0.15$ and the primary vortex foot **L2** for $x_s > -0.25$. The maximum and minimum vorticity lines, **L3** and **L4**, are dictated by the local minimum of the streamwise component of the velocity in correspondence to the rounded portion of the wing.

SECTION 5

Unsteadiness of the vortex formation via hot film

Based on the preliminary information gathered from the measurement of the pressure fluctuations in Section 3.2.(b), hot film measurements were taken on the **M2** wing in order to study the low frequency unsteadiness of the flow in the region described by the characteristic lines which were found with the SPIV experiments in Section 3.4. The model was mounted in the Argyll wind tunnel in the same way as the SPIV experiments.

The hot films were deployed onto the surface at several positions and recordings of 100 s at 1 KHz were taken. In Figure 3.29 the characteristic lines are sketched for different cases (i.e. different tip geometry, Reynolds number and angle of attack) with the positions of the hot film measurements.

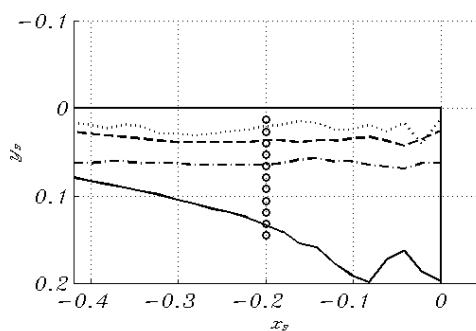
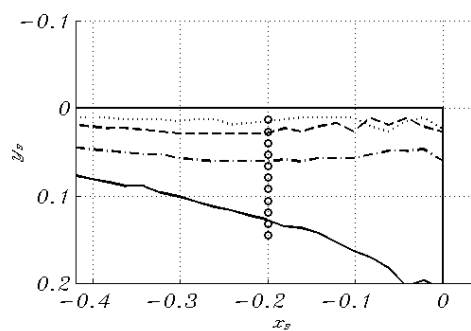
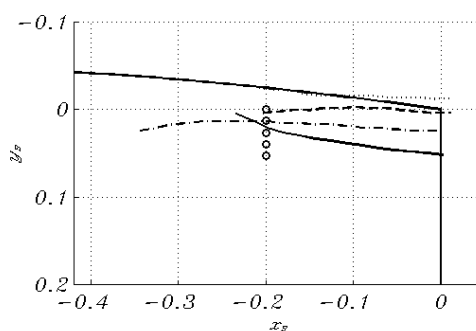
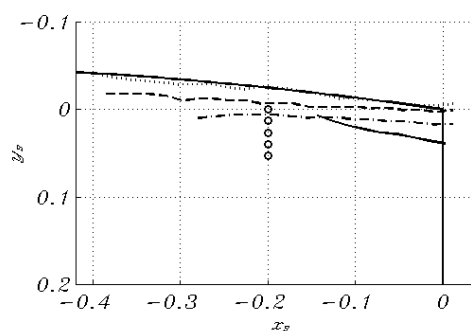
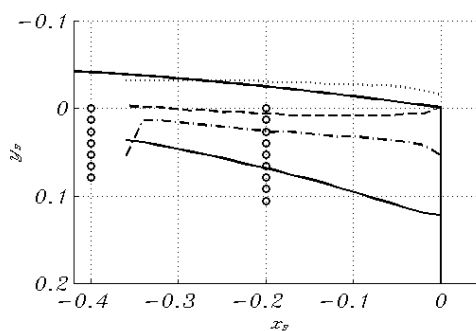
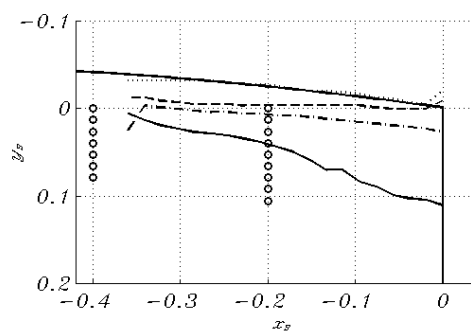
(a) Squared tip at $\alpha = 12^\circ$ and $Re = 10^5$.(b) Squared tip at $\alpha = 12^\circ$ and $Re = 10^6$.(c) Rounded tip at $\alpha = 4^\circ$ and $Re = 10^5$.(d) Rounded tip at $\alpha = 4^\circ$ and $Re = 10^6$.(e) Rounded tip at $\alpha = 12^\circ$ and $Re = 10^5$.(f) Rounded tip at $\alpha = 12^\circ$ and $Re = 10^6$.

Figure 3.29: Characteristic lines and hot film positions.

(a) Unsteadiness and intermittency Because the offset of each measurement was changed to have an output signal of zero average in order to maximize the gain, which was kept constant during all the tests, the standard deviation is expressed in the signal unit. In Figure 3.30, the standard deviation of the wall-mounted hot film signals are plotted as function of the spanwise coordinate y_s . The output signal of the hot film is related to the wall shear stress (Haselback & Nitsche, 1996), which, in this case, increases with the flow speed. Also, it is generally observed that for a higher Reynolds number (i.e. higher flow speed) the standard deviation is higher. The standard deviations from the hot film arrays on the squared tip as in Figures 3.29(a) and 3.29(b) are reported in Figure 3.30(a). For both the Reynolds numbers, the standard deviation trends are similar. The maximum value is encountered on the hot film probe nearest to the tip which is positioned in correspondence to **L4** which indicates the secondary vortex separation line. A local maximum is also observed in the vicinity of **L1**, which is the primary vortex reattachment line. As observed in the previous section, the squared tip fixes the separation point of the crossing flow generating similar vortices at different Reynolds numbers in terms of separation and reattachment line position and overall dimension. This similarity between vortices at different Reynolds numbers is observed here also in the unsteadiness level of the vortex.

The data from the rounded tip at low angle of attack (Figures 3.29(c) and 3.29(d)) are reported in Figure 3.30(b). At low angle of attack the vortex is smaller and less intense. Moreover, as observed from the characteristic lines, higher Reynolds numbers generate smaller vortices which start the rolling up nearer to the trailing edge. A high value of the standard deviation is observed also in this case in the region of the high vorticity intensity line **L4** (at $y_s = 0$). Moreover, for the Reynolds number of 10^6 , high unsteadiness is found in a region more inboard at $y_s = 0.04$. It is believed that this high standard deviation is due to the intermittency of the initial phase of the roll up as described in the sketch of Figure 3.23. From the average characteristic lines structure on the rounded wingtip (Figure 3.29(d)), a vortex system from the mean flow (i.e. presence of all the characteristic lines) is observed at around $x_s = -0.15$ which is more downstream than the hot films array. At $x_s = -0.20$, the boundary layer from the pressure side of the wing is intermittently separating and rolling up into a vortical structure on the suction surface depending on the instantaneous pressure gradient generated by freestream turbulence, freestream unsteadiness and unsteadiness of the vortex. It is this behaviour that generates the high standard deviation value at $y_s = 0.04$.

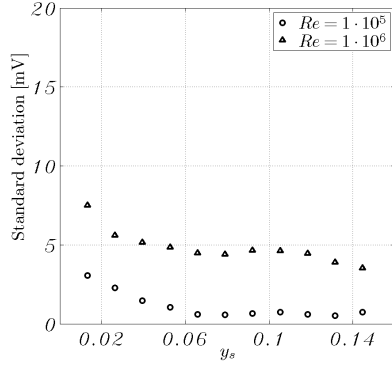
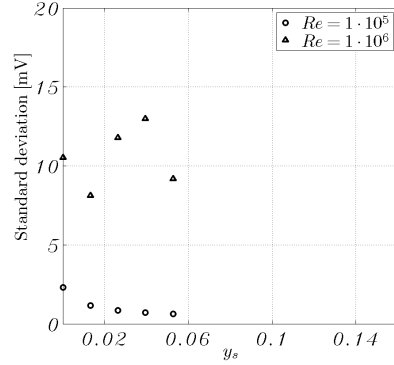
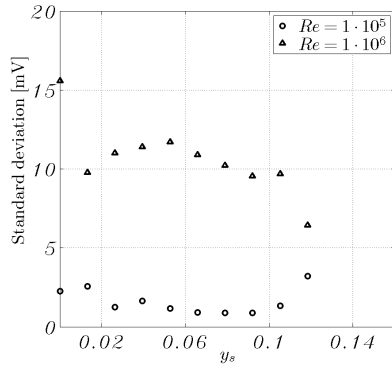
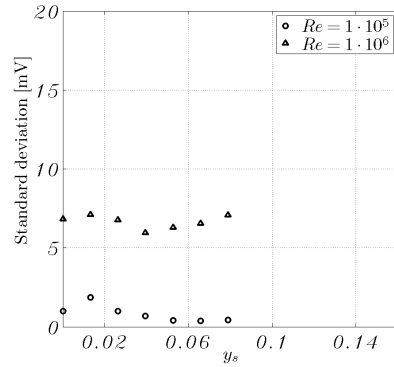

 (a) Squared tip at $\alpha = 12^\circ$ and $x_s = -0.20$.

 (b) Rounded tip at $\alpha = 4^\circ$ and $x_s = -0.20$.

 (c) Rounded tip at $\alpha = 12^\circ$ and $x_s = -0.20$.

 (d) Rounded tip at $\alpha = 12^\circ$ and $x_s = -0.40$.

Figure 3.30: Hot film signals standard deviations.

Finally, the standard deviation of a rounded tip at $\alpha = 12^\circ$ from the hot film arrays at $x_s = -0.40$ and $x_s = -0.20$ are reported respectively in Figures 3.30(d) and 3.30(c); the corresponding characteristic lines are shown in Figures 3.29(e) and 3.29(f). Similarly to the squared tip case, a high value on **L4** is observed at $x_s = -0.40$ and a local maximum around **L1** is also identified. A larger distance for the rounded tip than for the squared tip is observed between the curves at the two Reynolds numbers (comparing Figure 3.30(a) and 3.30(c)).

(b) Signal spectra on squared tip Further considerations of the unsteadiness of the vortex structure formed over the squared tip are made by comparing the power spectral density $|P(f)|$, scaled by the variance, of the hot film signals from different spanwise positions. The physical frequency is reported on the abscissa instead of a dimensionless variable (such as the Strouhal number) because of the difficulty in defining and measuring a meaningful length and velocity parameter for this flow. This problem will be discussed further in Section 3.6.

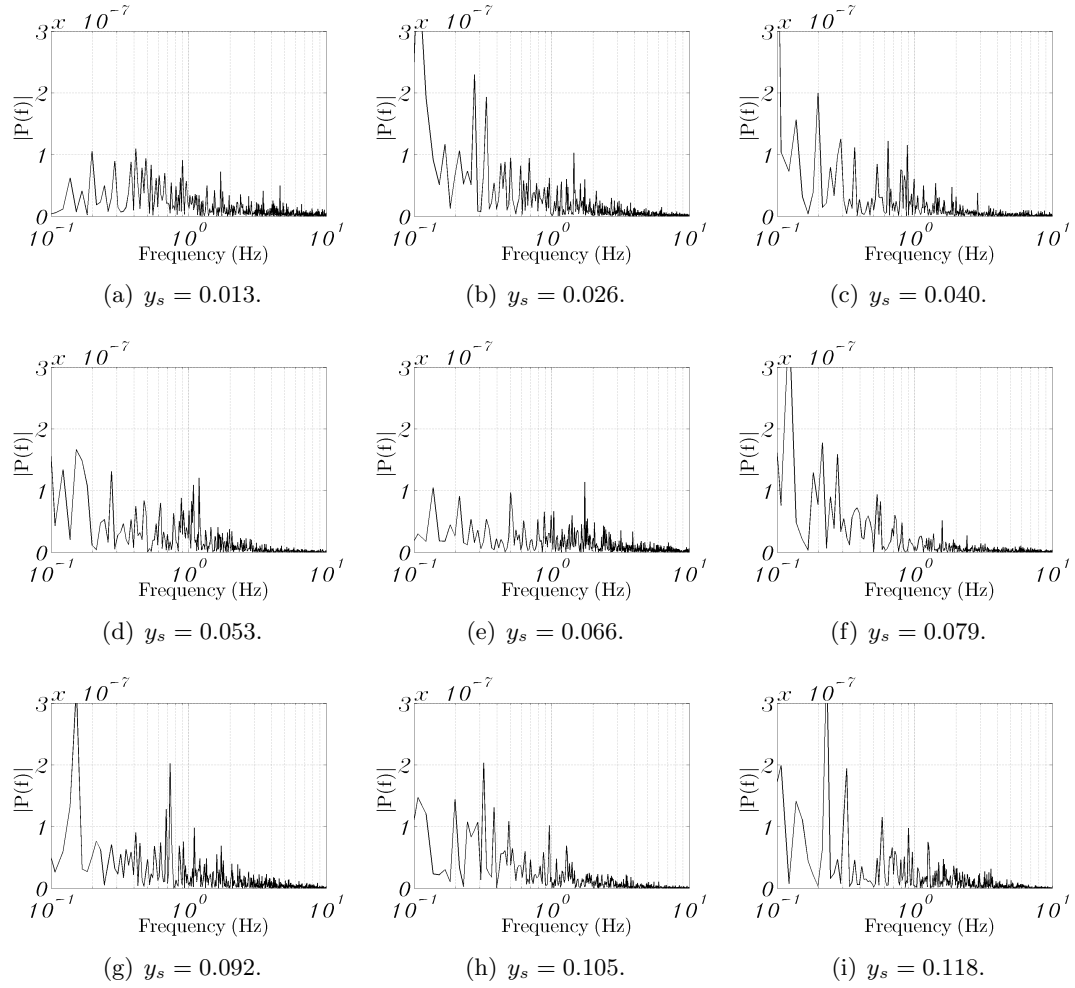


Figure 3.31: Square tip power spectra: $Re = 10^5$, $\alpha = 12^\circ$, $x_s = -0.20$.

The spectra from the two Reynolds numbers cases are reported in Figures 3.31 and 3.32. Peaks are observed below 5 Hz for both the cases. At the low Reynolds number, energy peaks appear at the different spanwise positions at a frequency around 1 Hz. Also, near to the edge ($y_s = 0.013, 0.026, 0.040$), higher energy is observed at a frequency range between approximately 0.3 Hz and 0.9 Hz corresponding to the region where **L4** and **L3** are found. At high Reynolds number (10^6) a high energy in the range between 0.8 and 3 Hz is found in the region next to the tip. Also, moving towards the root the energy decreases reflecting the same behaviour of the signal standard deviation. This suggests a link between periodic unsteadiness on wingtip vortices and secondary vortex movement. Strong interactions between secondary vortices and primary vortex during the formation were described also by Karakus *et al.* (2008) on a rectangular wing with squared tip.

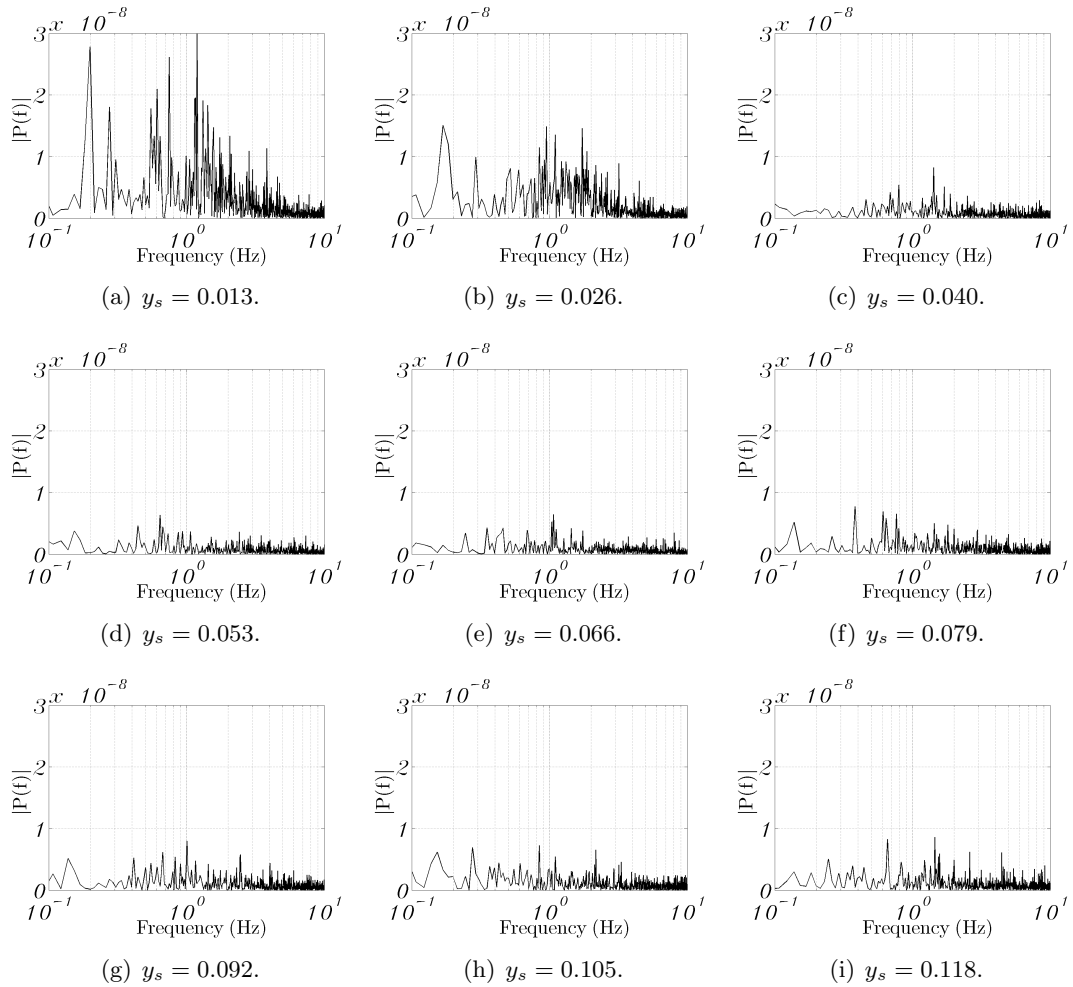


Figure 3.32: Square tip power spectra: $Re = 10^6$, $\alpha = 12^\circ$, $x_s = -0.20$.

(c) Signal spectra on rounded tip In Figure 3.33 the power spectra are reported for the high Reynolds number case on rounded tip at 12° and $x_s = -0.20$.

The energy density at low frequencies at $y_s = 0$ is higher than at the other positions. As also observed for the squared tip, this can be linked to the unsteadiness of the secondary vortex which dominates the unsteadiness of the entire vortical system. Also, a double peak energy distribution (peaks at around 1 Hz and 2.5 Hz) is noted at $y_s = 0.013$ and $y_s = 0.026$. Taylor & Gursul (2004) observed on delta wings similar double peak spectra and they related them to shear layer instabilities and vortex pairing processes.

At a lower angle of attack (Figure 3.34), a peak at a frequency between 0.4 and 0.7 Hz is noted in the region near the tip and it is related to the intermittency of the initial roll up of the boundary layer coming from the pressure surface of the wing, as discussed earlier.

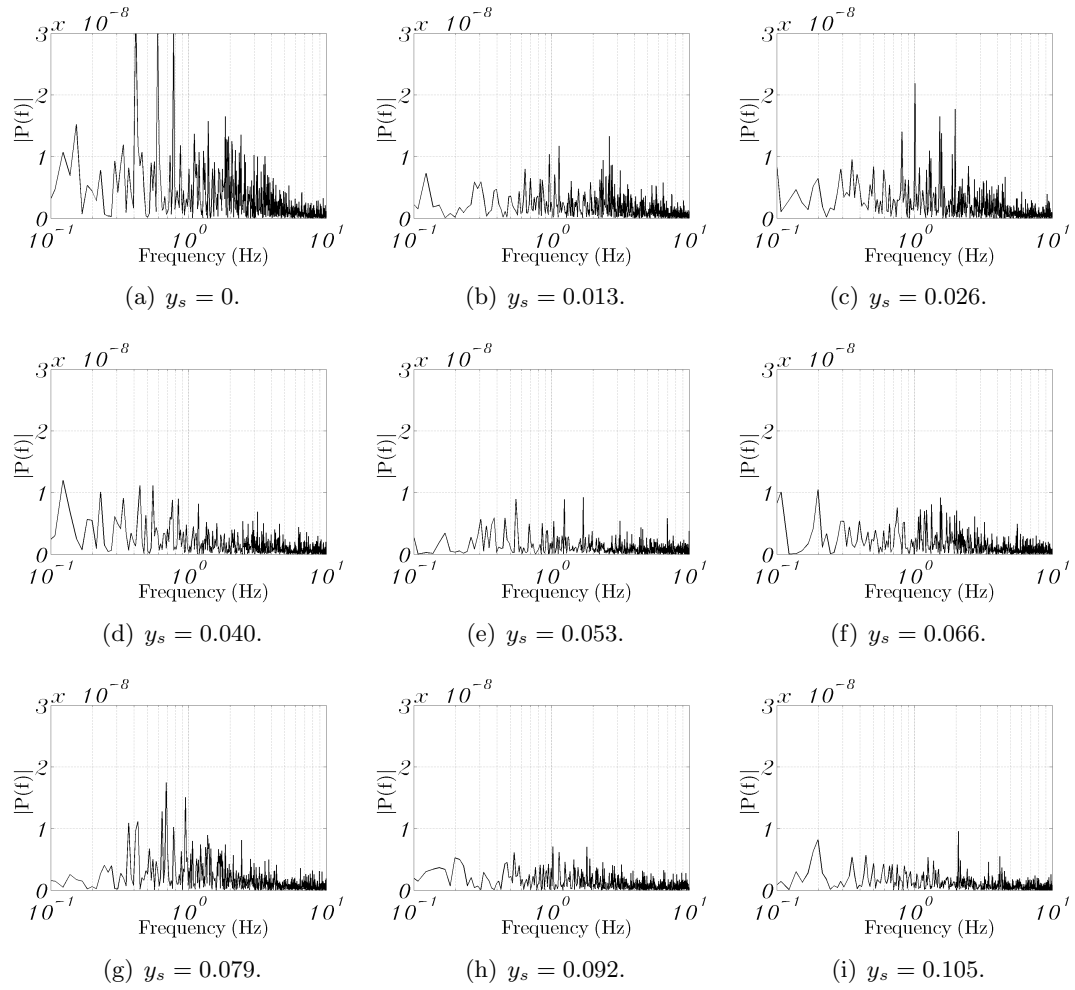


Figure 3.33: Rounded tip power spectra: $Re = 10^6$, $\alpha = 12^\circ$, $x_s = -0.20$.

SECTION 6

Unsteadiness of the vortex in the early wake

The unsteadiness information gathered in the previous section are compared here with a study on the unsteadiness of the vortex system in the near wake. When the vortex flow seeded with smoke is illuminated, the high centrifugal forces produce a darker region at the vortex centre which can be then located by detecting the centroid of the darker spot. A similar problem is solved by Del Pino *et al.* (2009) who used an appropriate threshold to convert the grayscale image into a binary image. However, in the current study, a routine based on the grayscale image is preferred to a method working on the black and white image because it avoids the problematic choice of the threshold level when the centrifugal forces are not strong enough to produce a clear dark region. A discussion and comparison of two different methods, respectively based on

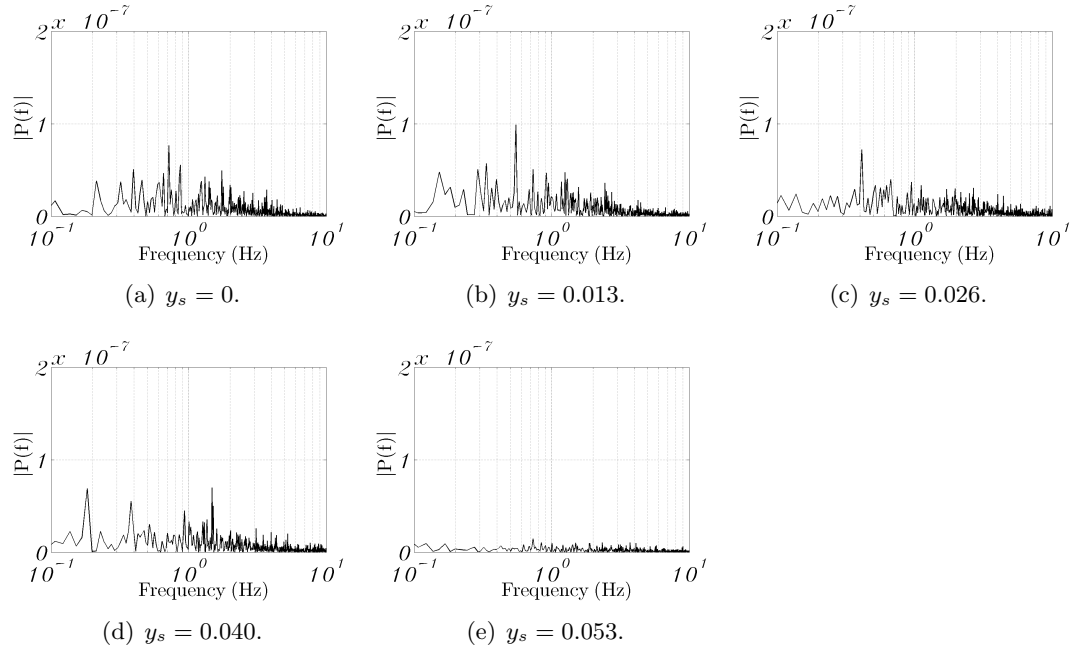


Figure 3.34: Rounded tip power spectra: $Re = 10^6$, $\alpha = 4^\circ$, $x_s = -0.20$.

binary and grayscale images, implemented on these experiments is found in Appendix B. In the method adopted, the grayscale image is analysed through circles of diameter N_{px} and iterative refinements on the position of the averaged darkest circle are performed. Tests on the sensitivity of the interrogation circle dimensions on instantaneous vortex position and movement frequency were carried out and a diameter of $N_{px} = 60$ was selected for this configuration (see Appendix B). This value corresponds to a physical size of 6 mm.

Recordings were composed of 190 pictures of smoke visualizations taken on planes in the wake of the wing. The laser plane was perpendicular to the freestream and different plane locations, angles of attack and Reynolds numbers were tested. The wing **M2** was mounted as in Section 3.5 and rounded tip geometry was installed. A typical meandering of the order of 2.5% of the chord was observed for the different configurations.

In this section, the power spectral density (PSD) of the displacements along the vortex plane axes y_v and z_v are presented, named respectively $|P_{yy}(f)|$ and $|P_{zz}(f)|$. Moreover, because wandering affects the v and w component of the velocity simultaneously, the cross spectral density (CSD) is also used in order to highlight more prominently the overall wandering frequency (Bailey & Tavoularis, 2008). Both the PSD and the CSD are scaled by the variance of the signal.

Based on the observations on the vortex unsteadiness dominant frequency from hot

film signals of Section 3.5, these experiments on smoke visualization recordings focus on low frequencies. Since the maximum number of frames was limited by the hardware to 190 and the relevant frequencies are below 5 Hz, in order to obtain a good frequency resolution a sampling time of 19 seconds at a sampling frequency of $F_S = 10$ Hz was adopted. Recordings of 6.3 seconds at a frequency of $F_S = 30$ Hz were also analysed and they confirmed that the major contribution to the unsteadiness in these experiments is observed at frequencies less than 5 Hz.

(a) Reynolds number effects In Figure 3.35, the Reynolds number effect on the vortex meandering is presented for tests at $x_w = 1$ and wing at 12° of incidence. A dominant peak in the PSD on both the translation axes z_v and y_v for $Re = 10 \cdot 10^5$ (Figure 3.35(c)) is seen at a frequency of approximately 0.8 Hz. Other weaker peaks are also seen at higher frequencies but they are not clear when the fluctuations on the y_v and z_v axes are correlated to form the CSD in Figure 3.35(f). At $Re = 5 \cdot 10^5$ a peak is observed at a frequency of 0.4 Hz (Figure 3.35(e)) which is characterized by a predominant movement along the y_v axis (Figure 3.35(b)). For the lower Reynolds number, $Re = 2 \cdot 10^5$, no predominant peaks are detected in the PSD (Figure 3.35(a)); however, the CSD reveals a peak around a frequency of 0.05 Hz (Figure 3.35(d)).

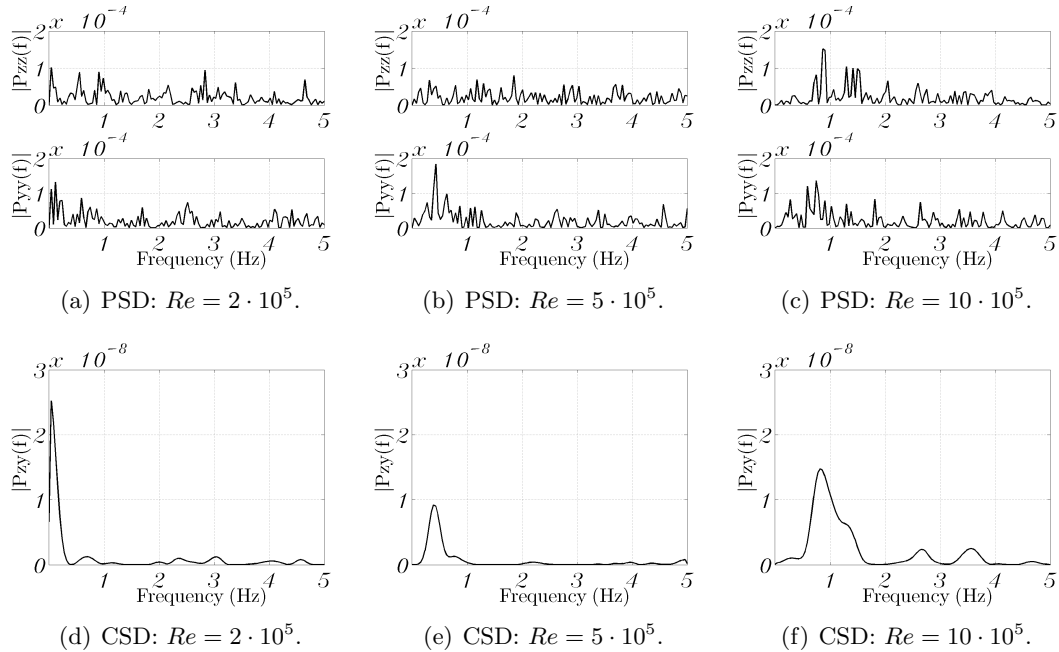


Figure 3.35: Signal spectra at $x_w = 1$ and $\alpha = 12^\circ$.

The amplitude of the peak on the CSD is higher when the PSD on the two axes show

a similar behaviour on the peak frequency which can be seen as a sign of axisymmetry of the meandering. The lowest peak in the CSD is observed for $Re = 5 \cdot 10^5$ where the meandering frequency on the y_v axis shows a higher energy compared to the z_v axis. This difference suggests a link between the vortex centre unsteadiness in the early wake and the vortex unsteadiness during the roll up, particularly with the vortex movement along the spanwise direction (y_s axis). Furthermore, a similarity of the PSD along the two axes suggests that when the Reynolds number is increased the vortex reaches a developed meandering stage sooner, which generates a meandering not oriented predominantly along one of the axes. Whether the meandering is axisymmetric, as observed by Beresh & Henfling (2010), or oriented along a different axes, as presented by Del Pino *et al.* (2009), is not clear from these experiments.

From the CSD plots in Figure 3.35, the frequency f of the peak increases with the Reynolds number. A scaling of the frequency such as $\bar{f} = fc/U_\infty$ would collapse the peaks for $Re = 5 \cdot 10^5$ and $Re = 10 \cdot 10^5$ at the same scaled frequency of $\bar{f} = 0.032$ and the peak for $Re = 2 \cdot 10^5$ at $\bar{f} = 0.010$. Whereas Del Pino *et al.* (2009) found a meandering scaled frequency of the same magnitude $\bar{f} \simeq 0.029$, Bailey *et al.* (2006) observed a frequency one order of magnitude higher of approximately $\bar{f} \simeq 0.35$. Such a difference can not be explained solely by the differences of those researches and the current one in the angle of attack, Reynolds number, wing chord, wing aspect ratio, freestream velocity or position in the wake. Although studies on low frequency unsteadiness would benefit from comparative tests of these parameters, the scaling parameters of the dimensionless frequency should be accurately chosen among quantities which are more characteristic of the vortex such as vortex core diameter, maximum swirl velocity and circulation.

(b) Angle of attack effects The results of an increase of the angle of attack on signal spectra of the vortex centre motion (Figure 3.36) show similar trends to the increase of the Reynolds number. On the CSD, the energy peak shifts toward a higher frequency and intensity increasing the angle of attack, from no distinct peak at $\alpha = 4^\circ$ (Figure 3.36(d)), to a peak at 0.9 Hz for $\alpha = 12^\circ$ (Figure 3.36(e)) and to an intense and well defined peak at 1 Hz for $\alpha = 15^\circ$ (Figure 3.36(f)). Also, where for the low angle of attack a peak at 0.5 Hz is observed only on $|P_{yy}(f)|$ (Figure 3.36(a)), a more developed and symmetric vortex movement is observed at $\alpha = 15^\circ$ (i.e. similarity of the PSD on the two axes in Figure 3.36(c) and higher peak in the CSD). This behaviour is confirmed by studies on the age and development of a trailing vortex. Gerz *et al.* (2001) introduced a vortex age parameter based on the circulation

of the wing in order to properly compare trailing vortices produced by different wings. Giuni & Benard (2011) (see also Giuni *et al.*, 2010) studied the relationship between the increase of the angle of attack and the increase of the vortex circulation and applied the vortex age parameter on a test similar to the present work. They found that in the very near wake, a higher angle of attack corresponds to an older vortex with a more symmetric and developed structure. Also, a vortex core rotation estimation, presented in Section 4.2, shows that increasing the angle of attack, the vortex core rotation rate is higher which contributes to an earlier development of an axisymmetric flow.

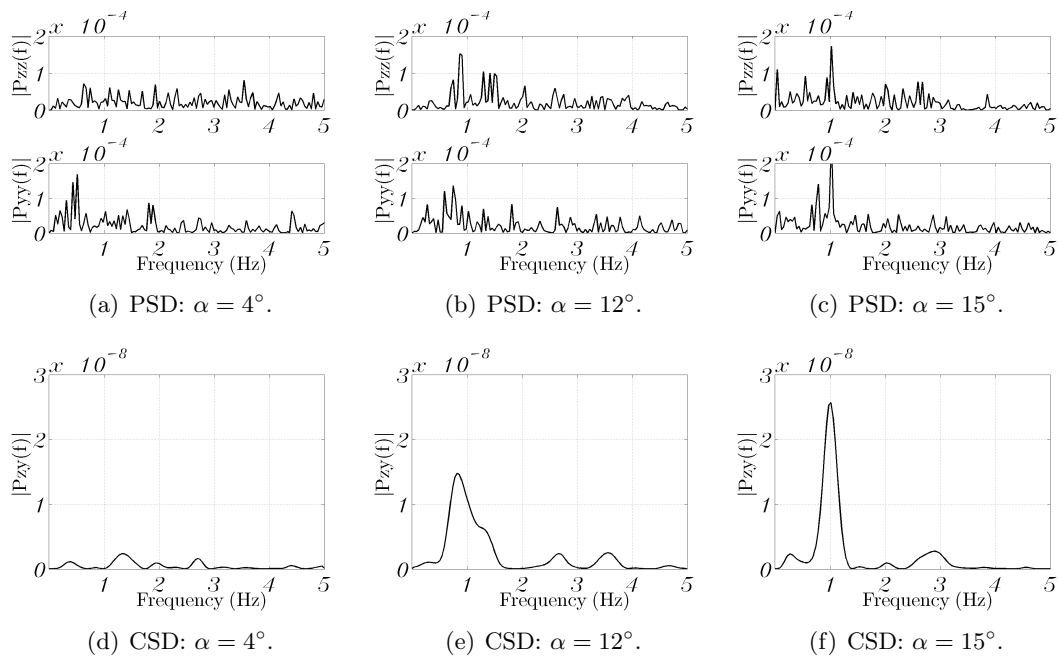


Figure 3.36: Signal spectra at $x_w = 1$ and $Re = 10 \cdot 10^5$.

(c) Downstream distance effects The vortex centre fluctuation at two different planes in the wake of the wing at Reynolds number of $5 \cdot 10^5$ and angle of attack of 15° are presented in Figure 3.37. The vortex centre movement at the furthest plane from the trailing edge of the wing appears the same on the y_v and the z_v axis (Figure 3.37(b)) which suggests symmetry of the vortex core. The peak in the CSD appears at a frequency of around 0.6 Hz (Figure 3.37(d)). At $x_w = 0.25$, there is not a unique peak in the PSD (Figure 3.37(a)) which can be detected but instead numerous and less intense peaks in the whole range 0–5 Hz. This is confirmed also by the almost flat distribution in the CSD (Figure 3.37(c)). This plane is in the region where the rolling up of the vorticity sheet around the vortex core is still very intense. Also, at $x_w = 0.25$ the darker spot in the picture indicating

the vortex centre was very faint compared to the $x_w = 1$ case which confirms a not fully developed vortical structure at this early stage of the wake.

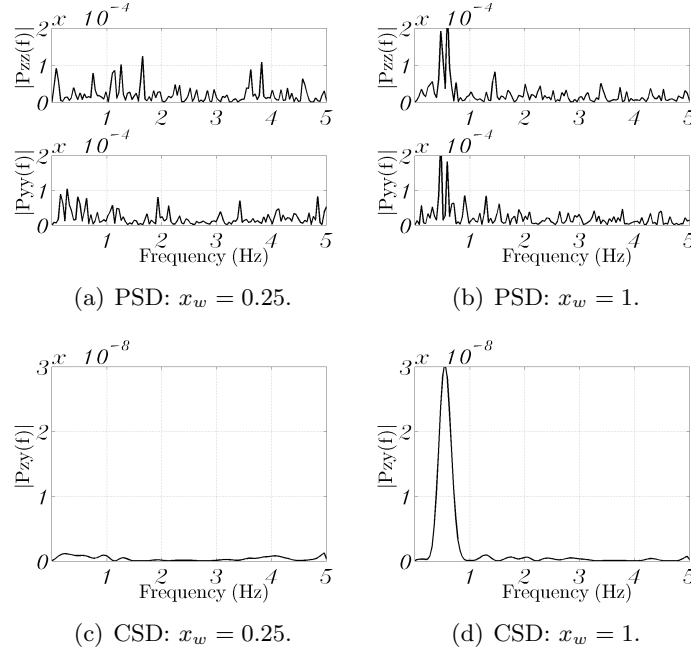


Figure 3.37: Signal spectra at $\alpha = 15^\circ$ and $Re = 5 \cdot 10^5$.

SECTION 7

Summary

The low frequency unsteadiness in the formation and in the early wake of a rectangular wing was studied for Reynolds numbers between 10^5 and 10^6 , angles of attack between 4° and 15° and for squared and rounded tips. Measurements in the tip vortex region on the wing surface and in the early wake behind the trailing edge show a low frequency movement which links the meandering of the vortex in the wake with the unsteady phenomenon of the cross-flow separation.

The three-dimensional vector field on a plane parallel and very close to the wing surface near the trailing edge was calculated with stereoscopic particle image velocimetry. The wingtip vortex structure is described on this plane by defining characteristic lines. These characteristic lines are a good tool to describe a vortex structure and its development along the wing. A secondary vortex is observed between the primary vortex and the tip and maximum turbulent kinetic energy is measured at the primary vortex

separation line. The primary vortex movement on the wing is forced by the secondary vortex which is affected by the boundary layer separation unsteadiness on the tip. The comparison between squared and rounded tip geometry shows how the first, forcing the separation of the flow at the sharp edges, generates a vortex which is less sensitive to other parameters.

The wingtip unsteadiness was measured by hot film probes installed on the wing surface and by smoke visualizations in the near wake. At the early stage on the wing, the primary vortex intermittently rolls up to form a vortical structure depending on the instantaneous pressure gradient so that the vortex origin is not fixed but moves in the chordwise direction. The main source of periodic unsteadiness on the wingtip vortex is associated with a low frequency movement of the secondary vortex which is directly related to the separated crossing flow coming from the tip. The unsteady motion of the vortex centre in the near field shows a similar frequency peak to the secondary vortex movement on the wing surface and a predominantly spanwise direction pattern. An increase in the wandering dominant frequency was observed with an increase of Reynolds number and angle of attack suggesting a link between the wandering and the intensity of the vortex.

Moreover, the wandering movement in the very early wake is oriented predominantly along the spanwise direction. During the formation of the vortex on the wing, the vortex is attached on the wall and since the movement normal to the surface is bounded, its movement is predominantly oriented parallel to the surface. In the context of wingtip vortices simulated with numerical methods and in particular using RANS equations, Petterson Reif *et al.* (1999) sensitized the model $\overline{v^2}-f$ (where $\overline{v^2}$ is the stress component normal to the wall and f is its source term (Durbin, 1991; Laurence *et al.*, 2004)), which accounts for the damping of the turbulent fluctuations in the direction normal to the surface incorporating some near wall turbulence anisotropy, to frame rotation effects. Duraisamy & Iaccarino (2005) implemented it on the wingtip vortex flow obtaining an accurate prediction of the vortex physics during the formation.

Changes in the tip geometry strongly affect formation and early development of the vortex system. The square tip presents two sharp edges and it produces a multiple vortex structure with highly unsteady secondary structures. Secondary vortices strongly contribute to disturb the primary vortex generating more unsteadiness on the model and in the wake. In the present experiments on the formation and early wake of wingtip vortices, a major source of meandering can be related to the unsteadiness of the primary vortex generated by the interaction with secondary vortices. A vortex formed by a wing

with rounded tip reaches the axisymmetric structure at an earlier stage than one from a squared tip.

Wingtip vortex early wake

For every complex problem there is an answer that is clear, simple, and wrong.

HENRY LOUIS MENCKEN

I have yet to see any problem, however complicated, which, when you looked at it in the right way, did not become still more complicated.

POUL WILLIAM ANDERSON

The vortex system develops quickly after leaving the trailing edge of the wing and understanding the mechanisms of the development is crucial in the prediction of the formed trailing vortex characteristics in the far wake. The physics of the vortex flow in the early wake is very complex and it is directly linked to the vortex formation process on the wing surface. The wingtip geometry, the distribution of the wing circulation and the roll up of the wake sheet are extremely vital in the setting of the early evolution of the vortex and an asymmetric vortex flow is observed at this stage. The aim of this chapter is to elucidate the link between aspects of this vortical flow playing significant roles in the characterization and comparison of wingtip vortices. A more comprehensive understanding of the mechanisms of the vortex formation is achieved in this study by comparing several configurations of angle of attack, Reynolds number, distance from the trailing edge, wingtip geometry, wing chord and aspect ratio (as summarized in Table 2.3). More specifically, the relations between turbulent fluctuations and the axial flow, wingtip geometry and turbulence inside the vortex, roll up of the wake sheet and the rotation of the vortex core are studied.

SPIV provides instantaneous and global measurements which, nowadays, are one of the best tools for the description of wingtip vortices. Even though a widely accepted

definition of a vortex has not been found yet, in particular regarding the study of coherent structures in turbulent flows (Jeong & Hussain, 1995; Cucitore *et al.*, 1999; Adrian *et al.*, 2000; Haller, 2005), wingtip vortices present a structure which is well identifiable. Rotation of a large portion of fluid around a common centre and a region of high vorticity within the vortex core (hence net circulation) are major elements of trailing vortices. Nevertheless, there are a number of definitions of the wingtip vortex centre and the identification of the wingtip vortex centre is still a matter of study. Moreover, the definition adopted and the method implemented can significantly affect the results (Ramasamy *et al.*, 2009a). In Section 4.1, the meandering of the vortex is defined and the problem of centering and averaging instantaneous velocity fields is addressed. A comparison and a critical discussion in adopting different methods is presented. The statistical convergence of the average of velocity, vorticity, velocity fluctuations, Reynolds shear stresses and shear strain is discussed in Section 4.1.(d).

In the early wake, a unique definition of the vortex core can present several difficulties because of the deformed shape of the vortical structure. The velocity distributions are deformed by the presence of secondary vortices. In Section 4.2, the deformation of the vortex core is analysed with focus also on the fluctuation and rotation rate. The effects of the angle of attack and the wingtip geometry on the vortex structure are also addressed. Particular attention is given to the axial flow which behaviour in the early wake is strongly dependent on the vortex intensity and formation. In Section 4.3, the shape of the axial flow within the core as function of the vortex strength is presented. The interaction of the primary vortex with secondary vortices and wake sheet is also shown. The examination of the axial velocity at the centre of the vortex leads to the definition of a vortex circulation parameter as the decisive element, along with the tip geometry, for the occurrence of jet-like or wake-like flow in the vortex core.

The turbulence inside the vortex and the relaminarization process is discussed in Section 4.4. The evolution of the vortex in the far wake and the prediction with numerical methods strongly depend on the nature of the vortex core flow. Therefore, the turbulence structure, distribution and production is examined in detail. Lastly, in Section 4.5, the wakes behind squared and rounded tips are compared. The two geometries generate vortex flows which appear and evolve very differently in the early wake. The relation and difference between meandering and turbulence is addressed in this section. In Section 4.5.(d), the double vortex structure observed behind a symmetric wing at $\alpha = 0^\circ$ is described.

SECTION 1

Localization of the vortex centre and averaging of velocity vector fields

The need to identify the wingtip vortex centre comes from the fact that these vortices are not stationary flows but they exhibit small random motions normal to the vortex axis. This phenomenon is called meandering (or wandering) of the wingtip vortex, or referred to as aperiodicity for rotorcraft because the motion represents the variation or scatter in the vortex centre location from one period (rotor evolution) to another (Ramasamy *et al.*, 2009a).

In Figure 4.1, instantaneous velocity vectors and vorticity contours are reported on planes perpendicular to the freestream. Assuming that it is possible to detect the vortex core in each instantaneous frame, the wandering can be defined as the fluctuation of these locations. The vortex meandering moves the centre by few percent of the chord and different instantaneous positions of the vortex are observed in the four snapshots. Whatever the source of the wandering, the vortex centre movement and the mean flow properties are important properties to study. Moreover, centering each realization before taking the average is needed for an accurate description of the vortex structure. The movement of the vortex introduces an artificial spreading effect when averaging, resulting in a larger apparent vortex core size and a smaller peak swirl velocity than any of the instantaneous measurements. Although the meandering phenomenon has more impact on the mid field, correcting for the wandering effects is also essential when the objective of the study is to accurately quantify the turbulence in the wake and inside the tip vortex (Ramasamy *et al.*, 2009b). The centering of the instantaneous realizations of the vortex can also be seen as a filtering operation which separates the solid translation of the vortex with the turbulent fluctuation of the vortex. The solid translation is what is referred to as meandering.

The implementation of the method which extracts the meandering information and the average vortex flow field requires special care. Birch (2012) proved that for isotropic and Gaussian wandering amplitudes, within the range of those usually observed experimentally, any axisymmetric flow field having zero velocity at $r = 0$ and $r \rightarrow \infty$ converges upon the circulation profile obtained for the case of a Batchelor q -vortex. This means that a good agreement of the averaged swirl velocity profile and the Batchelor q -vortex may not necessarily imply that the instantaneous profiles also agree well with the q -

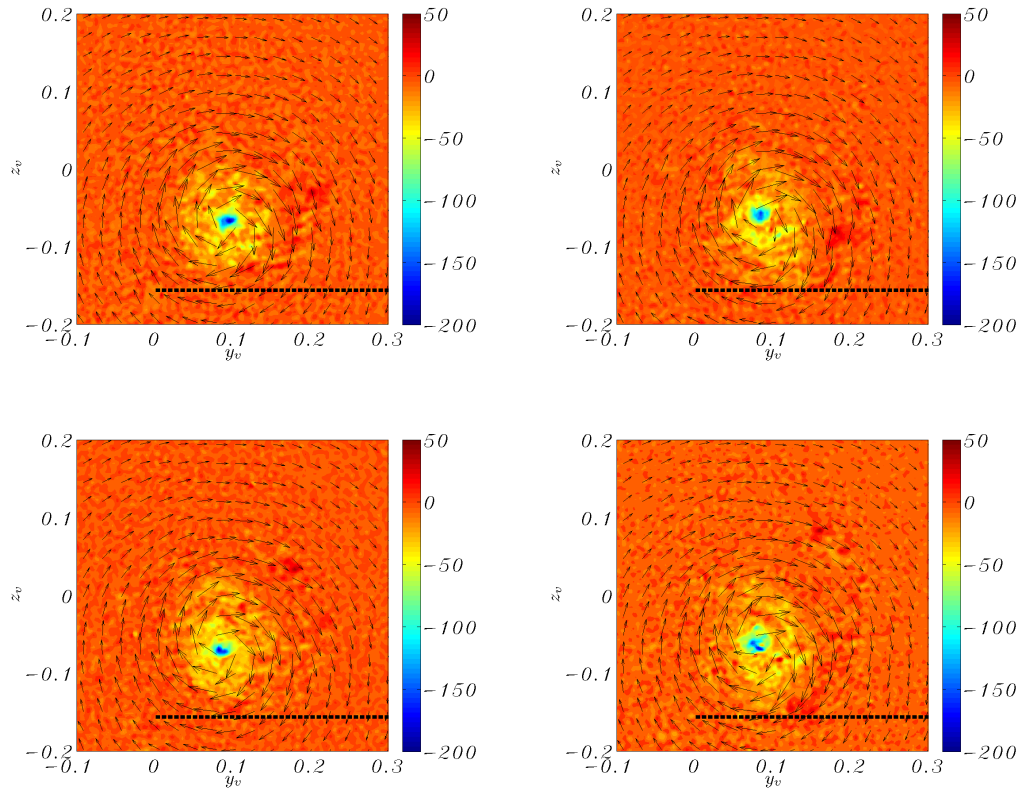


Figure 4.1: Instantaneous velocity vectors and vorticity at $x_w = 1$, $Re = 5 \cdot 10^5$ and $\alpha = 12^\circ$; projection of the trailing edge in dashed line.

vortex.

A common method used in particle image velocimetry, is to align the instantaneous realizations of the vortex localizing their centres. This averaging procedure assumes a wandering as a solid translation of the vortex on planes perpendicular to its axis and that velocities associated with the wandering movement itself are negligible compared to those generated by the vortex (Devenport *et al.*, 1996). The challenge therefore is in identifying a robust method that can be used to define the vortex centre. Two different approaches can be found in the literature: the identification of the vortex centre from the flow field properties in the region of the vortex core (e.g. Ramasamy *et al.*, 2009a; Beresh & Henfling, 2010) or from the convolution of the measurements with a discrete mask based on an assumed vortex model (e.g. van der Wall & Richard, 2006; Ramasamy *et al.*, 2011). The first approach relies mostly on the accuracy of the measurements around the vortex centre and in particular on the presence of seeding particles in the vortex core and on their fidelity in following the flow. The second is based on an appropriate least squares fit on a number of variables (such as vortex centre

position and velocity, orientation of the vortex axis with respect to the measurement plane, vortex circulation, vortex core radius) to a reasonable vortex analytical model.

For fixed wing tip vortices, peaks of properties such as vorticity or swirling strength well describe the primary vortex centre in contrast to, for example, the tip vortices of lightly loaded rotors in forward flight, especially those created on the advancing side, which are often very weak, hard to detect and coexistent with similar secondary vortices (van der Wall & Richard, 2006). Also, in the early wake, the vortex is not axisymmetric and it is not well described by analytical models. Moreover, enough particles were present in the core and the SPIV measurements resulted in a high spatial accuracy and reliability of the data in the vortex core. Therefore, in this study, the first approach for the vortex centre identification was adopted. In Figure 4.2, the instantaneous seeding distribution for a reference case¹ is shown along with the average core dimension for that case. A darker region is observed at the vortex centre of size less than 2% of the chord and less than a tenth of the vortex core diameter. However, particles are still detected in this area which is of the order of the interrogation window size adopted and a reliable and accurate description of the flow in the core is achieved with a measurement grid spacing of around 3% of the core radius which is much higher than most of the experiments on wingtip vortices found in the literature.

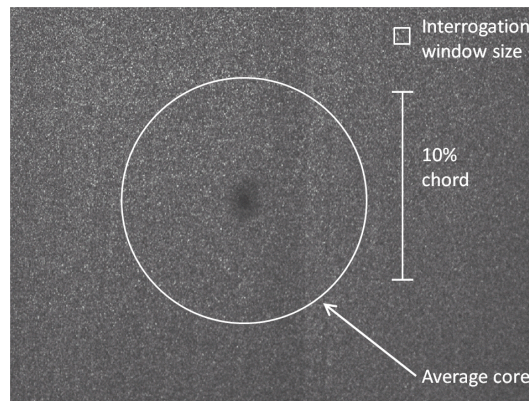


Figure 4.2: *Instantaneous seeding distribution at $x_w = 1$, $Re = 5 \cdot 10^5$ and $\alpha = 12^\circ$.*

Methods for the detection of the vortex centre from measurements in the core can be based on different properties of the vortex even though, for an analytical vortex, all these methods lead to the same location of the vortex centre. A discussion of the most common vortex centre localization methods is presented as follows.

¹The reference case is the trailing vortex at 1 chord of distance from the trailing edge of the wing model **M1**, at 12° of incidence and Reynolds number of $5 \cdot 10^5$. This case is a medium condition in terms of vortex properties and experimental arrangement of all tests.

1. *Centroid of the seed darker region.* The darker region formed by centrifugal forces on the seed particles at the vortex centre (see Figure 4.2) is only qualitative in nature and it is not usually circular or in any repeatable shape in the instantaneous pictures. It depends on several factors such as image contrast, seed particle distribution, particles mass and size, bit resolution of the camera, vortex dimension and strength making an automatic and general method based on this concept not very reliable compared to quantitative properties. However, these problems can be reduced with an appropriate use of seeding and equipment.
2. *Zero in-plane velocity (or swirl centre).* The swirl centre represents the spatial location at which the in-plane velocity component is zero:

$$\sqrt{v^2 + w^2} = 0 \quad (4.1)$$

This method can lead to erroneous results when the vortex axis is not straight and in particular when the axis curvature is high, such as for rotor wingtips. Moreover, the error grows if the vortex bulk motion is large or in PIV measurements if the light sheet is misaligned. A similar approach is represented by the calculation of the centroid of the planar streamlines.

3. *Peak axial velocity.* At the vortex centre, a perturbation of the axial velocity is commonly observed and it can be either away from the wing or toward the wing depending on the tip loading on the wing and the roll up of the wake sheet. When this perturbation is strong, the vortex centre can be identified as the point of maximum axial velocity perturbation.
4. *Centre point between the swirl velocity peaks.* The velocity profile of the component perpendicular to a cut across the vortex core reveals two peaks on the two sides of the centre. The centre point between these two peaks is an indication of the vortex centre coordinate. If this process is iteratively done also on cuts at different positions and directions, the vortex centre is identified. However, this method addresses only the swirl velocity peaks and not also its profile within the core and in case of asymmetry of the vortex, this procedure leads to wrong results. Nevertheless, this technique is commonly used in point measurements such as with pressure tubes and hot wire probes or when the accuracy of measurements in the vortex core is low.
5. *Peak of vorticity.* Vorticity is a three-dimensional vector. However, PIV mea-

measurements made on a single plane can only provide the velocity gradients on that plane. As a result, only one component of the vorticity can be calculated, that is the streamwise component ω_x when the plane is perpendicular to the freestream. For this method, the location of the vorticity peak is taken as the vortex centre.

6. *Peak of helicity.* Helicity is a conserved quantity which measures the helical motion of a vortex. It is defined as the dot product of the velocity and the vorticity so that the result indicates the inclination between the vorticity vector and the velocity vector. Because only the streamwise vorticity is available, only the streamwise component of the helicity can be calculated. In these experiments, where the wing is fixed and the vortex moves downstream with the freestream flow, a more appropriate definition is the scalar product of the axial velocity disturbance and the vorticity. In order to take into account either an axial velocity excess or defect, the absolute disturbance is used:

$$H_x = |u - U_\infty| \cdot \omega_x \quad (4.2)$$

As for the vorticity peak method, the peak of the helicity identifies the vortex centre.

7. *Q-criterion (or peak of the swirling strength).* Special singular points, typical of vortical features of spiral or close streamlines, are mathematically described by complex eigenvalues of the velocity gradient tensor which is composed of the strain tensor Σ and the vorticity tensor Ω , and expressed as follows:

$$\begin{aligned} \frac{d\mathbf{V}}{d\mathbf{x}} = \Sigma + \Omega &= \begin{bmatrix} \varepsilon_{yy} & \varepsilon_{yz} \\ \varepsilon_{zy} & \varepsilon_{zz} \end{bmatrix} + \frac{1}{2} \begin{bmatrix} 0 & -\omega_x \\ \omega_x & 0 \end{bmatrix} = \\ &= \begin{bmatrix} \frac{\partial v}{\partial y} & \frac{1}{2} \left(\frac{\partial v}{\partial z} + \frac{\partial w}{\partial y} \right) \\ \frac{1}{2} \left(\frac{\partial w}{\partial y} + \frac{\partial v}{\partial z} \right) & \frac{\partial w}{\partial z} \end{bmatrix} + \begin{bmatrix} 0 & \frac{1}{2} \left(\frac{\partial v}{\partial z} - \frac{\partial w}{\partial y} \right) \\ \frac{1}{2} \left(\frac{\partial w}{\partial y} - \frac{\partial v}{\partial z} \right) & 0 \end{bmatrix} \quad (4.3) \end{aligned}$$

A vortex is characterized by the invariance of the velocity gradient tensor (Jeong & Hussain, 1995) which requires the discriminant Q of the characteristic equation of the velocity tensor gradient to be below zero. It follows that the centre of the

vortex is defined as the point of minimum Q defined as:

$$Q = \frac{\left(\frac{\partial v}{\partial y} + \frac{\partial w}{\partial z}\right)^2}{4} + \frac{\partial v}{\partial z} \frac{\partial w}{\partial y} - \frac{\partial w}{\partial z} \frac{\partial v}{\partial y} \quad (4.4)$$

Because this method involves the calculation of velocity gradients, the measurement spatial resolution can greatly affect the accuracy of this vortex centre identification method, especially in the case of high gradients and not fully developed vortices.

8. *Peak of the eigenvalues of the velocity gradient tensor, λ_2 .* Starting from the gradient operator applied to the Navier–Stokes equations, Jeong & Hussain (1995) found a definition of a vortex that leads to the eigenvalues of the tensor $\Sigma^2 + \Omega^2$ which must be negative. This method leads to the identification of the vortex centre as the point of minimum λ_2 , defined as:

$$\lambda_2 = \frac{\left(\frac{\partial v}{\partial y}\right)^2 + \left(\frac{\partial w}{\partial z}\right)^2}{2} + \frac{\partial v}{\partial z} \frac{\partial w}{\partial y} \quad (4.5)$$

and same considerations on the measurement spatial resolution as in the previous method can be made.

In the vortex centre of an analytical vortex, the following relation is true (van der Wall *et al.*, 2002):

$$\omega_x^2 = |Q| = |\lambda_2| \quad (4.6)$$

In Figure 4.3, some of the vortex properties described earlier for the localization of the vortex centre are reported for an instantaneous realization of the reference case. Methods 1 is not implemented since the localization of the vortex centre is strongly affected by the algorithm which includes the calculation of centroids of closed shapes. Method 4 also is not implemented since it relies on an iterative searching technique of the cutting diameter and does not refer to the flow structure around the vortex centre. Therefore these two methods are not taken into consideration in this discussion. The scaling of all the quantities is accordingly accomplished using the freestream velocity U_∞ and the wing chord c .

The calculation of the in-plane velocity (Figure 4.3(a)) and the axial velocity perturbation (Figure 4.3(b)) involves only the local velocity vector. It is assumed that the vortex axis direction is aligned with the freestream velocity (as discussed in Section

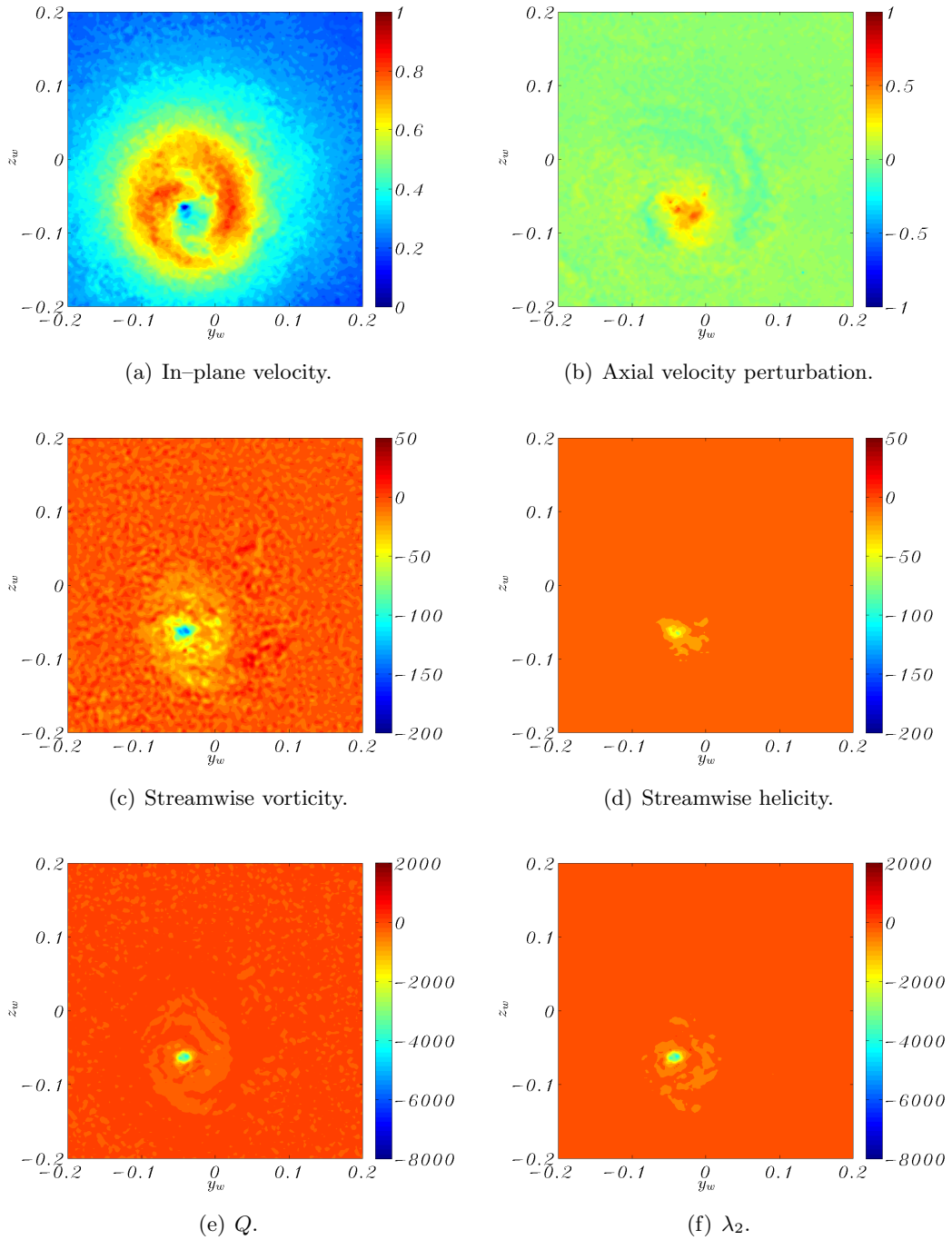


Figure 4.3: Centering methods for an instantaneous realization at $x_w = 1$, $Re = 5 \cdot 10^5$ and $\alpha = 12^\circ$.

2.4.(a)) so that the out-of-plane component measured by the SPIV is the actual vortex axial velocity. The contours show a non-axisymmetric vortex core which is still affected by the spiral roll up of the wake sheet. Also, the region of high axial velocity excess in the vortex core ($\max(u) \simeq 1.5$) is not developed as a distinct peak as it should be for

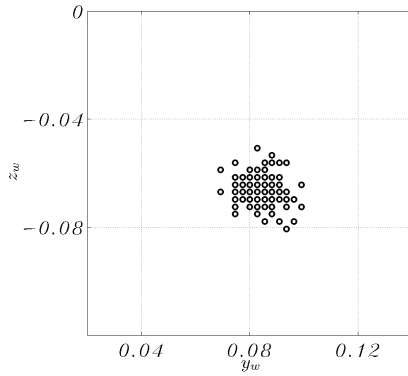
fully developed trailing vortices. The streamwise vorticity (Figure 4.3(c)) is calculated with the 8 node circulation method described by Raffel *et al.* (2007) which performs better than other schemes in terms of error and smoothness of the results. A region of high vorticity is observed in the vortex core. A similar result is observed in Figure 4.3(d) where a concentration of helicity (calculated as the point product of streamwise vorticity and axial velocity perturbation) is observed within the core. The helicity highlights the vorticity peak when an axial velocity perturbation is present in the vortex core, which exists in most of the trailing vortices. Also, the helicity is the only vortex property that includes in its calculation all the three velocity components which are available from a SPIV. The derivatives for the calculation of Q and λ_2 (Figures 4.3(e) and 4.3(f)) are estimated with the 4 points centered least-square approach (Raffel *et al.*, 2007). The two contours look very similar and around the peak in the vortex centre the shapes are identical. This is because in the vortex core the planar elongational strains ε_{yy} , ε_{zz} are negligible compared to the shear strains ε_{yz} , ε_{zy} and in particular, at the vortex centre:

$$\left(\frac{\partial v}{\partial y}\right)^2, \left(\frac{\partial w}{\partial z}\right)^2, \frac{\partial v}{\partial y} \frac{\partial w}{\partial z} \ll \frac{\partial v}{\partial z} \frac{\partial w}{\partial y} \quad (4.7)$$

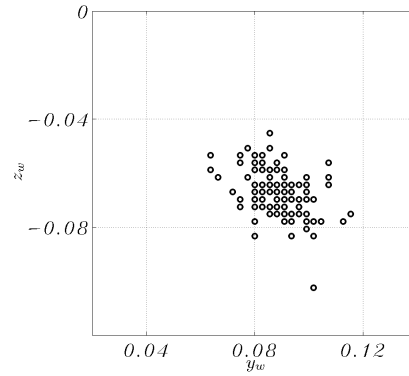
which leads to identical definition of Q and λ_2 from Equations (4.4) and (4.5) around the vortex centre.

The 121 instantaneous vortex centre positions of the reference case are calculated with these vortex centre localization methods and reported in Figure 4.4. The pattern of the distribution of the instantaneous centres reveals that they are strongly affected by the grid spacing of the vector field which is of the order of one tenth of the movement of the centres. However, because the grid spacing is a small fraction of the core radius (and around 0.3% of the chord), the alignment of the individual measurements with the closest grid node does not lead to a significant error. In fact, this results in a residual vortex wandering in the measurements which is less than half the diagonal grid spacing. Based on analysis by Devenport *et al.* (1996), this would result in less than 0.8% error in the measured peak swirl velocity and core radius. Therefore, alignment based on the grid node closest to the vortex centre was followed in the present work.

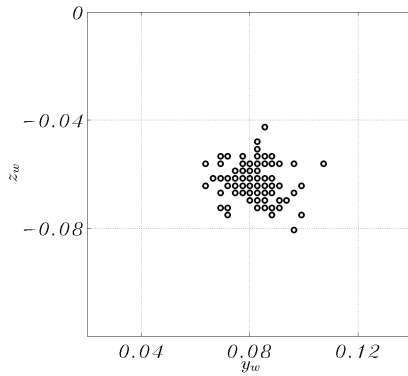
For this case, the scattering of the vortex centres (the wandering of the vortex) is of about 4% of the wing chord and the axial velocity perturbation method shows the highest dispersion compared to the other methods. The Q and the λ_2 methods show identical distributions of the instantaneous centres. Analysing the vortex centre distributions of all the configurations, no particular orientation of the meandering was



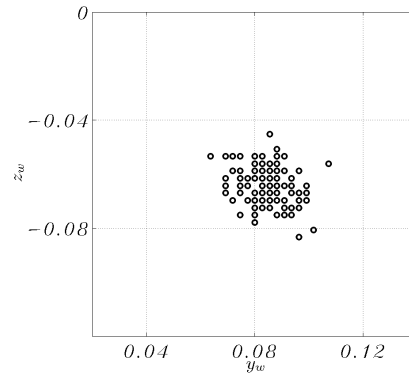
(a) In-plane velocity zero.



(b) Axial velocity perturbation maximum.



(c) Streamwise vorticity minimum.



(d) Streamwise helicity minimum.

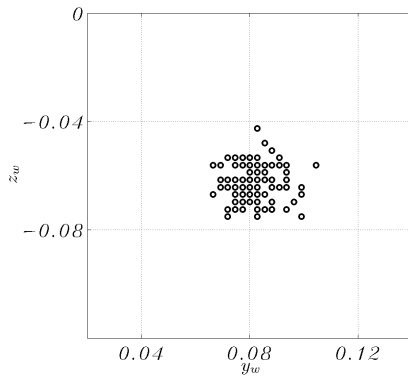
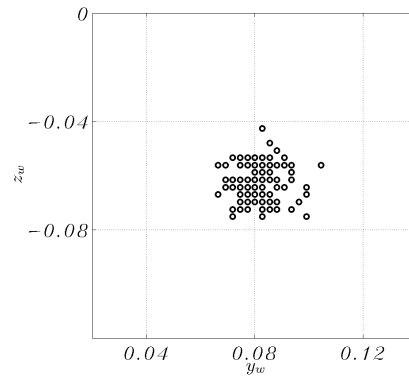
(e) Q minimum.(f) λ_2 minimum.

Figure 4.4: Instantaneous vortex centre positions calculated with different centering methods at $x_w = 1$, $Re = 5 \cdot 10^5$ and $\alpha = 12^\circ$.

observed. In the range of cases studied here, therefore, a isotropic wandering amplitude can be assumed.

The effects of the vortex centre localization method adopted for the evaluation of the wandering and the centering of each instantaneous realization is discussed as follows

with particular attention to the swirl velocity distribution, the axial velocity and the turbulent quantities. The average of the 121 instantaneous vector fields is calculated for each vortex centre localization method and it involves the centering of each of the vortex realizations. The average of the instantaneous vector fields without the centering will be referred to as simple average. The study on the statistical convergence of vortex properties, which leads to the choice of 121 vector fields, is presented in Section 4.1.(d).

(a) Swirl velocity distribution As discussed earlier, without centering each instantaneous flow field, the mean vortex shows a larger radius and a smaller maximum swirl velocity than the same mean properties when the centering is applied. This behaviour is true for a fully developed vortex, that is a wingtip vortex in the far wake. At an early stage, as observed in these experiments, this smearing effect is partially masked by the high asymmetry of the vortex. On the simple averaged in-plane velocity distribution around the vortex in Figure 4.5(a), an anti-clockwise spiral structure of higher velocity around the core is observed (which indicates the clockwise rotation of the vortex). Thus, the gradient of the swirl velocity and the location of the maximum swirl velocity (which defines the vortex radius) are expected to be different when different directions of the cuts across the centre are done. The averaged axial velocity distribution in Figure 4.5(b) also shows an asymmetric structure. The centres calculated as minimum in-plane velocity and as maximum axial velocity, indicated by respectively a black and a white cross in Figure 4.5, are positioned at a distance 1% of the chord which corresponds to about 15% of the core radius (the origin of the reference system of Figure 4.5 was arbitrarily chosen at the vorticity peak). This indicates that the vortex is still strongly affected by the formation process on the wing, the rolling up of the wake sheet and the interaction with secondary vortices. At this stage, the effects of applying the simple average of the instantaneous flow fields or applying some centre localization method, are small compared to the strong asymmetry of the vortex structure.

In Figure 4.6, swirl velocity profiles calculated from the averaged vector fields after different centering methods are shown; the velocity is calculated by a cubic interpolation of the velocity vector field along 36 radii equispaced around the centre (although only 12 are reported in the graph) adopting a cubic interpolation from the cartesian grid of the original velocity vectors. In Figure 4.6(a) the swirl velocity from the simple averaged vector field is calculated. The effect of the spiral structure observed in Figure 4.5 is observed here as a collection of profiles with very different vortex radii (from $r = 0.03$

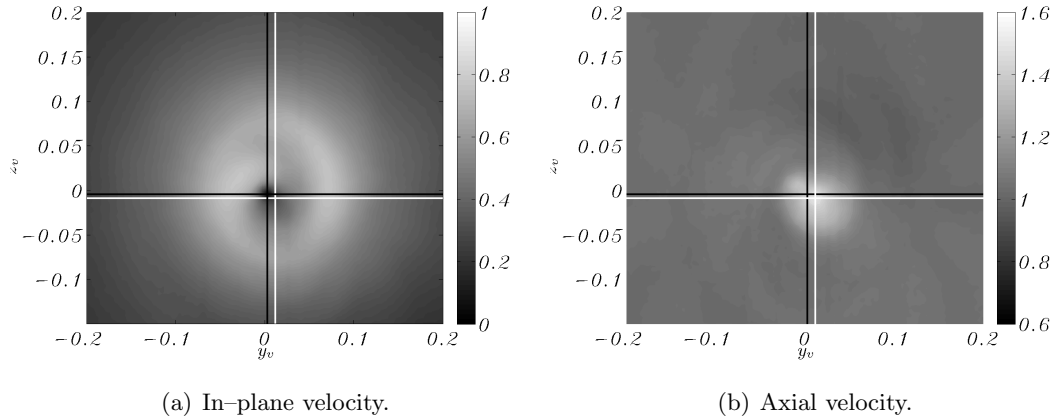


Figure 4.5: Simple averaged flow field at $x_w = 1$, $Re = 5 \cdot 10^5$ and $\alpha = 12^\circ$; in-plane velocity minimum (black cross), axial velocity maximum (white cross).

to $r = 0.07$). The drop and the interruption of one of the profiles at $r = 0.15$ is due to the reaching of one of the edges of the SPIV plane (outside the calibrated area) and not a vortex feature. The mean value of the swirl velocity profiles (red line) shows a double gradient structure in the vortex core which reflects the vortical shape of the vortex. A vortex core composed of three regions with constant but different slopes inside the vortex core was found by Vogt *et al.* (1996) on a plane at 4 chords behind the trailing edge. The double gradient structure is more distinct for the in-plane velocity, vorticity, helicity and Q based centering methods (Figures 4.6(b), 4.6(d), 4.6(e), 4.6(f)). For the axial velocity centering method (Figure 4.6(c)) the mean value of the swirl velocity does not reveal such a distinct double gradient structure although the vortical shape of the vortex is still identifiable. The swirl velocity at the centre of the vortex is very close to zero for the in-plane velocity centering method whereas it shows a scatter up to $\Delta u_\theta = \pm 0.25$ for the Q based correction. This indicates a translation of the vortex centre calculated with the Q method of around 6% of the vortex core (1% of the chord) from the vortex centre calculated with the in-plane velocity method which proves the high asymmetry around the vortex centre in the very early wake and the great impact on the averaged vortex of the centering method. The velocity profiles obtained from the λ_2 correction method is not shown since it does not differ from the profiles obtained applying the Q method.

The vortical structure of the vortex in the early wake leads to an asymmetric swirl velocity distribution indicating that a correct description of the velocity needs global measurements on the vortex plane.

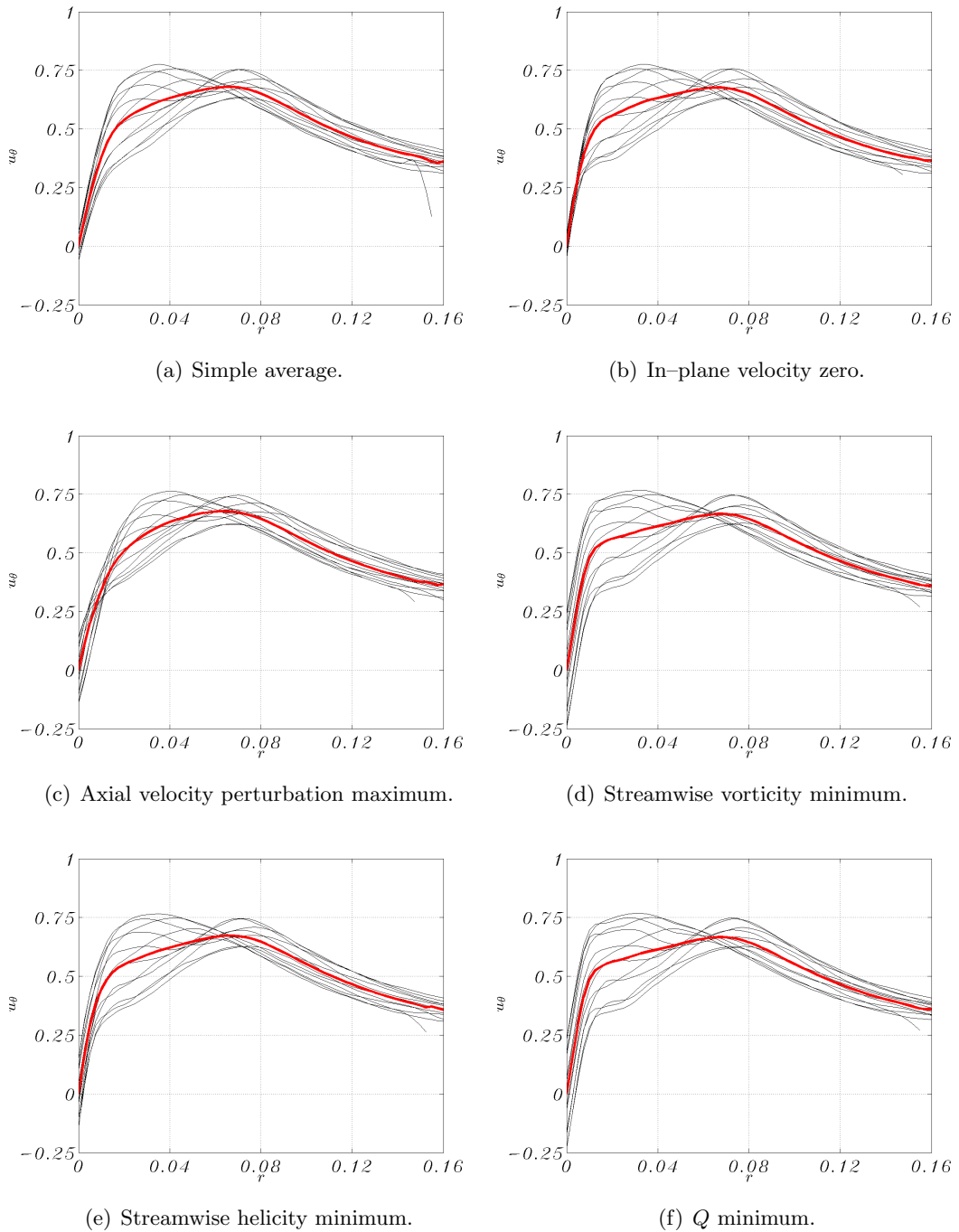


Figure 4.6: Average swirl velocity profiles and mean values (red line) calculated with different centering methods at $x_w = 1$, $Re = 5 \cdot 10^5$ and $\alpha = 12^\circ$.

(b) Axial velocity distribution Differences in the vortex description when simple average or centered average is applied, are remarkable when the axial velocity profiles (out-of-plane component of the SPIV) are viewed. In Figure 4.7, axial velocity profiles of the simple and corrected averaged vector fields are

reported along 12 radii and the mean values are also drawn.

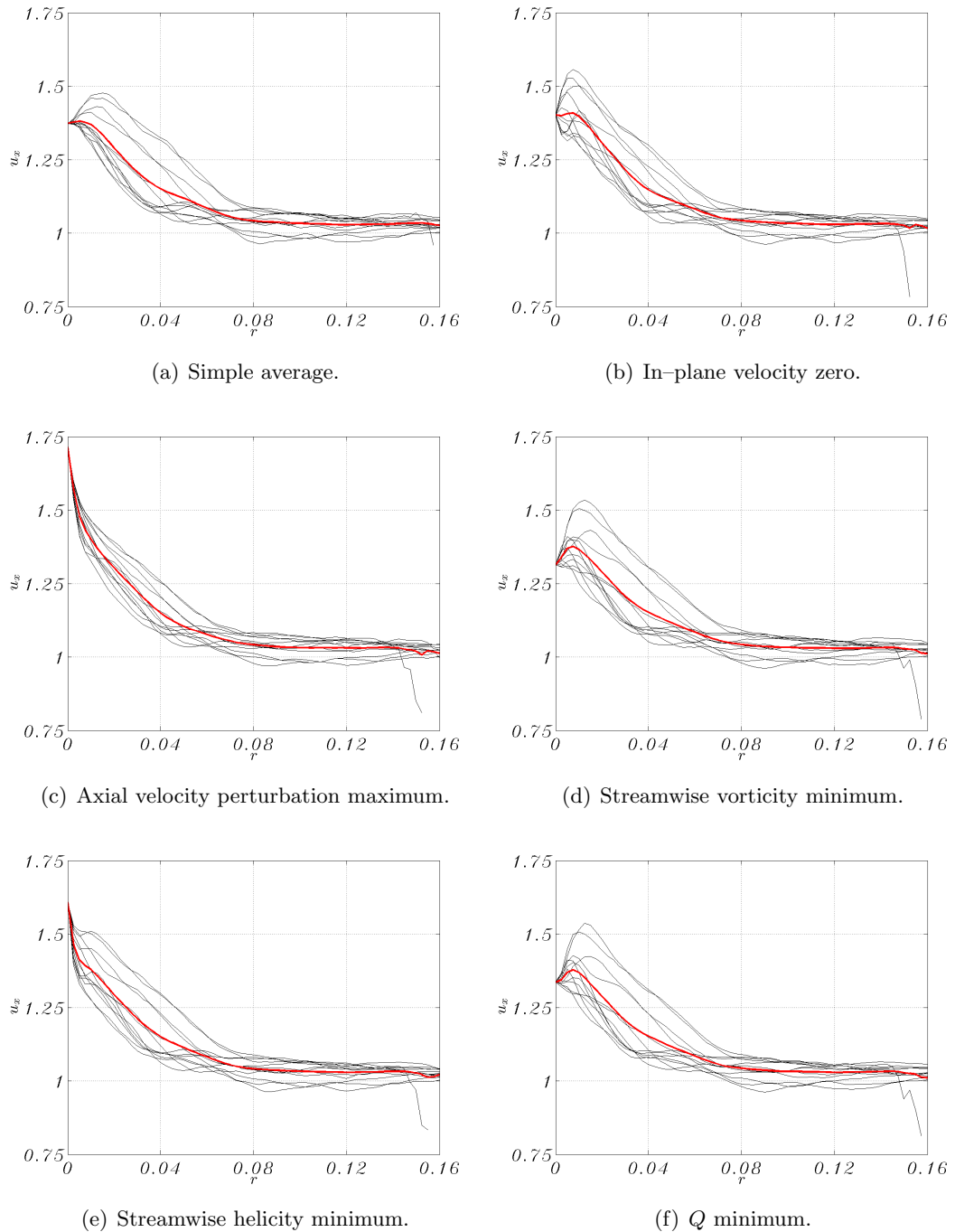


Figure 4.7: Average axial velocity profiles and mean values (red line) calculated with different centering methods at $x_w = 1$, $Re = 5 \cdot 10^5$ and $\alpha = 12^\circ$.

All the profiles reveal an axial velocity excess region which is contained in the vortex core and outside the core the axial velocity rapidly reaches the streamwise velocity. Simple averaged profiles (Figure 4.7(a)) shows a maximum axial velocity at a distance

of 2% of the chord from the centre. This peak, of intensity of 1.48 times the reference velocity, is lower than the peaks observed from any other corrected profile, as a consequence of the smearing effect. In contrast, the axial velocity based average (Figure 4.7(c)) show, as expected by definition, the highest axial velocity perturbation with $u_0 = 1.71$ located in the centre. For the in-plane velocity (Figure 4.7(b)), the vorticity (Figure 4.7(d)) and the Q method (Figure 4.7(f)) the profiles are similar, with region of axial velocity peak ($u_x = 1.53$ – 1.56) away from the centre of the vortex where the axial velocity is $u_0 = 1.31$ – 1.40 . It appears from these profiles that, like the swirl velocity, also the axial velocity in the vortex core shows a high asymmetry. The helicity centering method (Figure 4.7(e)) still indicates asymmetry in the vortex core but it is the only one, besides the axial velocity method, that shows the maximum axial velocity perturbation at the vortex centre ($u_0 = 1.61$).

(c) Turbulent quantities Some of the turbulent quantities are also compared for different centering methods although the discussion of the turbulence in the vortex will be presented in a later section. The instantaneous velocity at one point of the flow field is expressed as sum of the average velocity at that point during the experiment and the fluctuating component:

$$\mathbf{u} = \bar{\mathbf{u}} + \mathbf{u}' \quad (4.8)$$

The root mean square of the velocity fluctuations (square root of the turbulent normal stresses) defined as follows is scaled by the freestream velocity U_∞ :

$$\sigma_u = \sqrt{u'^2} = \sqrt{(u_i - \bar{u})^2} \quad (4.9)$$

$$\sigma_v = \sqrt{v'^2} = \sqrt{(v_i - \bar{v})^2} \quad (4.10)$$

$$\sigma_w = \sqrt{w'^2} = \sqrt{(w_i - \bar{w})^2} \quad (4.11)$$

The Reynolds stresses, scaled by U_∞^2 , are defined as follows:

$$\overline{v'w'} = \overline{(v_i - \bar{v})(w_i - \bar{w})} \quad (4.12)$$

$$\overline{u'v'} = \overline{(u_i - \bar{u})(v_i - \bar{v})} \quad (4.13)$$

$$\overline{u'w'} = \overline{(u_i - \bar{u})(w_i - \bar{w})} \quad (4.14)$$

where $\overline{v'w'}$ are the stresses on the SPIV plane.

The shear strain ε_{yz} and the normal strain ε_{xx} are calculated with an eight point scheme as described by Raffel *et al.* (2007) where, for the latter, incompressibility is assumed:

$$\varepsilon_{yz} = \varepsilon_{zy} = \frac{1}{2} \left(\frac{\partial v}{\partial z} + \frac{\partial w}{\partial y} \right) \quad (4.15)$$

$$\varepsilon_{xx} = \frac{\partial u}{\partial x} = - \left(\frac{\partial v}{\partial y} + \frac{\partial w}{\partial z} \right) \quad (4.16)$$

The maximum Mach number found in the flow fields is of the order of $M = 0.15$ so that the assumption of $\nabla \cdot \mathbf{u} = 0$ is very reasonable. The normalisation of the strains is with U_∞/c .

The turbulent kinetic energy is also calculated and defined as half the sum of the variance of the velocity fluctuations:

$$k = \frac{1}{2} \left(\overline{u'^2} + \overline{v'^2} + \overline{w'^2} \right) \quad (4.17)$$

In Figures 4.8 and 4.9 the turbulent fluctuations of the three velocity components calculated from simple averaged and centered flow fields are compared. High fluctuation is observed within the vortex core on all the components. Both the in-plane fluctuations σ_v and σ_w exhibit an elliptical shape, with the major axes aligned respectively along the y axis direction and the z axis direction whereas the axial fluctuation σ_u shows a circular shape. The elliptical structure of the in-plane components, which is observed also by Ramasamy *et al.* (2009b), is less clear for in-plane centering method compared to the other methods. The rolling up wake sheet also shows high fluctuations relatively to the external flow (light blue region around the centre at radius approximately equal to 0.1).

The peak in the fluctuation on each contour in Figures 4.8 and 4.9 is observed at the centre of the vortex (at the origin of the reference system). The maximum peak value of the in-plane fluctuations σ_v and σ_w is observed for the axial velocity perturbation centering method whereas it is minimum for the in-plane velocity centering method. Also, the maximum peak value of the axial fluctuation σ_u is observed for the in-plane velocity centering method although for all the averaging methods a similar fluctuation level is observed.

In Figure 4.10, the maximum instantaneous axial velocity u_x found in the vortex core is reported for each one of the 121 vortex realizations. The fluctuation level is very high with velocity peak values between 1.4 and 2.1 and standard deviation of 9.5% of the

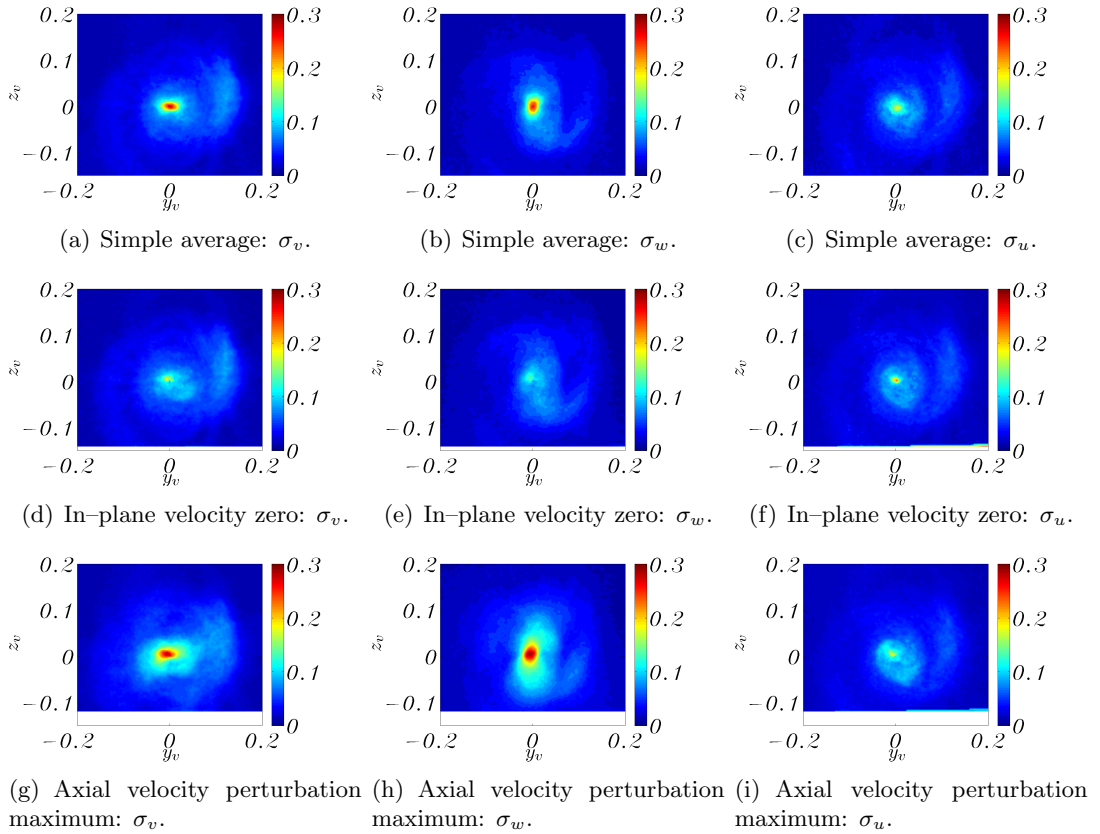


Figure 4.8: Velocity fluctuations at $x_w = 1$, $Re = 5 \cdot 10^5$ and $\alpha = 12^\circ$; part 1 of 2.

freestream velocity which indicates strong turbulent fluctuations within the vortex core. It is important to notice that these values do not correspond necessarily to the vortex centre velocity but they refer to a point in the vortex core. They would correspond by definition to the vortex centre in the case of adopting the peak axial velocity centering method. Therefore, the fluctuation of these peak velocities is not directly related to the wandering of the vortex but only to its instantaneous intensity. However, such axial velocity are higher than most of other experiments but coherent with the results presented by Green & Acosta (1991) and Chow *et al.* (1997a). Several factors influence the development of the velocity excess including angle of attack, tip shape and Reynolds number. The measurements of Figure 4.10 were performed at a high angle of attack, at a relatively high Reynolds number and there was not the problem of probes affecting the flow. These factors are shared with the studies mentioned above.

The Reynolds shear stress on the SPIV plane, the corresponding shear strain and the turbulent kinetic energy are shown in Figures 4.11 and 4.12 for the different averaging methods. The relative rotation of 45° between the Reynolds stresses and shear stresses, observed also by Chow *et al.* (1997b) and Ramasamy *et al.* (2009b), reveals

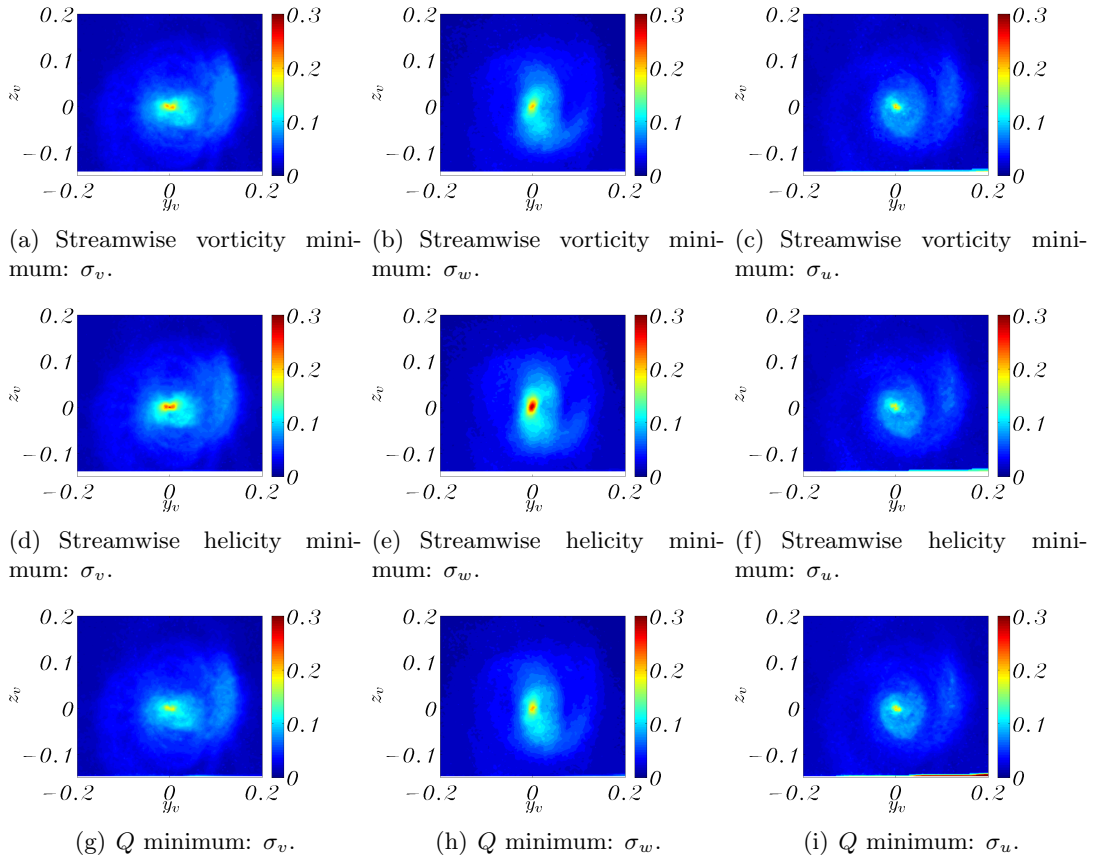


Figure 4.9: Velocity fluctuations at $x_w = 1$, $Re = 5 \cdot 10^5$ and $\alpha = 12^\circ$; part 2 of 2.

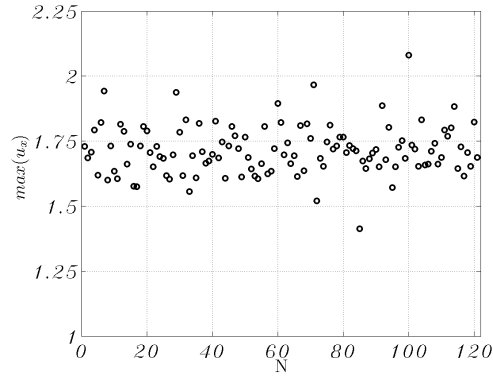


Figure 4.10: Instantaneous axial velocity peaks at $x_w = 1$, $Re = 5 \cdot 10^5$ and $\alpha = 12^\circ$.

the anisotropic eddy viscosity in the vortex core. Although the shear strains show the same four lobed pattern independently from the averaging method used, the Reynolds stresses change in magnitude when adopting different averages. As observed also for the in-plane turbulent fluctuations earlier, the axial velocity centering method shows a high level of turbulence in the vortex core and the in-plane velocity centering method gives a low level of turbulence. The turbulent kinetic energy behaves in the same way.

Also, regardless of the centering method adopted, a peak of turbulence is calculated at the vortex centre. The peak of the turbulent kinetic energy at the vortex centre is dictated by the high turbulence level of all the velocity components within the core. At this stage, the turbulent fluctuations are still present in the core and the laminarization process is not observed. More details on the relaminarization of the vortex core are presented in the next sections.

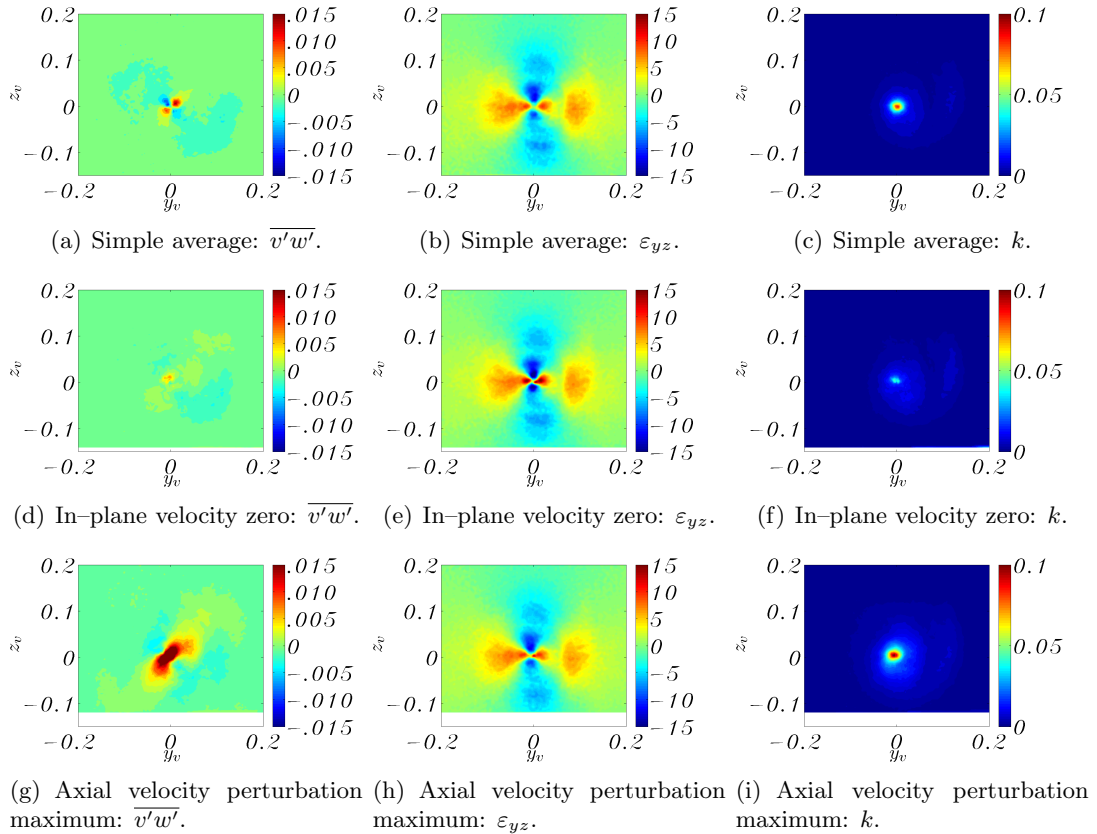


Figure 4.11: *Turbulence at $x_w = 1$, $Re = 5 \cdot 10^5$ and $\alpha = 12^\circ$; part 1 of 2.*

The wingtip vortex flow in the early wake is dominated by interaction with secondary vortices and by the rolling up of the wake sheet. Although discussions could be done on the best and most appropriate centering method, the final decision has to take into consideration the particular interest of the undertaken study. For instance, in order to study the maximum axial velocity encountered in the vortex core or to study the shape of the rolling up of the vortex sheet or the interaction between the several secondary vortices with the primary vortex, different centering methods might be adopted before taking the average in order to highlight the particular feature of the vortex system. Nevertheless, vortex meandering is observed also in the early wake and centering the instantaneous frames leads to different descriptions of the vortex velocity field and

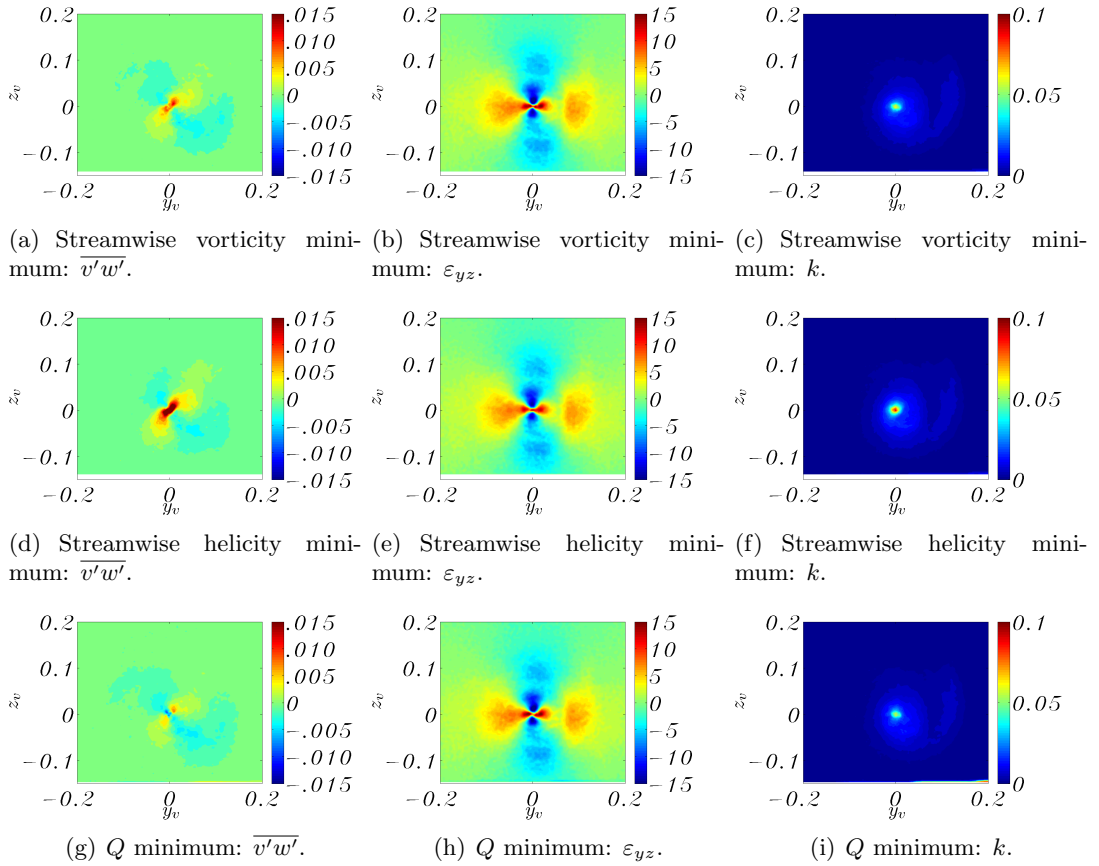


Figure 4.12: Turbulence at $x_w = 1$, $Re = 5 \cdot 10^5$ and $\alpha = 12^\circ$; part 2 of 2.

turbulent quantities.

The vortex often shows a distinctive excess or deficit of axial velocity in the centre with reference to the freestream and the helical motion of the vortex is identified when combining vorticity and axial velocity perturbation. The helicity based correction method is the only method discussed here which uses all the velocity components, giving accurate description of swirl velocity, axial velocity and turbulent quantities. The impossibility of detecting the centre with the axial velocity perturbation method when the deficit or the excess is small, does not cause problems also in the helicity method because of the robustness given by the vorticity. The Q and the λ_2 methods are complex and computationally costly methods and they introduce more errors from the calculation of the gradients and the operation between operators (Raffel *et al.*, 2007) without revealing noticeable benefits. The in-plane velocity method and the axial velocity perturbation method can not describe accurately the structure of the axial velocity at the vortex centre and of the turbulent fluctuations. Therefore, if not differently indicated, the helicity minimum centering method is used throughout this chapter having revealed

to be the most appropriate in describing the swirl velocity distribution, axial velocity, turbulent fluctuation, Reynolds stresses and shear strains. Ramasamy *et al.* (2009a) arrived at the same conclusion for the study of rotor blade tip vortices.

(d) Convergence of averages The effects of varying the number of instantaneous velocity vector fields used in the averaging process is studied to determine the minimum number of samples that are needed to achieve statistical convergence. The assessment of the statistical convergence of some vortex flow quantities is performed adopting the helicity centering method on 1000 velocity vector fields of the reference case. Also, since the PIV hardware used during these experiments limits the number of samples acquired at a constant frequency to 121, the errors incurred adopting this number of vector fields is also identified. At this stage of the vortex flow, the shape of such quantities is as important as the peak or characteristic values. In fact, the comparison of the different configurations will often show different distributions of flow properties which will reveal different development and structure of the vortex flow.

The contours of some of these quantities such as swirl velocity, axial velocity, vorticity, in-plane velocity fluctuation, Reynolds shear stress and shear strain are reported as averages of an increasing number N of instantaneous realizations respectively in Figures 4.13, 4.14, 4.16, 4.18, 4.19 and 4.20. On the contours, the reaching of the convergence is seen as the reaching of a smooth and distinct shape.

Convergence curves are also presented in Figures 4.15, 4.17 and 4.21 on some of the vortex characteristic values. A cubic interpolation on 1600 points on 36 radius equispaced around the centre is performed in order to evaluate the circumferential average. On radial distribution so obtained, the maximum swirl velocity, the vortex core radius, the axial velocity peak, the vorticity peak, the helicity peak, the swirling strength peak and the in-plane fluctuation peak are identified. Because the Reynolds shear stress and the shear strain show a four lobes pattern with alternatively positive and negative values, the convergence curve on these properties is presented for the average of the absolute values of those peaks. On all these graphs, the trend of the percentage distance from the average value calculated with 1000 samples is also reported.

Both the swirl and the axial velocity components (Figures 4.13 and 4.14) show a distinct and converged shape already with 25 samples. From the convergence curves in Figure 4.15, the value of the swirl velocity peak shows an error which goes below 1% with just few samples and the estimation of the vortex core radius and axial velocity

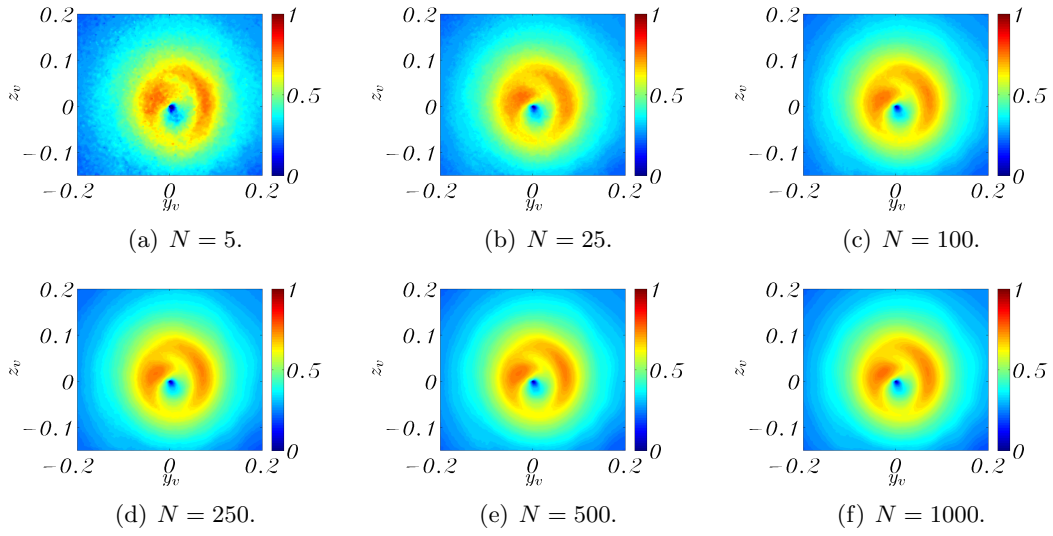


Figure 4.13: Swirl velocity at $x_w = 1$, $Re = 5 \cdot 10^5$ and $\alpha = 12^\circ$.

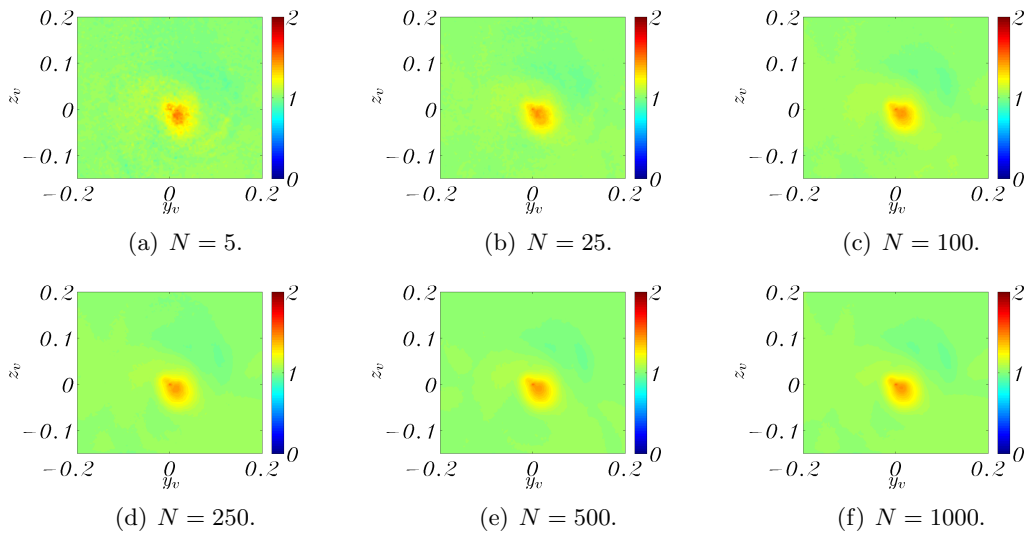


Figure 4.14: Axial velocity at $x_w = 1$, $Re = 5 \cdot 10^5$ and $\alpha = 12^\circ$.

peak is below 2% with 121 samples.

The convergence of the shape of the vorticity distribution, which involve derivatives of the velocity vector fields, (Figure 4.16) requires a higher number of samples around 100. The convergence of the peak value (Figure 4.17), found in the centre of the vortex, also is slower than the velocity peaks and with 121 samples an error of 5% is expected. With the same number of samples, the helicity shows an error of around 5% and the swirling strength of around 6% which reflects the increasing number of operations needed for their evaluation. However, the location where these peaks are found does not change when the number of samples has reached a value of around 50.

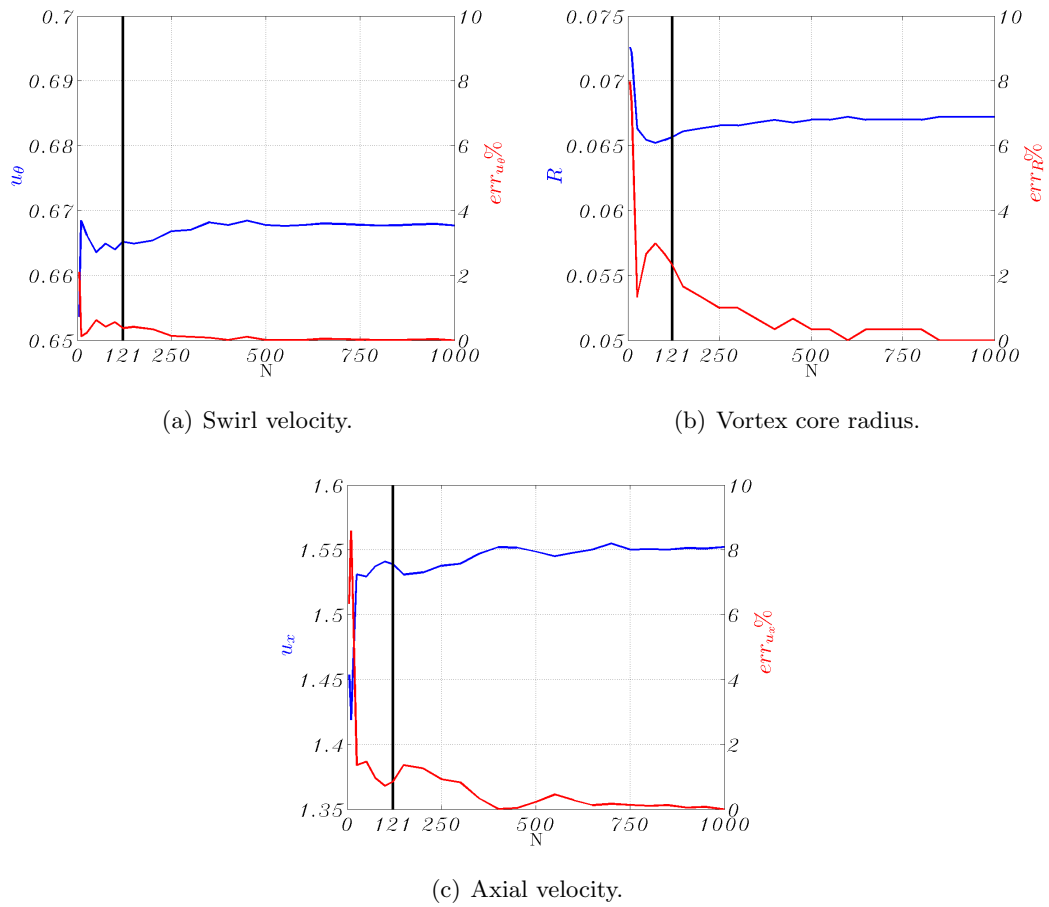


Figure 4.15: Convergence and errors of velocity and core radius at $x_w = 1$, $Re = 5 \cdot 10^5$ and $\alpha = 12^\circ$.

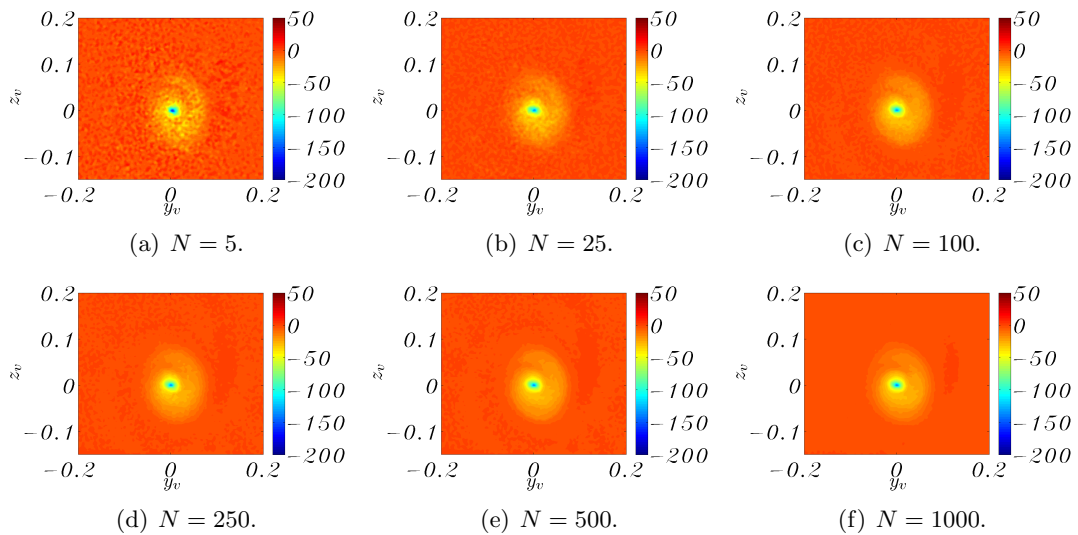


Figure 4.16: Vorticity at $x_w = 1$, $Re = 5 \cdot 10^5$ and $\alpha = 12^\circ$.

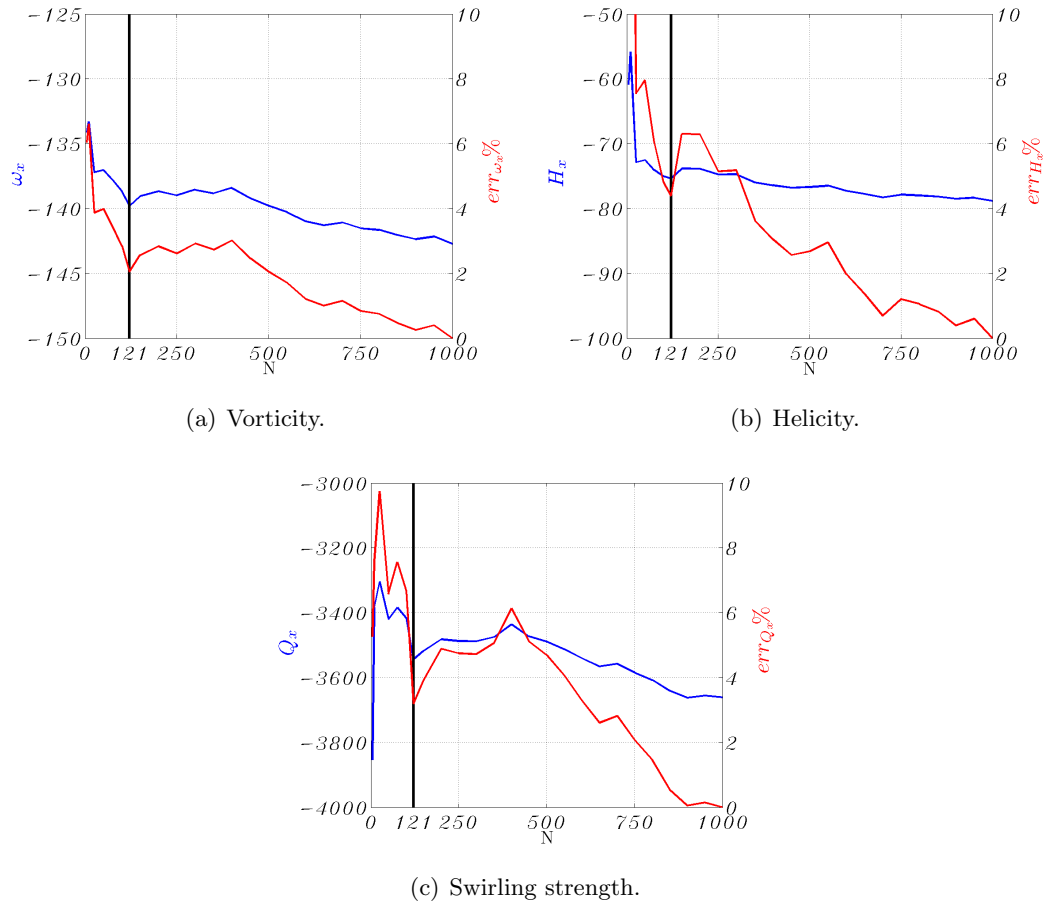


Figure 4.17: Convergence and errors of vorticity, helicity and swirling strength at $x_w = 1$, $Re = 5 \cdot 10^5$ and $\alpha = 12^\circ$.

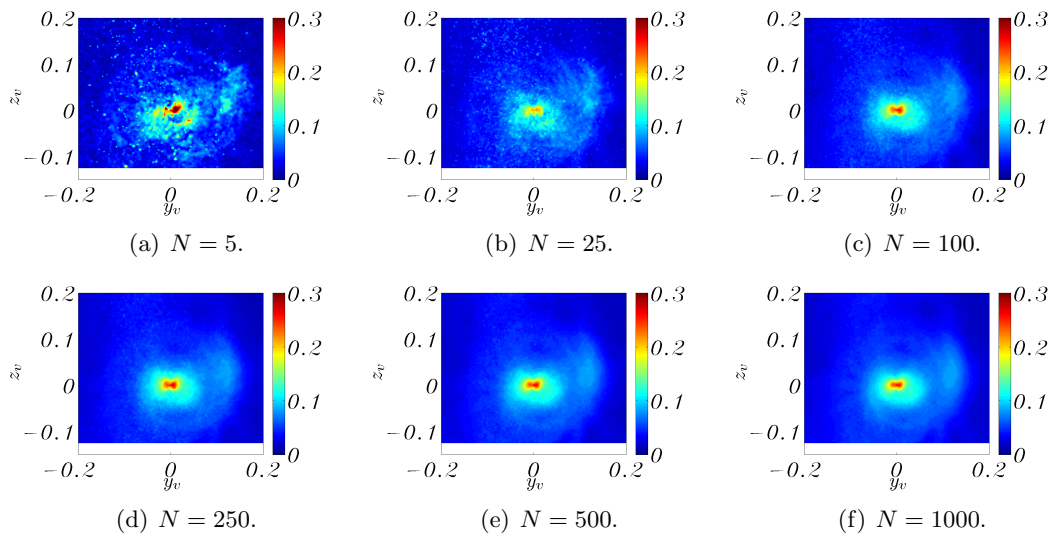


Figure 4.18: In-plane velocity fluctuation σ_v at $x_w = 1$, $Re = 5 \cdot 10^5$ and $\alpha = 12^\circ$.

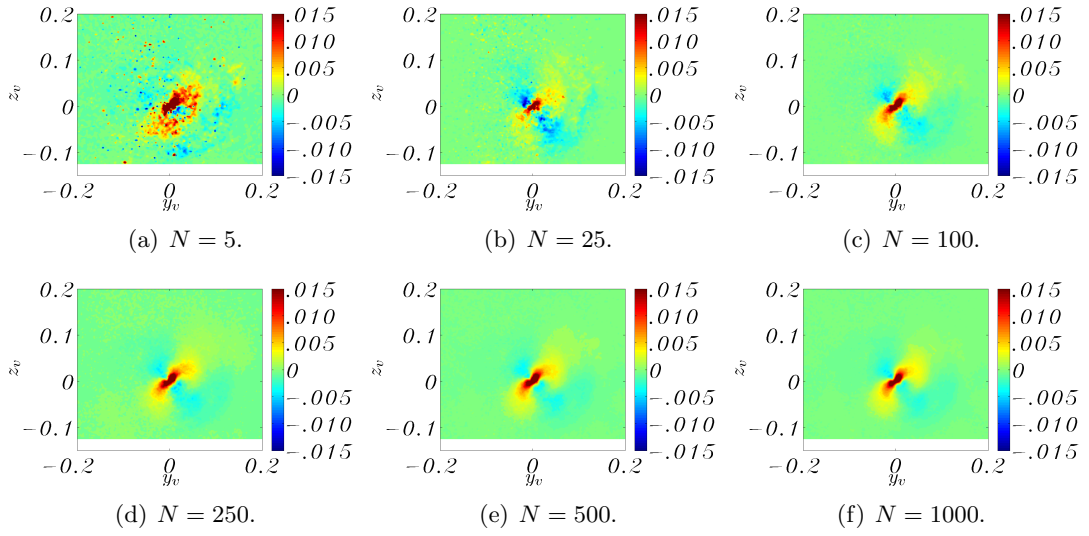


Figure 4.19: Reynolds shear stress $\overline{v'w'}$ at $x_w = 1$, $Re = 5 \cdot 10^5$ and $\alpha = 12^\circ$.

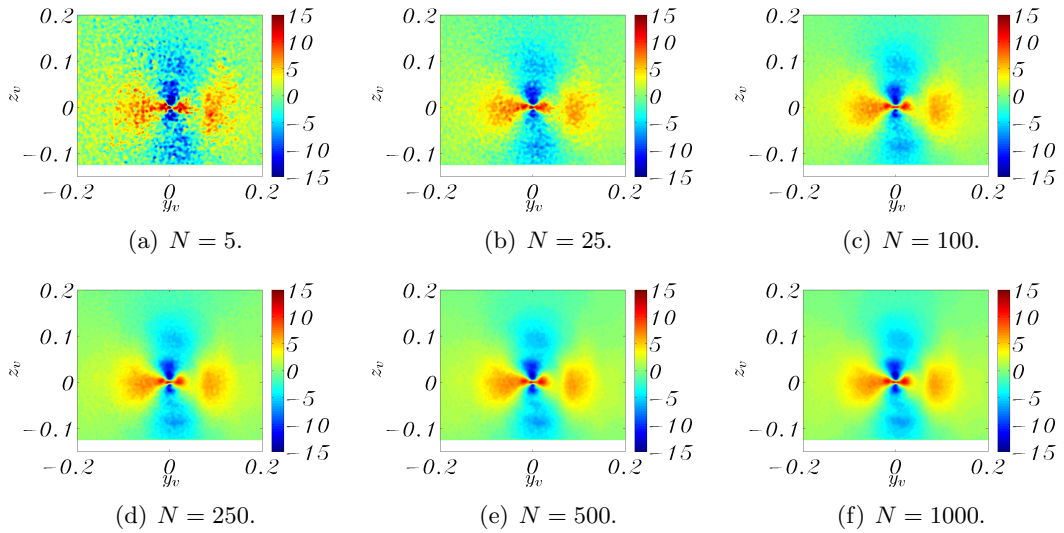


Figure 4.20: Shear strain ε_{yz} at $x_w = 1$, $Re = 5 \cdot 10^5$ and $\alpha = 12^\circ$.

The convergence of velocity fluctuations (Figure 4.18), first order turbulent quantities, show a trend similar to the convergence of the velocity. The convergence of the distribution is observed with 100 samples and the percentage error of the peak value with 121 samples is below 3 (see Figure 4.21). The turbulent kinetic energy, not shown here, also shows a similar convergence curve. Second order turbulent quantities, such as the Reynolds shear stress in Figure 4.19, are expected to require a higher number of images to converge. In fact, after 250 images the distribution seems to have reached a converged level although the final shape is observed already after 100 samples. With 121 frames, the error in the evaluation of the mean of the absolute value of the maxi-

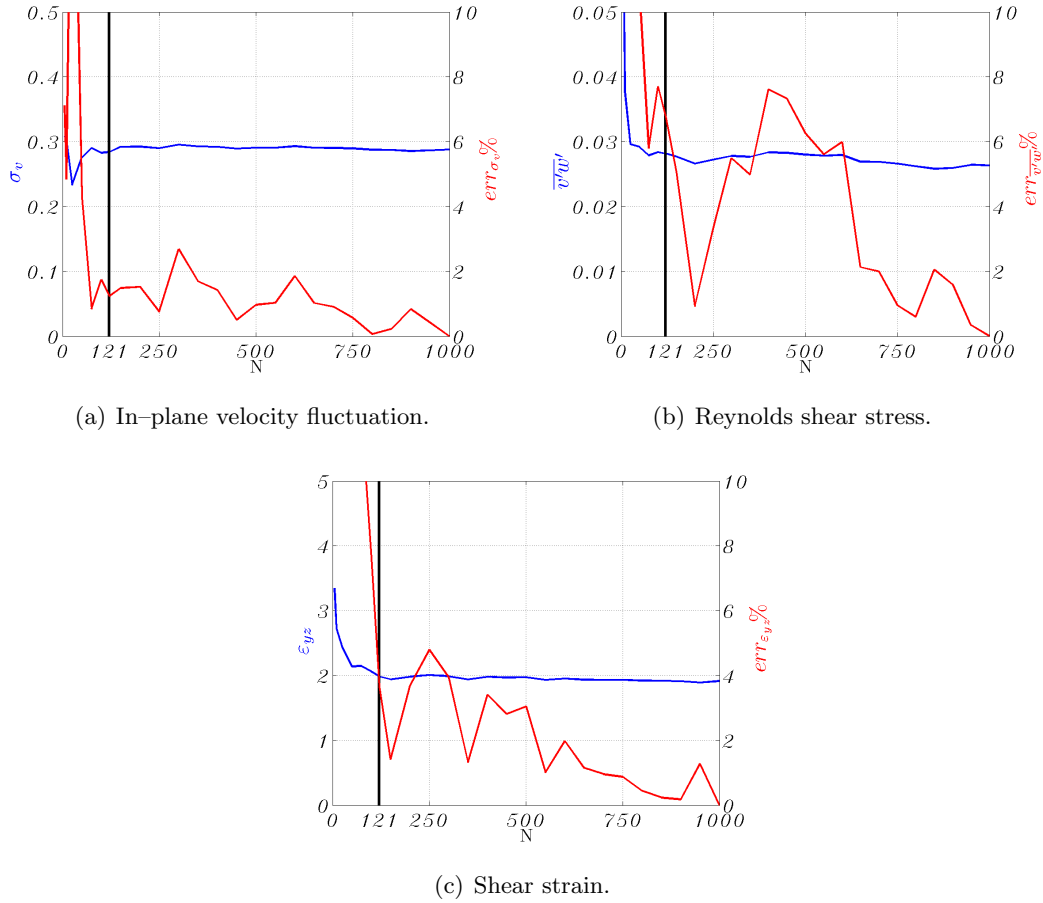


Figure 4.21: Convergence and errors of velocity fluctuation, Reynolds stress and shear strain at $x_w = 1$, $Re = 5 \cdot 10^5$ and $\alpha = 12^\circ$.

imum and minimum peaks is around 7%. A similar evaluation of statistical convergence on a rotor wingtip was performed by Ramasamy *et al.* (2009b) who found a minimum number of vector fields required for the turbulent quantities equal to 250 for the first order characteristics and about 750 samples for the second order characteristics. The different number of samples required for a statistical convergence can be attributed to the higher unsteadiness of the rotor wake compared to the fixed wing.

A better convergence is observed for the shear strain (Figure 4.20) because it is based on velocity gradients and not on turbulent fluctuation terms. Similarly to the convergence curve of the vorticity, the error from the shear strain at 121 samples, calculated in the same way as the Reynolds shear stress, is around 4%.

As a result of this convergence study, a number of 121 velocity vector fields (sampled at a constant acquisition rate of 2 Hz) was seen to reach a satisfactorily convergence level for the quantities presented in this chapter. The estimation of the errors presented

in this section incurred adopting 121 samples is to be taken as an overestimation of the global measurement errors since they all refer to the peak values.

SECTION 2

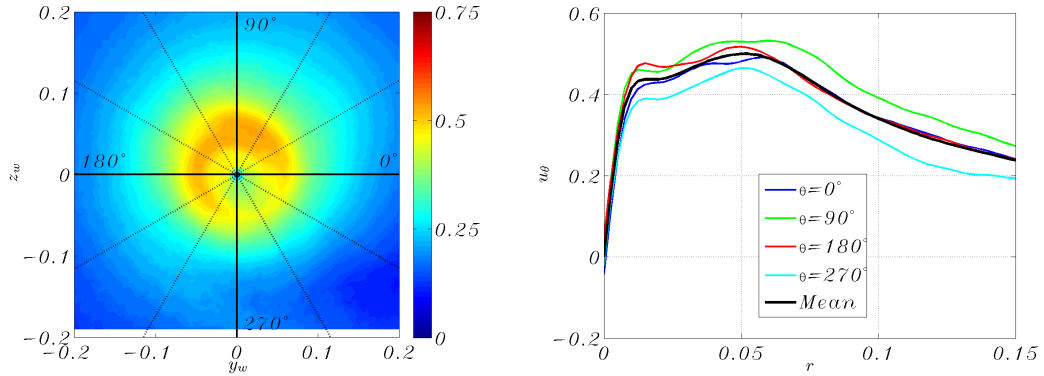
Shape of the vortex core

The wingtip vortex in the early wake reveals particular features which are directly related to the wing geometry and loading condition. These features involve wake sheet rolling up, merging of secondary vortices and a lack of axisymmetry of the early vortex. However, the vortex evolves into an axisymmetric vortex quite rapidly and at 1.5 chords of distance from the trailing edge these phenomena may be not observed anymore (Chow *et al.*, 1992; Birch *et al.*, 2004). A strong asymmetry in the swirl velocity profiles has been described in the previous section. The mean swirl velocity profile as a function of the radius shows two peaks as a consequence of this asymmetry, which merge quickly downstream.

Data from experiments on the **M1** model with a squared tip at different Reynolds numbers, angles of attack and laser plane locations are analysed in this section with particular attention paid to the early evolution and shape of the trailing vortex. The data presented in this study are the averages of 121 velocity vector fields applying the helicity centering method.

(a) Vortex core shape definition Generally, the vortex core radius R is defined as the distance between the vortex centre and the point of maximum swirl velocity. As the vortex in the early wake does not show an axisymmetric structure, different values of the core radius are expected to be found depending on the orientation (with θ as the azimuth coordinate) of the cut along which the swirl velocity is measured. In Figure 4.22(a) a number of slicing cuts across the centre of the vortex are sketched on an averaged swirl velocity contour. In Figure 4.22(b) the swirl velocity measured along some of those cuts is plotted and an inner and an outer peak are observed. The profiles show high discrepancies in the shape, asymptotic value, maximum swirl velocity and its location. The mean value of the 36 profiles calculated is also plotted in Figure 4.22(b). Since the profile appears different depending on the direction, it is clear how a description of the vortex system based on several directions around the centre is essential for a deeper understanding of the vortex evolution in the early wake. For instance, Ramasamy *et al.* (2009a) found that two slicing cuts across

the tip vortex (producing 4 profiles) provide an acceptable measurement of the vortex core dimension.



(a) Swirl velocity contour and various slicing cuts (b) Swirl velocity profile along various cuts and mean value.

Figure 4.22: Swirl velocity and slicing cuts at $\alpha = 8^\circ$, $x_w = 1$ and $Re = 5 \cdot 10^5$.

In the early wake, the calculation of the vortex core radius as point of maximum swirl velocity leads to different values depending on the direction of the cut and the average value does not contain all the information of the shape of the core. In this section, the vortex core is presented as the locus of the points of maximum swirl velocity around the vortex centre. In other words, the core shape is described by the directional radius as function of the azimuth angle, that is $R(\theta)$ normalised by the chord. The directional vortex core radius is calculated from the swirl velocity profiles along 36 directions around the vortex centre. In Figures 4.23 and 4.24, the radius values are plotted on a polar plot as function of θ for different Reynolds numbers, plane locations and angles of attack. In the present reference system, the vortex rotates clockwise and the cases reported here are chosen as the conditions where an asymmetric structure of the core is better observed although it resembles the behaviour of all the other cases in the near wake of the present study.

In Figure 4.23, at the closest plane to the trailing edge $x_w = 0.25$, the peak value of $R(\theta)$ is observed around $\theta = 150^\circ$ and it moves to $\theta = 30^\circ$ at $x_w = 0.5$. An anti-clockwise spiral is observed at $x_w = 1$ with a discontinuity at $\theta = 180^\circ$. The discontinuity is due to the switch of the maximum swirl velocity from the inner to the outer of the two peaks discussed previously. At 2 chords from the wing, very early wake phenomena are not observed and a nearly axisymmetric shape of the core is formed. A similar behaviour is observed for the case reported in Figure 4.24. A spiral shape of the core is observed at planes closer than 1 chord from the trailing edge which rotates and

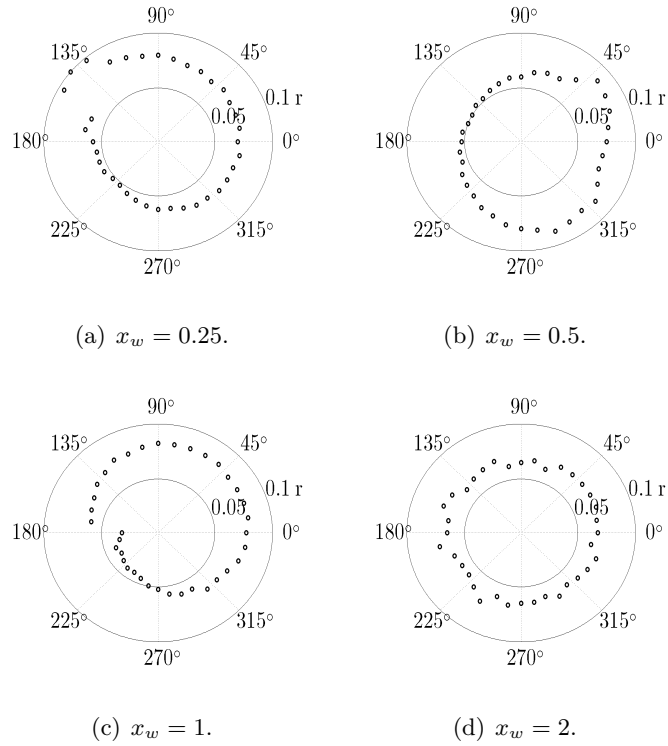


Figure 4.23: Vortex core shape at $Re = 1 \cdot 10^5$ and $\alpha = 12^\circ$.

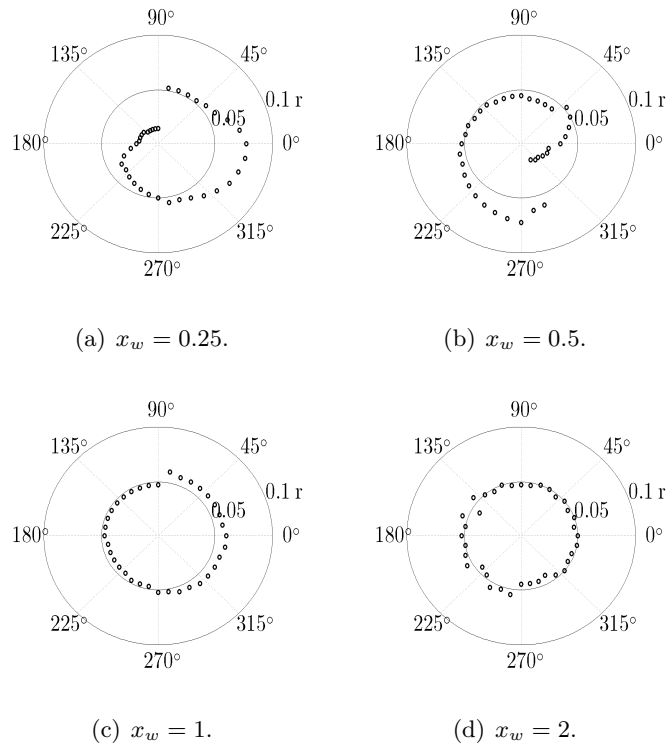


Figure 4.24: Vortex core shape at $Re = 5 \cdot 10^5$ and $\alpha = 8^\circ$.

reaches an almost circular shape at $x_w = 2$.

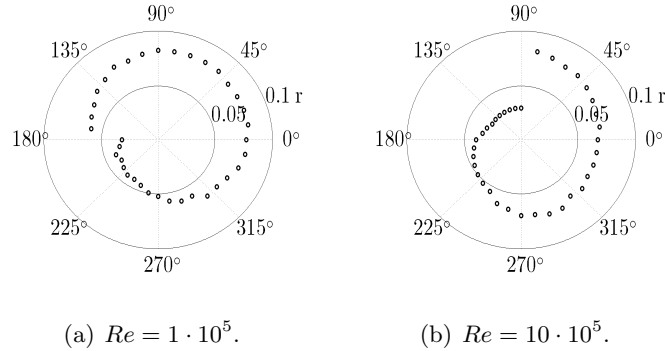


Figure 4.25: Vortex core shape at $\alpha = 12^\circ$ and $x_w = 1$.

In Figure 4.25, the comparison of the vortex core shape for different Reynolds numbers at one chord of distance from the trailing edge and $\alpha = 12^\circ$ is reported. The low Reynolds case exhibits a slightly wider core shape (bigger vortex core) and a smaller jump at the discontinuity (near to axisymmetry) than the high Reynolds number. The phase difference (delay) between the two cases is of 90° .

(b) Vortex core shape fluctuation The vortex core shape, as defined previously, highlights the asymmetry of the vortex structure in the early wake behind the wing where highly unsteady and asymmetric phenomena are observed before the vortex structure develops into an axisymmetric vortex. The fluctuation of the core shape σ_R is expected to be function of the azimuth angle and it is evaluated as the root mean square of the instantaneous directional core radius, normalised by the the average core radius.

In Figure 4.26 the core shape fluctuation is reported on polar plots for the cases presented previously. Comparing Figures 4.26(a) and 4.26(b) respectively with Figures 4.23 and 4.24, it is noted that higher values of core shape fluctuation are found at the position of the discontinuity of the core shape and they are proportional to the jump of $R(\theta)$ across the discontinuity. This high fluctuation is due to the switching of the location of maximum swirl velocity between the inner and the outer peak. The unsteadiness of the core shape can also be expressed as a revolving fluctuation angle that indicates an angular range around which the azimuth angle of the instantaneous discontinuity moves. In Figure 4.26(b), $\sigma_R(\theta)$ for $x_w = 0.25$ and $x_w = 0.5$ shows distinct peaks at the discontinuity of the core shape. The width of the peak increases with the measurement plane moving downstream: a revolving fluctuation angle of 40° is observed for $x_w = 0.25$, an angle of 80° at $x_w = 0.5$ and an oval shape is then observed

at $x_w = 1$. This indicates that for an increase of the downstream position, the revolving fluctuation angle increases and the fluctuation level decreases. In all the cases shown here, the fluctuation of the core shape is higher than 25% of the mean core radius.

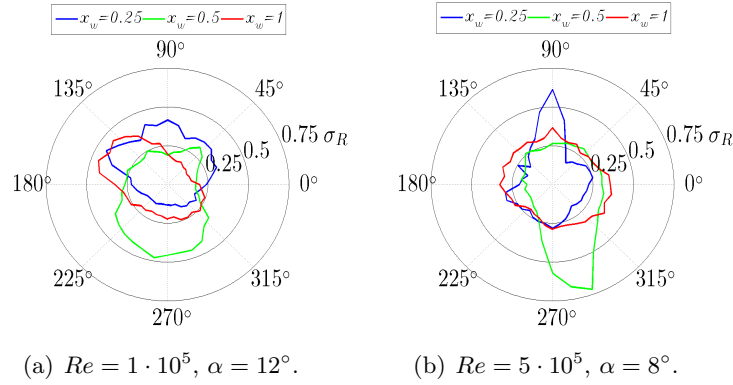
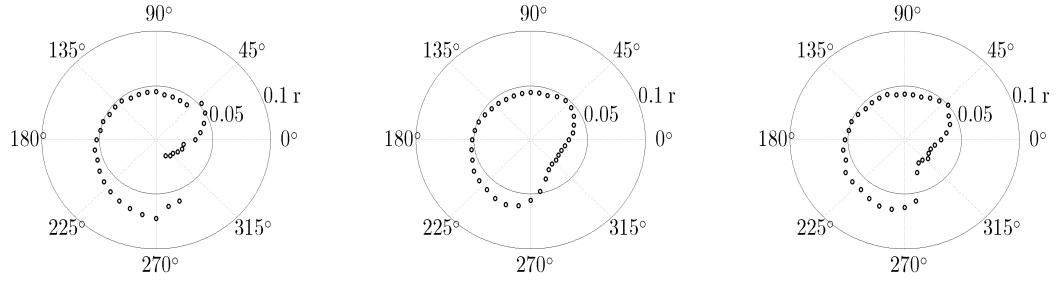


Figure 4.26: Core shape fluctuation.

Ramasamy *et al.* (2009a) studied the distribution of the average core size of a rotor blade tip vortex showing the median of a sample set as a better descriptive measure of the data than the mean value. When the distribution is not symmetric, the median gives the same emphasis to all the measured core sizes, whereas the mean gives a much greater weight to the tail of the distribution. In Figure 4.27, one core shape is reported where the directional core radii are calculated with three different methods: from the average flow field (Figure 4.27(a)); as the average of the 121 instantaneous directional core radii (Figure 4.27(b)); as the median of the instantaneous directional core radii (Figure 4.27(c)). The core shapes, and in particular around the discontinuity, appear different when a different method is applied. The second method masks the discontinuity observed earlier whereas the third method lies in between the other two confirming that the fluctuation of directional core radius does not assume a normal distribution. This suggests also the presence of outliers (very low values of $R(\theta)$ on the low side of the discontinuity and high values on the high side) which results in an overestimation of the discontinuity jump.

(c) Rotation of the core From the polar plots presented earlier, it is possible to retrieve information on the rotation of the vortex core. Because the initial stage is not axisymmetric but reveals a peculiar structure, the rotation of the core can be evaluated by following the bump or discontinuity of the core shape. As a first approximation, the rotation of the core in the wake Θ can be expressed as the product between the rotation rate of the vortex ϕ and the time elapsed from the trailing



(a) Core shape of the average flow field (method adopted in the previous graphs). (b) Average of the instantaneous core shapes. (c) Median of the instantaneous core shapes.

Figure 4.27: Vortex core shape for different averaging methods at $\alpha = 8^\circ$, $x_w = 0.5$ and $Re = 5 \cdot 10^5$.

edge Δt . Therefore, the vortex core rotation observed in the previous figures can be compared with an estimate based on the mean around the core of the maximum swirl velocity $u_{\theta,max}$ (which approximately corresponds to the velocity of the points in the polar plots), of the mean core radius R and the convection in the freestream direction driven by the axial velocity in a region of the order of the core size u_{core} .

$$\Theta = \phi \cdot \Delta t = \left(\frac{u_{\theta,max}}{R} \right) \cdot \left(\frac{\Delta x_w}{u_{core}} \right) \quad (4.18)$$

The mean maximum swirl velocity and the mean core radius are directly taken from the mean swirl velocity profiles. The axial velocity is evaluated from Figure 4.28 where the average axial velocity profile, measured at the different plane positions, is presented as function of the radius. It is observed in this range that the axial velocity profiles do not change remarkably.

In Table 4.1, different terms and the resulting core rotations for the two cases presented in Figures 4.23 and 4.24 are reported:

- the initial and ending plane of the evaluated range expressed in chords from the trailing edge;
- the distance Δx_w covered by the vortex;
- the maximum swirl velocity $u_{\theta,max}$ of the mean profile normalised by the freestream velocity;
- the mean core radius R normalised by the wing chord;
- the mean core angular velocity ϕ ;

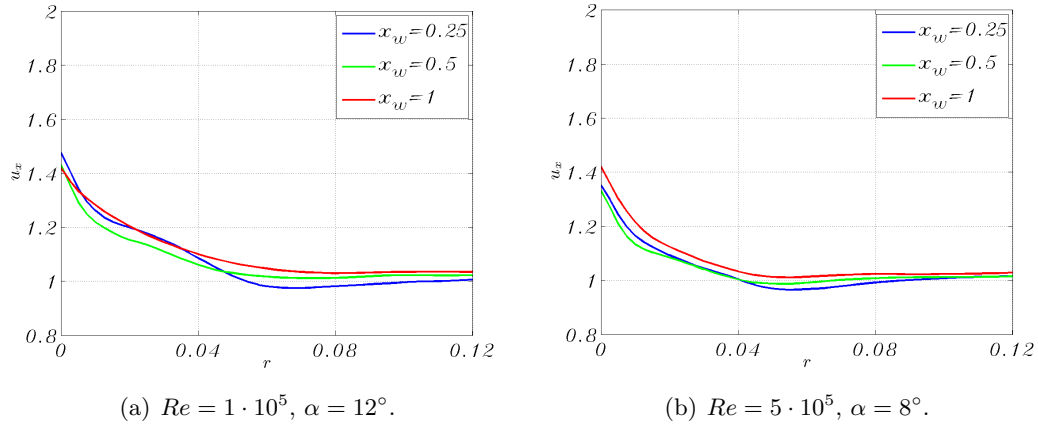


Figure 4.28: Axial velocity profiles.

- the core axial velocity u_{core} evaluated as the mean value in the region $0 < r < \max(R)$ and normalised by the freestream velocity;
- the elapsed time Δt between the two planes of the range;
- the core rotation Θ .

The swirl and axial velocities in the wake are taken as step functions of the downstream distance from the trailing edge, supported by the fact that these values do not change significantly within the range of these experiments. Therefore, the values measured at $x_w = 0.25$ are used as the values representative of the range $0 < x_w < 0.25$, the measures at $x_w = 0.5$ are used for $0.25 < x_w < 0.5$ and the measures at $x_w = 1$ for $0.5 < x_w < 1$.

| <i>range</i> | 0–0.25 | 0.25–0.5 | 0.5–1 |
|-------------------|------------|------------|------------|
| Δx_w | 0.25 | 0.25 | 0.5 |
| $u_{\theta, max}$ | 0.686 | 0.692 | 0.710 |
| R | 0.067 | 0.065 | 0.070 |
| ϕ [rps] | 13.3 | 14.0 | 13.3 |
| u_{core} | 1.16 | 1.20 | 1.29 |
| Δt [ms] | 26 | 25 | 47 |
| Θ [deg] | 125 | 127 | 225 |

Table 4.1: Core rotation estimate: $Re = 1 \cdot 10^5, \alpha = 12^\circ$.

| <i>range</i> | 0–0.25 | 0.25–0.5 | 0.5–1 |
|-------------------|------------|------------|------------|
| Δx_w | 0.25 | 0.25 | 0.5 |
| $u_{\theta, max}$ | 0.489 | 0.498 | 0.500 |
| R | 0.052 | 0.052 | 0.052 |
| ϕ [rps] | 61.1 | 62.2 | 62.4 |
| u_{core} | 1.04 | 1.05 | 1.10 |
| Δt [ms] | 6 | 6 | 11 |
| Θ [deg] | 128 | 130 | 249 |

Table 4.2: Core rotation estimate: $Re = 5 \cdot 10^5, \alpha = 8^\circ$.

Although Equation (4.18) comes from rough and preliminary considerations and treats the core spiral structure as solid rotation, the computed results are well related with the polar plots.

Looking at the polar plots of Figure 4.23, a peak in the core radius is observed around an angle of 150° at $x_w = 0.25$ and it is also observed around an angle of 40° at

$x_w = 0.5$. The vortex rotates clockwise therefore a rotation of around 110° is observed where on Table 4.1 a rotation of 127° is calculated. A similar structure is also observed at $x_w = 1$ with a relative rotation of about 210° and a calculated one of 225° . At 2 chords, as observed earlier, there is no memory of the vortex rolling up phase and to visually follow the rotation of the core by its shape is not possible.

Regarding Figure 4.24, a clockwise rotation of the spiral structure is observed in the polar plots between $x_w = 0.25$ and $x_w = 0.5$ of about 150° where the calculation leads to 130° . From 0.5 to 1 chords in the wake of the wing, a core rotation of about 210° is observed while a rotation of 249° is calculated.

A good agreement is found between the observations in the polar plots and the results from Equation (4.18). A link between the travel of the vortex in the wake and its rotation is also found, showing that with less than 3 full rotations of the core an axisymmetric vortex is achieved. Similar rotations are found for the two cases of Tables 4.1 and 4.2; this implies that the effects of the increase of Reynolds number of a factor of 5 compensate the effects of the decrease of the angle of attack from 12° to 8° . In fact, a factor of about 4.4 is observed in the angular velocities ϕ and in the elapsed times Δt .

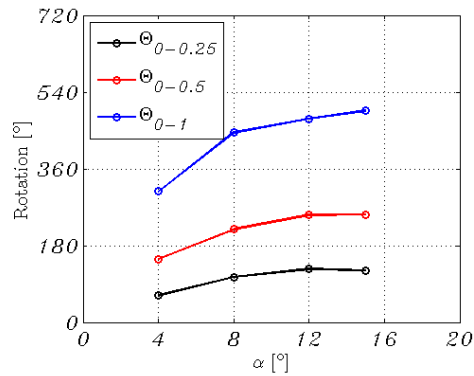


Figure 4.29: Core rotation estimation as function of the angle of attack at $Re = 1 \cdot 10^5$.

In Figure 4.29, the vortex rotation in the range between the trailing edge and 1 chord downstream is evaluated as a function of the angle of attack for different tests. Increasing the angle of attack, the lift on the wing increases and so increases the pressure difference between the lower and the upper surface of the wing resulting in a higher driving force for the tip crossing flow although not following a linear relation. An increase of the angle leads to an increase in the core rotation which corresponds also to an increase in the angular velocity.

(d) Vortex core shape for different tip geometries Since the tip geometry is one of the main influences on the vortex structure in the early wake, a comparison of the vortex core shape behind the squared and rounded tips mounted on the wing **M2** is presented in Figure 4.30. The core shape behind the wing **M1** is also reported for a similar condition. The same freestream, angle of attack and wing model generate a very different vortex when a different tip is mounted. This reinforces the reason of the efforts in the studies on wingtips: even small changes in the geometry are able to generate trailing vortices with very different properties.

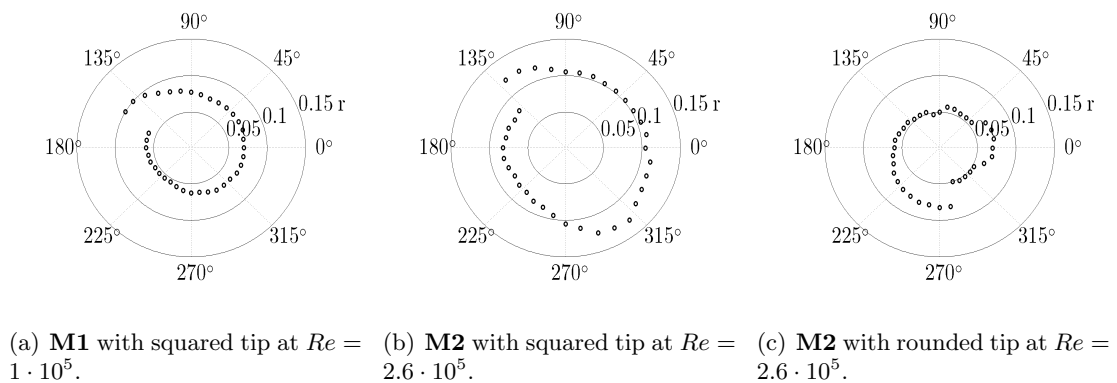


Figure 4.30: Vortex core shape for different tip geometries at $x_w = 0.25$ and $\alpha = 12^\circ$.

Comparing firstly Figure 4.30(a) with Figure 4.30(b) for similar Reynolds number, same tip geometry but different wing chord and aspect ratio, it is observed that **M2** (bigger wing chord) generates a bigger vortex when scaled by the chord but only a small relative rotation of about 20° is observed between the two Figures. This indicates that the vortex dimension is dependent also to the wingspan which dictates the total lift and overall circulation of the wing.

Comparing the same condition and wing but with different tip geometry (Figures 4.30(b) and 4.30(c)), a much bigger core is observed for the squared tip which forces the separation of the crossing boundary layer at an earlier stage compared to the rounded tip and a different position of the discontinuity in the shape is also observed. Since the rounded tip generates a vortex with higher maximum swirl velocity and higher axial velocity within the core (which will be discussed later), the rotation of the rounded tip is higher than of the squared tip. Applying Equation (4.18) on these cases in the range 0–0.25, a core rotation of 97° is calculated for the squared tip. In the same range, the rounded tip case generates a core rotation of 195° . Different position of the discontinuities at $x_w = 0$ are therefore estimated and they are sketched in Figure 4.31

(with the current reference system, the wing is horizontal).

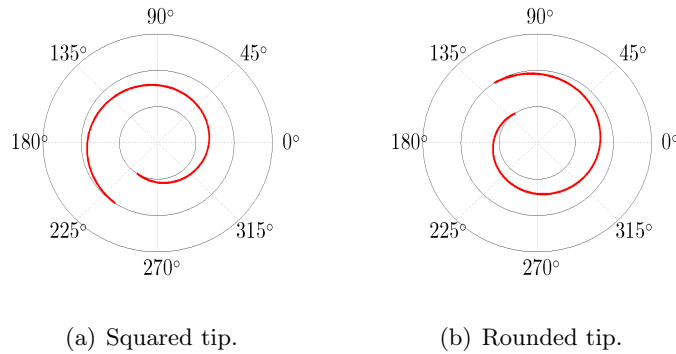


Figure 4.31: *Estimation of the vortex core structure at the trailing edge.*

This result confirms the different structure of the vortex during the formation on the wing when the tip geometry is changed and in particular the different position of the maximum swirl velocity. Topological differences during the formation on squared and rounded wingtips were observed also in the smoke visualizations of Section 3.3 and suggested by the characteristic lines in Section 3.4.

SECTION 3

Axial flow

The axial flow in the core of a wingtip vortex has been intensively studied throughout the years and has been shown to either be directed towards the wing (wake-like or deficit, as behind a non-lifting drag-producing body) or away from the wing (jet-like or excess). Although a number of analytical and experimental studies have presented different models and tools to predict the axial flow, a unique solution is not present to date. Moreover, like all the other vortex properties, the axial flow of a trailing vortex in the near wake is influenced by several concurrent factors and presents a complex structure.

The fact that experiments show either an excess or a deficit in the axial velocity was explained by Spalart (1998) as the result of the acceleration of the flow described by inviscid theory and the total pressure losses by viscosity of the boundary layer fluid layered around the vortex. The axial velocity excess at the vortex centre can be introduced in two mathematically equivalent ways: from considerations of the helical shape of vortex lines and from equating the pressure from different points of the vortex. Both

the approaches leads to the following equation:

$$\frac{d(u_x^2 + u_\theta^2)}{dr} + 2\frac{u_\theta^2}{r} = 0 \quad (4.19)$$

Since the circulation profile can be expressed as $\Gamma(r) = 2\pi r u_\theta$, substituting u_θ in Equation (4.19) with $\frac{\Gamma(r)}{2\pi r}$, the resulting equation is:

$$2\pi^2 r^2 \frac{d u_x^2}{dr} + \frac{d\Gamma(r)^2}{dr} = 0 \quad (4.20)$$

Because it is generally observed that Γ increases with r , it is clear that u_x increases as the vortex axis is approached (jet-like flow). In a real flow, the fluid around the vortex core is layered with the boundary layer fluid and the wake sheet which introduces strong shear layers and viscous losses that contribute to the deceleration of the flow. Spalart (1998) introduces then a circulation parameter which indicates the balance between viscous effects and inviscid acceleration of the axial flow for each experiment. Large values of the circulation parameter result in an excess and low values in a deficit of axial velocity.

Bailey *et al.* (2006) stated that in the initial stages of the vortex formation, the pressure in the vortex core gradually decreases along the vortex axis generating a favourable axial pressure gradient that accelerates the core fluid in the streamwise direction, possibly resulting in a jet-like core having an axial velocity surplus (Devenport *et al.*, 1996). Farther downstream, viscous actions decelerate the flow, tending to convert the core to wake-like. It was also observed that the axial velocity gradient introduces a possible mechanism of turbulence production in the core (Singh & Uberoi, 1976; Chow *et al.*, 1997a).

Although the excess or deficit of the axial velocity can be small in comparison to the swirl velocity, its presence dictates to a large extent the stability and decay of the vortex. Based upon previous theoretical, experimental and computational studies, Spall *et al.* (1987) and Mudkavi (1993) proposed a criterion for the onset of the vortex breakdown which is based on a swirl parameter. Such swirl parameter is evaluated from the axial velocity, the vortex core radius and the rotation rate. Billant *et al.* (1998) defined a swirl parameter as the ratio between the maximum swirl velocity and the axial velocity in the centre of the vortex measured at an initial plane. Different magnitudes of excess of the axial velocity were applied on a rotating fluid and the onset and structure of the breakdown of the vortex was observed for those different values of the swirl parameter.

They observed an earlier breakdown for higher values of the swirl parameter, which is for weaker axial velocity excess. Hallett & Toews (1987) also deduced that a flow exhibiting axial velocity profiles with a maximum on the axis requires a higher swirl to produce vortex breakdown, that is a higher positive pressure gradient.

To date, there is still no established method which can reliably predict the magnitude or even the direction of this axial velocity perturbation for a given wingtip geometry and flow condition. Furthermore, the physical mechanism of the formation of axial flow is still poorly understood. Batchelor (1964) proposed an analytical description of the axial flow inside an idealized vortex and the following result was derived²:

$$u_0^2 = U_\infty^2 + \int_r^\infty \frac{1}{4\pi^2 r^2} \frac{\partial \Gamma(r)^2}{\partial r} dr - 2\Delta H \quad (4.21)$$

with u_0 the axial velocity in the vortex centre, U_∞ the freestream velocity, r the radial cylindrical coordinate, $\Gamma(r)$ the circulation profile across the vortex and ΔH an arbitrary function added to account for the dissipation along a streamline passing through a viscous region of the flow (for example, the boundary layer shed from the wing trailing edge and rolling around the tip vortex). This result was obtained from steady axisymmetric cylindrical incompressible Navier–Stokes equations with the assumption of small axial gradients compared with the radial gradients and small radial velocity compared to axial and swirl velocity (boundary layer type approximation). With assumptions of a constant dissipation term and vortex radius, Equation (4.21) shows an increase of axial velocity with an increase of overall circulation and a velocity excess in inviscid fluids where $\Delta H = 0$. The presence of viscous losses competes with the inviscid acceleration mechanism. As a result, in cases of large Reynolds numbers and high angles of attack, the inviscid mechanism is prevailing and an axial velocity excess is expected. Under moderate angles of attack and low Reynolds numbers, the viscous losses are dominant and axial velocity deficits are expected.

Equation (4.21) relates the radial distribution of the circulation with the axial flow. However, the relation between the streamwise evolution of the vortex and the axial flow can be also quite relevant. The redistribution of the vorticity due to the development of the vortex towards axisymmetry and the increasing of circulation due to the initial rolling up of fluid are strongly related to the axial velocity by the mechanism called vortex stretching (for the mathematical background of the vortex stretching and considerations on the vorticity equation see Appendix C.2). As a result, a positive axial

²Equation (4.20) by Spalart (1998) can be also seen as the radial differentiation of Equation (4.21) by Batchelor (1964) when the losses term ΔH is ignored.

gradient of the circulation will contribute to the acceleration of the axial flow. However, in the axial range of the present investigation, a remarkable effect of the vortex stretching was not observed.

Del Pino *et al.* (2011) compared analytical and experimental results of the axial flow in the range $x_w = 0.5\text{--}16$. The authors found a good agreement between experiments and the model presented by Moore & Saffman (1973) who arrived at a more complex equation for the axial flow in laminar trailing vortices taking also into account the boundary layer shed by the wing and entrained in the core. In addition to the above laminar flow studies, significant models on the development of turbulent vortices where the axial flow is expressly addressed were presented by Govindaraju & Saffman (1971), Saffman (1973) and Saffman (1974).

As also observed in the previous sections, the wingtip vortex in the very early wake presents a complex structure. The axial velocity, consequently, is expected to reveal a similarly complex structure and development. Moreover, the experimental technique affects the description of the vortex with its measurement resolution, intrusivity and format of the data for further processing. Recent studies (Anderson & Lawton, 2003; Lee & Pereira, 2010) compared the wide range of results in the literature and performed parametric experiments on the axial velocity in the vortex core. Anderson & Lawton (2003) showed a linear trend between the axial velocity peak and the vortex circulation strength and they suggested the presence of a maximum deficit limit for trailing vortices. Lee & Pereira (2010) observed that the axial velocity and vorticity at the vortex centre increase along the tip reaching their maxima in the vicinity of the trailing edge. During the formation, they also observed a region of jet-like fluid at the vortex centre regardless of the tip condition and the angle of attack. In the wake of a wing at small incidence, this region was entrained by the shear layer and the wing wake resulting in a wake-like axial flow as it progressed downstream of the wing trailing edge.

(a) Shape of the axial flow Based on considerations on smoke visualizations of the vortex over the wing, Equation (3.2) states that the vortex formed over a wing at a high angle of attack produces an axial flow that is considerably higher than the vortex for a low angle of attack. In Figure 4.32, instantaneous and simple averaged axial velocity fields are presented for the **M1** wing at 4° and 12° for two exemplifying cases. In the instantaneous flow for the wing at high angle of attack (Figure 4.32(b)), a region of flow at higher velocity than the freestream is observed in the vortex core with a peak of around $1.6U_\infty$. The simple averaged velocity

field reveals a profile which is smoother and more diffuse as effect of the meandering and the unsteadiness of the vortex (peak of around $1.3U_\infty$). At a lower incidence, the instantaneous velocity field in Figure 4.32(a) shows a region of the order of the vortex core with deficit of axial velocity which contains smaller regions of negative and positive axial velocity perturbations. The averaged field (Figure 4.32(c)) reveals a region of axial velocity deficit which has a circular shape.

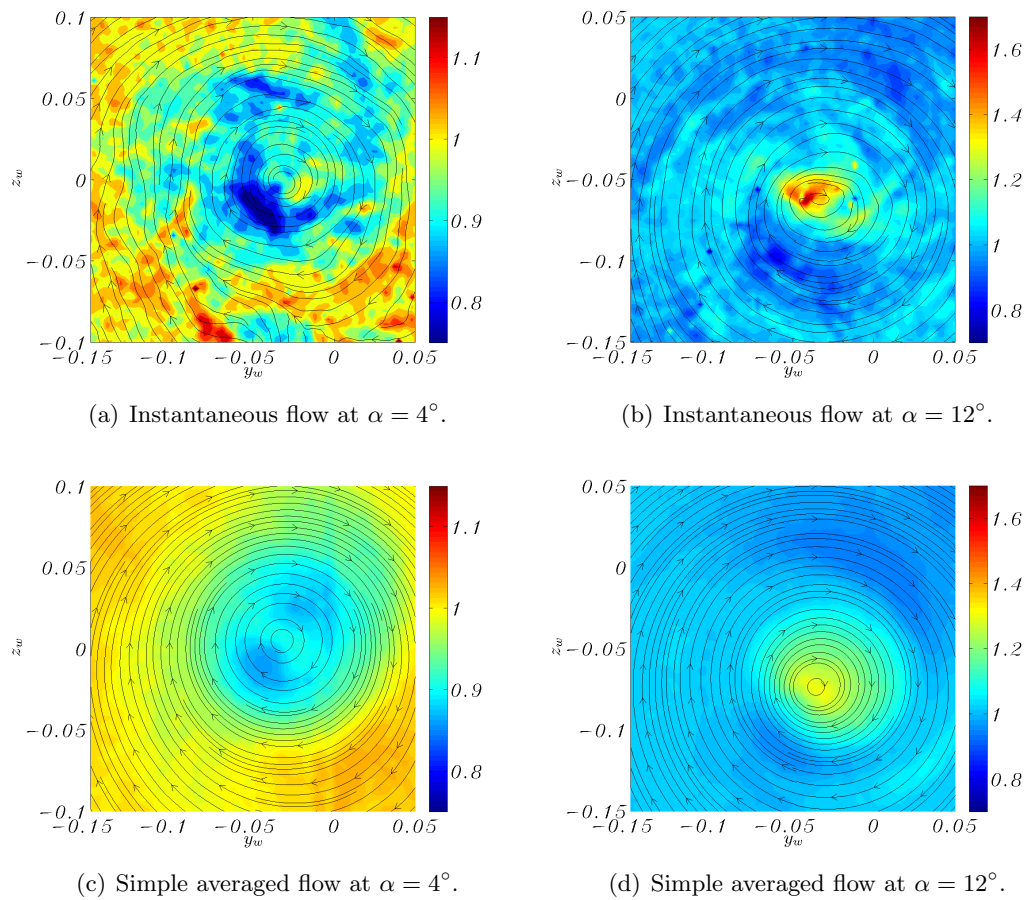
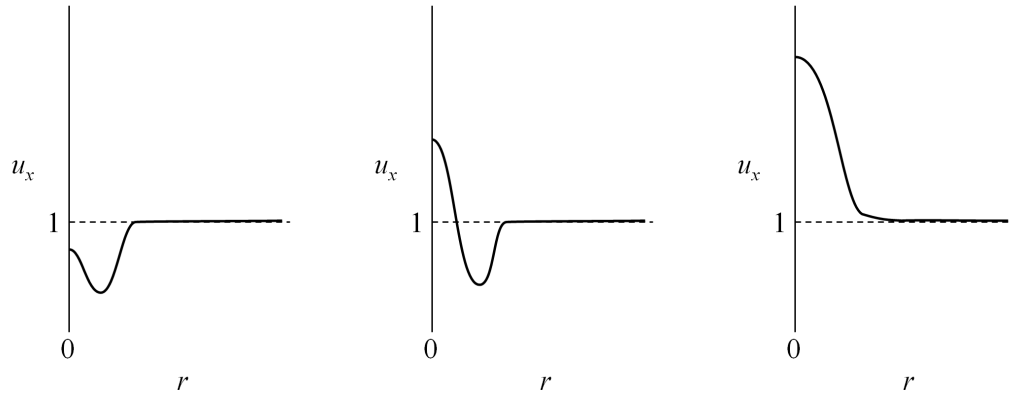


Figure 4.32: Axial velocity contours and planar streamlines at $x_w = 1$ and $Re = 1 \cdot 10^5$ (*M1* model).

At low angles of attack, hence lower circulation and vortex strength, the inviscid acceleration of the flow on the vortex axis is counterbalanced by the deceleration of the viscous effects. The mixing of the fluid in the vortex core with the “slow” fluid from the boundary layer and the wake sheet is more intense and generates a more complex region. For this reason, at low angles of attack, the identification of axial velocity perturbation peaks (either as excess of deficit with respect to the freestream velocity) is critical. This leads the centering methods based on the solely axial velocity to a poor robustness

and questionable results, being strongly dependent on the searching technique and peak definition.



(a) Low angle of attack. (b) Moderate angle of attack. (c) High angle of attack.

Figure 4.33: Schematic of generic profiles of the axial velocity across the vortex in the early wake for different angles of attack.

In Figure 4.33, illustrative axial velocity profiles across the vortex are sketched for a low, a moderate and a high angle of attack. Based on the previous observations, it is believed that the axial velocity at the centre of an early vortex is affected by the inviscid acceleration mechanisms and it always appears as an excess compared to the flow in the vortex core which might be, in some instances, lower than the freestream (Figure 4.33(a)). This last scenario is related to weak vortices interacting with large shear layers (i.e. low wing circulation, thick boundary layer, large regions of separated flow). For moderate angles (Figure 4.33(b)), the deficit around the centre is of the same order of the excess at the centre. This scenario highlights the importance of high resolution measurements in the vortex core to be able to describe the evolution of the vortex in the early wake. At high angles of attack (Figure 4.33(c)), the axial velocity peak (jet-like) is well defined and more intense. As the vortex progresses downstream and axisymmetry by diffusion is reached, the axial velocity will tend to a bell-shaped profile which may be observed either later in the wake or just downstream the trailing edge or already during the formation of the vortex on the wing depending on the situation.

In Figure 4.34, the helicity based average method is applied on the cases of Figure 4.32. For the high incidence case, the velocity excess region appears more intense than for the simple averaged velocity field and it shows a peak of about $1.4U_\infty$. The low angle of attack case reveals a small jet-like region of peak intensity equal to the freestream

velocity at the centre of the vortex surrounded by a rounded patch of wake-like flow.

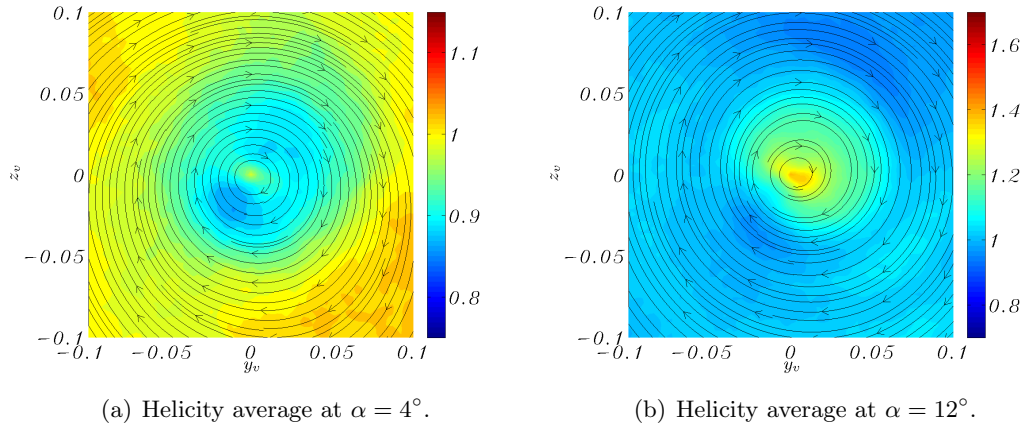


Figure 4.34: Average axial velocity contours and planar streamlines at $x_w = 1$ and $Re = 1 \cdot 10^5$ (**M1** model).

Following the inviscid mechanism presented by Spalart (1998), jet-like flow is induced by the helical shape of the vortex lines. Hence, a second axial velocity peak can be expected in the case of a secondary vortex of strength comparable to the primary vortex and when viscous effects are low. In Figure 4.35, the evolution in the wake of axial velocity, vorticity and planar streamlines are reported for the **M1** wing with squared tip at $\alpha = 15^\circ$. The helicity based centering method is applied although the same behaviour was observed also from simple averaged velocity fields.

The high angle of attack produces a strong secondary vortex which induces a secondary axial velocity peak. The two axial velocity peaks, clearly distinguishable inside the vortex core at $x_w = 0.25$, are merged into a unique peak at $x_w = 0.5$ which quickly loses strength downstream: from a maximum of about $1.7U_\infty$ at $x_w = 0.25$ to $1.5U_\infty$ at $x_w = 1$. The deficit of axial velocity, which characterizes the wake sheet, surrounds the vortex core and dissipates moving downstream of the wing. The axial velocity peak, the centre of the streamlines and the vorticity peak appear at different locations because of the distortion of the flowfield due to the interaction between primary vortex, secondary vortices and wake sheet.

The vorticity in the core at $x_w = 0.25$ reveals a region of positive vorticity (anti-clockwise rotation) on the right side of the primary vortex, which is identified by the negative vorticity peak inducing the overall clockwise rotation of the fluid. This region is attributed to the secondary vortex generating the secondary axial velocity peak. At the centre of the vortex the vorticity, like as the axial velocity peak, decreases in strength moving downstream and the counter rotating secondary vortex merges with the primary

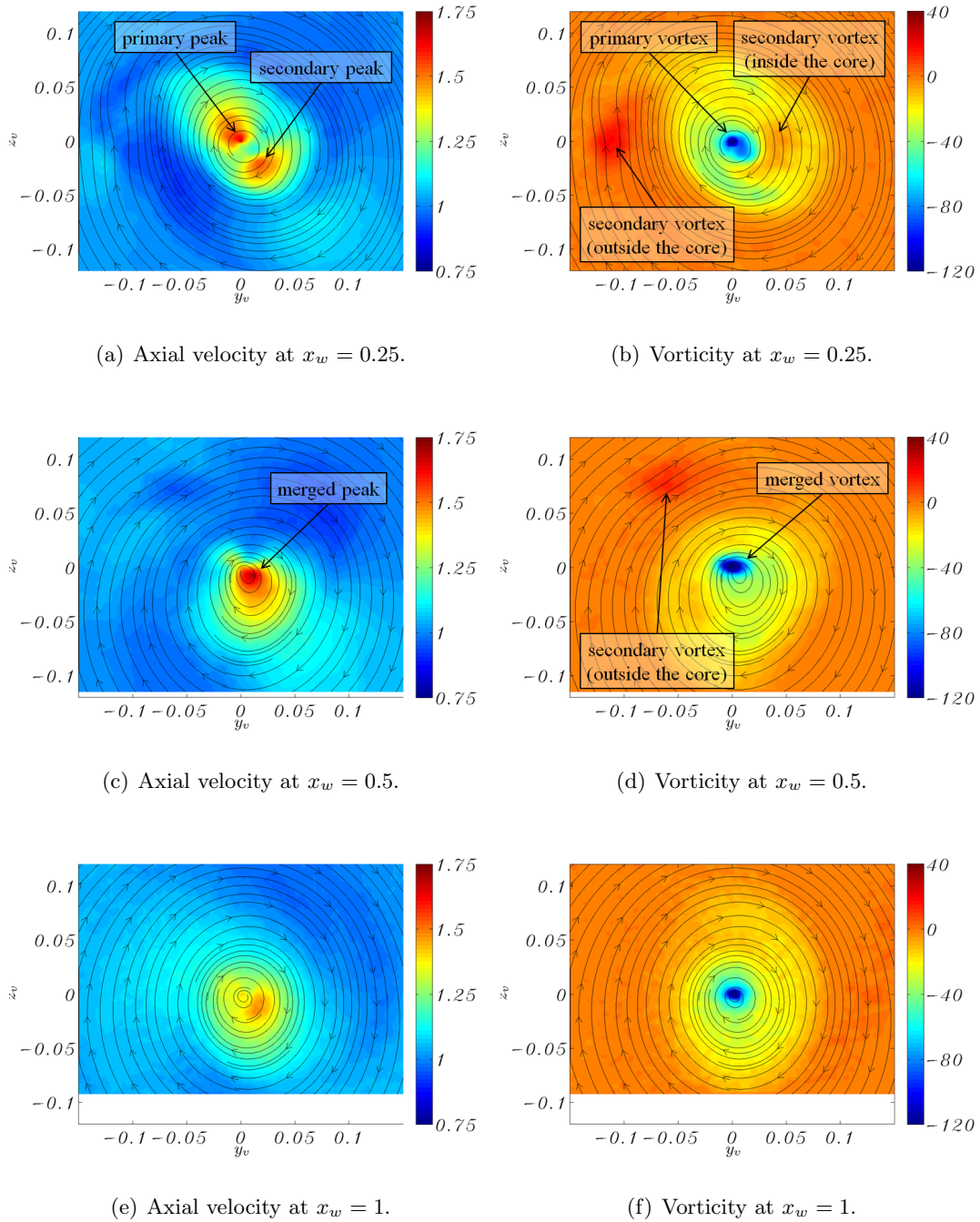


Figure 4.35: Axial velocity, vorticity and planar streamlines at $\alpha = 15^\circ$ and $Re = 5 \cdot 10^5$ (*M1* model).

vortex and it is not visible at $x_w = 1$. Another region of positive vorticity is observed outside the vortex core on the left side of the primary vortex at $x_w = 0.25$ which rotates around the centre of the vortex and is not characterized by a notable axial velocity perturbation. Since the secondary vortices are expected to oscillate with respect to the

primary vortex, and being the centering based on the primary vortex movement only, the secondary vortices on these contours are expected to appear wider and less intense (smearing effect) than the instantaneous realizations.

The development of the vortex toward an axisymmetric structure is indicated by the plane streamlines which appear more circular moving downstream. In general, the peak of the axial velocity rapidly decreases especially when the mixing of the fluid within the core is intense, that is when several secondary vortices interact with the primary vortex. The vorticity shape also changes drastically within a few chords from the trailing edge. The characteristics of the axisymmetric vortex observed in the mid wake (such as axial velocity peak, vortex core radius, maximum swirl velocity) are therefore strongly influenced by the vortex system dynamics during the formation on the wing and the rolling up in the very early wake.

(b) Axial velocity at the centre of the vortex Recent parametric studies on the axial velocity in the centre of the vortex have allowed a deeper understanding of the vortex axial flow although the mechanisms responsible for the wake-like and jet-like axial flows are not fully understood.

Anderson & Lawton (2003) tested a low aspect ratio wing ($AR = 0.8$) with squared and rounded tip at several downstream distances, Reynolds numbers and angles of attack. They found a linear relationship between the scaled vortex circulation $\frac{\Gamma}{U_\infty b}$ and the angle of attack. Because the circulation of a single trailing vortex is equal to the circulation of the bound vortex at the wing root, the vortex circulation will increase in direct proportion to the lift produced, that is to the angle of attack. Consequently, the axial velocity at the centre of the vortex also appeared proportional to the angle of attack with a higher gradient for the rounded tip, and greater peaks were generated by the rounded tip than the peaks generated by the squared tip. The effects of Reynolds number and downstream distance in the range studied were small compared to the angle of attack and tip geometry effects.

Lee & Pereira (2010) studied the vortex generated by squared and rounded tips on a rectangular wing with $AR = 1.8$ during its formation on the wing and to a maximum distance from the trailing edge of $x_w = 4$. They found similar vortex circulation values for both the tip geometries although they observed a different circulation distribution within the core. The vortex generated by a rounded tip appeared more concentrated (smaller core radius) and more intense (higher vorticity and axial velocity peaks) than the squared tip case. The effect of the tip shape was to change the interaction intensity

between the vortex with the wake and secondary vortices. The axial velocity peak at the trailing edge was similar for the two wingtips but the decrease with x_w was quicker for a squared tip than for a rounded tip. They also found a critical angle of attack of 7° below which the axial flow eventually became wake-like.

Lastly, Chow *et al.* (1997a) meticulously performed several measurements in the near wake of a low aspect ratio wing with rounded tip at a Reynolds number equal to $4.6 \cdot 10^6$ where a jet-like axial velocity was observed with a peak of $1.77U_\infty$.

In Figure 4.36, the axial velocity at the centre of the vortex as a function of the circulation of all the SPIV experiments in the wake of the two wing models is presented (test matrix in Table 2.3). The circulation is scaled by the freestream velocity and the chord which is equivalent to the circulation parameter used by Anderson & Lawton (2003) multiplied by the aspect ratio of the wing. The circulation profile is calculated as the integration of the average swirl velocity profile and the vortex circulation is identified as the maximum value of such profile. In the range of distance from the trailing edge presented here, the axial velocity at the vortex centre did not decrease substantially as observed also by Chow *et al.* (1997b). In general, the axial velocity peak increases with the intensity of the vortex, measured by the circulation, which is directly related to the angle of attack of the wing (Anderson & Lawton, 2003; Lee & Pereira, 2010). The vortex circulation, which is concentrated in a region of the order of the vortex core, is a distinctive and comparable property of vortices and it does not change with the position downstream of the wing although it is influenced by the tip geometry (further details on the effects of the tip geometry will be given in Section 4.5).

The two linear trendlines, sketched in Figure 4.36 and referring to the two tip geometries, show that the rounded wingtip generates a higher axial velocity in the vortex core. A minimum axial flow deficit limit in the wing wake was suggested by Anderson & Lawton (2003) based on the trend of their experimental results. In the current study, although a minimum limit can not be clearly identified, it may occur at around $u_0 = 0.7$ and it is believed to be related to the viscous deceleration effect of the boundary layer flow developing along the wing surface and interacting with the vortex.

The results from this study are grouped in several clusters in order to make insightful observations. Four groups corresponding to the four angles of attack tested on the wing **M1** lie on the squared tip trendline where an increase in both circulation and axial velocity peak correspond to an increase of the incidence. Within each of these groups, an increase of the Reynolds number coincides with an increase of the peak. However, as discussed by Chow *et al.* (1997a) who empirically fitted several experimental data

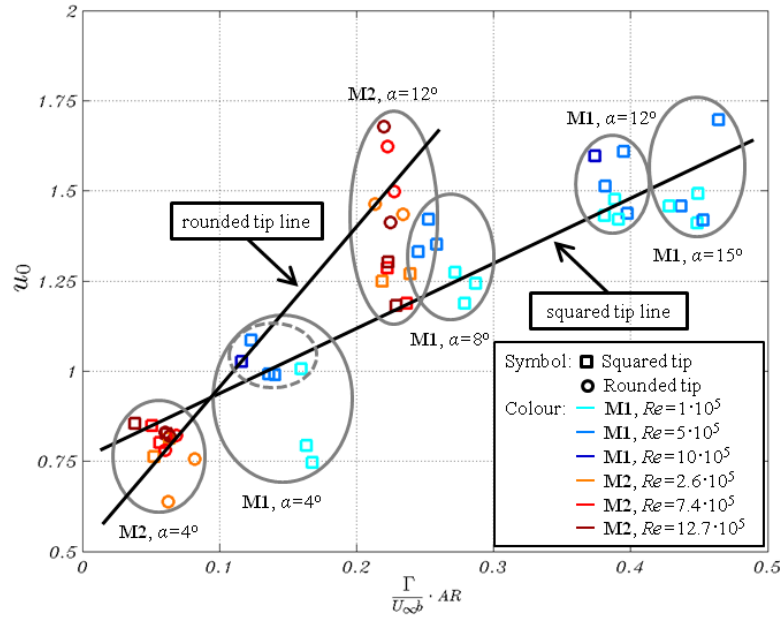


Figure 4.36: Axial velocity at the centre of the vortex as function of the circulation parameter.

with a parametric curve, the influence of the Reynolds number to the axial velocity is negligible compared with the influence of the angle of attack.

Two other clusters refer to the two angles of attack tested on the model **M2**. At the same angle of attack, the low aspect ratio wing **M2** generates remarkably lower dimensionless circulation than the high aspect ratio wing **M1** mainly because of the very different aspect ratio. In particular, wing **M2** at $\alpha = 12^\circ$ generates a dimensionless circulation equivalent to **M1** wing at 7° and the circulation generated at 4° by **M2** is equivalent to **M1** at an incidence of about 2° .

The axial velocity peaks for **M2** with squared tip correlate very well with the results for **M1** which mounts the same tip geometry (see cluster of **M2** at $\alpha = 12^\circ$). It is believed therefore that the effect of the different aerofoil shape (i.e. NACA 0012 and 0015) is not relevant in the current investigation.

For same dimensionless circulation, higher peaks are observed in the rounded tip cases than for the squared tip cases particularly for $\alpha = 12^\circ$ which suggests the presence of different trendlines for different wingtip geometries. The switchover angle between jet-like and wake-like behaviour of the axial flow is estimated to be around 4° for the squared tip and around 7° for the rounded tip. It is important to note that the vortex circulation is not the only parameter that dictates the intensity of the axial flow but the formation process is equally important.

As observed also by Lee & Pereira (2010), the tip geometry greatly influences the strength of the axial flow but it is not itself the cause of the jet-like or wake-like flow. The tip vortex interaction with the wing and the surrounding flow structures ultimately determines the wake-like or jet-like nature of the axial flow and the downstream location when the trailing vortex is fully formed. Birch *et al.* (2004) compared a NACA 0015 aerofoil with a cambered aerofoil showing a linear increase of the vortex circulation with the angle of attack. However, the increase of the axial velocity centre value was linear only for the symmetric profile; the cambered aerofoil generated an axial velocity peak which was almost constant in the range of angles of attack between 6° and 13° . This attests that the axial velocity peak is strongly affected by the interaction between flow and wing, that is by the tip geometry and aerofoil shape, more than by the vortex strength and lift of the wing. Different slopes of the trendlines for different tip geometries are therefore expected.

It is important to remind also that, for low angles of attack, the axial flow may appear as a jet-like flow at the centre of the vortex superimposed on a region of wake-like flow with size of the order of the vortex core. This is the case for the sub-cluster of the **M1** wing at 4° where axial velocity centre values around 1 are measured and the axial flow shape appear as sketched in Figure 4.33(a). This sub-cluster highlights also another important phenomenon in the development of the axial flow in the range $x_w = 0.25-1$. In particular for the Reynolds number of $1 \cdot 10^5$, the two centre values at $x_w = 0.5$ and $x_w = 1$ appear considerably lower than the centre value at $x_w = 0.25$. At the earliest stage, the axial flow appears as a small excess superimposed to a strong deficit (as in Figure 4.33(a)), while at a later plane the axial flow has reached a bell-shaped profile with a centre value of $0.75U_\infty$. The axial flows of the **M2** model at $\alpha = 4^\circ$ are all observed as a wake-like flow with bell-shaped profile. This suggests that as the vortex is less intense (lower circulation and axial velocity peak), it is also less persistent and the distance required to reach a mature phase (i.e. axisymmetric bell-shaped profile) is shorter than a stronger vortex.

In Figure 4.37, the trendlines found in the present study are compared with similar experimental data obtained in recent years and summarized in Table 4.3. All these experiments are based on rectangular wings with symmetric NACA profiles and squared or rounded wingtips. The measurements are taken in the near wake at Reynolds numbers within the range $2.01 \cdot 10^5-4.6 \cdot 10^6$. These data, and especially the gradients of the experimental results, well correlate with the trendlines of both the geometries found in this study. Particularly remarkable is the agreement of the study by Lee & Pereira

| Authors | c [m] | b [m] | AR | Aerofoil | Wingtip |
|--------------------------------|---------|---------|------|-----------|-----------------|
| Lee & Pereira (2010) | 0.28 | 0.508 | 1.81 | NACA 0015 | rounded |
| Birch <i>et al.</i> (2004) | 0.254 | 0.379 | 0.67 | NACA 0015 | squared |
| Anderson & Lawton (2003) | 0.762 | 0.610 | 0.8 | NACA 0015 | rounded&squared |
| Chow <i>et al.</i> (1997b) | 1.22 | 0.91 | 0.75 | NACA 0012 | rounded |
| Devenport <i>et al.</i> (1996) | 0.203 | 0.879 | 4.33 | NACA 0012 | squared |
| Present data | 0.42 | 1.3 | 3.1 | NACA 0015 | squared |
| | 0.76 | 0.57 | 0.75 | NACA 0012 | rounded&squared |

Table 4.3: Wing models characteristics and experiments of references in Figure 4.37.

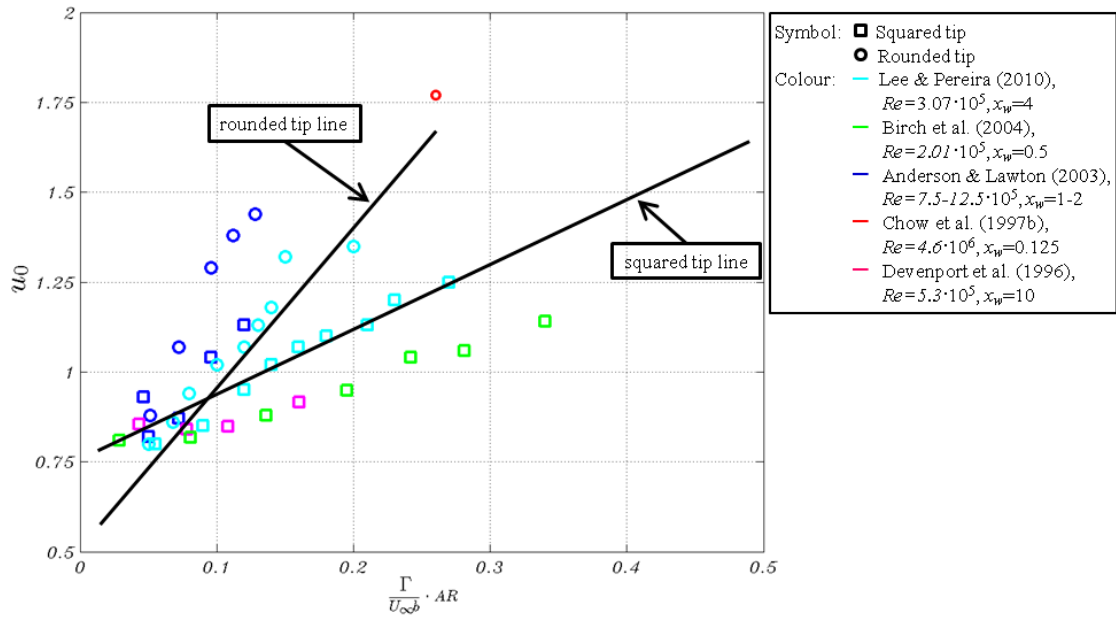


Figure 4.37: Trendlines of the present work compared with other experimental data.

(2010) with gradients and intercepts of both the trendlines. The experiment presented by Chow *et al.* (1997b) shows the maximum average axial velocity at the centre of the vortex which can be explained by the uniquely high Reynolds number and the measurement plane very close to the trailing edge. A minimum deficit limit of $u_0 = 0.75$ is suggested also by observing this collection of results and it is related to a trailing vortex with a dimensionless circulation value very low, corresponding to low angles of attack and intense interaction of shear layers with the vortex. The maximum dimensionless circulation of the present experiments (for **M1** at $\alpha = 15^\circ$) is 25% higher than the maximum of the experiments reported in Figure 4.37. This wider extension of the data was made possible by the big size of the Argyll wind tunnel which gave room for the **M1** wing model. This model has a bigger span than that tested on previous similar experiments on trailing vortices (see Table 4.3) which attests to the uniqueness of this

work.

The dispersion of the data shown in Figures 4.36 and 4.37 around the trendlines indicates once more the complexity of this phenomenon. The acceleration of the flow at the centre of trailing vortices is the result of the balance of several features including interaction between fluid and wing, induced velocity by secondary vortices, rolling up of shear layers and turbulence within the vortex core. Particularly important in this process is the shape and evolution of the turbulence in the core which is presented in the next section.

SECTION 4

Turbulence in the vortex core

Despite the high Reynolds numbers typically encountered in flight conditions (of the order of 10^7), vortices in the far wake grow with a rate typical of laminar flows. This explains the persistence and strength of airplane trailing vortices in the far field. The dissipation rate follows one of a laminar flow which is much slower and less dissipative than the turbulent flow (Cotel & Breidenthal, 2002). The strong rotation within the core can strongly inhibit turbulent transport of fluid leading to a stratified flow (Cotel & Breidenthal, 1999). Airplane trailing vortices, and in particular vortex cores, are examples of relaminarization of the flow induced by rotation in which the contribution of the turbulent fluctuation to the mean flow dynamics becomes negligible and a laminar flow is eventually found (Narasimha & Sreenivasan, 1979).

However, as described in Chapter 3, the physics of the wingtip vortex flow is extremely complex in the near field region as the process is largely turbulent, highly three-dimensional and involves multiple cross flow separations. Streamwise vorticity, mainly in the form of a feeding sheet, is seen to separate from the wing surface and roll up into the tip vortex along with a variety of minor structures. Downstream of the trailing edge, these structures eventually evolve into the axisymmetric and coherent tip vortex. Experimental studies on wing tip vortices (Chow *et al.*, 1997b) have reported a reducing turbulence level in the vortical core in the near field. This is attributed to the laminar rotation that develops in the inner part of the vortex core as a result of progressive damping of disturbances such as turbulent fluctuations. An analytical study of isolated vortices based on linear stability theory was performed by Jacquin & Pantano (2002) who supported this argument. As a result, far enough from the trailing edge,

the major diffusion mechanism appears to be driven by viscosity rather than turbulence (Zeman, 1995).

In this section, turbulence measurements in the vortex, which benefit from the high spatial resolution of the SPIV arrangement, are presented. The turbulent kinetic energy at the vortex centre is presented for different Reynolds numbers, angles of attack and distances of the measurement plane from the trailing edge. The distribution of Reynolds shear stresses and shear strains in cartesian and cylindrical coordinates is presented along with a brief discussion of the turbulent closure problem for the simulation of wingtip vortices with RANS. The mechanism of the turbulence production and dissipation in the near wake towards a laminar vortex core is also addressed. As discussed at the beginning of this chapter, the helicity based centering method is applied on sets of 121 instantaneous velocity vector fields.

(a) Turbulent kinetic energy evolution In Section 4.1.(c), the turbulent stresses were presented on cartesian coordinates because such is the usual reference system of PIV measurements. A concise description of the structure of the different quantities was given. However, turbulence inside the vortex in cylindrical coordinates adds important aspects to the study. The governing equations and the relation between velocities and Reynolds stresses in cartesian and cylindrical coordinates are presented in Appendix C.

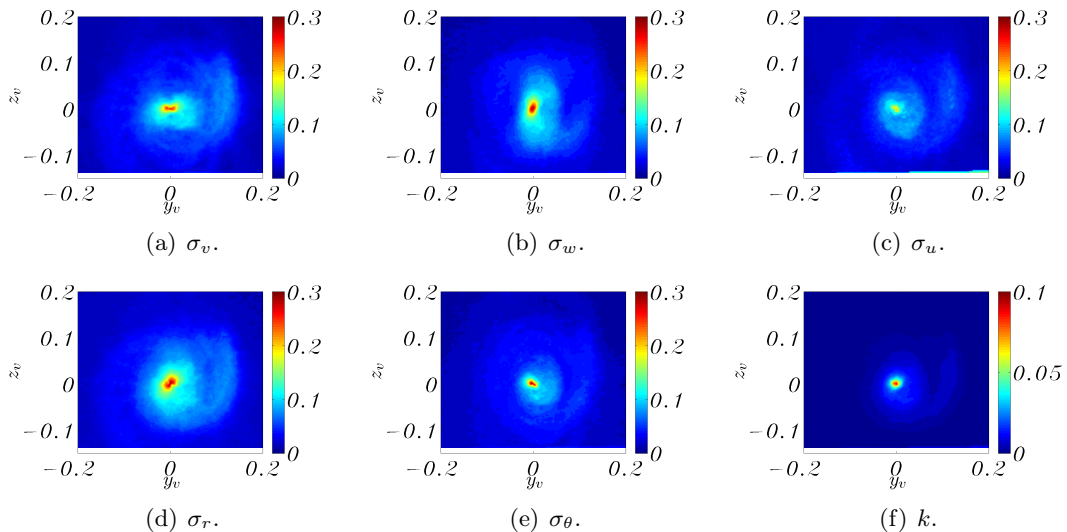


Figure 4.38: Velocity fluctuations in cartesian and cylindrical coordinates and turbulent kinetic energy in the wake of the *M1* wing at $\alpha = 12^\circ$, $x_w = 1$ and $Re = 5 \cdot 10^5$.

In Figure 4.38, the velocity fluctuations in cartesian coordinates and the relative cylindrical fluctuations are presented for a reference case (scaled by the freestream

velocity). The axial velocity fluctuation and the turbulent kinetic energy are the same in both reference systems. A lower level of the axial velocity fluctuation compared to the other components is noted so that $\sigma_r > \sigma_\theta > \sigma_u$. The contours of the horizontal and vertical fluctuations σ_v and σ_w are roughly elliptical in shape with major axes respectively along the horizontal and vertical directions. These shapes, observed also in all the other cases, represent, in cylindrical coordinates, a level of radial fluctuation σ_r higher than the azimuthal fluctuation σ_θ . This anisotropy was explained by Chow *et al.* (1997a) analysing the governing equations as consequence of the production of the Reynolds shear stress $\overline{u'_r u'_\theta}$ within the vortex core in the early wake. The contours of all the velocity fluctuations show a peak at the vortex centre. Consequently, the turbulent kinetic energy also presents a peak at the vortex centre which indicates a non-laminar core at this stage.

The evolution of the velocity fluctuations and the turbulent kinetic energy in the wake of the **M1** wing are presented in Figure 4.39. As observed earlier, for all the measurement planes the radial fluctuations are always higher than the azimuthal fluctuations which in turn are higher than the axial fluctuations. Their shapes become more circular and the maximum values at the vortex centre decrease as they travel downstream. The decrease between $x_w = 0.25$ and $x_w = 1$ is of around 10% for the in-plane fluctuations and around 20% for the axial fluctuation. The kinetic energy reflects this behaviour of the velocity fluctuations decreasing of around 50% from 0.25 to 1 chords from the trailing edge. The turbulence contained in the wake sheet and in the secondary structures around the primary vortex at $x_w = 0.25$ is almost completely dissipated at $x_w = 1$.

Although the vortex core is turbulent at the most downstream measurement plane, the effect of the quick relaminarization of the core can be implied. The reduction of the turbulent kinetic energy at the centre of the vortex is shown in Figure 4.40 where k_0 , scaled by the square of the freestream velocity, is plotted against the plane position and the Reynolds number for different angles of attack. A higher rate of decrease is observed for higher angles of attack (Figure 4.40(a)) which are characterized also by higher initial turbulence level. The level of k_0 at the most upstream plane $x_w = 0.25$ does not increase linearly with the angle of attack and the lines group together in high angles of attack ($\alpha = 12^\circ$ and 15°) and low angles of attack ($\alpha = 4^\circ$ and 8°) which suggests different mechanisms in the evolution of the turbulence. A quicker increase of the turbulent kinetic energy at the centre of the vortex for higher angles of attack is observed also by Igarashi *et al.* (2011) on similar experiments. Considering

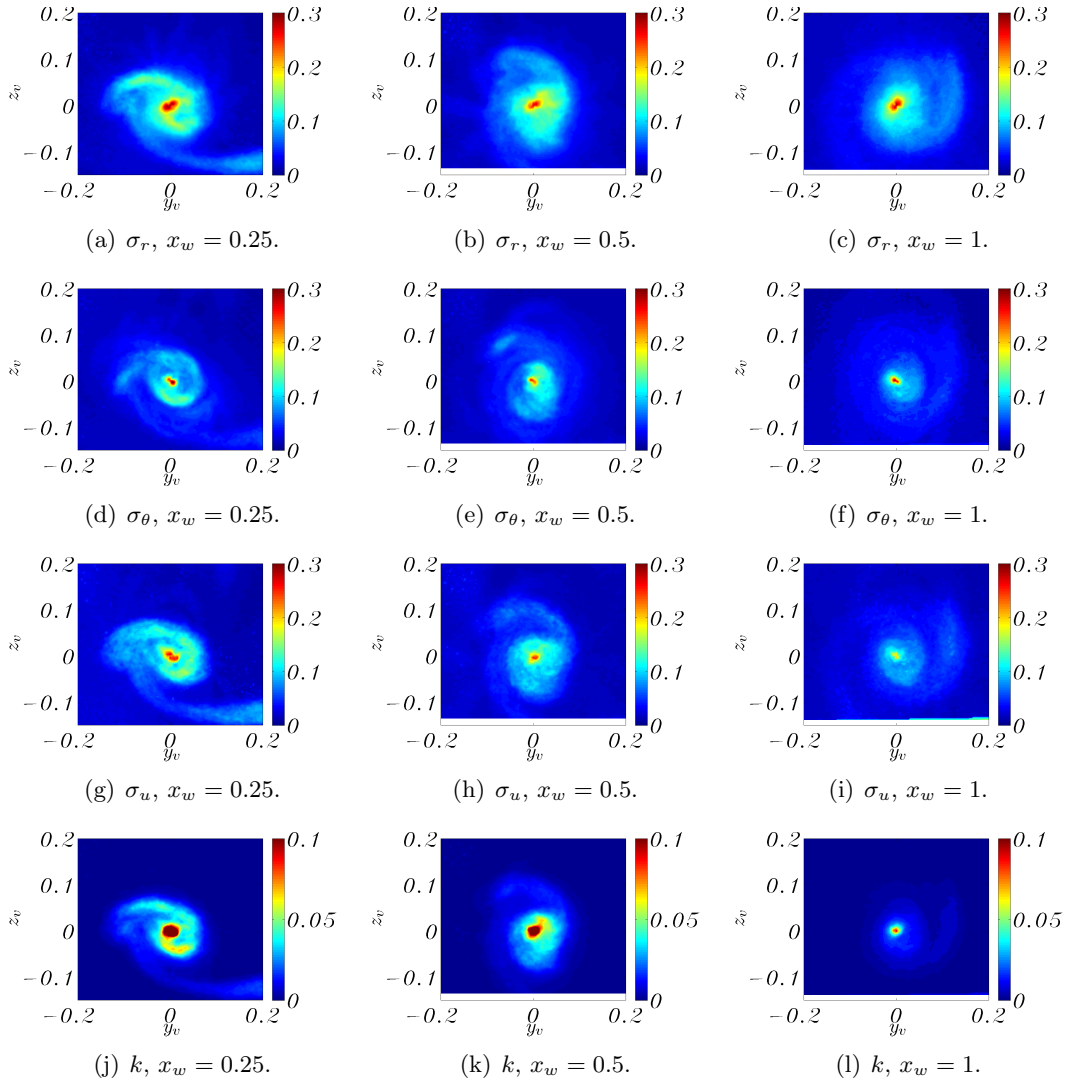
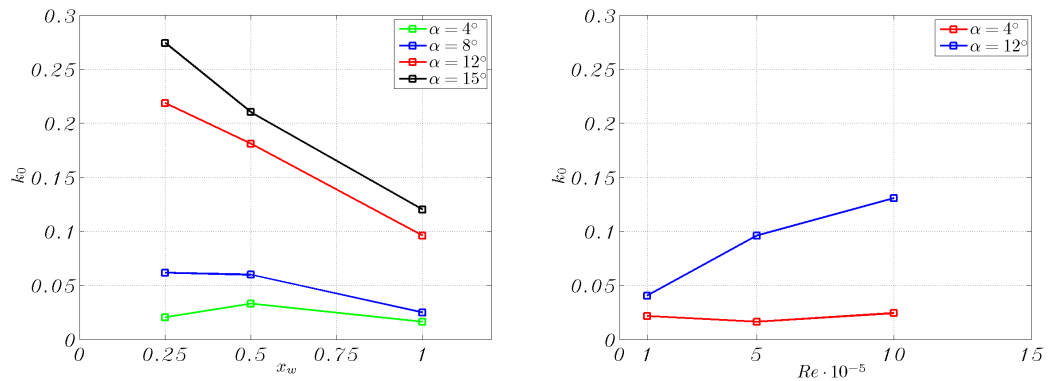


Figure 4.39: Evolution in the wake of the velocity fluctuations and turbulent kinetic energy for $\alpha = 12^\circ$ and $Re = 5 \cdot 10^5$.

the axial velocity peaks for these cases (Figure 4.36) and the axial flow schematic of Figure 4.33, the origin and development of the turbulence of the vortex can be seen in light of the shape and behaviour of the axial flow. For low angles of attack, the presence of a ring of wake-like flow around the centre of the vortex acts as a buffer region and is accompanied by low levels of turbulence at the vortex centre. On the other hand, a vortex with intense jet-like flow is characterized by high turbulence level. Following the trends of Figure 4.40(a), at about 2 chords of distance from the trailing edge the vortex core is expected to be laminar (i.e. zero turbulence) for all the angles of attack. Increasing the Reynolds number from $1 \cdot 10^5$ to $10 \cdot 10^5$ (Figure 4.40(b)), the dimensionless turbulence kinetic energy triples for an angle of attack of 12° whereas



(a) Evolution in the wake for different angles of attack and $Re = 5 \cdot 10^5$. (b) Reynolds number effect for different angles of attack at $x_w = 1$.

Figure 4.40: Turbulent kinetic energy at the centre of the vortex.

for $\alpha = 4^\circ$, k_0 does not show any substantial increase. This can be attributed to the interaction with secondary vortices which are stronger for the high angle of attack than for the low angle. Secondary vortices become more intense and persistent as the Reynolds number increases (dissipating viscous forces are less important) so that they induce higher disturbances to the primary vortex core.

(b) Reynolds shear stress and shear strain The evolution and angle of attack dependency of the in-plane Reynolds shear stress $\overline{v'w'}$ is represented in Figure

4.41 for the M1 wing at Reynolds number of $5 \cdot 10^5$. The orientation of the shear stress along axes at $\pm 45^\circ$ will be discussed later. As expected, the shear stress intensity increases for planes closer to the trailing edge and as the angle of attack increases. Although the tendency of these vortices to axisymmetry is visible, they show peculiar asymmetric characteristics in the near wake. For the wing at $\alpha = 4^\circ$ and 8° , at $x_w = 1$ the shear stress has decayed to almost zero. For higher angles, a longer development range is required and the shear stress shows peak values at two different radii, which are clearer at early planes: an inner radius of about 0.01 chords and an outer radius of 0.06.

Although large eddy simulations (LES) are becoming more popular and feasible also for wingtip vortices (see Jiang *et al.* (2007) for a study on the interaction of the flow with the tip surface and the early development of the vortex), the high Reynolds numbers encountered in typical flight conditions render the cost of LES on full wings still prohibitive. Therefore, a robust and high fidelity Reynolds-averaged Navier-Stokes (RANS) simulation is essential in studying this flow even though RANS models cannot be expected to accurately describe all the intricate details of the turbulent flowfield. Sev-

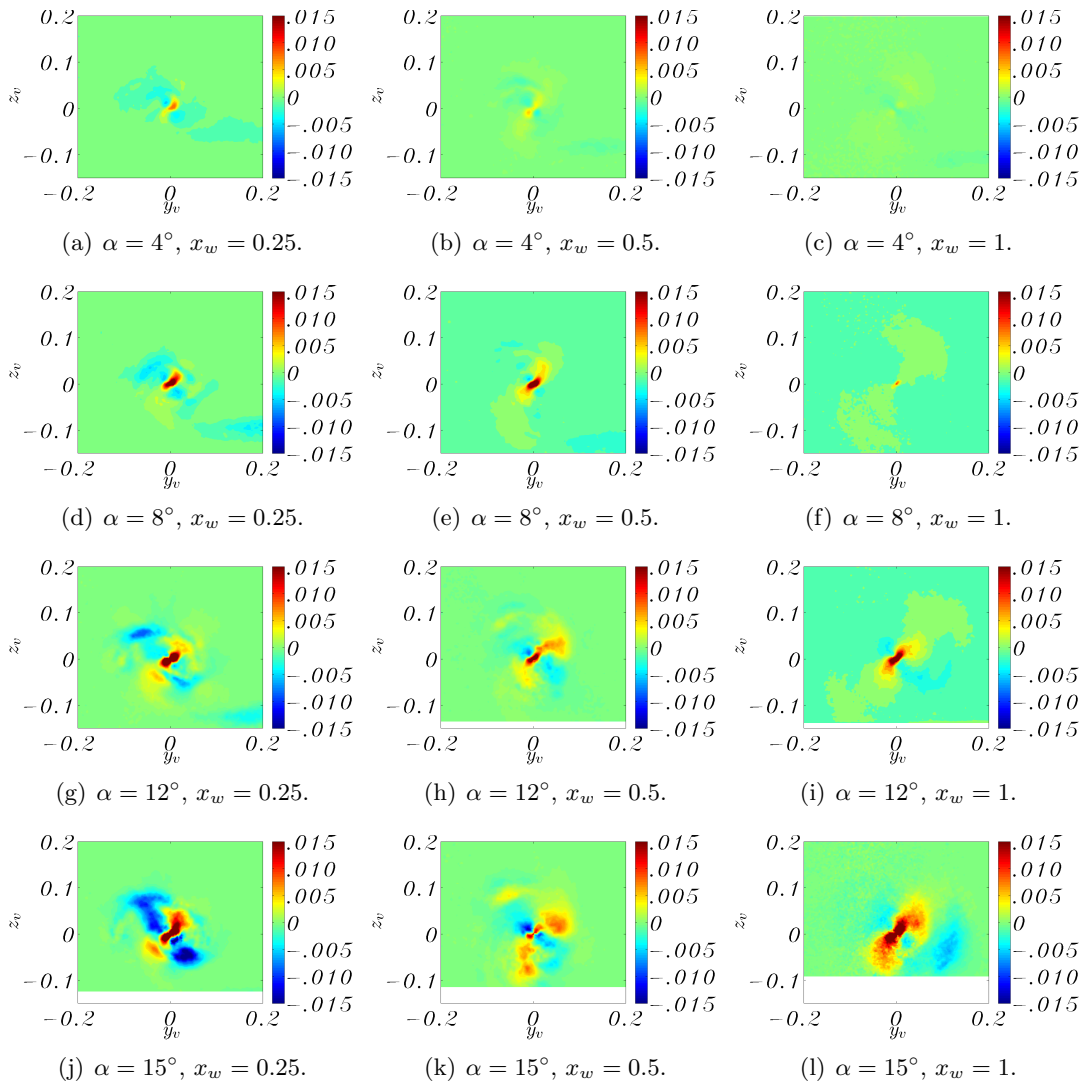


Figure 4.41: Evolution of the shear stress $\overline{v'w'}$ in cartesian coordinate for different angles of attack at $Re = 5 \cdot 10^5$.

eral techniques can be adopted to solve the closure problem and to model the Reynolds stresses. A common approach is the isotropic eddy viscosity model which expresses the Reynolds shear stresses as linear functions of the shear strains. These linear functions would be represented by the alignment of the Reynolds stresses and the shear strains. The contours of the shear strains, corresponding to the shear stresses of Figure 4.41, are reported in Figure 4.42. The first important observation is that they are oriented differently from the Reynolds shear stresses and in particular they are rotated by 45° . Therefore, the first conclusion is that the linear eddy viscosity model can not be expected to be capable of describing the vortex evolution in the near wake and doubtfully will be able to correctly link the vortex in the far wake with the wing where it was gen-

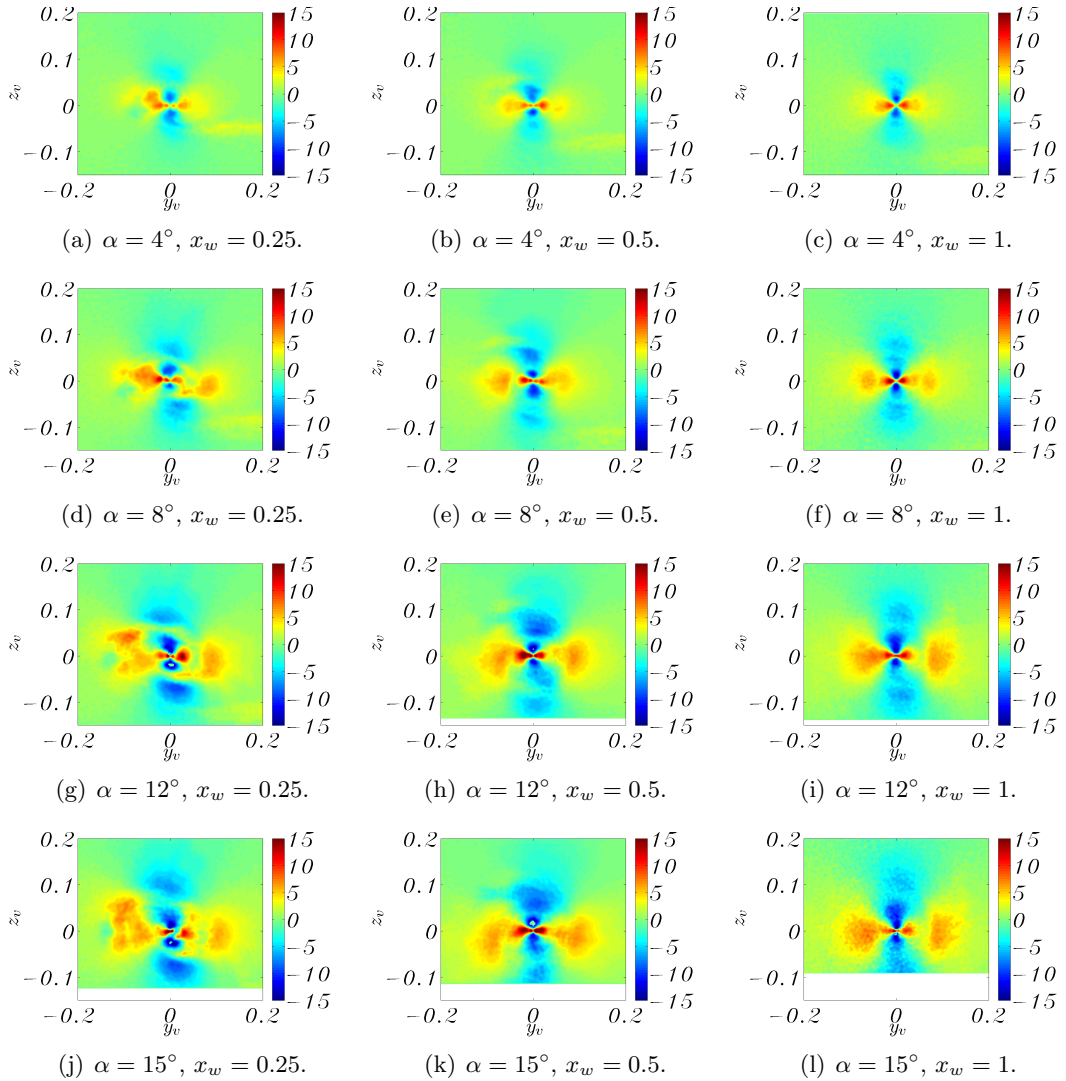


Figure 4.42: Evolution of the shear strain ε_{yz} in cartesian coordinate for different angles of attack at $Re = 5 \cdot 10^5$.

erated. However, some features of the mean flow, such as the formation of a multiple vortex system on the wing, the vortex centerline static pressure and the axial velocity can be correctly described. However, these models can be misleading concerning the turbulence measurements in the vortex core, as demonstrated by Churchfield & Blaisdell (2009). Therefore, non-linear eddy viscosity models or Reynolds stress models (RSM) have to be adopted when an accurate description of the core evolution is needed. An example of a non-linear eddy viscosity model is the $\overline{v^2}$ - f model which was applied on wingtip vortices by Duraisamy & Iaccarino (2005) who accurately predicted formation and early development. The structure and evolution of the tip vortex turbulence in the far field region was accurately described with numerical simulations also by Zeman

(1995) who adopted RSM as closure to the equations.

What also appears from the shear strains is that two radii of the local peaks can be detected. The inner radius at about $r = 0.015$ does not change significantly over the cases in Figure 4.42. The outer radius increases with the angle of attack from a value of 0.04 for $\alpha = 4^\circ$ to a value of 0.1 for $\alpha = 12^\circ$. These radii do not correspond with the position of the peaks observed in the Reynolds stresses in Figure 4.41. Also, higher angles of attack generate vortices with a wider region of high level of shear strain. A good symmetry at $x_w = 1$ for all the angles is observed.

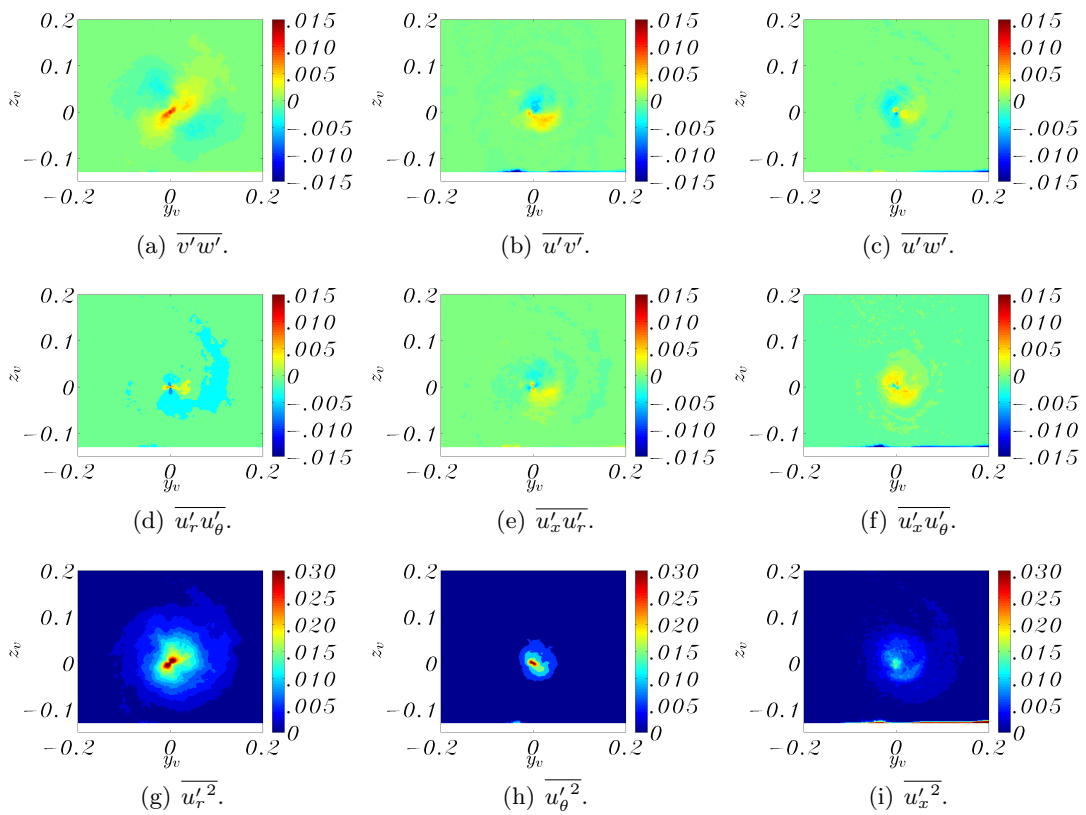


Figure 4.43: Reynolds stresses in cartesian and cylindrical coordinates at $x_w = 1$, $\alpha = 12^\circ$, $Re = 1 \cdot 10^5$.

In order to understand the reasons and implications of the shape of the shear stress $\overline{v'w'}$ observed earlier, in Figure 4.43 the three components of the shear stress in cartesian and cylindrical coordinates are reported along with the normal stresses in cylindrical coordinates for one case. The stresses $\overline{u'v'}$ and $\overline{u'w'}$ (Figures 4.43(b) and 4.43(c)) present two-lobes patterns with positive lobes respectively at -90° and 0° . Equation 4.22 presents the kinematic relation between the shear stress $\overline{v'w'}$ and the stresses in

cylindrical coordinates (a full presentation is provided in Appendix C.4):

$$\overline{v'w'} = \left(u_r'^2 - u_\theta'^2\right) \sin \theta \cos \theta + u_r' u_\theta' (\cos^2 \theta - \sin^2 \theta) \quad (4.22)$$

Looking at this relation, orientation along $\pm 45^\circ$ implies that $\overline{u_r'^2} > \overline{u_\theta'^2}$ and that $\overline{u_r'^2}, \overline{u_\theta'^2} > \overline{u_r' u_\theta'}$ (see Chow *et al.*, 1997a, for further explanations on this relation). The comparison between Figures 4.43(d), 4.43(g) and 4.43(h) confirms this observation.

(c) Turbulence production From Reynolds stress transport equations and with a careful weighting of the terms in those equations, Chow *et al.* (1997a) showed that the low level of $\overline{u_r' u_\theta'}$ within the vortex core is observed because its production is inhibited by a solid body rotation of fluid. In Figure 4.43(d), weak Reynolds stresses $\overline{u_r' u_\theta'}$ are measured in a small portion of the flowfield around the vortex centre. In Table 4.4, the key terms of the production of the Reynolds stresses are highlighted (from Chow *et al.*, 1997a). The production of $\overline{u_x' u_r'}$ and $\overline{u_x' u_\theta'}$ (Figures 4.43(e) and 4.43(f)), which are the Reynolds shear stresses involving the axial velocity fluctuation, are governed by the radial gradient of the mean axial flow which is higher in the core region compared to elsewhere. The radial gradient of the axial velocity is the key term in the production of Reynolds shear stresses until there are turbulent fluctuations in the vortex core, which is in the near wake before relaminarization. In fact, the axial flow gradient multiplies other stresses. In particular, the first production term of each Reynolds stress is coupling the two equations and the second is composed by the axial velocity gradient which multiplies either the radial fluctuation or the turbulent stress on the vortex plane. The radial gradient of the averaged axial velocity is negative in the vortex core with a zero value at the vortex centre and a peak very close to it; the radial gradient of the swirl velocity and the swirl velocity divided by the radius are both positive quantities and they show similar distributions with peak at the vortex centre.

In order to illustrate the importance of the radial gradient of the axial velocity on the production of Reynolds stresses, the evolution of the mean flow and the turbulence of two vortices at different angles of attack are compared. A vortex at $\alpha = 4^\circ$ with axial flow deficit in the core and a more intense vortex at $\alpha = 12^\circ$ exhibiting jet like flow are described. Only the production terms of Table 4.4 that include the radial gradient of the axial velocity are investigated and compared, since the other terms are coupling terms between the two Reynolds stresses through the swirl velocity.

In Figure 4.44, averaged axial flow contours show the rolling up of the vortices. The effects of secondary vortices are visible at $x_w = 0.25$ by the shape of the rolling up wake

| Reynolds stresses | Important production terms |
|-----------------------------|---|
| $\overline{u'_x u'_r}$ | $\frac{\overline{u_\theta}}{r} \overline{u'_x u'_\theta}$ $-\overline{u'_r{}^2} \frac{\partial \overline{u_x}}{\partial r}$ |
| $\overline{u'_x u'_\theta}$ | $-\overline{u'_x u'_r} \frac{\partial \overline{u_\theta}}{\partial r}$ $-\overline{u'_r u'_\theta} \frac{\partial \overline{u_x}}{\partial r}$ |

Table 4.4: Important production terms of the Reynolds stresses.

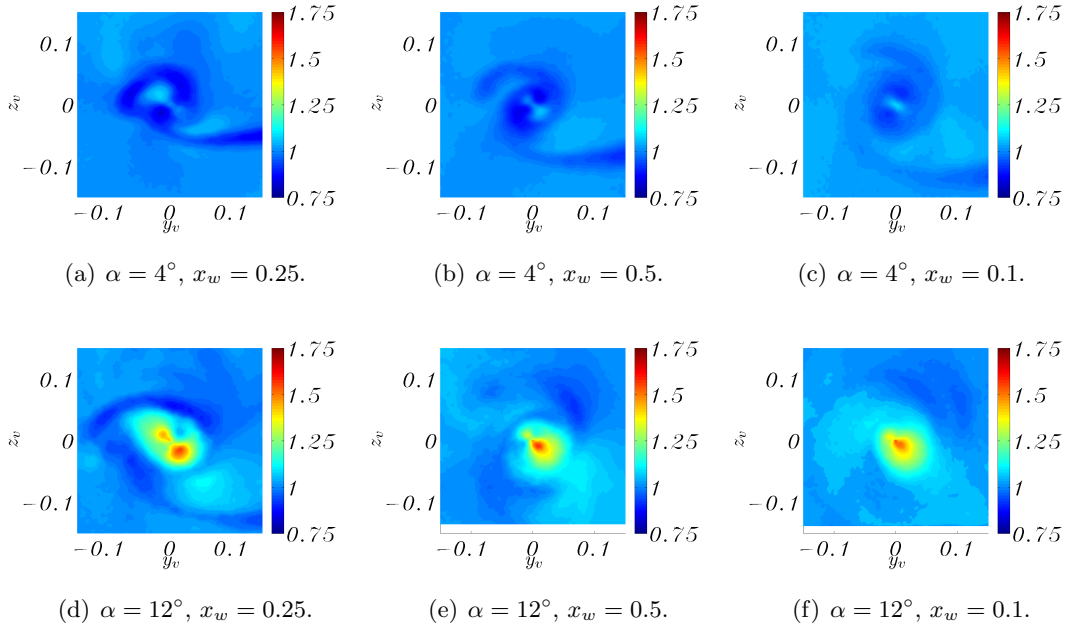


Figure 4.44: Evolution of the axial velocity in the wake for different angles of attack and $Re = 5 \cdot 10^5$.

sheet and the presence of a secondary axial velocity peak for the high angle of attack. The rolling up of the slow fluid from the wake sheet is observed for both the vortices at $x_w = 0.25$. At $x_w = 1$ the wake sheet is dissipated for $\alpha = 12^\circ$ whereas it is still visible for $\alpha = 4^\circ$. However, a more circular shape of the vortex core is observed at $x_w = 1$ for both vortices.

The mean radial gradient of the axial velocity field is measured as the average of 36 profiles around the vortex centre. The average profiles are reported in Figure 4.45, scaled by the freestream velocity and the wing chord, where at the vortex centre, the radial

gradients assume a near zero value. As a consequence of the decrease of the axial velocity fluctuations (see Figures 4.39(g), 4.39(h) and 4.39(i)), the undulations in the axial velocity gradient profiles become weaker as the vortex progresses downstream. Although the curves show several other local peaks which are less evident as the axisymmetric flow is reached, the radius at which the global peak is observed is almost constant and located at a value around 0.3% of the chord. The maximum gradient for the angle of attack of $\alpha = 4^\circ$ is approximately constant and around the dimensionless value of -8. For $\alpha = 12^\circ$, the axial flow maximum gradient increases from around -32 at $x_w = 0.25$, to -59 at $x_w = 0.5$ and then to -75 at $x_w = 1$. The increase in the axial flow gradient, although the axial velocity peak slightly decreases, is mainly due to the redistribution and merging of the high axial flow regions within the vortex core. The viscous dissipation of the peak and the transfer of momentum from the high velocity in the centre to the surrounding flow have still weak effects on the axial velocity distribution.

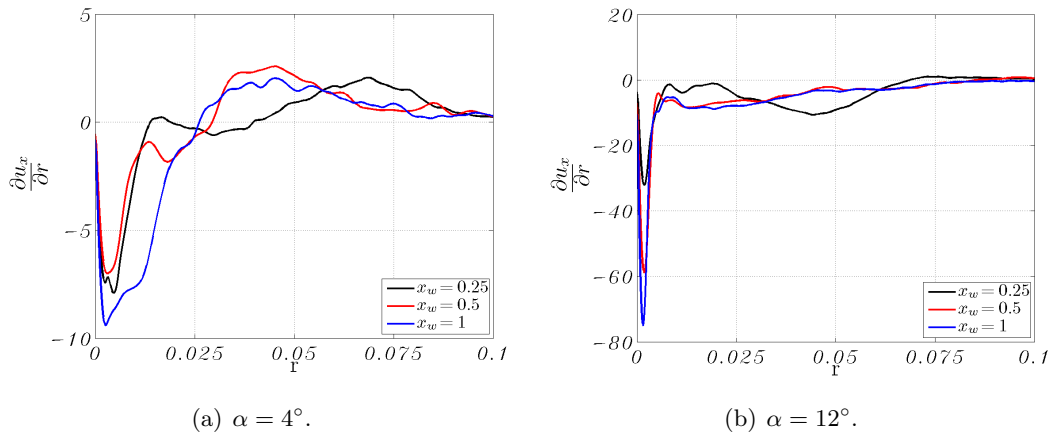


Figure 4.45: Radial gradient of the axial velocity at $Re = 5 \cdot 10^5$.

The Reynolds stress $\overline{u'_x u'_r}$ (left column of Table 4.4) of the study cases is reported in Figure 4.46. The evolution of such stress in the wake of the wing is, not surprisingly, characterized by a reshaping towards an axisymmetric pattern and a decrease of the peak value. The low angle of attack case shows very low shear stresses at $x_w = 1$ and the dimensionless peak value at $x_w = 0.25$ is much lower than the case at high incidence. For all the cases, four lobes, alternatively positive and negative, are observed around the vortex centre. The average of the absolute value of the minimum and maximum peak values is reported in Figure 4.47(a) where a decrease when the vortex moves downstream is observed. The same behaviour is observed for the Reynolds stress $\overline{u'_x u'_\theta}$ reported in Figure 4.47(b). It infers that, although the radial gradient of the axial velocity remains

almost the same between $x_w = 0.5$ and $x_w = 1$, the production of the Reynolds stresses in the vortex core greatly diminishes.

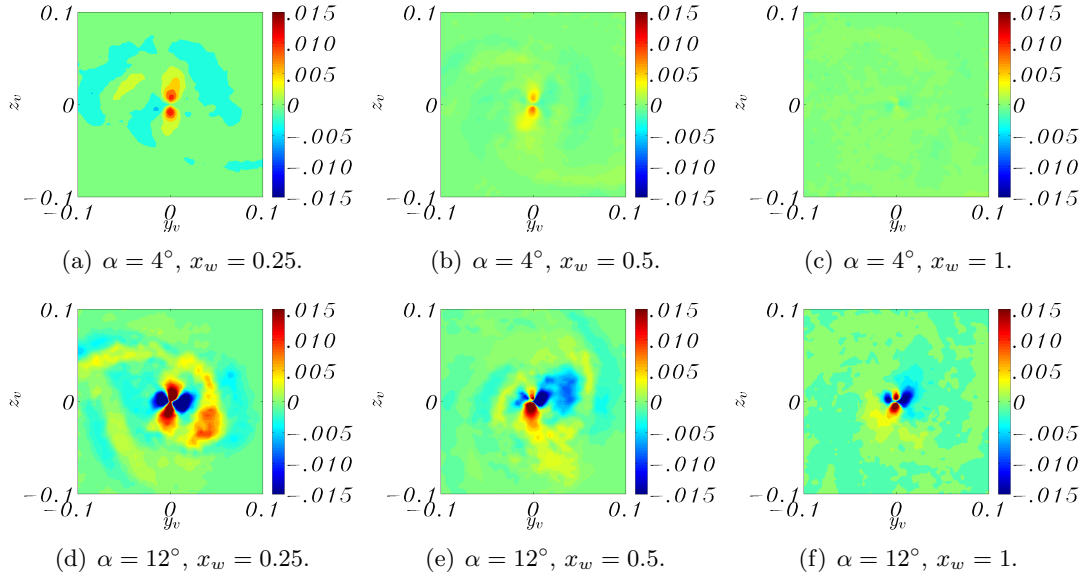


Figure 4.46: Evolution of the shear stress $\overline{u'_x u'_r}$ in cylindrical coordinate for different angles of attack at $Re = 5 \cdot 10^5$.

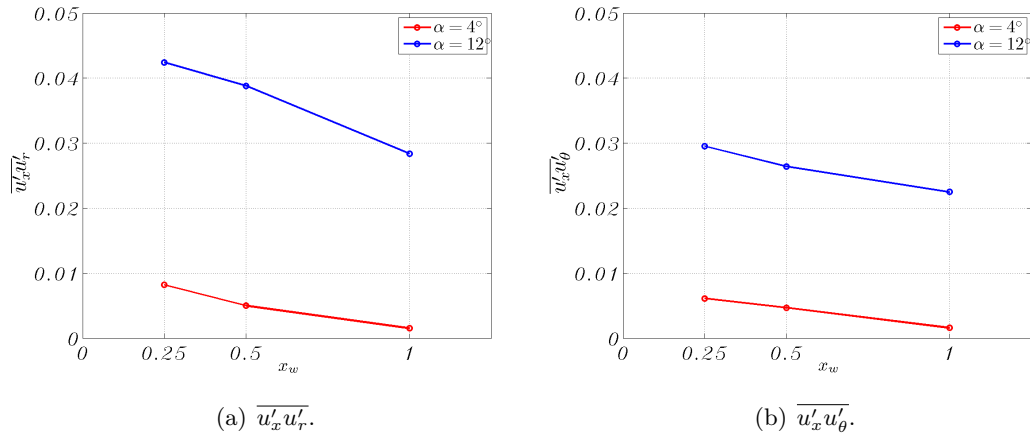


Figure 4.47: Evolution of the average of the absolute value of the minimum and maximum peak of shear stresses in cylindrical coordinate for different angles of attack at $Re = 5 \cdot 10^5$.

The radial velocity fluctuation $\overline{u_r'^2}$ and the vortex plane Reynolds stress $\overline{u'_r u'_\theta}$ are the terms that scale the axial gradient in the production terms of Table 4.4. The distribution of the first is reported in Figure 4.48 and the evolution in the wake of both of them is reported in Figure 4.48. For the high angle of attack, the two stresses are mainly subjected to a reshaping in a more circular form and the peak values are approximately constant. For the low incidence, they go to zero very quickly and at $x_w = 1$ almost zero

fluctuations are observed. These measurements are symptoms of a relaminarization of the vortex core, occurring for $\alpha = 4^\circ$ from $x_w = 0.5$ to $x_w = 1$, which inhibits turbulence fluctuations and generates a laminar flow in the core.

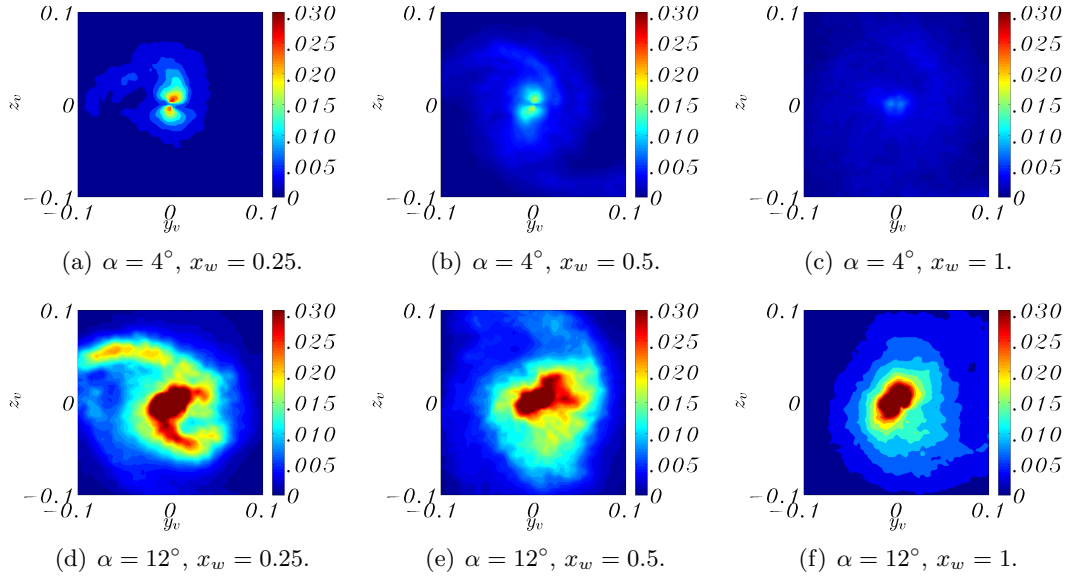


Figure 4.48: Evolution of the normal stress $\overline{u_r'^2}$ in cylindrical coordinate for different angles of attack at $Re = 5 \cdot 10^5$.

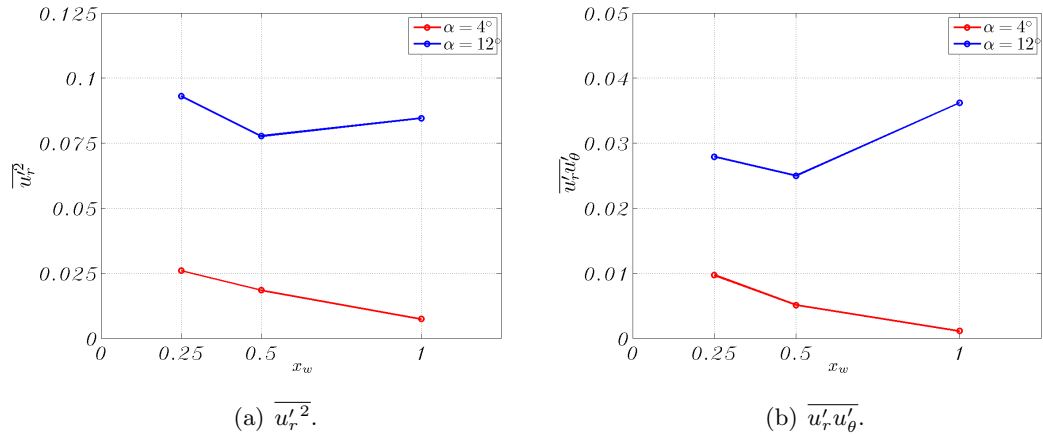


Figure 4.49: Evolution of the stresses in cylindrical coordinate for different angles of attack at $Re = 5 \cdot 10^5$.

The high radial gradient of the axial velocity and the jet-like flow in the vortex core of a more intense vortex ($\alpha = 12^\circ$) contribute to a higher turbulence production. The higher mixing rate of fluid between vortex layers, due to the turbulence contribution, generates mean axial flow contours which become rapidly axisymmetric (see Figure 4.44(f)). A low angle of attack ($\alpha = 4^\circ$) generates a vortex which develops over a longer

range; from Figure 4.44(c), the wake sheet is still visible at $x_w = 1$ and not fully rolled up around and merged with the vortex. However, the axial velocity gradient is low and the axial velocity peak is only slightly more than the freestream. This leads to a vortex core that presents a solid body rotation very early in the wake (i.e. at $x_w = 1$ the vortex core is laminar).

SECTION 5

Early wake behind squared and rounded wingtips

Since a change of wingtip geometry radically affects the pressure distribution on the wing and the behaviour of the flow in the early wake, a comparison between the tip vortex generated by a squared tip and a rounded tip is presented in this section in order to highlight some key mechanisms, in particular on the generation of meandering and turbulence. Specifically, the evolution of the wingtip vortex in the early wake of the wing **M2** with squared and rounded tips is presented.

(a) Development of averaged properties The averaged axial velocity contours (helicity based method applied) for the squared tip and rounded tip at $x_w = 0.25$ and $x_w = 1$ are presented in Figure 4.50. The wake sheet is clearly visible at $x_w = 0.25$ as a horizontal line with axial velocity deficit that rolls up around the vortex. A remarkable difference between the two geometries is the shape that the wake sheet takes during the rolling up. For the rounded tip, the wake follows a spiral structure, whereas for the squared geometry the induced velocity on the wake from the vortex system is affected by the presence of an intense counter rotating secondary vortex on the left of the primary vortex. The presence of the secondary vortex is noticeable at $x_w = 0.25$ where the wake sheet presents a very distinct “kink” (Chow *et al.*, 1997a). This structure generates a more diffuse vortex at $x_w = 1$ than the vortex generated by the rounded tip. The axial velocity within the core appears in all the cases as an excess compared to the freestream velocity. These contours refer to a Reynolds number equal to $12.7 \cdot 10^5$ and the results at $Re = 2.6 \cdot 10^5$ and $Re = 7.4 \cdot 10^5$ show the same features.

Vorticity contours are also reported in Figure 4.51 for the same cases. For the rounded geometry, the vorticity of the wake sheet is observed at $x_w = 0.25$ but is not visible at $x_w = 1$ where the vorticity is concentrated in the core. The effect of the squared tip is to generate a region of negative vorticity which is distributed on a wider area around the centre of the vortex. In order to quantify the dispersion of the vorticity,

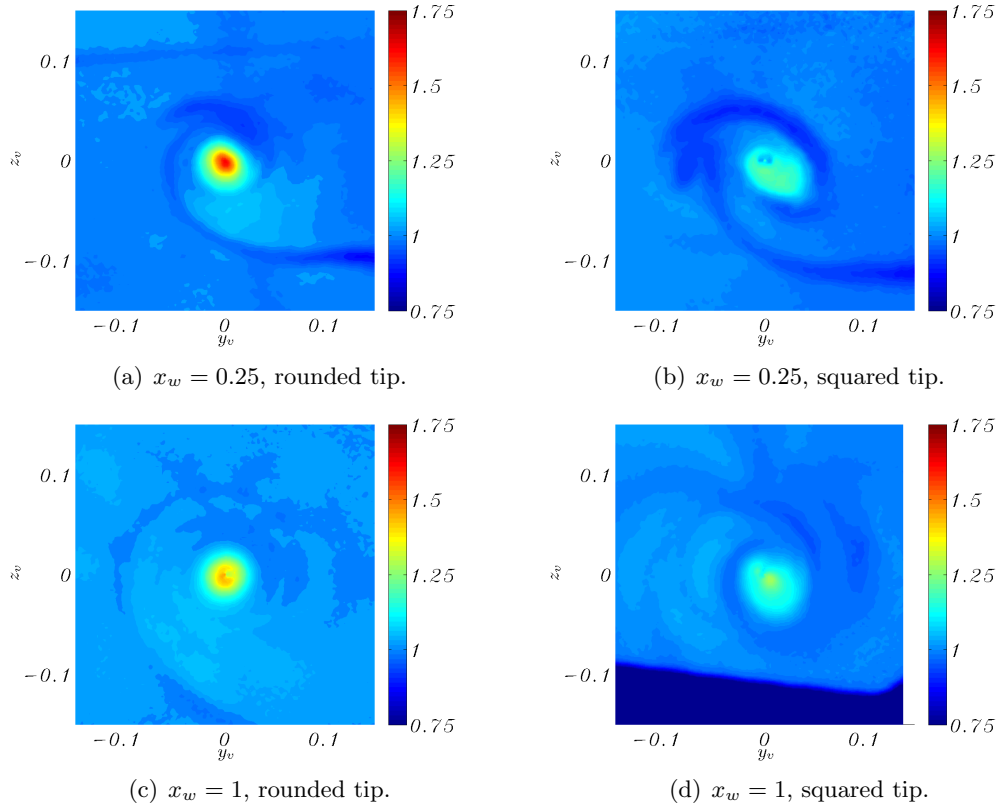


Figure 4.50: Axial velocity at $Re = 12.7 \cdot 10^5$ and $\alpha = 12^\circ$.

an enstrophy dispersion radius in a domain S of the flow is defined as follows:

$$r_{EN} = \sqrt{\frac{\int_S (\mathbf{x} - \mathbf{x}_0)^2 \omega_x(\mathbf{x})^2 dS}{\int_S \omega_x(\mathbf{x})^2 dS}} \quad (4.23)$$

where the denominator is the integrated enstrophy in the domain S , \mathbf{x} is the vector position in the flow field and \mathbf{x}_0 is the vector position of the vortex centre. This radius can also be seen as the radius of gyration of the enstrophy where a high value indicates an enstrophy distributed on a larger area around the vortex centre. Enstrophy is a preferable property to vorticity when the flow contains mixed areas of positive and negative vorticity (Nathan & Green, 2012), as it is for this case. In Table 4.5, the enstrophy radius of the cases reported in Figure 4.51 are calculated. The squared tip generates a vortex with about double dispersion radius with respect to the rounded tip. It is interesting to notice that between $x_w = 0.25$ and 1 the roll up of the wake sheet and the merging of secondary structures into the primary vortex result in a dispersion radius which decreases for both the tip geometries. However, the centerline vorticity

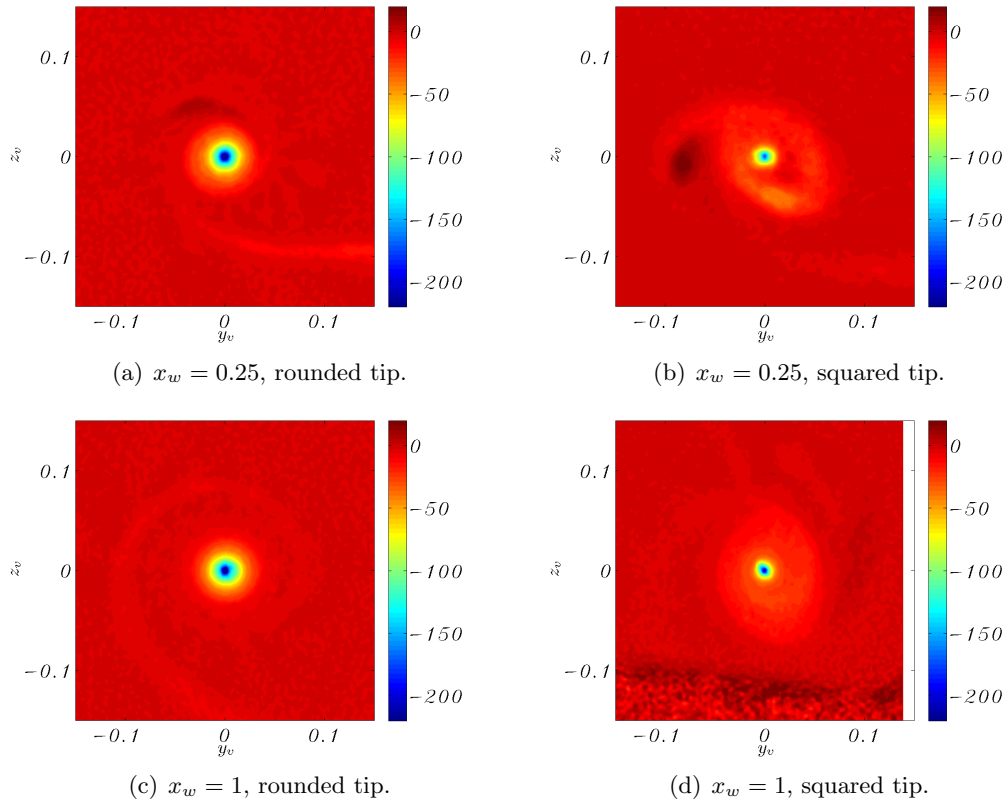


Figure 4.51: Vorticity at $Re = 12.7 \cdot 10^5$ and $\alpha = 12^\circ$.

increases of 22% for the squared tip and of 14% for the rounded tip as the vortex moves downstream, which is a sign of the uncompleted roll up, as observed also by Chow *et al.* (1997a).

| Tip | x_w | $r_{EN}/c\%$ |
|---------|-------|--------------|
| rounded | 0.25 | 1.56 |
| | 1 | 1.48 |
| squared | 0.25 | 3.41 |
| | 1 | 2.75 |

Table 4.5: Enstrophy dispersion radius in the wake of squared and rounded wingtips; $Re = 12.7 \cdot 10^5$ and $\alpha = 12^\circ$.

As observed also in Section 4.3, a region of positive vorticity, corresponding to a counter rotating secondary vortex, is observed on the left side of the primary vortex at 0.25 chords from the squared tip and it contributes to the wide dispersion radius. The fact that this secondary vortex is clearly visible in the average flow field indicates that it is intense and persistently found in that position. The position and intensity of other secondary vortices detected in the instantaneous fields are less persistent and they appear in the averaged contour only as a low vorticity ring around the primary vortex.

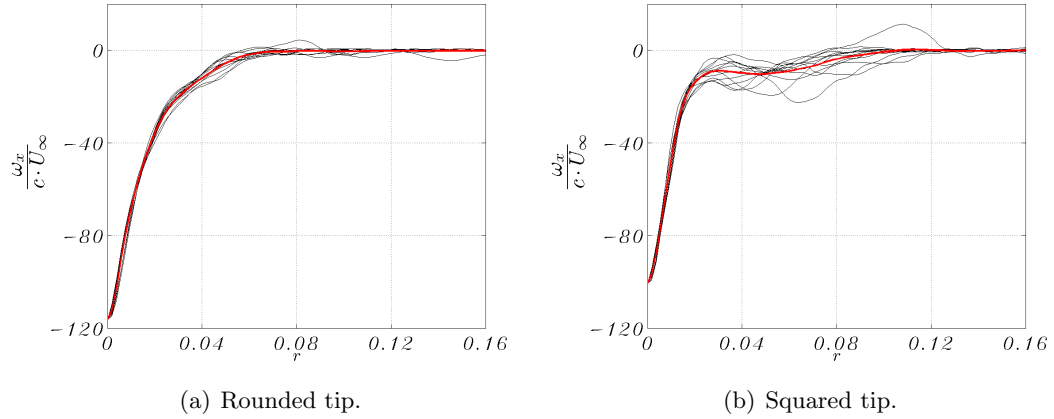


Figure 4.52: Vorticity profiles and mean value (red line) at $x_w = 0.25$, $Re = 12.7 \cdot 10^5$ and $\alpha = 12^\circ$.

For a more quantitative understanding, directional vorticity profiles are reported in Figure 4.52 as function of the distance from the vortex centre along 12 cuts around the vortex centre at $x_w = 0.25$. The mean value is also reported. A higher absolute value of the vorticity in the centre is calculated for the rounded tip where a small deviation from the mean value is also observed. A small bump at $r = 0.08$ is recorded and is related to cutting across the wake sheet. For the squared tip case, the distribution of the vorticity around the centre shows a smaller magnitude and it confirms the high asymmetry. In the mean profile, an inner region of high gradient is followed by a region with smaller gradient where secondary structures are indicated by drops and bumps of the directional profiles. In particular, the bump at $r = 0.11$ corresponds to the main secondary vortex on the left side of the primary vortex. As noted also from the contours of Figure 4.51, the vorticity field for the squared case reaches the asymptotic zero value at a considerably higher radius ($r \simeq 0.10$) than the rounded tip ($r \simeq 0.7$).

In Figure 4.53, the swirl velocity of the average velocity field at $x_w = 0.25$ is reported for the two tip geometries. The swirl velocity behind the squared tip shows a double-peak profile due to the spiral shape of the vortex core discussed in Section 4.2. A wider region of high gradient in the vortex core is observed for the rounded tip along all the cut directions and a considerably higher swirl velocity maximum is also observed. Even though the asymmetry is less compared to the squared tip, the difference in the maximum swirl velocity peak around the centre is about 12% of the mean value. For both the geometries, the swirl velocity mean profiles do not show significant changes at $x_w = 1$ although it reveals a smaller scatter of the directional profiles from the mean value. For the rounded tip case, a difference between the swirl velocity maxima of 6%

is found.

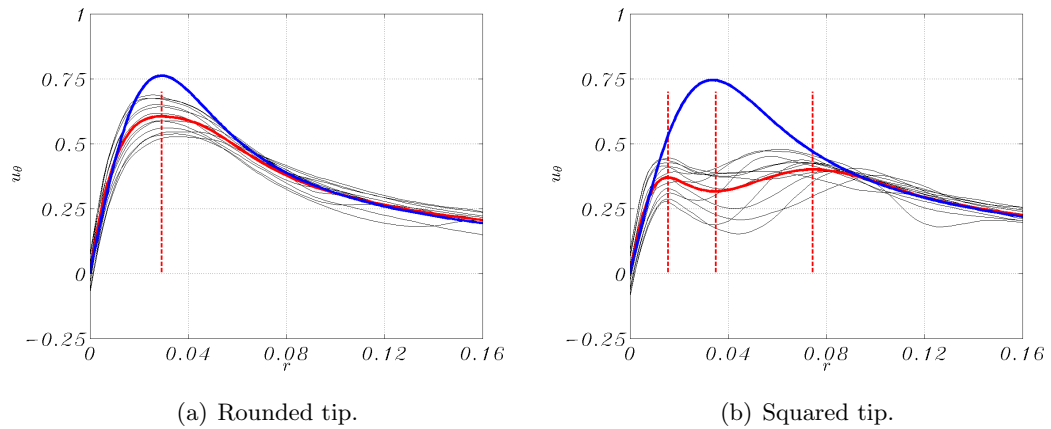


Figure 4.53: Swirl velocity profiles and mean value (continuous red line) at $x_w = 0.25$, $Re = 12.7 \cdot 10^5$ and $\alpha = 12^\circ$. Location of local maximum and minimum in dashed vertical red lines; velocity profile of the Lamb–Oseen vortex in blue.

In the same Figure, the swirl velocity profile as described in the Lamb–Oseen vortex is also reported. The parameters needed for the definition of the analytical profile (i.e. vortex circulation and radius) are adjusted in order to fit the inner core ($r < 0.01$) and the outer core profiles ($r > 0.08$). The analytical profile is in good agreement with the vortex measured behind the rounded tip at the exception of a swirl velocity peak 25% greater. A different situation is observed looking at the vortex generated by the squared tip where the swirl velocity profile has a different shape and it is much lower than the analytical vortex over a large area around the vortex core. This region is affected by a strong deformation of the vortex core shape which is far from being symmetric.

In Figure 4.54 the distribution of the vortex circulation $\Gamma(r)$, calculated by integration of the swirl velocity mean values and normalised by the freestream velocity and the chord, is presented for the two geometries. Although the circulation asymptote of the two cases tends to the same value, which means also that a similar overall circulation (hence lift) of the wing with the two different tips is generated, the radial distributions are different. The vortex behind the squared tip reaches the asymptotic value at a dimensionless radius around 0.1. A varying slope is observed within the core which reflects the asymmetry found in the swirl velocity. The position of the local maxima and minimum in the swirl velocity are also reported in this graph (vertical red lines) with reference to Figure 4.53. The three lines are all found before the asymptotic value is reached and they identify the position of a change of gradient in the circulation profile. The circulation for the rounded tip case shows a first inner region of high constant

gradient and a region of lower constant positive gradient afterwards. The maximum swirl is found before the change of gradient occurs.

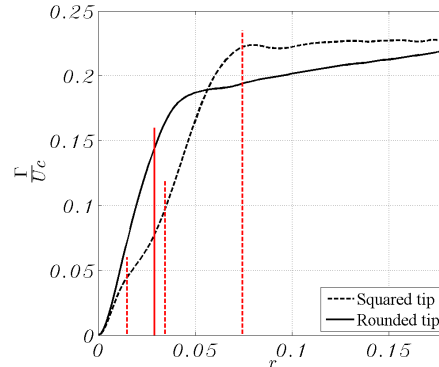


Figure 4.54: Circulation profiles and location of local maximum and minimum of swirl velocity (vertical red lines) at $x_w = 0.25$, $Re = 12.7 \cdot 10^5$ and $\alpha = 12^\circ$.

This suggests that the rounded tip generates a wake where the circulation from the wake sheet is gradually included into the vortex system. Also, secondary vortices found in the wake of the squared tip accelerate the rolling up and dissipation of the wake sheet so that the asymptotic circulation value is reached at an earlier stage. However, the squared tip generates a vortex which has a bigger core with a more complex structure than the rounded tip.

(b) Meandering and instantaneous behaviour of the vortex structure

In Figure 4.55, an instantaneous vorticity contour map of the vortex at $x_w = 0.25$ generated by a squared tip is shown. Many aspects in common with the flow visualizations in Figure 3.13 are found. Several vortices with opposite rotation can be detected by their vorticity peaks around the primary vortex. The strong counter rotating secondary vortex also is marked on the left side of the primary vortex. The ring of higher vorticity around the primary vortex observed in the average field in Figure 4.51(b) is due to secondary vortices rolling up and eventually merging with the primary vortex.

The instantaneous vorticity field of the vortex system generated by a wing with squared tip shows an intense interaction between primary vortex, vorticity sheet and secondary vortices. The effect is a rapid change over time of the primary vortex position and shape. The movement of the primary vortex centre can be quantified with the standard deviation of the distance of the instantaneous vortex centres (calculated with the helicity based method) from the average centre, which can be seen as a definition

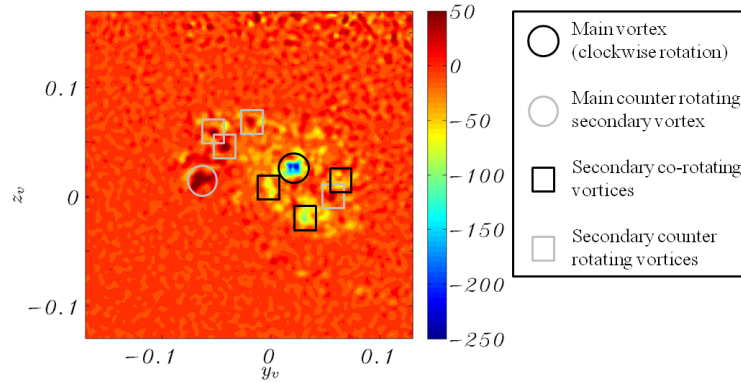


Figure 4.55: Instantaneous vorticity at $x_w = 0.25$, $Re = 12.7 \cdot 10^5$ and $\alpha = 12^\circ$ for squared wingtip.

of the meandering intensity:

$$\sigma_m = std \left[\sqrt{(x_0^i - \bar{x}_0)^2 + (y_0^i - \bar{y}_0)^2} \right] \quad (4.24)$$

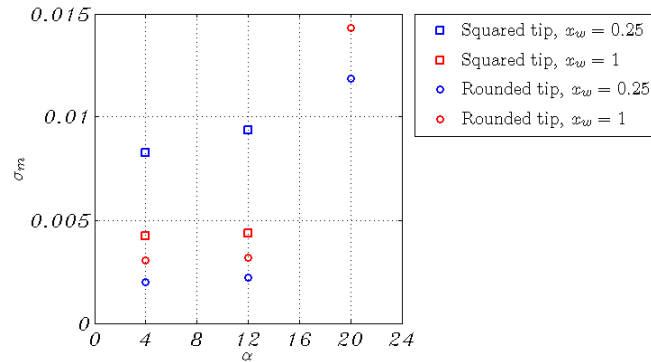


Figure 4.56: Vortex meandering for squared and rounded tips as function of the angle of attack at $Re = 7.4 \cdot 10^5$.

In Figure 4.56, σ_m is plotted as a function of the angle of attack for the vortices formed by squared and rounded wingtip at a Reynolds number of $7.4 \cdot 10^5$. The vortex meandering in the early wake of a wing with rounded tip is dominated by the essentially inviscid smoothing out process of the spiral vorticity sheet (Moore & Saffman, 1973). On the other hand, because of the presence of stronger satellite vortices, for a squared tip the meandering is higher than for a rounded tip. Also, as observed earlier in the vorticity contours, at $x_w = 0.25$ several secondary vortices are still present and not merged with the primary vortex as one defined vortical structure. The meandering in the early wake of the vortex from a squared tip is therefore dominated by secondary vortex interactions as observed also by Zuhail & Gharib (2001). This system of vortices

is the principal cause of the high meandering at this stage which decreases moving downstream as secondary structures merge with the primary vortex.

The meandering of the vortex seems almost independent of an increase in the angle of attack from 4° to 12° . However, it changes with the distance from the trailing edge. For a rounded tip, the meandering increases by about 50% from $x_w = 0.25$ to 1 because of the progressive rolling up of the vorticity sheet. For a squared tip, the meandering observed at $x_w = 0.25$ is double than the meandering at $x_w = 1$ which is coherent with the interactions of the primary vortex with satellite vortices. These interactions are stronger at $x_w = 0.25$ when secondary structures are not merged with the primary vortex. The meandering of the vortex created by a rounded tip at a stall angle of $\alpha = 20^\circ$ is also reported where the values are considerably higher than at lower angles of attack. A stalled wing creates a large region of separated flow that introduces intense chaotic motions and a more diffused vorticity distribution in the vortex core.

(c) Turbulence and shear strain evolution The shear strain and the in-plane Reynolds stresses for the vortex in the early wake of rounded and squared tip are compared in the following Figures (respectively in Figure 4.57 and 4.58) for the angle of attack of 12° and Reynolds number of $12.7 \cdot 10^5$.

The development of the four lobes pattern of the shear strain in the vortex core is quicker for the rounded tip than for the squared tip. Apart from the presence of the wake sheet, almost no differences in the shear strains from a rounded tip can be seen between the two measurement planes. The wake sheet shed by the trailing edge, characterized by a change of sign of the v -component of the velocity which results in a region of positive $\frac{\partial v}{\partial z}$, is visible at $x_w = 0.25$ and quickly dissipates by viscous effects.

For the squared tip, the shear strains at $x_w = 0.25$ are affected by secondary vortices which deform the four lobes pattern and create several secondary lobes around the vortex core. A more symmetric shape is found at $x_w = 1$. However, the size of the lobes for the rounded tip is much larger than for the squared tip and the velocity gradients are more intense. For a vortex from a rounded tip, the region within the core at constant and high swirl velocity gradient is bigger because the core does not show a spiral (asymmetric) structure like that from a squared wingtip (see Figure 4.53). The region within the vortex core of high velocity gradients observed for the rounded tip is responsible for the high shear strain.

Looking at Figure 4.58, higher values of Reynolds stresses are measured at $x_w = 1$ for the rounded tip compared to the squared one (Figures 4.58(c) and 4.58(d)), and

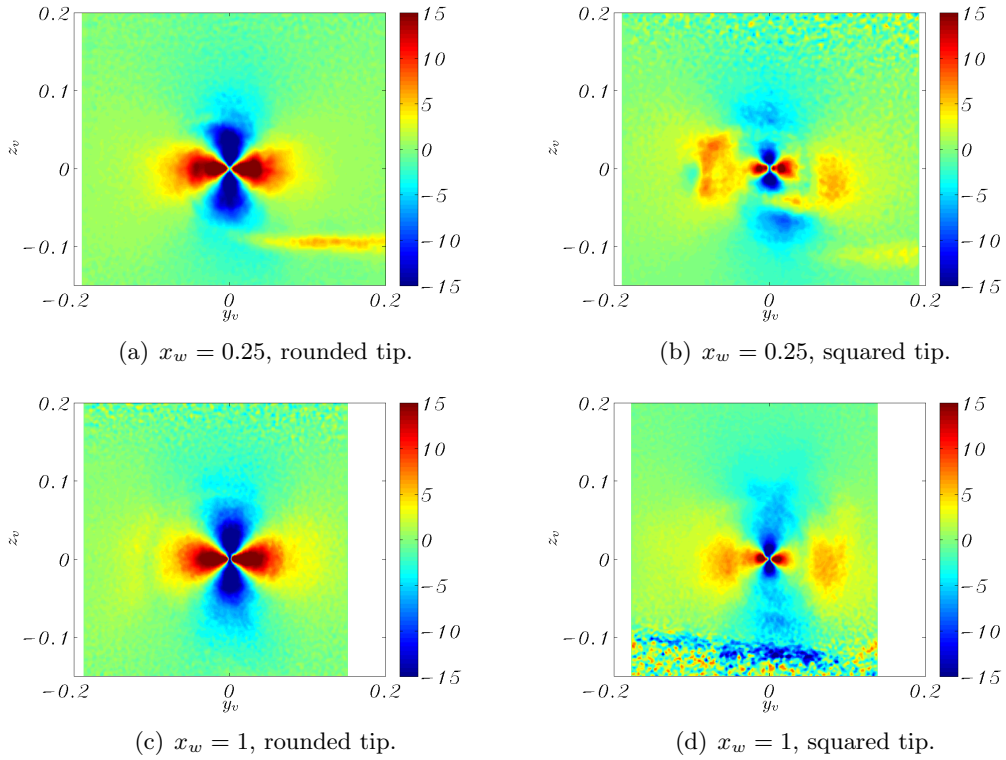


Figure 4.57: Evolution of the shear strain ε_{yz} for squared and rounded tip at $\alpha = 12^\circ$ and $Re = 12.7 \cdot 10^5$.

looking at the flow at $x_w = 0.25$ (Figures 4.58(a) and 4.58(b)), a different evolution of the stresses for the two geometries can be presumed. The rounded tip generates a vortex with high velocity gradients within the core which in turn generate higher turbulence stresses; the increase in the peak values of the Reynolds stress from $x_w = 0.25$ to $x_w = 1$ is indicative of the development of the axisymmetric vortex with a turbulent vortex core. The squared tip generates a vortex system of multiple vortices which interact and quickly dissipate the velocity gradients. The Reynolds stresses are higher at $x_w = 0.25$ than at $x_w = 1$ which indicates a strong interaction between primary and secondary vortices. The small Reynolds stress at the centre of the vortex at $x_w = 1$ indicates a core in an advanced stage of the relaminarization process. The relative rotation of 45° between shear stresses and Reynolds stresses (and discussed in Section 4.4.(b)) is observed in the same way for both the tip geometries.

This different evolution of the vortex cores for the two tip geometries can be observed also by looking at the turbulent kinetic energy at the vortex centre in Figure 4.59. Figure 4.59(a) shows the value of k_0 at the two measurement planes. For the squared tip, the same trends discussed with reference to Figure 4.40(a) are observed here: the turbulence is higher for a higher angle of attack and decreases with the distance from

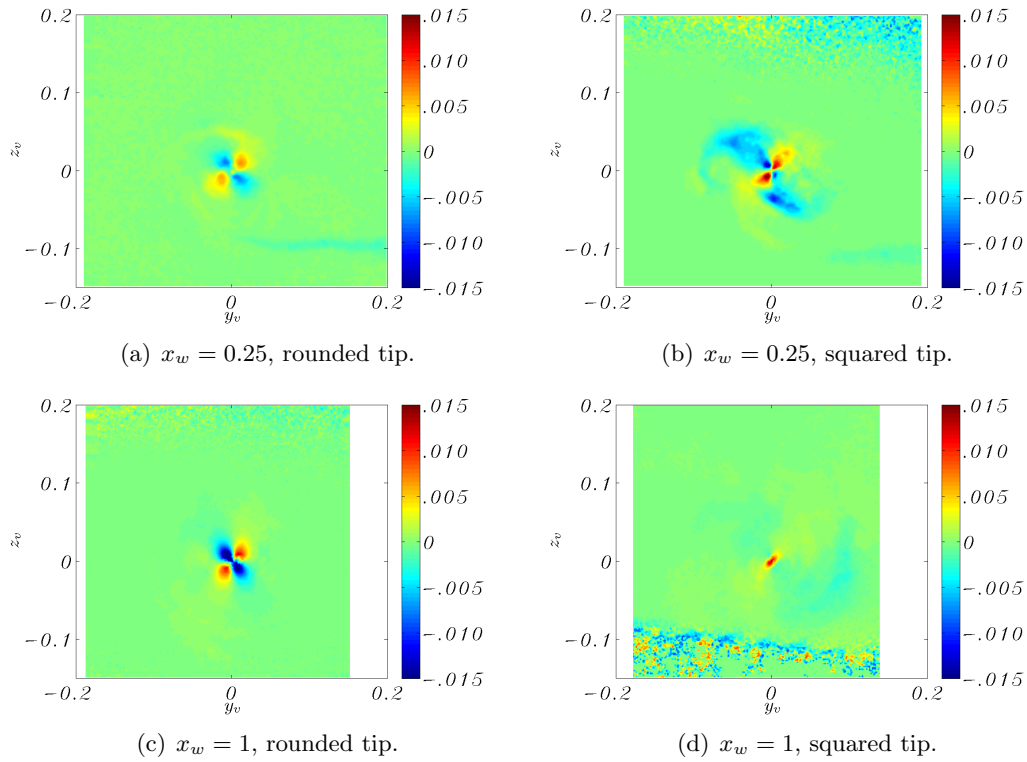


Figure 4.58: Evolution of the Reynolds shear stress $\overline{v'w'}$ for squared and rounded tip at $\alpha = 12^\circ$ and $Re = 12.7 \cdot 10^5$.

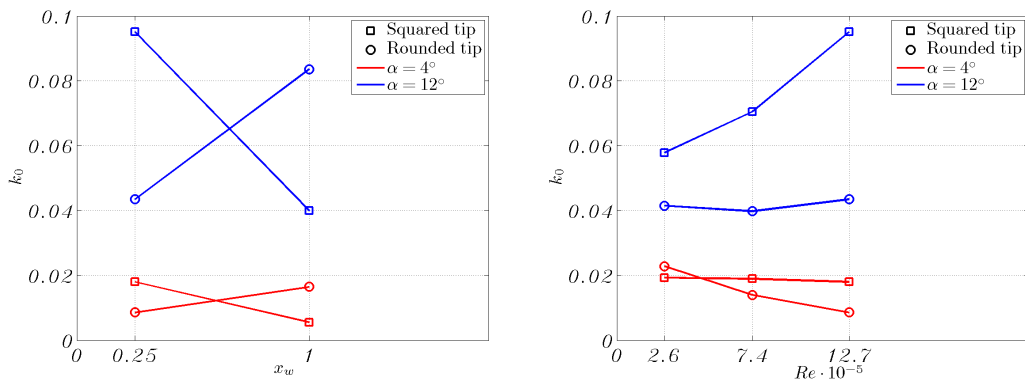


Figure 4.59: Turbulent kinetic energy at the centre of the vortex generated by rounded and squared tips.

the wing at different slopes depending on the intensity of the vortex. On the other hand, the turbulent kinetic energy in the core of the vortex generated by the rounded wingtip is higher at $x_w = 1$ than at $x_w = 0.25$. The early wake behind the rounded tip generates a vortex with high axisymmetry already at $x_w = 0.25$. Mixing of fluid by

viscous effects and by interaction with secondary structures is very low so that strong velocity gradients are observed around the centre, particularly the radial gradient of the axial velocity which in turn generates turbulence within the core. However, this is only a temporary process and the turbulence within the core will decrease moving more downstream towards a laminar vortex core. It is believed that a similar process is also seen in Figure 4.40(a) for the squared wingtip at $\alpha = 4^\circ$. With that configuration, similarly to the rounded tip case, secondary structures are weak and a quick development of the vortex into an axisymmetric structure is observed. The turbulence at the vortex centre increases between $x_w = 0.25$ and $x_w = 0.5$ and decreases then between $x_w = 0.5$ and $x_w = 1$.

The influence of the Reynolds number on the maximum turbulent kinetic energy is reported in Figure 4.59(b) for different wing angles. As observed also in Figure 4.40(b), for the squared tip at $\alpha = 4^\circ$ the turbulence remains approximately constant but it increases with the Reynolds number for $\alpha = 12^\circ$ by the formation of stronger secondary vortices. The rounded tip generates a vortex with fewer secondary vortices and less intense than the squared tip so that axisymmetry is reached earlier in the wake. At $\alpha = 12^\circ$ the vortex is less turbulent than for the case with squared tip and an almost constant turbulence is observed increasing the Reynolds number. At $\alpha = 4^\circ$, with smaller axial velocity gradients and less intense axial velocity perturbations, the effect of increasing the Reynolds number is as of an ageing of the vortex corresponding to a decrease of the turbulence level.

Comparing the values of k_0 measured behind squared tip mounted on the different wings, it appears that the turbulence behind the wing **M1** with bigger aspect ratio (Figure 4.40) is about double than the turbulence behind the low aspect ratio wing **M2** in Figure 4.59 (the same can be said comparing the Reynolds stresses in Figures 4.41(i) with Figure 4.58(d)). The overall circulation and its distribution is therefore strongly connected to the vortex core turbulence.

Lastly, the turbulence values of Figure 4.59(b) for $Re = 7.4 \cdot 10^5$ can be compared with the meandering for the same cases in Figure 4.56 ($x_w = 0.25$). What appears is that rounded tips generate a vortex with lower meandering and lower turbulence than the vortex generated by squared tips. However, the turbulence for the rounded tip at $\alpha = 12^\circ$ is higher than for the squared tip at $\alpha = 4^\circ$ despite the fact that the corresponding meandering is much lower. Meandering and turbulence, even if strongly connected by same causes like as secondary vortices and wake sheet interactions, are generated and evolve in different ways. The meandering is a solid movement of a big part

of fluid (of the order of the vortex core and usually identified by the movement of the vortex centre) dictated by disturbances on the wing and in the wake as consequence of interactions with secondary structures. These interactions contribute to the deformation of the velocity field within the vortex core which is balanced by asymmetric shear stresses. Turbulence is already present during the formation of the vortex flow on the wake surface, it is further produced in the early wake by velocity gradients and it diminishes moving downstream as effect of the relaminarization of the vortex core by centrifugal forces.

(d) Vortex pair formation without generation of lift Among the models and mechanisms of the wingtip vortex formation presented in Section 1.2, the shear layer interpretation is the only mechanism which predicts vorticity formation over a wingtip without producing lift. In this section, the wake behind the wing at no incidence is tested for the two tip geometries in order to give insights on this mechanism of vortex formation. The axial velocity and the vorticity contours in the wake of the **M1** wing are reported respectively in Figures 4.60 and 4.61. Both the rounded and the squared wingtips are studied at $x_w = 0.25$ and $Re = 7.4 \cdot 10^5$.

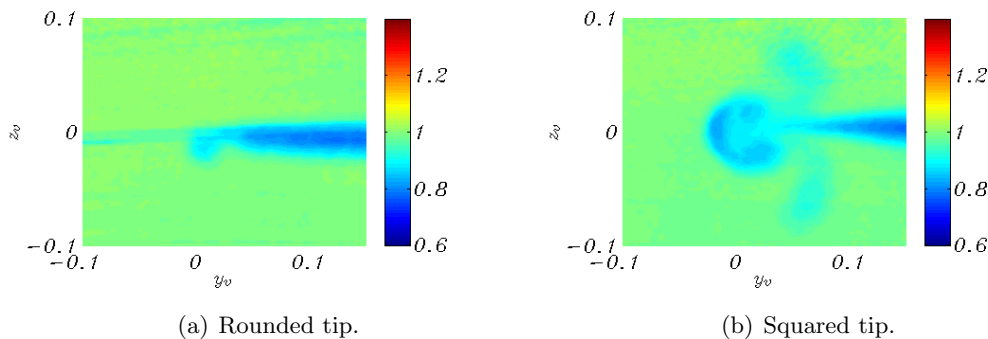


Figure 4.60: Axial velocity at $\alpha = 0^\circ$, $x_w = 0.25$ and $Re = 7.4 \cdot 10^5$.

On the squared tip, the vorticity contour shows the occurrence of two counter-rotating vortices of same magnitude. They are formed on the two wing surfaces and they are fed by the flow on the tip side forced to a separation by the sharp edges. This is the same mechanism seen on the wing at an incidence (smoke visualization in Figure 3.13) where the flow from the tip side separates at the sharp edge and forms the primary vortex. For the wing at zero incidence, the flow around the wing is symmetric about the chord plane and the flow on the tip side spills over both the wing surfaces forming two vortices. In the wake, the consequent induced velocity field feeds the vortex pair with the wake sheet which is identified by a region of flow with axial velocity lower

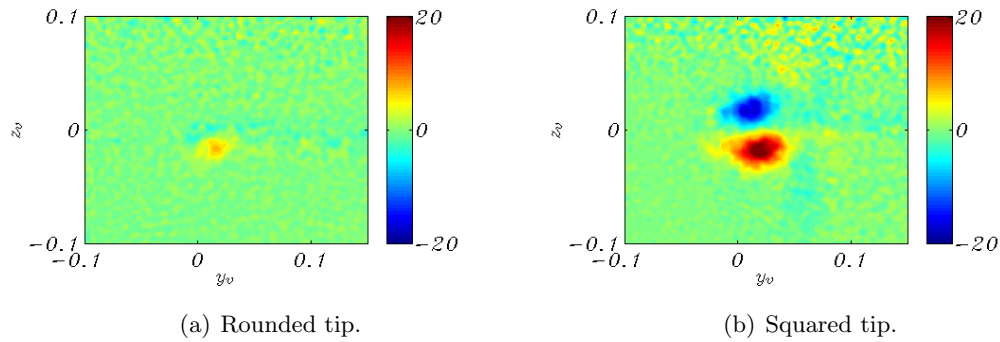


Figure 4.61: *Vorticity at $\alpha = 0^\circ$, $x_w = 0.25$ and $Re = 7.4 \cdot 10^5$.*

than the freestream flow. The flow around a rounded tip is not forced to a separation like the flow over a squared tip. For the rounded tip, the wake shows a smaller and weaker vortex pair than the squared tip case at the edge of the vorticity sheet and the interaction between vortices and wake sheet is weaker. Although the geometries are very simple, the importance of this mechanism in the initial wingtip vortex formation may present this test as a benchmark case for numerical analysis.

SECTION 6

Summary

Planar SPIV behind rectangular wings reveals that the very early wake is dominated by the rolling up of the wake sheet and the presence of several secondary vortices which interact with the primary vortex and strongly affect its dynamics. The vortex structure is not axisymmetric and turbulence affects the whole vortical flow. The importance of the centering procedure of the instantaneous vector fields is found in the clarification of a robust vortex centre definition which can take various forms. From a comparison of several vortex quantities such as vortex centre movement, axial velocity, swirl velocity, velocity fluctuations, turbulent kinetic energy, Reynolds stresses and shear stresses, the identification of the vortex centre with the peak of the streamwise helicity is found to give the highest reliability. Moreover, among the different quantities presented here, this is the only one which is calculated using all the three components of the velocity vector. However, different definitions of the vortex centre can be preferred for analysis of the flowfield which focus on specific aspects such as the rolling up of the wake sheet or the axial velocity peak.

The centering operation operates as a filter of the turbulent motions linked to a solid translation of the whole vortical flow on a plane perpendicular to the vortex axis and related to its centre position. The axial velocity flow and the turbulence level in the vortex core are highly affected by the method adopted for the correction from this motion. However, after such correction, the fluctuation level of the vortex core is still high due to the presence of secondary vortices and rolling up of the wake sheet. The introduction of a directional vortex core radius reveals the spiral structure of the vortex core in the early stage and its development towards an axisymmetric structure. The rotation rate of the core increases with the intensity of the vortex and an axisymmetric vortex core is observed at 2 chords downstream of the trailing edge. The comparison between the vortex generated by a squared wingtip with a rounded wingtip highlights the effects of two main mechanisms in the vortex development: the rolling up of the wake sheet and the merging of secondary vortices. The same effects can be seen from the comparison between the development of a weak vortex (i.e. low angle of attack) with a strong vortex (i.e. high angle of attack). During the formation of the vortex on the wing, turbulence is already found in the rolling up spiral structure so that the vortex core in the very early wake is turbulent for both the geometries. Jiang *et al.* (2007) found that the turbulence inside the primary tip vortex is not created by the tip vortex itself but the turbulent shear layer and the interaction between the primary and the secondary vortices are the major sources of turbulent activity in the core.

The trailing vortex behind a squared wingtip is bigger than the vortex behind a rounded wingtip; several secondary vortices orbit around the primary vortex and eventually merge with it. The interaction between these vortical structures contributes to a high mixing of fluid between the flow in the vortex core and the external flow and a high meandering is generated. Also, this interaction quickly dissipates the high velocity gradients within the vortex core so that a relaminarization process is promoted at an earlier stage. On the contrary, the rounded tip generates a vortex with an axisymmetric shape at a more upstream plane with high velocity gradients within the core which generate higher turbulence stresses and a later relaminarization. Also, the meandering of the vortex behind a rounded tip is mostly dictated by the smooth and progressive rolling up of the wake sheet.

The difference in the development processes of the trailing vortex generated by the two different wingtip geometries gives insight on the difference between the turbulence within the vortex core and the meandering of the vortex system. Meandering is linked to secondary structures interacting with the vortex such as secondary vortices and wake

sheet. Turbulence in the vortex core is generated by the high velocity and pressure gradients and in particular by the radial gradient of the axial flow. The turbulent quantities inside the vortex increase with the angle of attack and quickly become symmetric moving downstream. The relaminarization of the vortex core is observed at a earlier stage when the angle of attack of the wing is low and the consequent radial gradient of the axial velocity is also low.

The axial flow in the vortex core is the result of the acceleration mechanism caused by the spiral structure of the vortical flow and the deceleration due to the mixing of the wake sheet and the boundary layer with the core flow. The equilibrium between these mechanisms is dictated by the wingtip geometry and the intensity of the vortex so that different shapes of the axial flow distribution can be observed. However, an axial velocity excess at the vortex axis compared to the surrounding core flow is always observed in the early wake although its magnitude might be lower than the freestream velocity for weak vortices. The development of the axial flow is quicker than the development of the swirl velocity and the axial velocity contours do not show the presence of secondary structures at already one chord from the trailing edge. These findings are very important when a centering method for the vortex in the early wake has to be selected and also when a comparison of the axial velocity peaks is performed. In the present parametric study, both axial velocity excess and deficit compared to the freestream velocity are observed. A linear relation between the axial flow peak with a vortex circulation parameter is suggested and a good correlation with other studies is found. Furthermore, different linear trends are found for the two different wingtip geometries with the rounded tip showing a higher gradient than the squared tip. The switchover angle between jet-like and wake-like behaviour of the axial velocity peak is estimated to be around 4° for the squared tip and around 7° for the rounded tip.

Measurement accuracy and error

Results from several experimental techniques have been presented and discussed in this dissertation. Each technique contributed to create a deeper and more comprehensive understanding of the main aspects of the formation of the wingtip vortex on the surface of the wing. Moreover, a wide range of conditions have been tested which have revealed important trends, patterns and mechanisms in the wingtip vortex formation and early wake. Some of techniques adopted are purely qualitative, such as the smoke and the surface oil flow visualizations, and their validity relies on a good set up of the experimental apparatus and a sensible interpretation of the results (details in Sections 2.3.(a) and 2.3.(c)). As regards to the other experimental techniques, a discussion and quantification of the experimental accuracy and error encountered in this work is presented in the following sections with a particular attention on the measurements using the SPIV (Section 5.2), which played the major role in the investigation of the wingtip vortex flow.

SECTION 1

Pressure, frequency and meandering

Pressure measurements gave insight on the effects of the wingtip vortex on the pressure distribution on the wing surface at different angles of attack. Pressure transducers with very high linearity were used (see Section 2.3.(b)) and a resolution of 0.14% of the maximum suction peak is calculated. The comparison between the results found in this work and the results of McAlister & Takahashi (1991) revealed that a high spatial resolution of the pressure tappings is essential for an accurate description in the region of high gradients around the suction peak (see Section 3.2). The suction peaks found in the present study were around 15% lower than the peaks found by McAlister & Taka-

hashi (1991) for a similar case. However, a similar shape of the pressure distribution (i.e. lowering of the suction peak moving outboard and undulation generated by the wingtip vortex suction) was found.

The dominant frequencies of the pressure measurements presented in Section 3.2.(b) are one decade below the resonance frequency of the experimental apparatus, as discussed in Section 2.3.(b). Also, due to the small tubing diameter, the damping of the system is very high so that the measurement errors in the pressure fluctuations presented in this research are negligible.

As discussed in Section 2.3.(d), the hot film was used following the manufacturer guidelines and only for frequency measurements avoiding the particularly challenging calibration procedure needed for velocity measurements. The sampling parameters and the filtering of the signals were set so that the measurement errors in the signal spectra were minimized. The hot film measurements confirmed and extended the observations from pressure fluctuations on low frequency unsteadiness on the wing surface as effect of the initial rolling up of the vortex.

Smoke visualizations in the early wake (presented in Section 3.6) further studied the unsteadiness of the trailing vortex and in particular the movement of the vortex centre. Two methods for the localization of the vortex centre from smoke visualizations were implemented and compared in Appendix B where a comparative study on the main parameters is also presented. The procedure used in the present investigation was then accurately chosen. The validity of this technique is based on the reliability of the darker region centroid as a good description of the vortex centre, which is a good assumption when smoke particles accurately follow the flow, for high smoke density, for low buoyancy forces, for high image resolution and for darker spots of the order of the vortex core. All these factors were satisfied for these experiments.

SECTION 2

SPIV

Errors in the velocity information derived from SPIV come from a variety of sources such as from the optical system, experimental set-up, image reconstruction method, image digitisation, seeding quality, correlation process and post-processing of the images (for some theoretical and applied accounts, see for example Raffel *et al.*, 2007; Ramasamy & Leishman, 2007; Nathan, 2010; Gupta, 2011). However, some of the errors

can be rectified through implementation of post-processing algorithms and by following guidelines from other similar experiments (Raffel *et al.*, 2007).

The set-up of the camera position and angular displacement, the choice and positioning of the calibration plate, the focusing of the image, the calibration procedure and the calculation of the mapping function were accomplished following the guidelines of the PIV system manufacturer (DaVis, 2007) and adopting the relative software DaVis 7.2. The quality of the calibration process was given by the software in terms of average deviation of the dewarped marker positions of the calibration plate to the ideal regular grid. A value always lower than 0.3 pixel was calculated, which ensured an *excellent* calibration of the system (DaVis, 2007).

The digitisation of the smoke visualizations can be one of the most limiting sources of errors for the velocity information accuracy (Nathan, 2010). Digitisation effects in PIV occur when the imaged flow seeding particles are too small in size to be adequately defined as a distinctive image, which is an effect of the limited spatial resolution of the CCD sensors used in digital cameras. The limited pixel size of these cameras results in reduced fine detail resolution, at a given magnification. The small tracer particles in the flowfield are thus imaged without an accurate profile (Green, 2012) and the displacements derived from the correlation processes tend to be biased to integer-values resulting in clusters of vectors in the derived velocity maps to have block-like appearances. This phenomenon is known as *peak-locking* and histograms relating to the velocities will show peaks at integer values (Raffel *et al.*, 2007).

The camera lenses and the position of the cameras during the experiments were accurately chosen in order to minimize the peak-locking effects and the particle size on the image plane was between 1 and 2 pixels (Prasad *et al.*, 1992). Errors from an improper seeding density of the flowfield were minimized ensuring sufficiently populated interrogation windows (Hart, 2000; Keane & Adrian, 1992). The time delay between the two laser pulses was also accurately calculated (see Appendix A.1) and the peak-locking effect in the velocity maps was calculated by DaVis 7.2 to have an average value well within the acceptable range (DaVis, 2007).

The image processing procedure also can be a source of large errors in the velocity vector evaluation. An appropriate choice of interrogation window size, overlap and processing procedure is fundamental in the accuracy of the calculated velocity vector field (Adrian, 1991). A study on the effects of the different parameters is presented in Appendix A.2 and the vector field computation process used during these experiments is described in Section 2.3.(e).

From the discussion above, the results from the cross-correlation procedure optimization (in Appendix A.2) and referring to the work of Nathan & Green (2012) who also evaluated the accuracy of the same PIV system with a similar set-up, an absolute accuracy of the SPIV on the velocity vectors better than 2% can be claimed for the present investigation, which is adequate for quantitative analysis of the flow. This value has to be intended for a generalized error on the evaluation of the instantaneous velocity vector fields. From the convergence of the averages presented in Section 4.1.(d), an accuracy better than 2% can be taken also for the averaged velocity fields based on the 121 samples used throughout this work. Nevertheless, quantities involving derivatives and velocity fluctuations, such as vorticity, helicity, normal stress, Reynolds stress and shear strain, are expected to exhibit lower accuracy than the velocity vectors. In Section 4.1.(d), the highest error was equal to 7% and found for the Reynolds shear stress. However, the averaging convergence errors were calculated on the peak values of the quantities which leads to an overestimation of the global measurement errors.

Conclusions and recommendations for future work

If the research that we do does not change the way people think, the project is a fail.

GEORGE M. WHITESIDES

Behold, the fear of the Lord, that is wisdom, and to turn away from evil is understanding.

JOB, *Bible*

This chapter summarizes the major findings of the present research with reference to the unresolved issues presented in Section 1.4 and discusses some of their implications. In addition, recommendations are made for future research related to the wingtip vortex flow.

SECTION 1

Conclusions

The formation and the early wake of a trailing vortex behind a rectangular wing has been studied with different experimental techniques, specifically with surface oil flow visualization, surface pressure measurement through pressure tappings, smoke visualization of the vortex formation, measurement of the unsteadiness of the surface flow through wall pressure fluctuation and hot film mounted on the surface, stereoscopic particle image velocimetry on planes parallel to the wing surface and on planes perpendicular to the freestream velocity in the wake. The integration of complementary

results from these techniques reaches a deeper understanding of the physics and main mechanisms of the early stage of the vortex flow. The effects of several parameters on the interaction of these mechanisms have been addressed generating a fuller overall view of this flow based on a wide range of experiments. In particular, two symmetric NACA rectangular wing models with different chord (0.42 and 0.76 m) and aspect ratio (3.1 and 0.75) have been tested in a range of angle of attack of $\alpha = 0^\circ$ – 20° , Reynolds number of $Re = 3 \cdot 10^3$ – $1.27 \cdot 10^6$ and wake plane position of $x_w = 0.25$ – 2 . Also, the comparison between the vortex flow generated by squared and rounded wingtip geometries have been tested. The high spatial resolution on this vortex flow in the early wake achieved by the SPIV arrangement and the largeness of this parametric study represent a unique feature of these measurements which advances the current state of understanding on this particular flow.

A set of characteristic lines were defined based on the three components of the velocity on planes parallel to the suction surface and at a small distance from it. This small distance (of about 7% of the chord) allowed a good correlation between the velocity field obtained by SPIV and the surface flow experiments (oil visualization and wall pressure). These characteristic lines have been revealed to be a compact and accurate tool in describing the vortex structure and its development along the wing. The primary vortex is created by the separation of the flow coming from pressure surface which forms a vortical structure moving downstream along the wingtip region; depending on the instantaneous pressure field, the vortex origin is not fixed but showed oscillations in the chordwise direction. An intense secondary vortex is observed between the primary vortex and the tip and a high level of turbulent kinetic energy is measured at the primary vortex separation line. The primary vortex unsteadiness is forced by the secondary vortex dynamics which is then related to the boundary layer separation unsteadiness on the tip. The tip geometry is a major parameter in the formation mechanism and early development of the vortex system. The square tip presents two sharp edges and it produces a multiple vortex structure with highly unsteady and intense secondary structures. The rounded tip does not force the flow separation and a more axisymmetric structure of the vortical system is observed. Moreover, secondary vortices are weaker and the process of rolling up of the wake sheet around the primary vortex is smoother.

Despite the basic geometry of a rectangular wing with squared or rounded wingtip, the vortical flow in the early wake is extremely complex and reveals a number of peculiar and very challenging phenomena which are hardly described by current numerical

simulations. The vortex structure is not axisymmetric and the definition of a core shape based on directional core radii revealed a spiral geometry which rotation rate and evolution toward a circular shape are functions of wingtip geometry and vortex strength.

As commonly done nowadays in the mid field of trailing vortices, it was demonstrated also for the early wake the importance of centering each instantaneous vector field before the average was taken, particularly on the evaluation of the axial flow and the turbulence within the vortex core. This operation is based on a definition of vortex centre. Several definitions found in the literature have been compared and, for velocity fields obtained from a SPIV, the peak of the streamwise helicity component was found the most satisfactory. An analysis on the number of samples required for the description of the vortex has been performed showing that a number between 100 and 150 instantaneous samples is enough for the statistical convergence of shapes and centre values of most of the quantities of a trailing vortex from a fixed wing.

The comparison between the unsteadiness of the vortex system during the formation on the wing and the fluctuation of the vortex centre in the early wake revealed the interaction between primary and secondary vortex as the major source of meandering. The main source of periodic unsteadiness on the wingtip vortex (between 1 and 2 Hz) is associated to a low frequency movement of the secondary vortex, predominantly in the spanwise direction. An increase in the wandering dominant frequency was observed with an increase of Reynolds number and angle of attack suggesting a link of the wandering with the strength of the vortex. In the early wake of the wingtip vortex and its unsteadiness, the rolling up of the wake sheet and the merging of secondary vortices have been observed as the two main phenomena. Depending on the wingtip geometry and the angle of attack, and so on the strength of secondary vortices, one of the two mechanisms was predominant and a different turbulence development inside the vortex was observed. Intense secondary vortices interactions (promoted by high angles of attack and squared tip) generated a remarkable asymmetric structure and enhanced the fluid mixing between the flow within the vortex core and the external flow which promoted the dissipation of the turbulence near the vortex axis. An initial increase of the turbulence at the centre of the vortex with the distance from the trailing edge was observed in cases with high radial gradients of the axial velocity and low mixing of fluid (which is promoted by moderate angles of attack and rounded tip). However, this process is only temporary and a partial or complete relaminarization of the vortex core was observed throughout the experiments depending on the radial gradient of the axial velocity and the initial turbulence level within the core.

The vortex axial flow has been deeply studied. In particular, the study of the equilibrium between the acceleration mechanism (due to the helical shape of the vortex lines and the radial pressure gradient balancing the centrifugal forces) and the viscous dissipation (from the mixing of the wake sheet and the boundary layer with the flow within the core) revealed different shapes of the axial flow distribution. The axial flow quickly tended to a bell-shaped profile with flow in the vortex core showing either deficit (wake-like flow) or excess (jet-like flow). However, in the very early wake, the axial velocity at the vortex axis always appeared as an excess compared to the surrounding flow although, for weak vortices, its magnitude was lower than the freestream velocity. A linear relationship between the axial velocity peak with the vortex circulation parameter $\left(\frac{\Gamma}{U_\infty b} AR\right)$ was suggested which correlated quite well also with other studies. The gradient of this curve was found to be function of the wingtip geometry with a higher gradient for the rounded tip intersecting the squared tip curve for a parameter value of 0.95. Switchover angles between jet-like and wake-like flows were found of around 4° and 7° respectively for the squared tip and the rounded tip, corresponding to vortex circulation parameters of around 0.13 and 0.11. The maximum averaged axial velocity found in this study was of $1.7U_\infty$ and the maximum instantaneous velocity was of around $2.2U_\infty$.

SECTION 2

Recommendations for future work

With the contributions of this work, the description of the vortex flow have reached a basic understanding of the physics involved in the formation and in the development in the early wake. While SPIV experiments provided adequate spatial resolution of the vortex characteristic lines and the vortical system development in the near wake, the only temporal information was recorded on the wing surface and at the vortex centre in the wake. Additional measurements of frequency spectra during the formation of the vortex could be performed and temporal information during the development in the wake could be investigated. High speed SPIV measurements are now established and could give more insights into the unsteadiness source and structure of the vortex flow.

Moreover, accurate and detailed measurements of a wide range of parameters have built a precise qualitative and quantitative picture of the main aspects of this vortical flow which can support the next steps in a further development of prediction methods,

wingtip modifications and active control devices. The use of these data as a benchmark for computational fluid dynamics results is advised especially regarding the vortex system structure during the formation on the wing; the interaction between secondary vortices, wake sheet and primary vortex in the near wake; formation of the axial velocity; the shape of the Reynolds stresses in relation to the shear strains; turbulence organization and relaminarization process within the core. Also, the formation of a pair of vortices and their interaction with the wake sheet in the case of wing at zero angle of attack is suggested as a benchmark test for a correct prediction of the vortex system formation mechanism.

The relation between the structure of the vortex in the early wake, its early development and the wingtip geometries tested was identified in terms of vortex shape, vortex intensity, flow structure and turbulence production. It is believed that squared and rounded tips highlight the fundamental physics of the wingtip vortex formation. However, similar experiments on other wingtip geometries are suggested in order to verify the fundamental mechanisms on a wider range. For such studies, wing force measurements are advisable in order to relate the trailing vortex with the effect on the lift, drag and moment coefficients.

Lastly, the information on the dominant frequency of the vortex unsteadiness and the position of the vortical system on the wing surface offer a good base for experiments on active control devices. The positioning, intensity and frequency of such devices can be chosen in relation to the information gathered in this study. For example, blowing jets or surface mounted actuators could be used to promote and excite the flow at the unsteadiness frequency in order to enhance and accelerate the development of the vortex or to promote the occurrence of instabilities.

Bibliography

- ADRIAN, R. J. 1988 Double exposure, multiple-field particle image velocimetry for turbulent probability density. *Optics and Lasers Engineering* **9** (3-4), 211–228.
- ADRIAN, R. J. 1991 Particle-imaging technique for experimental fluid mechanics. *Annual Review of Fluid Mechanics* **23**, 261–304.
- ADRIAN, R. J., CHRISTENSEN, K. T. & LIU, Z. C. 2000 Analysis and interpretation of instantaneous turbulent velocity fields. *Experiments in Fluids* **29**, 275–290.
- ADRIAN, R. J. & WESTERWEEL, J. 2010 *Particle image velocimetry*. Cambridge University Press.
- ALBANO, F., DE GREGORIO, F. & RAGNI, A. 2003 Trailing vortex detection and quantitative evaluation of vortex characteristics by PIV technique. In *20th International Congress on Instrumentation in Aerospace Simulation Facilities*.
- ANDERSON, E. A. & LAWTON, T. A. 2003 Correlation between vortex strength and axial velocity in a trailing vortex. *Journal of Aircraft* **40** (4), 699–704.
- ANDERSON, JR., J. D. 2001 *Fundamentals of aerodynamics*, 3rd edn. Mc Graw-Hill International Edition.
- ARNDT, R. E. A. 2002 Cavitation in vortical flows. *Annual Review of Fluid Mechanics* **34**, 143–175.
- ARORA, P. R., HOSSAIN, A., EDI, P., JAAFAR, A. A., YOUNIS, T. S. & SALEEM, M. 2005 Drag reduction in aircraft model using elliptical winglet. *Journal of the Institution of Engineers, Malaysia* **66** (4).
- BAILEY, S. C. C. & TAVOULARIS, S. 2008 Measurements of the velocity field of a wing-tip vortex, wandering in grid turbulence. *Journal of Fluid Mechanics* **601**, 281–315.

- BAILEY, S. C. C., TAVOULARIS, S. & LEE, B. H. K. 2006 Effects of freestream turbulence on wing–tip vortex formation and near field. *Journal of Aircraft* **43**, 1282–1291.
- BAKER, G. R., BARKER, S. J., BOFAH, K. K. & SAFFMAN, P. G. 1974 Laser anemometer measurements of trailing vortices in water. *Journal of Fluid Mechanics* **65** (2), 325–336.
- BANDYOPADHYAY, P. 1990 The organized nature of a turbulent trailing vortex. In *AIAA 21st Fluid Dynamics, Plasma Dynamics and Lasers Conference, 18-20 June*. Seattle, WA.
- BATCHELOR, G. K. 1964 Axial flow in trailing line vortices. *Journal of Fluid Mechanics* **20** (4), 645–658.
- BELLHOUSE, B. J. & SCHULTZ, D. L. 1966 Determination of mean and dynamic skin friction, separation and transition in low–speed flow with a thin–film heated element. *Journal of Fluid Mechanics* **24** (2), 379–400.
- BERESH, S. J. & HENFLING, J. F. 2010 Meander of fin trailing vortex and the origin of its turbulence. *Experiments in Fluids* **49**, 599–611.
- BILLANT, P., CHOMAZ, J. M. & HUERRE, P. 1998 Experimental study of vortex breakdown in swirling jets. *Journal of Fluid Mechanics* **376**, 183–219.
- BIRCH, D. M. 2012 Self–similarity of trailing vortices. *Physics of Fluids* **24** (025105).
- BIRCH, D. M. & LEE, T. 2005 Investigation of the near–field top vortex behind an oscillating wing. *Journal of Fluid Mechanics* **544**, 201–241.
- BIRCH, D. M., LEE, T., MOKHATARIAN, F. & KAFYEKE, F. 2003 Rollup and near–field behavior of a tip vortex. *Journal of Aircraft* **40** (3), 603–607.
- BIRCH, D. M., LEE, T., MOKHATARIAN, F. & KAFYEKE, F. 2004 Structure and induced drag of a tip vortex. *Journal of Aircraft* **41** (5), 1138–1145.
- BOILLOT, A. & PRASAD, A. K. 1996 Optimization procedure for pulse separation in cross–correlation PIV. *Experiments in Fluids* **21**, 87–93.
- BRADSHAW, P. 1969 The analogy between streamline curvature and buoyancy in turbulent shear flow. *Journal of Fluid Mechanics* **36** (1), 177–191.

- BREITSAMTER, C. & ALLEN, A. 2009 Transport aircraft wake influenced by oscillating winglet flaps. *Journal of Aircraft* **46** (1), 175–188.
- CAI, J. 2006 LES for wing tip vortex around an airfoil. PhD thesis, University of Texas at Arlington, Arlington, TX.
- CHAMBERS, J. R. 2003 Concept to reality: contribution of the NASA Langley Research Center to U.S. civil aircraft of the 1990s. Nasa sp-2003-4529. NASA.
- CHATTOT, J. 2007 Helicoidal vortex model for wind turbine aeroelastic simulation. *Computers and Structures* **85**, 1072–1079.
- CHIGIER, N. 1974 Vortexes in aircraft wakes. *Scientific American* **230**, 76–83.
- CHIGIER, N. A. & CORSIGLIA, V. R. 1971 Tip vortices - Velocity distributions. Nasa technical memorandum x-62,087. NASA.
- CHIGIER, N. A. & CORSIGLIA, V. R. 1972 Wind-tunnel studies on wing wake turbulence. *Journal of Aircraft* **9** (12), 820–825.
- CHOW, J., ZILLIAC, G. & BRADSHAW, P. 1997a Turbulence measurements in the near field of a wingtip vortex. Nasa technical memorandum 110418. NASA.
- CHOW, J. S., ZILLIAC, G. G. & BRADSHAW, P. 1992 Initial roll-up of a wingtip vortex. In *Proceedings of the aircraft wake vortices conference*, , vol. 2. Federal Aviation Administration.
- CHOW, J. S., ZILLIAC, G. G. & BRADSHAW, P. 1997b Mean and turbulence measurements in the near field of a wingtip vortex. *AIAA Journal* **35** (10), 1561–1567.
- CHURCHFIELD, M. J. & BLAISDELL, G. A. 2009 Numerical simulations of a wingtip vortex in the near field. *Journal of Aircraft* **46** (1), 230–243.
- CONLISK, A. T. & KOMERATH, N. M. 2001 The origin and structure of trailing vortices in aerodynamics. Final report. Georgia Institute of Technology.
- COTEL, A. J. & BREIDENTHAL, R. E. 1999 Turbulence inside a vortex. *Physics of Fluids* **11** (10), 3026–3029.
- COTEL, A. J. & BREIDENTHAL, R. E. 2002 Turbulence inside a vortex: take two. *Physics of Fluids* **14** (8), 2933–2934.

- CRAFT, T. J., GERASIMOV, A. V., LAUNDER, B. E. & ROBINSON, C. M. E. 2006 A computational study of the near-field generation and decay of wingtip vortices. *International Journal of Heat and Fluid Flow* **27**, 684–695.
- CROUCH, J. D. 1997 Instability and transient growth for two trailing-vortex pairs. *Journal of Fluid Mechanics* **350**, 311–330.
- CROW, S. C. 1970 Stability theory for a pair of trailing vortices. *AIAA Journal* **8** (12), 2172–2179.
- CUCITORE, R., QUADRIO, M. & BARON, A. 1999 On the effectiveness and limitations of local criteria for the identification of a vortex. *European Journal of Mechanics - B/Fluids* **18** (2), 261–282.
- DACLES-MARIANI, J. S. & KWAK, D. 1996 Accuracy assessment of a wingtip vortex flowfield in the near-field region. In *34th AIAA Aerospace Sciences Meeting & Exhibit*. Reno, NV.
- DACLES-MARIANI, J. S., ROGERS, S., KWAK, D., ZILLIAC, G. G. & CHOW, J. S. 1993 A computational study of wingtip vortex flowfield. In *24th AIAA Fluid Dynamics Conference*. Orlando, FL.
- DACLES-MARIANI, J. S., ZILLIAC, G. G., CHOW, J. S. & BRADSHAW, P. 1997 Numerical/experimental study of a wingtip vortex in the near field. *AIAA Journal* **33** (12), 1561–1568.
- DAVIS 2007 *DaVis 7.2 Software - Product Manual*. Germany: LaVision GmbH.
- DEL PINO, C., FERNANDEZ-PRATS, R., LOPEZ-ALONSO, J. M., PARRAS, L. & FERNANDEZ-FERIA, R. 2010 Experimental axial evolution of the wing-tip vortex in the near field of a NACA 0012 airfoil. In *RAeS Aerodynamic Conference 2010. Applied Aerodynamics: Capabilities and Future Requirements*. Bristol, UK.
- DEL PINO, C., LOPEZ-ALONSO, J. M., PARRAS, L. & FERNANDEZ-FERIA, R. 2009 Dynamics of the wing-tip vortex in the near field of a NACA 0012 airfoil. In *CEAS 2009 European Air and Space Conference, 26-29 October*. Manchester, UK.
- DEL PINO, C., PARRAS, L., FELLI, M. & FERNANDEZ-FERIA, R. 2011 Structure of trailing vortices: comparison between particle image velocimetry measurements and theoretical models. *Physics of Fluids* **23**.

- DELERY, J. M. 2001 Robert Legendre and Henri Werle: toward the elucidation of three-dimensional separation. *Annual Review of Fluid Mechanics* **33**, 129–154.
- DEVENPORT, W. J., RIFE, M. C., LIPIAS, S. I. & FOLLIN, G. J. 1996 The structure and development of a wing-tip vortex. *Journal of Fluid Mechanics* **312**, 67–106.
- DEVENPORT, W. J., ZSOLDOS, J. S. & VOGEL, C. M. 1997 The structure and development of a counter-rotating wing-tip vortex pair. *Journal of Fluid Mechanics* **332**, 71–104.
- DIETERLE, L., EHRENFRIED, K., STUFF, R., SCHNEIDER, G., COTON, P., MONNIER, J. C. & LOZIER, J. F. 1999 Quantitative flow field measurements in a catapult facility using particle image velocimetry. In *18th International Congress on Instrumentation in Aerospace Simulation Facilities*.
- DURASAMY, K. 2005 Studies in tip vortex formation, evolution and control. PhD thesis, University of Maryland, College Park, MD.
- DURASAMY, K. & IACCARINO, G. 2005 Curvature correction and application of the $\overline{v^2}$ - f turbulence model to tip vortex flows. In *Center for Turbulence Research, Annual Research Briefs*.
- DURASAMY, K. & LELE, S. K. 2008 Evolution of isolated turbulent trailing vortices. *Physics of Fluids* **20** (035102).
- DURBIN, P. A. 1991 Near-wall turbulence closure modelling without damping functions. *Theoretical and Computational Fluid Dynamics* **3**, 1–13.
- FABRE, D. & JACQUIN, L. 2000 Stability of a four-vortex aircraft wake model. *Physics of Fluids* **12** (10), 2438–2443.
- FABRE, D., JACQUIN, L. & LOOF, A. 2002 Optimal perturbations in a four-vortex aircraft wake in counter-rotating configuration. *Journal of Fluid Mechanics* **451**, 319–328.
- FRANCIS, M. S. 1976 An experimental investigation of wing trailing vortex formation. Final report. United States Air Force Systems Command.
- FRANCIS, T. B. & KATZ, J. 1988 Observations on the development of a tip vortex on a rectangular hydrofoil. *Journal of Fluids Engineering* **110**, 208–215.

- FRANCIS, T. B. & KENNEDY, D. A. 1979 Formation of a trailing vortex. *Journal of Aircraft* **16** (3), 148–154.
- GERZ, T., HOLZAPFEL, G. & DARRACQ, D. 2001 Aircraft wake vortices -A position paper-. In *WakeNet Position Paper*.
- GIUNI, M. & BENARD, E. 2011 Analytical/Experimental comparison of the axial velocity in trailing vortices. In *49th AIAA Aerospace Sciences Meeting*. Orlando, FL.
- GIUNI, M., BENARD, E. & GREEN, R. B. 2010 Near field core structure of wing tip vortices. In *Experimental Fluid Mechanics 2010*. Liberec, Czech Republic: EFM.
- GOVINDARAJU, S. P. & SAFFMAN, P. G. 1971 Flow in a turbulent trailing vortex. *The Physics of Fluids* **14** (10).
- GRANT, I. 1997 Particle image velocimetry: a review. In *Proceedings Institute of Mechanical Engineers*, , vol. 211, pp. 55–76.
- GREEN, R. B. 2012 Optical methods. In *Experimental Aerodynamic 5 – Lectures Notes*.
- GREEN, S. I. 1995 Fluid vortices. In *Fluid Mechanics and its Applications*, pp. 427–470. Kluwer Academic Publisher.
- GREEN, S. I. & ACOSTA, A. J. 1991 Unsteady flow in trailing vortices. *Journal of Fluid Mechanics* **227**, 107–134.
- GREENBLATT, G. 2005 Management of vortices trailing flapped wings via separation control. In *43rd AIAA Aerospace Sciences Meeting and Exhibit*. Reno, NV: AIAA.
- GREENBLATT, G. & MEYER, R. 2009 Flap vortex management using active Gurney flaps. *AIAA Journal* **47** (12), 2845–2856.
- GROW, T. L. 1969 Effect of a wing on its tip vortex. *Journal of Aircraft* **6** (1), 37–41.
- GUPTA, M. 2011 Investigation of active control of aircraft wing tip vortices and wake turbulence. Master’s thesis, Auburn University, AL.
- GURSUL, I. 2004 Recent development in delta wing aerodynamics. *The Aeronautical Journal* pp. 437–452.
- GURSUL, I., VARDAKI, E., MARGARIS, P. & WANG, Z. 2007 Control of wing vortices. In *Active Flow Control*, pp. 137–151. Springer.

- HALLER, G. 2005 An objective definition of a vortex. *Journal of Fluid Mechanics* **525**, 1–26.
- HALLETT, W. L. H. & TŌEWS, D. J. 1987 The effects of inlet conditions and expansion ratio on the onset of flow reversal in swirling flow in a sudden expansion. *Experiments in Fluids* **5**, 129–133.
- HART, D. P. 2000 PIV error correction. *Experiments in Fluids* **29**, 13–22.
- HASELBACK, F. & NITSCHKE, W. 1996 Calibration of single-surface hot films and in-line hot-film arrays in laminar or turbulent flow. *Measurement Science and Technology* **7**, 1428–1438.
- HAVERKAMP, S., NEUWERTH, G. & JACOB, D. 2005 Active and passive vortex wake mitigation using control surfaces. *Aerospace Science and Technology* **9**, 5–18.
- HELMAN, J. L. & HUSSELINK, L. 1989 Representation and display of vector field topology in fluid flow data sets. *IEEE Computer* **22** (8), 27–36.
- HEYES, A. L., JONES, R. F. & SMITH, D. A. R. 2004 Wandering of wing-tip vortices. In *12th International Symposium on Application of Laser Techniques to Fluid Mechanics*. Lisbon, Portugal.
- HEYES, A. L. & SMITH, D. A. R. 2004 Spatial perturbation of a wing-tip vortex using pulsed span-wise jets. *Experiments in Fluids* **37**, 120–127.
- HINSCH, K. D. 1995 Three-dimensional particle velocimetry. *Measurement Science and Technology* **6**, 742–753.
- HODSON, H. P. 1985 A blade to blade prediction of a wake generated unsteady flow. *ASME Journal of Engineering for Gas Turbines and Power* **107**.
- HOFFMANN, E. R. & JOUBERT, P. N. 1963 Turbulent line vortices. *Journal of Fluid Mechanics* **16**, 395–411.
- HOLZÄPFEL, F., GERZ, T. & BAUMANN, R. 2001 The turbulent decay of trailing vortex pairs in stably stratified environments. *Aerospace Science and Technology* **5**, 95–108.
- HOUGHTON, E. L. & CARPENTER, P. V. 2003 *Aerodynamics for engineering students*, 5th edn. Butterworth Heinemann.

- HUMMEL, D. 1983 Aerodynamic aspects of formation flight in birds. *Journal of Theoretical Biology* **104**, 321–347.
- HÜNECKE, K. 2001 Wake vortex control - A challenge for large transport aircraft. *Air & Space Europe* **3**, 209–213.
- IGARASHI, H., DURBIN, P. A., HU, H., WALTERMIRE, S. & WEHRMEYER, J. 2011 The effects of wind tunnel walls on the near-field behavior of a wingtip vortex. In *49th AIAA Aerospace Sciences Meeting*. Orlando, FL.
- IGARASHI, H., DURBIN, P. A., MA, H. & HU, H. 2010 A stereoscopic PIV study of a near-field wingtip vortex. In *48th AIAA Aerospace Sciences Meeting*. Orlando, FL.
- IGLESIAS, S. & MASON, W. H. 2002 Optimum spanloads in formation flight. In *40th AIAA Aerospace Sciences Meeting*. Reno, NV.
- IVERSEN, J. D. 1976 Correlation of turbulent trailing vortex decay data. *Journal of Aircraft* **13** (5), 338–342.
- JACQUIN, L., FABRE, D. & GEFFROY, P. 2001 The properties of a transport aircraft wake in the extended near field: an experimental study. In *39th AIAA Aerospace Sciences Meeting & Exhibit*. Reno, NV: AIAA.
- JACQUIN, L., FABRE, D., SIPP, D. & COUSTOLS, E. 2005 Unsteadiness, instability and turbulence in trailing vortices. *Comptes Rendus Physique* **6**, 399–414.
- JACQUIN, L. & PANTANO, C. 2002 On the persistence of trailing vortices. *Journal of Fluid Mechanics* **471**, 159–168.
- JEONG, J. & HUSSAIN, F. 1995 On the identification of a vortex. *Journal of Fluid Mechanics* **285**, 69–94.
- JIANG, L., CAI, J. & LIU, C. 2007 Large eddy simulation of wing tip vortex in the near field. *Tech. Rep. 13*. The University of Texas, Arlington.
- KADEN, H. 1931 Aufwicklung einer unstablen unstetigkeitsfläche. *Ingenieur Archiv* **2**, 140–168, English translation, Royal Aircraft Establishment 403.
- KARAKUS, C., AKILLI, H. & SAHIN, B. 2008 Formation, structure, and development of the near-field wing tip vortices. *Proceedings of the Institution of Mechanical Engineers, Part G: Journal of Aerospace Engineering* **222**, 13–22.

- KEANE, R. D. & ADRIAN, R. J. 1990 Optimization of particle image velocimeters. Part I: double pulsed systems. *Measurements Science and Technology* **1**, 1202–1215.
- KEANE, R. D. & ADRIAN, R. J. 1992 Theory of cross-correlation analysis of PIV images. *Applied Scientific Research* **49**, 191–215.
- KENWRIGHT, D. N. 1998 Automatic detection of open and closed separation and attachment lines. In *IEEE Computer Society Press* (ed. IEEE Visualization Proceedings), pp. 151–158. Los Alamitos, CA.
- KHORRAMI, M. R. 1991 On the viscous modes of instability of a trailing line vortex. *Journal of Fluid Mechanics* **225**, 197–212.
- KIM, S. E. & RHEE, S. H. 2005 Prediction of tip-vortex flow past a finite wing. In *43th AIAA Aerospace Sciences Meeting & Exhibit*. Reno, NV.
- KRASNY, R. 1987 Computation of vortex sheet roll-up in the Trefftz plane. *Journal of Fluid Mechanics* **184**, 123–155.
- LAURENCE, D. R., URIBE, J. C. & UTYUZHNIKOV, S. V. 2004 A robust formulation of the v2-f model. *Flow, Turbulence and Combustion* **73**, 169–185.
- LAWSON, N. J. & WU, J. 1997 Three-dimensional particle image velocimetry: error analysis of stereoscopic techniques. *Measurements Science and Technology* **8**, 894–900.
- LEE, T. & PEREIRA, J. 2010 Nature of wakelike and jetlike axial tip vortex flows. *Journal of Aircraft* **47** (6), 1946–1954.
- LEISHMAN, J. G. 1998 Measurements of the aperiodic wake of a hovering rotor. *Experiments in Fluids* **25**, 352–361.
- LEWEKE, T. & WILLIAMSON, C. H. K. 1998 Cooperative elliptic instability of a vortex pair. *Journal of Fluid Mechanics* **360**, 85–119.
- LIN, J. C. 2002 Review of research on low profile vortex generators to control boundary layer separation. *Progress in Aerospace Sciences* **38**, 389–420.
- LOCKARD, D. P. & MORRIS, P. J. 1998 Wing-tip vortex calculations using high-accuracy scheme. *Journal of Aircraft* **35** (5), 728–738.
- LOCKNEY, D., SCHWERIN, B. & RADEMAKERS, L. 2010 Winglets save billions of dollars in fuel costs. In *Spinoff - NASA technologies benefit society*.

- LU, F. K. 2010 Surface oil flow visualization (still useful after all these years). *The European Physical Journal Special Topics* **182**, 51–63.
- LUCCA-NEGRO, O. & O'DOHERTY, T. 2001 Vortex breakdown: a review. *Progress in Energy and Combustion Science* **27**, 431–481.
- MARSHALL, J. S. 2005 Particle dispersion in a turbulent vortex core. *Physics of Fluids* **17** (025104).
- MASSOUH, F. & DOBREV, I. 2007 Exploration of the vortex wake behind of wind turbine rotor. In *Journal of Physics: Conference Series*, , vol. 75.
- MCALISTER, K. W. & TAKAHASHI, R. K. 1991 Wing pressure and trailing vortex measurements. Technical report 3151. NASA.
- MELLING, A. 1997 Tracer particles and seeding for particle image velocimetry. *Measurements Science and Technology* **8**, 1406–1416.
- MERZKIRCH, W. 1987 *Flow visualization*, 2nd edn. Academic Press.
- MITCHELL, A. M. & DELERY, J. 2001 Research into vortex breakdown control. *Progress in Aerospace Sciences* **37**, 385–418.
- MOORE, D. W. & SAFFMAN, P. G. 1973 Axial flow in laminar trailing vortices. *Proceedings of the Royal Society A* **333**, 491–508.
- MORTON, B. R. 1969 The strength of vortex and swirling core flows. *Journal of Fluid Mechanics* **38** (2), 315–333.
- MUDKAVI, V. Y. 1993 The phenomenon of vortex breakdown. In *Proceedings of the Fluid Dynamics Symposium in honour of Professor R. Narashima on his 60th birthday*. Sikim, India.
- NAIMAN, A. D., LELE, S. K., WILKERSON, J. T. & JACOBSON, M. Z. 2009 A low-order contrail model for use with global-scale climate models. In *47th AIAA Aerospace Sciences Meeting*. Orlando, FL.
- NARASIMHA, R. & SREENIVASAN, K. R. 1979 Relaminarization of fluid flows. *Advances in Applied Mechanics* **19**, 221–309.
- NATHAN, N. D. 2010 The rotor wake in ground effect and its investigation in a wind tunnel. PhD thesis, University of Glasgow, Glasgow, UK.

- NATHAN, N. D. & GREEN, R. B. 2012 The flow around a model helicopter main rotor in ground effect. *Experiments in Fluids* **52**, 151–166.
- OKADA, A. & LANE, D. 1997 Enhanced line integral convolution with flow feature detection. *SPIE* **3017**, 206–217.
- ORLOFF, K. L. 1974 Trailing vortex wind-tunnel diagnostics with a laser velocimeter. *Journal of Aircraft* **11** (8), 477–482.
- PAGENDARM, H. G. & WALTER, B. 1994 Feature detection from vector quantities in a numerically simulated hypersonic flow field in combination with experimental flow visualization. In *Proceedings of IEEE Visualization*, pp. 117–123.
- PETTERSSON REIF, B. A., DURBIN, P. A. & OOI, A. 1999 Modeling rotational effects in eddy-viscosity closures. *International Journal of Heat and Fluid Flow* **20**, 563–573.
- PHILLIPS, W. R. C. 1981 The turbulent trailing vortex during roll-up. *Journal of Fluid Mechanics* **105**, 451–467.
- PHILLIPS, W. R. C. & GRAHAM, J. A. H. 1984 Reynolds-stress measurements in a turbulent trailing vortex. *Journal of Fluid Mechanics* **147**, 353–371.
- PIVTEC 2007 User manual: Aerosol generator PivPart40 series. *Tech. Rep.*. PIVTEC - GmbH.
- PRASAD, A. K. 2000 Stereoscopic particle image velocimetry. *Experiments in Fluids* **29**, 103–116.
- PRASAD, A. K., ADRIAN, R. J., LANDRETH, C. C. & OFFUTT, P. W. 1992 Effect of resolution on the speed and accuracy of particle image velocimetry interrogation. *Experiments in Fluids* **13**, 105–116.
- PRASAD, A. K. & JENSEN, K. 1995 Scheimpflug stereocamera for particle image velocimetry in liquid flows. *Applied Optics* **34** (30), 7092–7099.
- QUACKENBUSH, T. R., BILANIN, A. J. & CARPENTER, B. F. 1999 Test results from an SMA-actuated vortex wake control system. In *Proceedings of the society of photo-optical instrumentation engineers The international society for optical engineering*, p. 8494. Bellingham, WA: Society of Photo-Optical Instrumentation Engineers The International Society for Optical Engineering.

- R. A. HUMBLE, F. SCARANO, B. W. VAN OUDHEUSDEN 2007 Particle image velocimetry measurements of a shock wave/turbulent boundary layer interaction. *Experiments in Fluids* **42**, 173–183.
- RAFFEL, M., WILLERT, C., WERELEY, S. & KOMPENHANS, J. 2007 *Particle image velocimetry: a practical guide*, 2nd edn. Springer.
- RAMAPRIAN, B. R. & ZHENG, Y. 1997 Measurements in rollup region of the tip vortex from a rectangular wing. *AIAA Journal* **35** (12).
- RAMASAMY, M. 2004 Contributions to the measurement and analysis of helicopter blade tip vortices. PhD thesis, University of Maryland, College Park, MD.
- RAMASAMY, M., JOHNSON, B., HUISMANN, T. & LEISHMAN, J. G. 2009a Digital particle image velocimetry measurements of tip vortex characteristic using an improved aperiodicity correction. *Journal of the American Helicopter Society* **54** (012004).
- RAMASAMY, M., JOHNSON, B., HUISMANN, T. & LEISHMAN, J. G. 2009b Procedures for measuring the turbulence characteristics of rotor blade tip vortices. *Journal of the American Helicopter Society* **54** (022006).
- RAMASAMY, M., JOHNSON, B. & LEISHMAN, J. G. 2009c Turbulent tip vortex measurements using dual-plane stereoscopic particle image velocimetry. *AIAA Journal* **47** (8).
- RAMASAMY, M. & LEISHMAN, J. G. 2004 A generalized model for transitional blade tip vortices. In *American Helicopter Society 60th Annual Forum*. Baltimore, MD.
- RAMASAMY, M. & LEISHMAN, J. G. 2007 Benchmarking particle image velocimetry with laser doppler velocimetry for rotor wake measurements. *AIAA Journal* **45** (11).
- RAMASAMY, M., PAETZEL, R. & BHAGWAT, M. J. 2011 Aperiodicity correction for rotor tip vortex measurements. In *American Helicopter Society 67th Annual Forum*. Virginia Beach, VA.
- RENNICH, S. C. & LELE, S. K. 1999 Method for accelerating the destruction of aircraft wake vortices. *Journal of Aircraft* **36** (2), 398–404.
- ROSSOW, V. J. 1999 Lift-generated vortex wakes of subsonic transport aircraft. *Progress in Aerospace Sciences* **35**, 507–660.

- SAFFMAN, P. G. 1973 Structure of turbulent line vortices. *The Physics of Fluids* **16** (8), 1181–1188.
- SAFFMAN, P. G. 1974 The structure and decay of trailing vortices. *Archives of Mechanics* **26** (3), 423–439.
- SCARANO, F. 2002 Iterative image deformation methods in PIV. *Measurements Science and Technology* **13**, R1–R19.
- SHAPIRO, L. G. & STOCKMAN, G. C. 2001 *Computer vision*. Prentice Hall.
- SHARPKAYA, T. & DALY, J. J. 1987 Effect of ambient turbulence on trailing vortices. *Journal of Aircraft* **24**, 399–404.
- SHEKARRIZ, A., FU, T. C. & KATZ, J. 1993 Near-field behaviour of a tip vortex. *AIAA Journal* **31** (1), 112–118.
- SINGH, P. I. & UBEROI, M. S. 1976 Experiments on vortex stability. *The Physics of Fluids* **19** (12), 1858–1863.
- SNYDER, JR, M. H. & ZUMWALT, G. W. 1969 Effects of wingtip-mounted propellers on wing lift and induced drag. *Journal of Aircraft* **6** (5), 392–397.
- SOHN, M. H. & CHANG, J. W. 2011 Visualization and PIV study of wing-tip vortices for three different tip configurations. *Aerospace Science and Technology* **in press**.
- SPALART, P. R. 1998 Airplane trailing vortices. *Annual Review of Fluid Mechanics* **30**, 107–138.
- SPALL, R. E. 2001 Numerical study of a wing-tip vortex using the Euler equations. *Journal of Aircraft* **38** (1), 22–27.
- SPALL, R. E., GATSKI, T. B. & GROSCH, C. E. 1987 *On a criterion for vortex breakdown*. NASA, Langley Research Center.
- SQUIRE, L. C. 1961 The motion of a thin oil sheet under the steady boundary layer on a body. *Journal of Fluid Mechanics* **11** (2), 161–179.
- SURANA, A., GRUNBERG, O. & HALLER, G. 2006 Exact theory of three-dimensional flow separation. Part 1. Steady separation. *Journal of Fluid Mechanics* **564**, 57–103.
- TAYLOR, G. S. & GURSUL, I. 2004 Buffeting flows over a low-sweep delta wing. *AIAA Journal* **42** (9), 1737–1745.

- THOM, A. D. 2011 Analysis of vortex–lifting surface interactions. PhD thesis, University of Glasgow, Glasgow, UK.
- THOMPSON, D. H. 1983 A flow visualisation study to tip vortex formation. *Australian Aeronautical Research Lab Aero Note* **421**.
- TOBAK, M. & PEAKE, D. J. 1982 Topology of three–dimensional separated flows. *Annual Review of Fluid Mechanics* **14**, 61–85.
- TROOLIN, D. R., LONGMIRE, E. K. & LAI, W. T. 2006 Time resolved PIV analysis of flow over a NACA 0015 airfoil with Gurney flap. *Experiments in Fluids* **41**, 241–254.
- VERMEER, L. J., SØRENSEN, J. N. & CRESPO, A. 2003 Wind turbine wake aerodynamics. *Progress in Aerospace Sciences* **39**, 467–510.
- VOGT, A., BAUMANN, P., GHARIB, M. & KOMPENHANS, J. 1996 Investigations of a wing tip vortex in air by means of DPIV. In *19th AIAA Advanced Measurement and Ground Testing Technology Conference*. New Orleans, LA.
- VYSHINSKY, V. V. 2001 Flight safety, aircraft vortex wake and airport operation capacity: collection of papers. *Air & Space Europe* **3**, 206–208.
- VAN DER WALL, B. G., JUNKER, B., YU, Y. H., BURLEY, C. L., BROOKS, T. F., TUNG, C., RAFFEL, M., RICHARD, H., WAGNER, W., MERCKER, E., PENDEL, K., HOLTHUSEN, H., BEAUMIER, P. & DELRIEUX, Y. 2002 The HART II test in the LLF of the DNW A major step towards rotor wake understanding. In *28th European rotorcraft forum*. Bristol, UK.
- VAN DER WALL, B. G. & RICHARD, H. 2006 Analysis methodology for 3C-PIV data of rotary wing vortices. *Experiments in Fluids* **40**, 798–812.
- WHITMORE, S. A., LINDSEY, W. T., CURRY, R. E. & GILYARD, G. B. 1990 Experimental characterization of the effects of pneumatic tubing on unsteady pressure measurements. *Tech. Rep.*
- WIDNALL, S. E. 1975 The structure and dynamics of vortex filaments. *Annual Review of Fluid Mechanics* **7**, 141–165.
- WU, J. C. 2005 *Elements of vorticity aerodynamics*. Tsinghua University Press.
- WU, J. Z., MA, H. Y. & ZHOU, M. D. 2006 *Vorticity and vortex dynamics*. Springer.

- YANG, W. J. 1989 *Handbook of flow visualization*. Hemisphere Publishing Corporation.
- YANG, Z., SARKAR, P. & HU, H. 2012 Visualization of the tip vortices in a wind turbine wake. *Journal of Visualization* **12**, 39–44.
- YATES, J. E. & DONALDSON, C. 1986 Fundamental study of drag and an assessment of conventional drag–due–to–lift reduction devices. Nasa contractor report 4004. NASA.
- YAVUZ, M. M., ELKHOORY, M. & ROCKWELL, D. 2004 Near surface topology and flow structure on a delta wing. *AIAA Journal* **42** (2), 332–340.
- ZEMAN, O. 1995 The persistence of trailing vortices: a modeling study. *The Physics of Fluids* **7** (1), 135–143.
- ZILLIAC, G. G. 1988 Computational/experimental study of the flowfield on a body of revolution at incidence. *AIAA Journal* **27** (8), 1008–1016.
- ZUHAL, L. 2001 Formation and near–field dynamics of a wing tip vortex. PhD thesis, California Institute of Technology, Pasadena, CA.
- ZUHAL, L. & GHARIB, M. 2001 Near field dynamics of wing tip vortices. In *31st AIAA Fluid Dynamics Conference & Exhibit*. Anaheim, CA: AIAA.

Appendices

PIV: laser pulse separation and image processing

Particle image velocimetry measurements involve the choice and the finding of the best compromise of several parameters. The sensitivity of the measurements on such parameters and the resulting accuracy are addressed in this appendix with particular focus on the estimation and effect of the laser pulse separation in a double-exposure technique and the image processing procedure for the calculation of the vector field.

In Section A.1, the flowfields corresponding to the adoption of three different laser pulse separations of a reference wingtip vortex flow are compared in terms of averaged velocity, vorticity and turbulent fluctuations. The searching for the best compromise of the image processing procedure is presented in Section A.2 where the effects of the main parameters of the procedure are also individually discussed.

SECTION 1

Laser pulse separation tests

Time separation between successive laser pulses in PIV is a parameter that necessarily needs to be taken into special consideration. In a simplistic way, the pulse separation should be short enough in order to do not lose too many particles in the interrogation window and long enough to allow the slowest particles to move a resolvable distance.

As described by Boillot & Prasad (1996), the restrictions change if the correlation is an auto-correlation (two pulses on the same frame) or a cross-correlation (two pulses on two different frames). In cross-correlation, the delay time is independent on the interrogation window size d_I because the image processing procedure correlates an interrogation window with a second one which is displaced from the first window by an

amount equal to the local particle displacement vector $\Delta\mathbf{x}$ and possibly deformed by the shear stress (Scarano, 2002) as evaluated in a previous step.

Keane & Adrian (1992) showed that to achieve a valid detection probability of at least 90%, the image density (defined as the average number of particles per interrogation spot) must be greater than 15 with $\Delta\mathbf{x}/d_I < 0.3$. This means that the pulses separation can also be seen as the time that the particles need to cover 30% of the interrogation window. In this way it is possible to link Δt with geometric quantities and a pre-knowledge of the flow (i.e. maximum in-plane velocity):

$$\Delta t < \frac{0.3d_I}{\max|\mathbf{u}_{in-plane}|} \quad (\text{A.1})$$

When the out-of-plane velocity component is high and so is the probability of particle not being detected in the second pulse, a second pulse separation relation can be written changing the interrogation window dimension d_I with the laser sheet thickness d_L and using the maximum out-of-plane velocity component:

$$\Delta t < \frac{0.3d_L}{\max|\mathbf{u}_{out-of-plane}|} \quad (\text{A.2})$$

(a) Calculation of the pulse separation

The evaluation of the pulse separation for a reference vortex flow is here presented. The trailing vortex behind the **M1** at $x_w = 0.5$ for $\alpha = 12^\circ$ and $Re = 5 \cdot 10^5$ is adopted as reference. The corresponding freestream velocity is $U_\infty = 17.26$ m/s. For such a Reynolds number, a maximum in-plane velocity (swirl component) of around $0.9U_\infty$ and a maximum axial velocity of around $1.6U_\infty$ are expected (McAlister & Takahashi, 1991; Chow *et al.*, 1997a).

For these analysis, a double step image processing on an interrogation window of 64 by 64 pixels with 25% of overlap followed by other two steps with interrogation window of 32 by 32 pixels with 50% of overlap is adopted. The helicity peak method is applied for the centering of 121 vector fields before the average is taken.

Equation (A.1) can be applied indifferently either on the object plane or on the image plane (that is on the chip). In the first case, the interrogation window size will use a scale factor of 0.07145 mm/pixels (calculated during the calibration process) whereas in the latter case the equation will use the pixel dimension on the chip of 0.009 mm/pixel (from camera specifications) and the magnification of the lens of 7.94 (from calibration).

For an interrogation window size of 32 by 32 pixels, Equation (A.1) becomes:

$$\begin{aligned} \Delta t &< \frac{0.3 \cdot (32 \cdot 0.07145 \cdot 10^{-3})}{0.9 \cdot 17,26} = 44 \mu\text{s} && \text{on the object plane} \\ &< \frac{0.3 \cdot (32 \cdot 0.009 \cdot 10^{-3})}{(0.9 \cdot 17,26)/7.94} = 44 \mu\text{s} && \text{on the image plane} \end{aligned} \quad (\text{A.3})$$

The thickness of the laser sheet along the object plane is constant and equal to 3 mm. The laser pulse separation from Equation (A.2) can be then evaluated (on the object plane):

$$\Delta t < \frac{0.3 \cdot 0.003}{1.6 \cdot 17,26} = 33 \mu\text{s} \quad (\text{A.4})$$

The two separation times from Equations (A.3) and (A.4) show a similar value which implies a good experimental arrangement and accurate results for both the in-plane and out-of-plane velocity components. The in-plane separation is affected by the interrogation window size chosen during the image analysis where the out-of-plane separation is dictated by the laser sheet thickness.

In order to study the sensitivity of the laser pulse separation on the results, three time separations are compared: $\Delta t_1 = 15 \mu\text{s}$, $\Delta t_2 = 35 \mu\text{s}$ and $\Delta t_3 = 55 \mu\text{s}$.

One of the error affecting digital PIV is the peak-locking (Raffel *et al.*, 2007) where the computed velocity fields are biased toward discrete values, resulting in a velocity vector map to have block-like appearances. As a consequence, the velocity histogram for a peak-locked velocity field appears distorted, namely it is not continuous but it contains peaks at discrete values. This situation occurs primarily because of small size of the seeding particles producing a sub-pixel particle image on the camera chip or because particles, between the two pulses, move of a short distance on the image plane comparable to the pixel size. In-plane and out-of-plane velocity histograms were calculated for the three pulses delays showing no peak-locking effects, which indicates a well-conditioned experiment and analysis.

(b) Pulse separation comparison Cuts every 10 degrees around the vortex centre were made and the swirl velocity profiles along these radii were calculated. In Figure A.1, 12 of these profiles are shown along with the mean value.

The topology of the swirl velocity profiles change radically when the laser pulse separation changes. The two lower pulse separations show a high asymmetry of the vortex and a clear double peak, as observed also by McAlister & Takahashi (1991). A longer pulse separation does not show a double peak distribution but it only shows a

high asymmetry. The maximum swirl velocity also changes suggesting that with a Δt of $55 \mu\text{s}$ some faster particles are lost. It is also noted that the radius where the maximum averaged velocity is found is around the same position of about 0.05 chords.

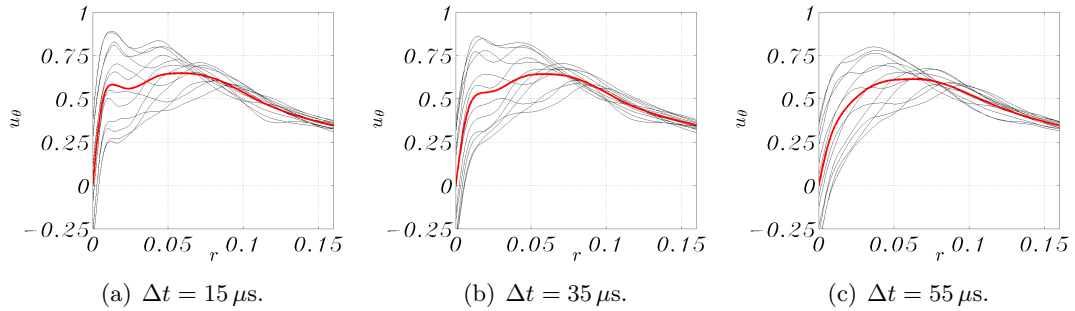


Figure A.1: Swirl velocity profiles for different laser pulse separations.

Axial velocity profiles are shown in Figure A.2. As for the swirl velocity, a similarity between the profiles obtained with laser pulse separation of $15 \mu\text{s}$ and $35 \mu\text{s}$ is found. Also, the same conclusions of loss of fast particles can be made since the longer pulse separation case shows a velocity deficit of 0.6 at the vortex centre compared to an excess of 0.5 for the shorter separations.

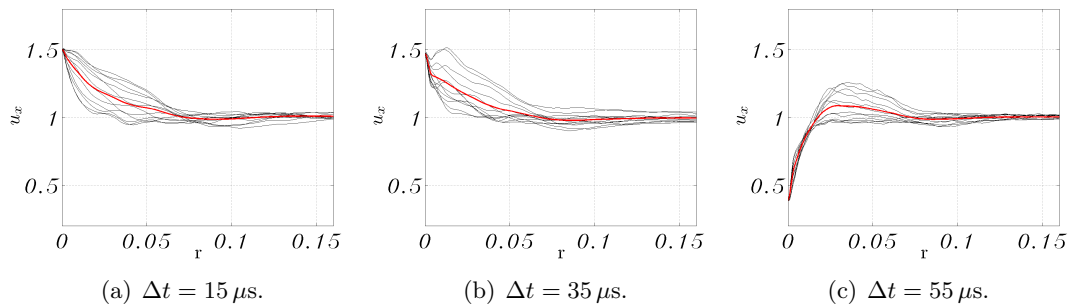


Figure A.2: Axial velocity profiles for different laser pulse separations.

Vorticity contours are compared in Figure A.3. A similar pattern is observed for all the cases although decreasing peak values on the vortex axis are found when the pulse separation is increased, respectively of 212, 170 and 119.

Velocity fluctuations in Figure A.4 show an increasing intensity with the increase of the pulse separation. For $\Delta t = 15 \mu\text{s}$ and $35 \mu\text{s}$, the tail due to the wake sheet rolling up around the main vortex can be clearly detected, whereas for $\Delta t = 55 \mu\text{s}$, contours show intense fluctuations more spread around the centre. However, developments along horizontal and vertical axis of σ_v and σ_w for all the cases is observed.

The results showed that a long pulses separation introduces more turbulence and

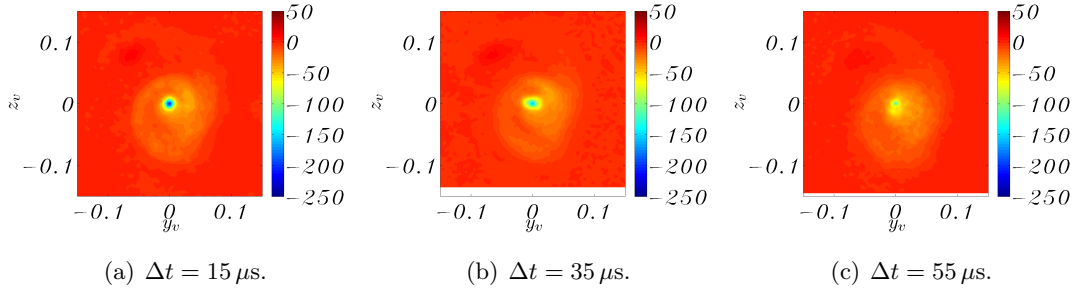


Figure A.3: Vorticity contours for different laser pulse separations.

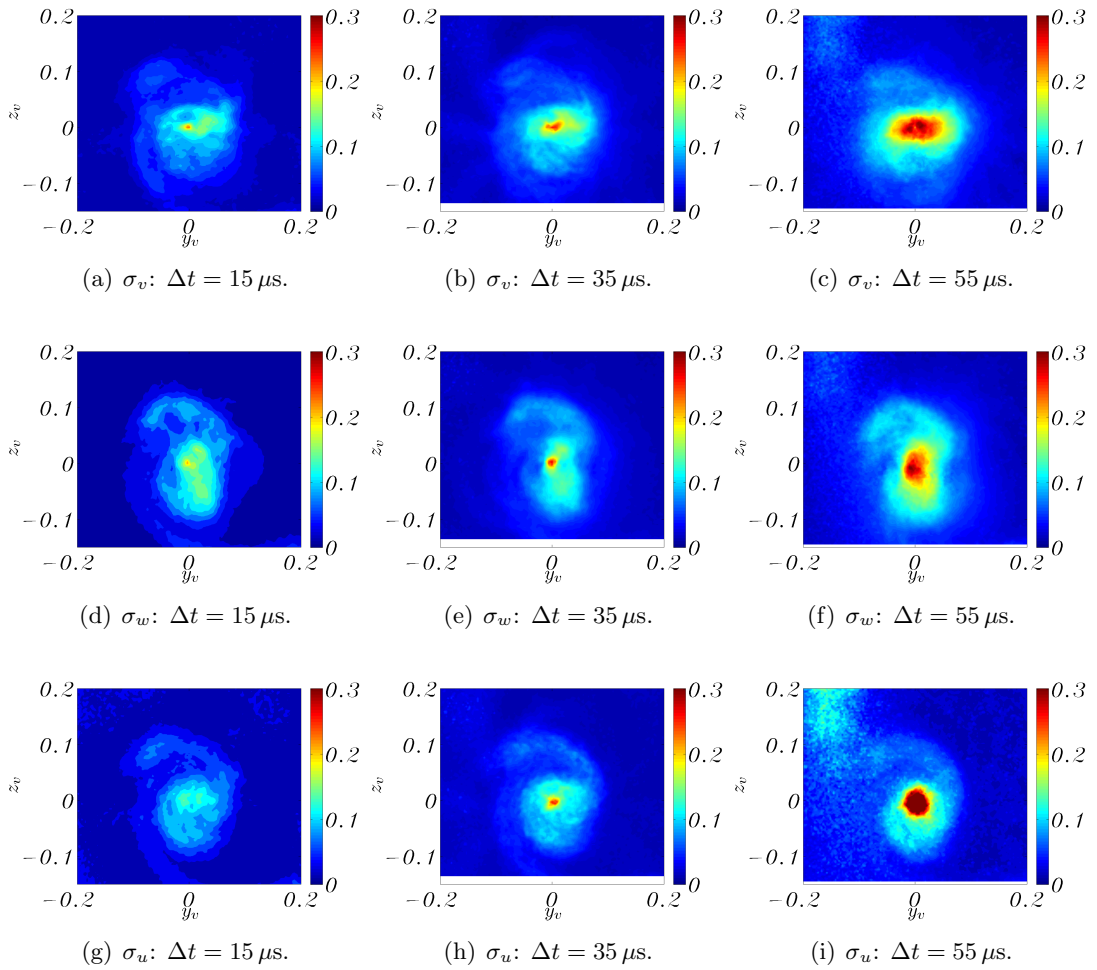


Figure A.4: Velocity fluctuations for different laser pulse separations.

loses information in the region of high cross velocity (i.e. at the vortex core). The loss of particles moving across the laser plane reduces the accuracy of the displacement vector evaluation. In reverse, a short time drastically reduces the turbulence level without giving any additional information on the velocity profiles in respect to the results for a

middle pulse separation. This behaviour can be attributed to the fact that decreasing the separation, particles move by a smaller quantity which eventually is comparable to the uncertainty on the displacements (i.e. pixel). In other words, the minimum detectable in-plane velocity difference is the pixel size over pulse separation so that decreasing Δt the minimum detectable velocity difference increases which eventually masks the turbulent fluctuations. For the out-of-plane velocity, this mechanism is amplified: cross displacements are detected by the camera as a shorter vector than same in-plane displacements. It is observed that the σ_u fluctuation for short pulse separation is indeed very low compared to the other cases.

SECTION 2

Image processing procedure tests

For the evaluation of images via correlation, the complete image is divided into interrogation windows. The correlation function operates a FFT algorithm on the light intensity of each interrogation window and passes through the complete PIV recording with a specified window shift. The evaluation will yield one velocity vector for each interrogation window. Different type of correlations and procedures can be used in relation of the image acquisition system as described by Adrian (1991). A stereoscopic arrangement with double-pulse/double-frame mode processed with a *stereo cross-correlation* is adopted in these experiments with a LaVision system. With this set-up, each sample is composed by two cameras recording two frames each in correspondence to two laser pulses with separation of $35\mu\text{s}$. The first frame contains the first exposure while the second frame contains the second exposure. The algorithm computes the cross-correlation of all the interrogation windows between frame 1 and frame 2. The highest peak in the cross-correlation is the most likely displacement vector (see Figure A.5). The out-of-plane component of the velocity is then calculated by a geometrical reconstruction of the two-dimensional three-component velocity vector field from the pair of two-dimensional two-component vector fields.

The *interrogation window size* defines the size in pixels of the square interrogation window. Each correlation operates only on the intensities inside the corresponding interrogation window. The *interrogation window overlap* defines the overlap among neighboring interrogation windows (see Figure A.6). The interrogation window size and the window overlap determine the grid size of the vector field corresponding to the

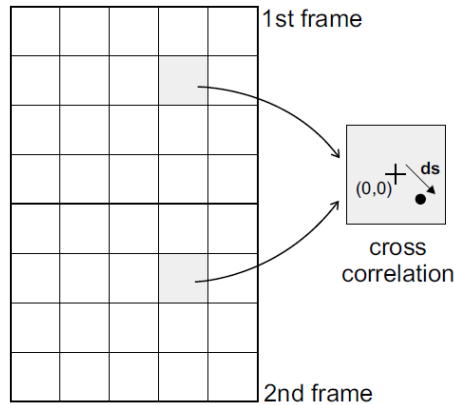


Figure A.5: Cross-correlation procedure scheme (DaVis, 2007).

effective spatial resolution between two neighboring vectors. The grid so formed has a homogeneous spacing between vectors.

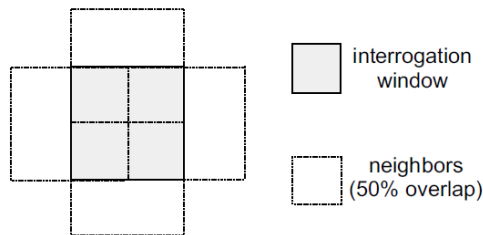


Figure A.6: Example of 50% interrogation window overlap (DaVis, 2007).

The calculation of the final vector field can be accomplished with a *single pass process* or with a *multi pass process* with either constant or decreasing interrogation window size. For the single pass process, the vector field calculation is accomplished with one calculation directly comparing the interrogation windows on each frame. For the multi pass process, the vector field is calculated by an arbitrary number of iterations, called also steps, on the same image. At each step, a reference vector for each interrogation window is calculated. Using the information of the previous step, the position of the interrogation windows in the new step is accordingly shifted (more sophisticated procedures can for example also deform the interrogation window from the information on the the shear). Moreover, the interrogation window size of the following step can be reduced. In this manner, the window shift is adaptively improved to compute the vectors in the following steps more accurately and more reliably.

In order to study the effects of the image processing parameters on the velocity field, no post-processing of the final vector fields is adopted such as median filters, removal and replacement of wrong vectors or smoothing of the vectors. Only the filling of empty spaces through interpolation of neighbors is applied. However, empty spaces were rare and the reduced number of particles in correspondence of the vortex centre due to centrifugal forces did not significantly affect the vector computation in that region as it was ensured a sufficient seeding for the correlations.

Other important aspects regarding the vector field computation are the *time* needed for the processing of the images and manipulations on the vector fields and the *memory* required to store the data.

In order to see how the image processing affects the results and define a satisfactory image processing procedure, different procedures have been compared. In particular, interrogation window size, number of iterations, interrogation window overlap, processing time and memory are studied in this Appendix in relation to a reference trailing vortex experiment. The test case is on a plane in the wake of the **M1** wing at 1 chord of distance from the trailing edge with angle of attack of 12° and Reynolds number of $Re = 5 \cdot 10^5$. The average vector field is calculated by applying a simple average on 121 instantaneous vector fields. The vortex centre of the average vector field is identified by the peak of the streamwise component of the helicity.

This comparative study can be split into three sections each one focusing on one of the aspect described earlier as summarized in Table A.1 where each case is described with a code. For example, the case 2x64ov25%+2x32ov50% indicates a multi step procedure composed by 2 steps with interrogation window size of 64 by 64 pixels and overlap of 25 percent followed by other 2 steps at interrogation window size of 32 by 32 pixels with 50 percent of overlap. This case represents the processing procedure selected at the end of these comparisons and it is present in each of the three sections.

The comparison of the different procedures is presented here through the comparison of swirl and axial velocity profiles scaled by the freestream velocity. Cuts every 10 degrees around the vortex centre were made and the velocity profiles along these radii were calculated. In the following Figures only 12 of these profiles are shown along with the mean value as function of the radius scaled by the wing chord. Comparisons of vorticity contours and turbulent quantities are not reported here as they led to same conclusions.

| |
|-------------------------------------|
| Interrogation window size |
| 2x128ov25%+2x64ov50% |
| 2x64ov25%+2x32ov50% |
| 2x32ov25%+2x16ov50% |
| 2x32ov25%+2x16ov25%+2x8ov50% |
| Number of iterations |
| 1x32ov50% |
| 1x64ov25%+1x32ov50% |
| 2x64ov25%+2x32ov50% |
| 2x128ov25%+2x64ov25%+4x32ov50% |
| Interrogation window overlap |
| 2x64ov0%+2x32ov0% |
| 2x64ov25%+2x32ov50% |
| 2x64ov50%+2x32ov75% |
| 2x64ov75%+2x32ov87% |

Table A.1: Summarizing table of the processing procedures tested.

(a) Interrogation window size To analyse the effects of the interrogation window size, a multi-pass procedure is selected with decreasing window size composed by 2 passes at 25% of overlap at a large window followed by other 2 passes at 50% of overlap on a window with half the sizes. For the last procedure, corresponding to the smallest final interrogation window size, an additional halving step was needed in order to obtain reasonable initial reference vector fields. At the specific experimental arrangement, the spatial resolutions of the final vector fields were decreasing with the interrogation window size respectively to 0.54%, 0.27%, 0.14% and 0.07% of the wing chord.

Observing the swirl and axial velocity profiles (Figures A.7 and A.8), the results from the final interrogation windows of 16x16 and 8x8 pixels show a high level of noise compared to procedures with bigger window sizes. This noise is higher for the axial velocity than for the swirl velocity. Moreover, whereas the mean lines of the swirl velocity profiles are similar for the four procedures (maximum swirl velocity, slope and core radius), the axial velocity mean profiles radically change showing a higher sensitivity to the processing procedure. For the smaller two window sizes a deficit at the vortex axis is observed whereas an excess of about 1.4 is observed for the bigger two. A smoother profile is shown by the procedure adopting the biggest interrogation window size (64x64). The difference effects of the swirl and axial velocity profiles are mainly due to the radically different operations involved in the calculation of the in-plane and the out-of-plane velocity. The first is through cross-correlation of the pair of images from

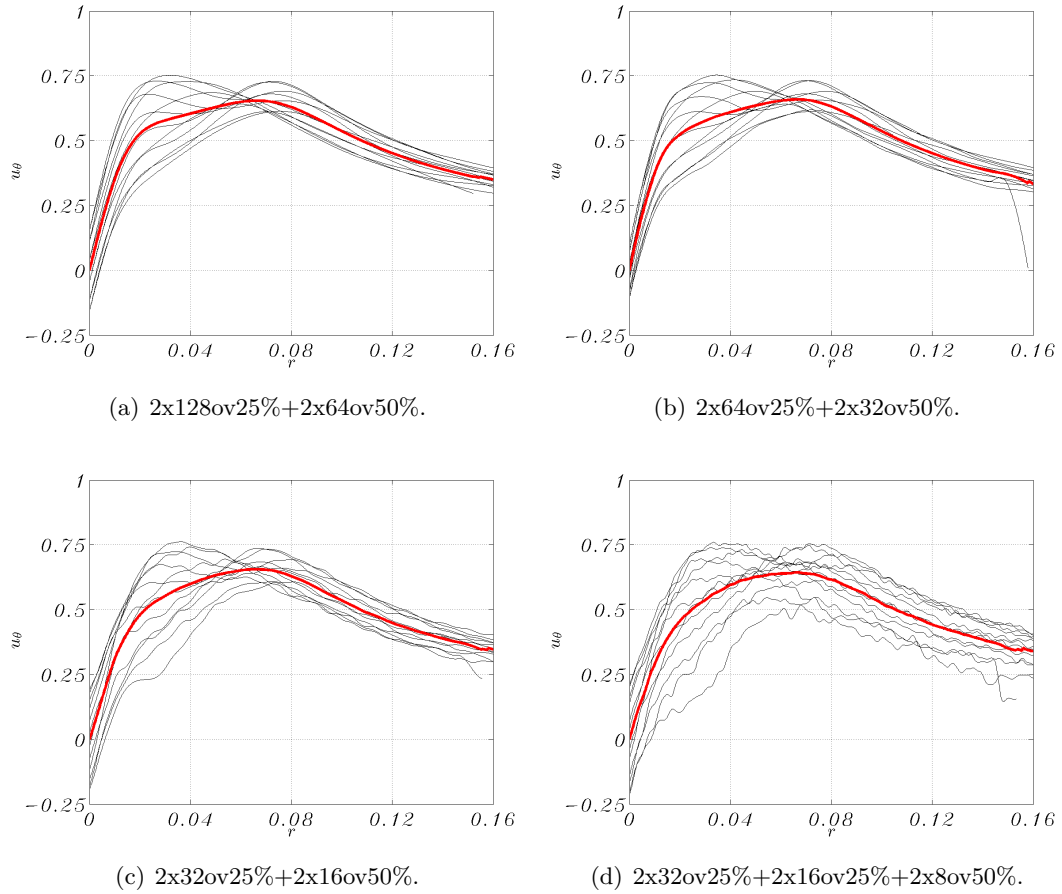


Figure A.7: Swirl velocity profiles for different interrogation window sizes.

the same camera; the latter is through the calibration function which correlates the two-components vector fields from the two cameras. The calibration process is usually affected by higher errors than the cross-correlation of the images. This leads the axial velocity to show higher errors than the swirl velocity.

Also, in order to correctly evaluate these results, it is important to point that the interrogation window operates as an average of the velocity of the particles which are found in it. The compromise should therefore be found between an interrogation window which is big enough to include a number of particles that gives a statistical convergence on the calculated velocity vector but also small enough to be able to accurately resolve small variations of the velocity.

(b) Number of iterations To study the effect of the number of iterations in the image processing procedure, a multi-pass scheme with final interrogation window size of 32 by 32 pixels with 50% of overlap is adopted. As reported in Table A.1, four different procedures are compared: a single–

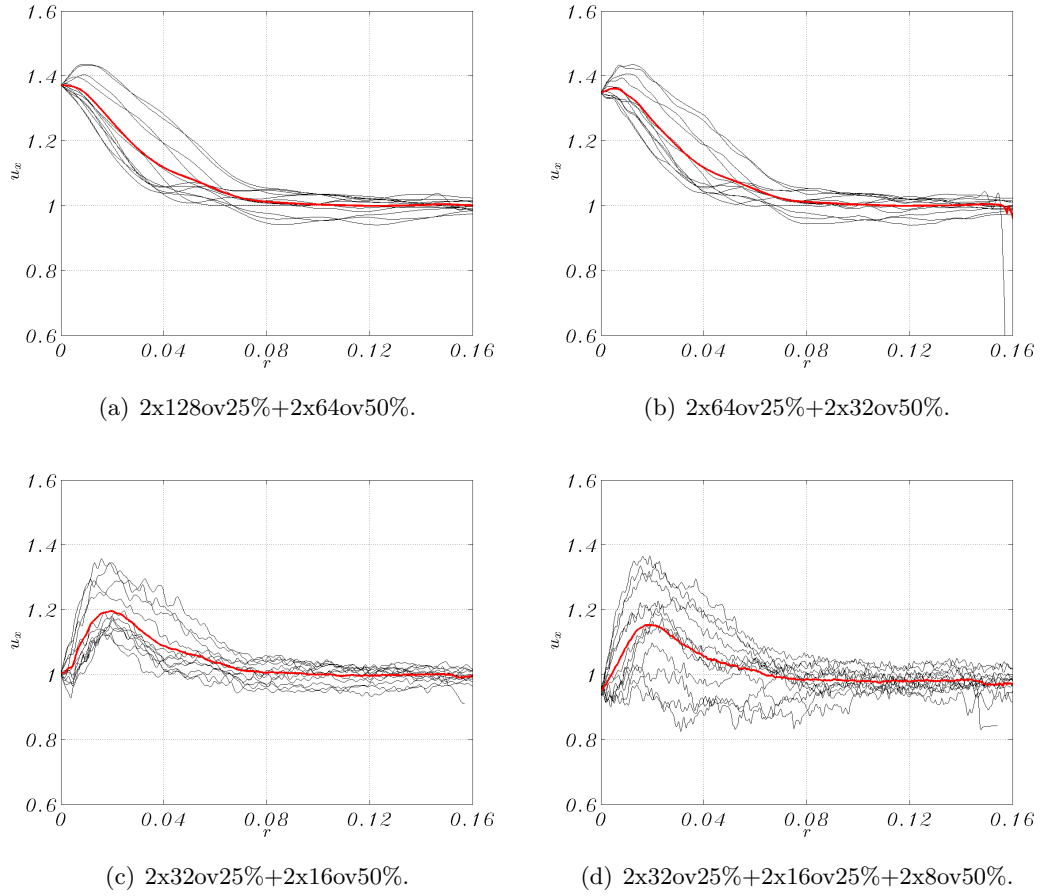


Figure A.8: Axial velocity profiles for different interrogation window sizes.

pass with 1 step each pass, a double-pass with 2 steps each pass and a triple-pass with 2 steps at 128 by 128 pixels, 2 steps at 64 by 64 pixels and 4 last steps at 32 by 32 pixels. The overlaps of the first passes are 25% and of the second passes are 50%.

The swirl velocity profiles of all the multi-pass procedures are almost identical (Figure A.9) whereas the single pass procedure is clearly not able to give accurate results. The inaccuracy of the single pass comes from the fact that no interrogation window shift (i.e. reference vector field) is applied between the first and the second frame on the same camera so that loss of particles leads to wrong cross-correlations. As observed also earlier, the axial velocity presents a higher sensitivity to the image processing procedure (Figure A.10). The axial velocity for the multi-pass single-steps procedure shows an inaccurate profile with axial velocity at the centre of the vortex 15% lower than the procedure with eight steps. The difference of the centre value between this last procedure and the one with 4 steps is of around 1.5%.

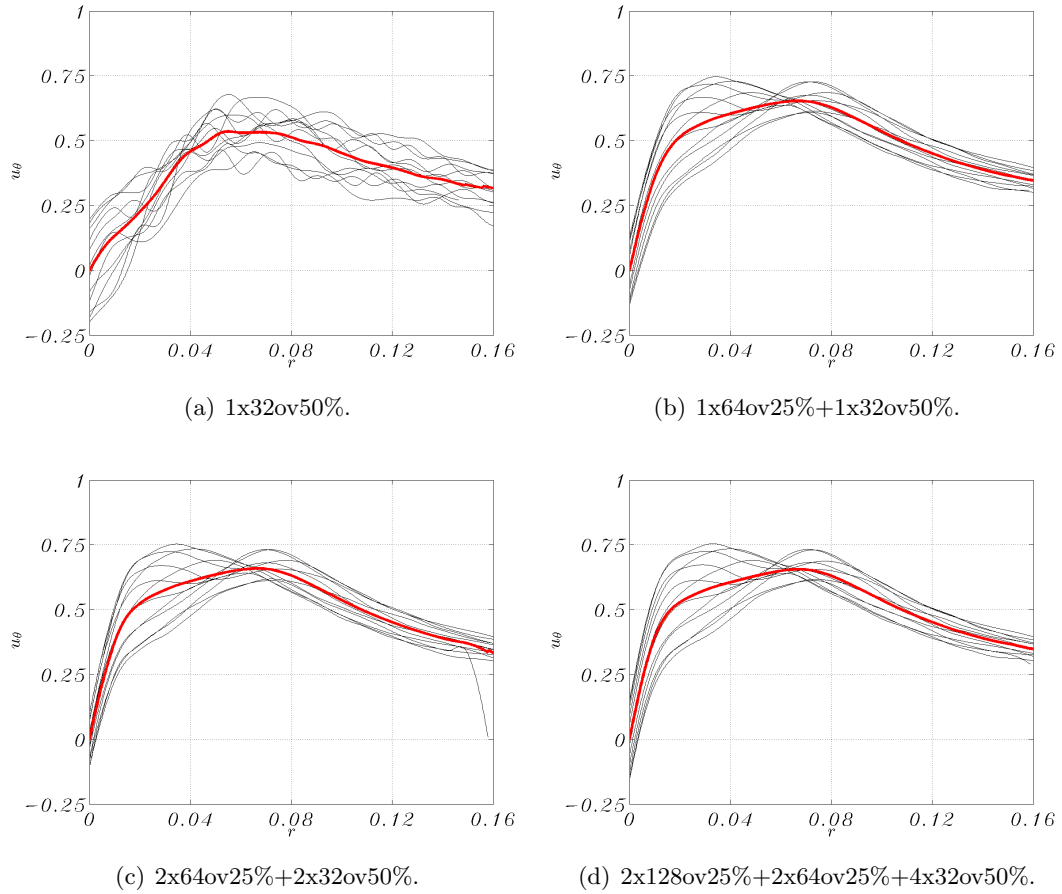


Figure A.9: Swirl velocity profiles for different numbers of iterations.

(c) Interrogation window overlap On the procedure composed by 2 steps on an interrogation window of 64 by 64 pixels followed by 2 steps on a 32 by 32 pixels, different window overlaps are compared. The spatial resolution of the final vector fields are exactly the same as with the decreasing of the interrogation window size, being respectively 0.54%, 0.27%, 0.14% and 0.07% of the wing chord.

All the processes show similar swirl velocity profiles (Figure A.11). However, the axial velocity profiles reported in Figure A.12 shows an increasing noise as the overlap is increased. Moreover, as the overlapping is increased, the average centre value remarkably decreases from 1.37 to 1.35, 1.27 and 1.07. As explained also by Raffel *et al.* (2007), the oversampling of the data is a useful tool in order to bring out small scale features of the flow. However, especially in regions containing high velocity gradients and low seeding densities (which is true near the vortex centre), the neighboring velocity vectors are correlated with each other because they are estimated partially from the

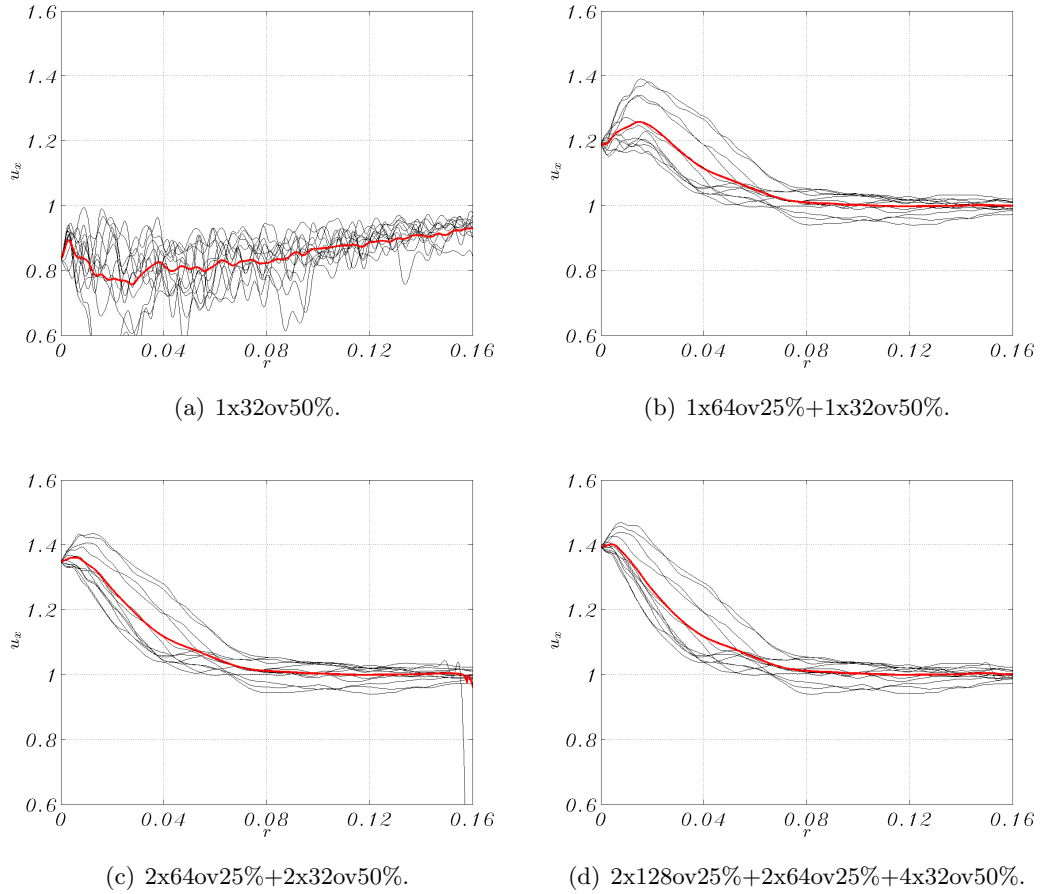


Figure A.10: Axial velocity profiles for different numbers of iterations.

same particle images. Because of this, overlaps greater than 50% are not common as they can lead to big errors, as clearly noted from Figure A.12.

(d) Processing time and memory The time required for the processing of the images in order to obtain vector fields is only the first part of the time

required for the analysis. A further processing of the vector fields regards for example centering, averaging and calculations of derivatives, radial velocity, swirl velocity and turbulent quantities. This second processing of the data can require a comparable time to the one required for the vector field extraction. On Table A.2, rough estimations of the required time for only the first part of the image processing (accomplished by DaVis 7.2) and of the memory required to store the 121 instantaneous vector fields are reported.

Looking at the processing time required for the vector field calculations, a reduction of the interrogation window size increases the time required for the image processing due to the increase of vectors to be calculated. For the same reason, an increase of the

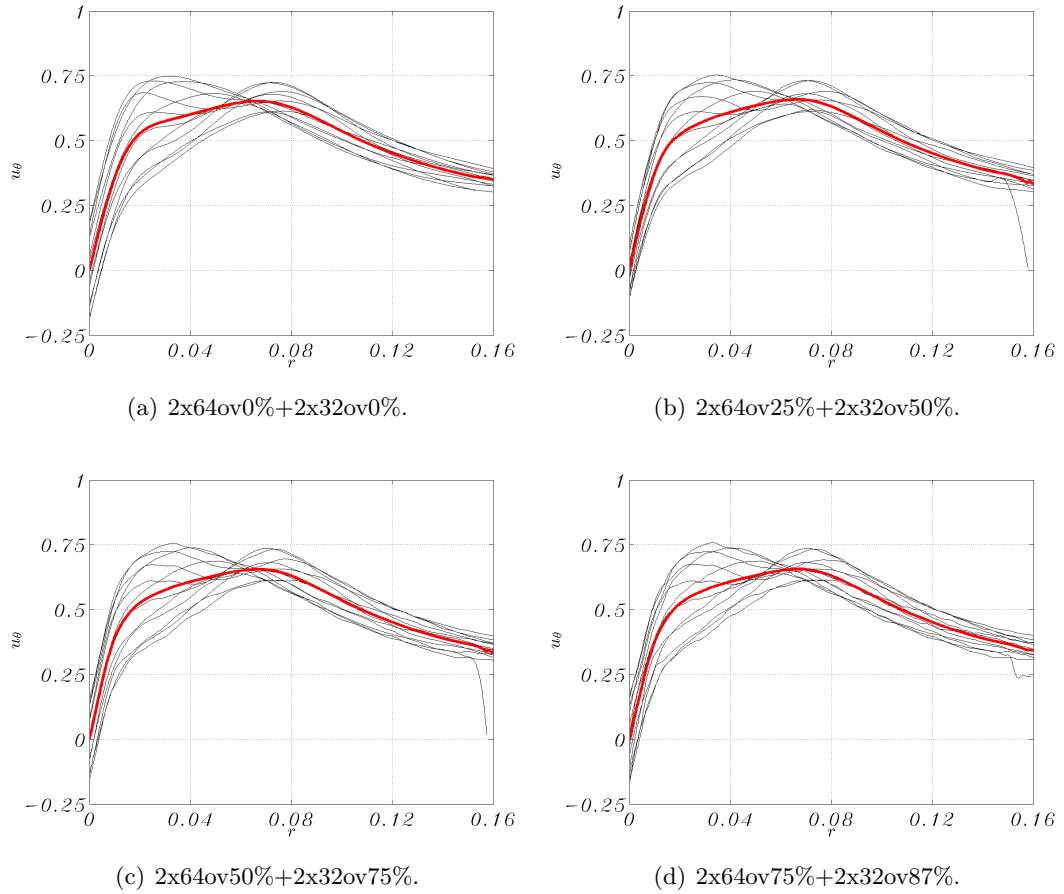


Figure A.11: Swirl velocity profiles for different interrogation window overlaps.

overlap leads to an increase of the processing time. An increase of the number of steps also requires more processing time even though the rate is lower than the for window overlap and size.

Similarly to the processing time, the required memory is strongly affected by the number of vectors in the flowfield. The memory spans from 19 Mb to 2.46 Gb, corresponding to a flowfield described respectively with 13330 and 853671 three-component velocity vectors. The change of the number iterations does not alter the size of the files because the vectors number remains the same. The higher space required by the single pass procedure is believed to be caused by the saving process of the image processing software.

The memory requirements for the vector fields reported on Table A.2 is just part of the total memory required. Raw images, vector fields converted into Matlab format, centered vector fields, averaged vector fields and other averaged quantities have to be added on those values. In particular, raw images can take a big role in the amount of

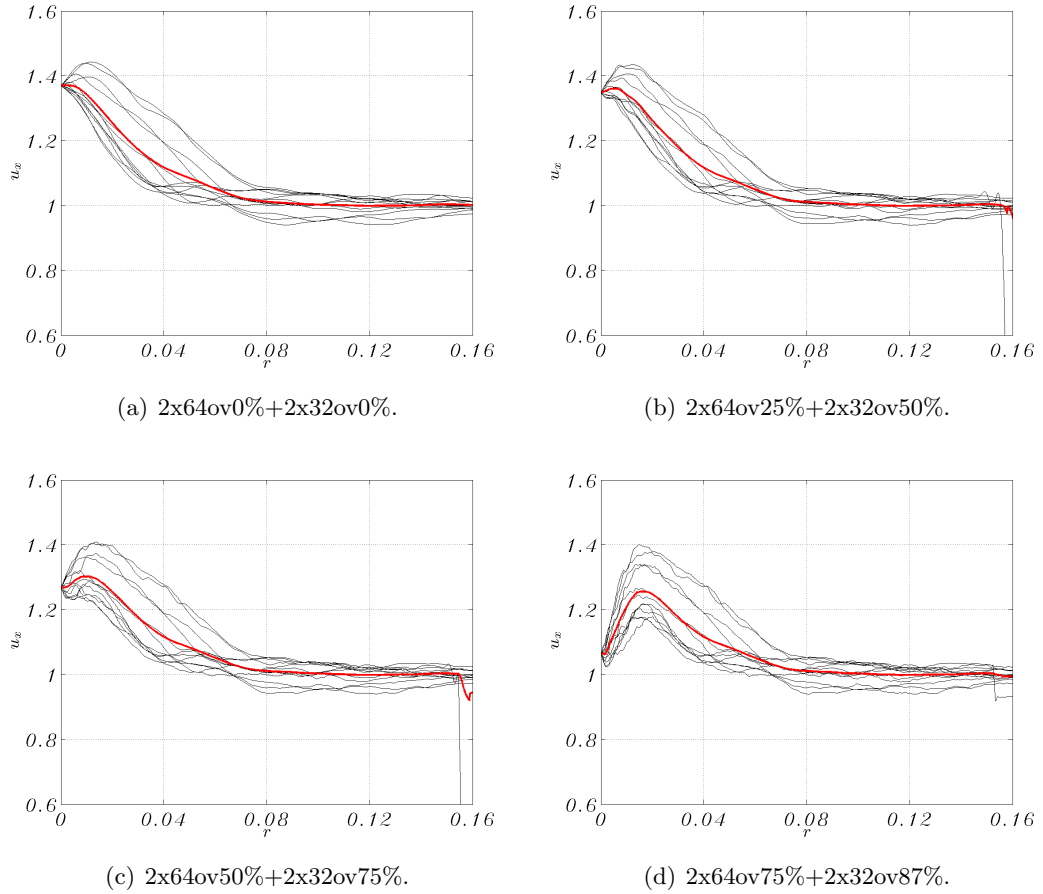


Figure A.12: Axial velocity profiles for different interrogation window overlaps.

the memory needed for a PIV. For instance, each test of 121 sets of 4 pictures recorded in these study required additional 4.8 Gb.

(e) Conclusive remarks Two different ways are found in order to decrease the spatial resolution of the final vector field: one is decreasing the interrogation window size and the other is increasing the overlap. The first is limited by a minimum number of particles in each interrogation window. The second is limited by the computational cost and by the increase of errors in the computed velocity field as the overlap is increased. However, as shown also by van der Wall & Richard (2006) from the analysis of PIV data on wing vortices, the interrogation window overlap is as important as the size of the window itself for converged estimates of the core radius and the maximum swirl velocity. From the comparison of several image processing procedures, it is shown that a final interrogation window of 32 by 32 pixels gives the best compromise between smoothness of the velocity profiles and spatial resolution. Since the minimum cross-correlation window size is limited, the overlap must be adjusted

| | Time | Memory |
|-------------------------------------|------|---------|
| Interrogation window size | | |
| 2x128ov25%+2x64ov50% | 3 h | 19 Mb |
| 2x64ov25%+2x32ov50% | 5 h | 91 Mb |
| 2x32ov25%+2x16ov50% | 9 h | 763 Mb |
| 2x32ov25%+2x16ov25%+2x8ov50% | 16 h | 2.46 Gb |
| Number of iterations | | |
| 1x32ov50% | 2 h | 263 Mb |
| 1x64ov25%+1x32ov50% | 3 h | 95 Mb |
| 2x64ov25%+2x32ov50% | 5 h | 91 Mb |
| 2x128ov25%+2x64ov25%+4x32ov50% | 10 h | 95 Mb |
| Interrogation window overlap | | |
| 2x64ov0%+2x32ov0% | 3 h | 25 Mb |
| 2x64ov25%+2x32ov50% | 5 h | 91 Mb |
| 2x64ov50%+2x32ov75% | 9 h | 358 Mb |
| 2x64ov75%+2x32ov87% | 18 h | 1.45 Gb |

Table A.2: Processing procedures: time and memory required.

in the optimization between the accuracy of the results and the time and memory required for the image processing. Moreover, the increase of the number of iterations can increase the accuracy and the time required but it does not change the memory required. A multi-pass procedure has revealed to be compulsory for this flow. Also, processing time and memory requirements have revealed to be a decisive factor in the choice of the image processing.

Following these considerations and due to the high number of different tests performed in this research, an optimum compromise is found in the image processing procedure 2x64ov25%+2x32ov50%. Moreover, the vector fields resulting from this procedure do not show a significant number of wrong vectors to be removed and replaced by interpolated value. This implies a good quality of the seeding and the experimental arrangement giving a high level of reliability to these results.

Vortex centre identification on grayscale pictures

From the pictures of the smoke on planes perpendicular to the vortex axis on the wake of a wing, it is possible to identify the vortex centre and then to study the unsteadiness of the instantaneous location. Because of the high centrifugal force within the vortex core, the smoke particle density is lower. When the plane is illuminated a darker spot in correspondence to the centre appears. The routine able to find the dark spot is called here vortex centre identification method and it is used to locate the vortex of each of the realizations. The validity of this technique is based on the reliability of the darker region centroid as a good description of the vortex centre, which is a good assumption when smoke particles accurately follow the flow, for high smoke density, for low buoyancy forces, for high image resolution and for darker spots of the order of the vortex core.

In order to find a consistent and robust vortex centre identification method, the location of the darker spots in the images, corresponding to the instantaneous vortex centres, has been carried out with two conceptually different routines: converting the grayscale image into a black and white image with an appropriate conversion threshold (BW method) and mapping the grayscale of the image with rounded interrogation windows (GRAY method).

SECTION 1

GRAY and BW methods

The first three steps of the methods are common and described as follows with reference to an image of the tip vortex at one chord behind the M1 model with rounded tip at an angle of attack of 12° and Reynolds number of 10^6 .

1. The analysis region of a set of records is reduced from the whole image (Figure B.1(a)) to a region containing the dark spot and large enough to contain all the dark spots of the other instants (Figure B.1(b)).
2. The horizontal gradient, due to the changing of laser intensity, is calculated on a region non affected by the vortex core dark spot (dashed line in Figure B.1(b)) or from the vertical average of the image and subtracted from the image (Figure B.1(c)). Similarly, the vertical gradient can also be subtracted.
3. The image is then divided into interrogation windows of $N_{px} \times N_{px}$ size. The average intensity is calculated for each one of them and the darkest is identified in order to find an initial region for the analysis.

(a) BW method

4. The grayscale image is firstly inverted so that the vortex centre becomes the lighter region and then converted into a black and white where the threshold is the average intensity of the initial window (Figure B.2(a)).¹
5. The small objects are removed in order to obtain one object of connected (8-connection type) white pixels (Figure B.2(b)).
6. The object is then increased with all the connected white pixels from the surrounding windows (Figure B.2(c)).
7. The object is filled and the centroid of the selected pixels is calculated (Figure B.2(d)).

(b) GRAY method

4. Around the centre of the darkest interrogation window, a matrix of 25 interrogation circles of N_{px} of diameter is drawn. The light intensity in each round region is calculated and the darkest region is selected (Figure B.3(a)).
5. The process is repeated around the centre of the darkest circle with same diameters and decreasing distances between the interrogation circles until the distance is equal to 1 pixel (Figure B.3(b)).

¹The BW method can be seen also in the context of image segmentation methods by using thresholding techniques where the threshold value is selected automatically and it is based on the grayscale level of a region near the vortex centre (Shapiro & Stockman, 2001). A similar approach was adopted by Del Pino *et al.* (2009)

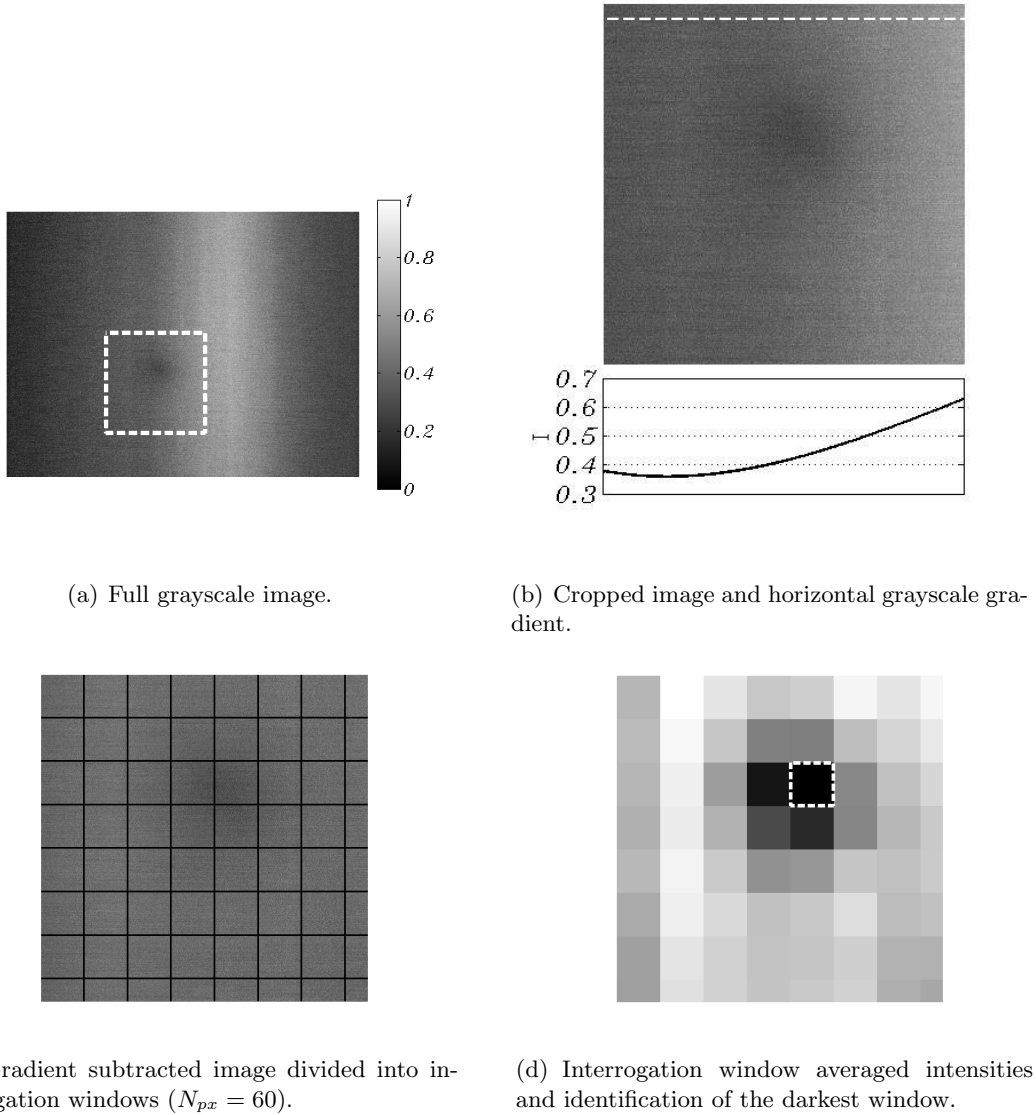


Figure B.1: *Common steps.*

SECTION 2

Position distribution and movement frequency

The advantage of the BW method is that it can identify the actual dark spot shape and so a good estimation of the centrifugal forces distribution. However, the threshold value is strongly affected by the size of the interrogation windows N_{px} and the relative position between the darkest window and the vortex core. Unfortunately, a fixed threshold value method is not a feasible solution because of the movement of the vortex in a non uniformly distributed laser intensity and because of the not clearly definable

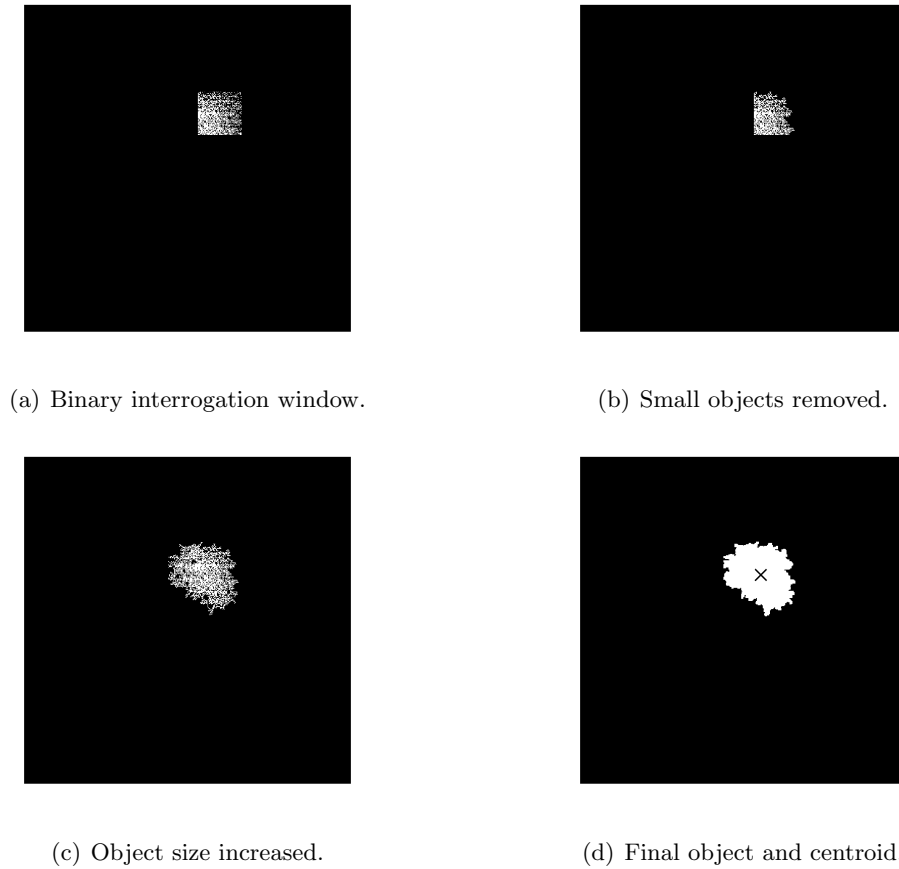
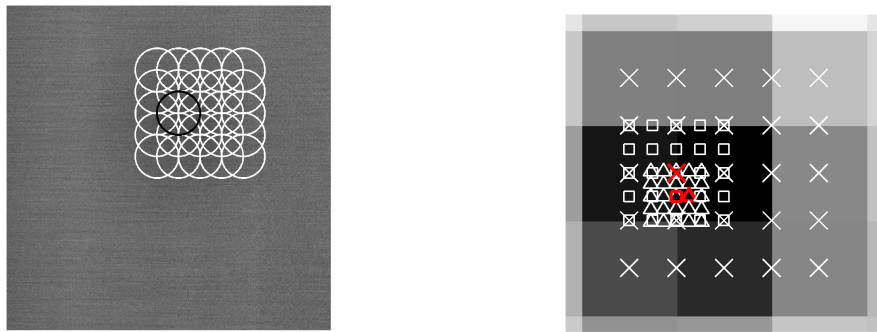


Figure B.2: *BW steps.*

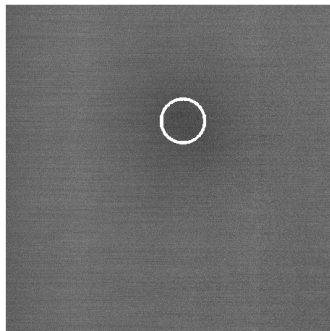
double-peaked grayscale histogram distribution that would occur if the darker spot was substantially darker than the surrounding region. In Figure B.4, the grayscale level histograms are reported for the full image, the reduced image and the gradient subtracted image (respectively in Figures B.1(a), B.1(b) and B.1(c)). The double-peaked distribution of the first two (Figures B.1(a), B.1(b)) is due by the superimposition of the vortex presence with the laser intensity changing along the image which, once the gradient is subtracted, does not effect the histogram (Figure B.1(c)).

The GRAY method necessitates an estimate of the vortex core dimension so that the round interrogation window diameter N_{px} can be set. Contrary to the BW method, GRAY method reveals a consistency in sizes and 1 pixel accuracy in the determination of the position. Moreover, it is observed that the shape of the darker region at 1 chord of distance from the trailing edge was satisfactorily described by a circle.

In Figure B.5, 190 instantaneous vortex centres taken at a sampling frequency of 10 Hz of a typical case are plotted as function of the interrogation window size N_{px} for the BW method. The centres distributions obtained with N_{px} between 20 and 60



(a) Interrogation windows mapping (25 circles). (b) Initial interrogation windows and 3 steps of refinement (zoom in image); centre of the darkest region at each step in red.



(c) Centre identification.

Figure B.3: *GRAY steps.*

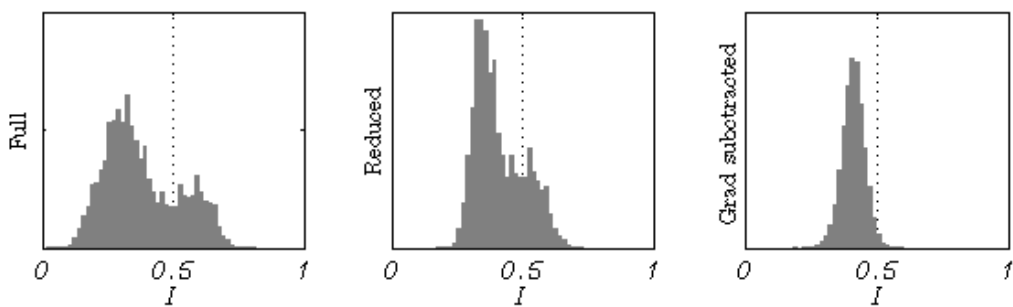


Figure B.4: *Histogram of the light intensity for steps 1, 2 and 3.*

are very similar and the differences in positions are very small. When a value of 80 and 100 is adopted, the distributions change in sizes (less scattered) and orientation (with a vertical principal axis). This behaviour can be explained by the presence of a residual horizontal gradient of the background gray level. In Figure B.6, the same cases

are analysed by the GRAY method. The results are very similar to the ones obtained with the BW method with the only difference that the GRAY method gives consistent results up to $N_{px} = 80$.

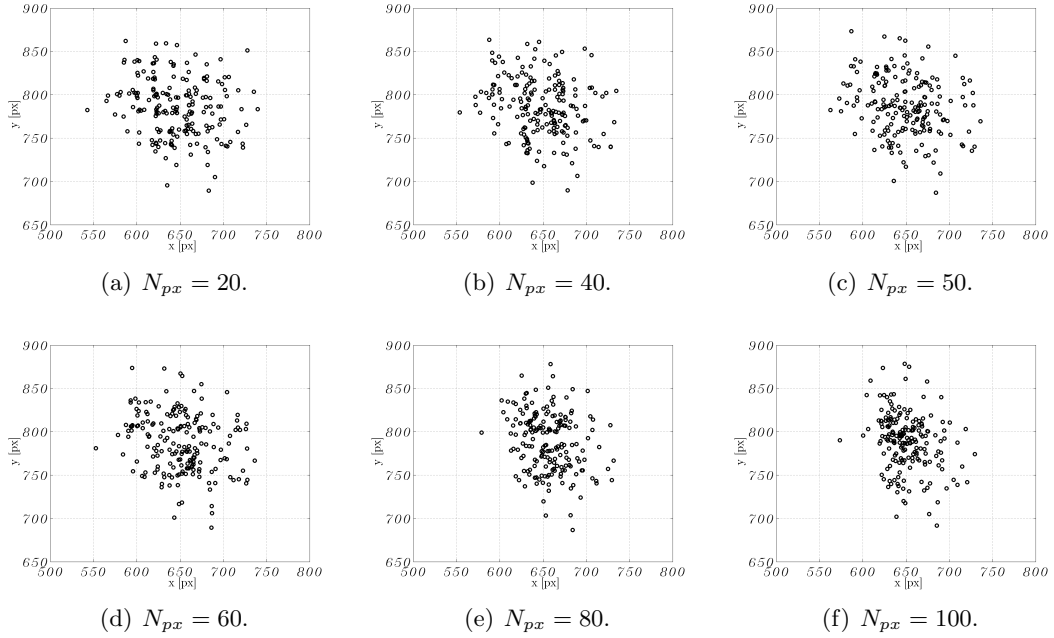


Figure B.5: *BW method: instantaneous vortex positions (rounded tip, $x_w = 1$, $\alpha = 12^\circ$, $Re = 10^6$).*

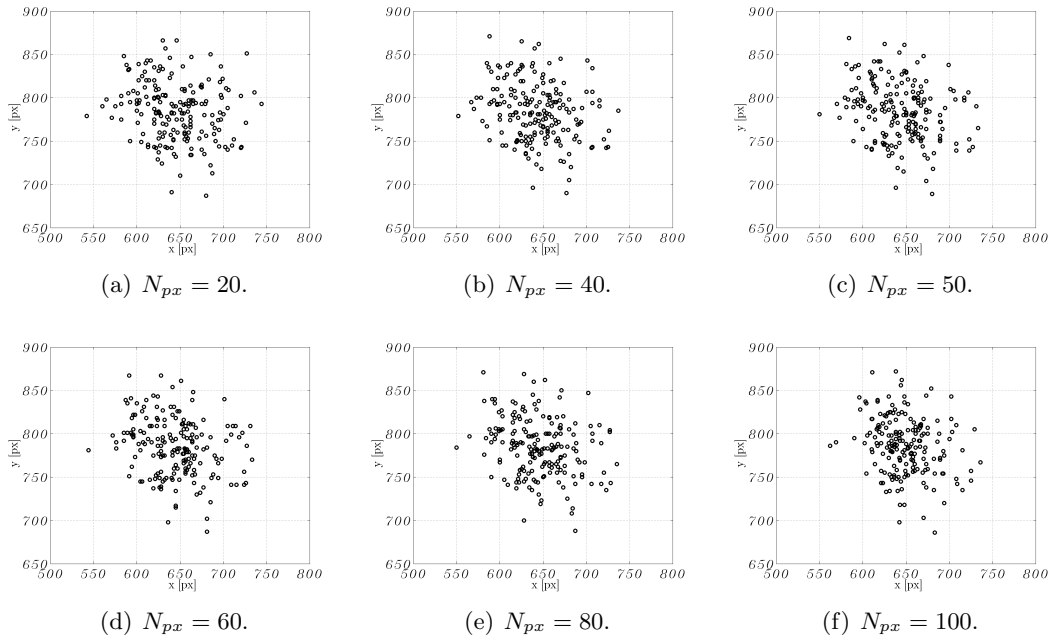


Figure B.6: *GRAY method: instantaneous vortex positions (rounded tip, $x_w = 1$, $\alpha = 12^\circ$, $Re = 10^6$).*

A comparison of the two vortex identification methods and interrogation window size was carried out also with respect to the frequency distributions of the vortex centre movement. The frequency distributions of the vortex centre translations along the y and z axis has been calculated and plotted in Figures B.7 and B.8, respectively adopting BW and GRAY method. The power is scaled by the variance of the movement along the same axis. The consistency of the results, when N_{px} is less than 80, appears in these plots and no major differences can be seen between the two methods whereas, for N_{px} equal or greater than 80, the frequency distributions change.

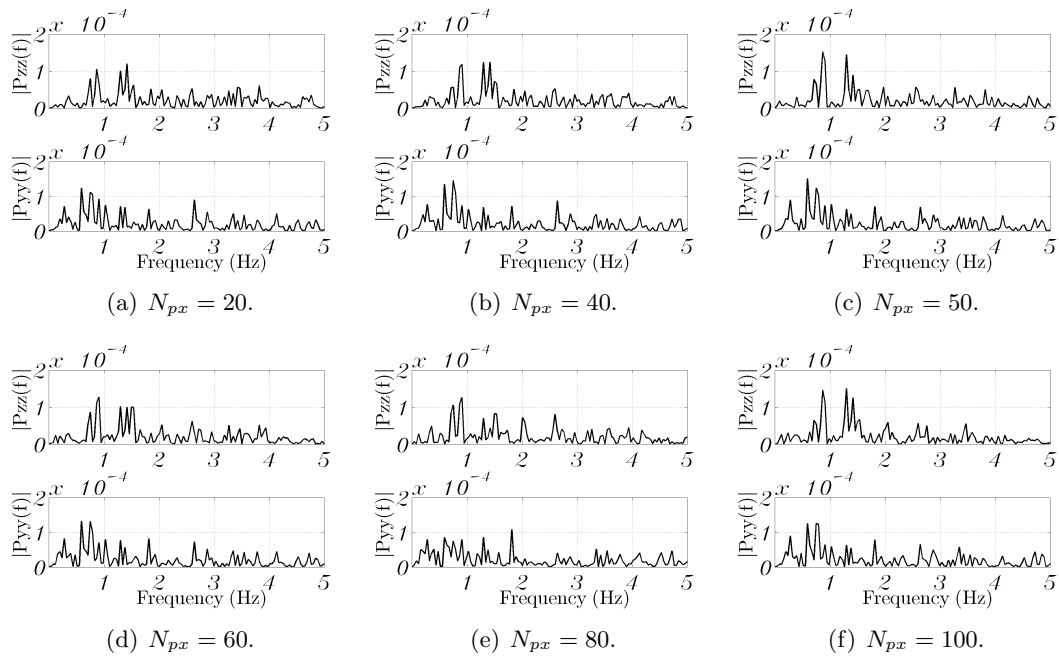


Figure B.7: *BW method: vortex movement power spectra (rounded tip, $x_w = 1$, $\alpha = 12^\circ$, $Re = 10^6$).*

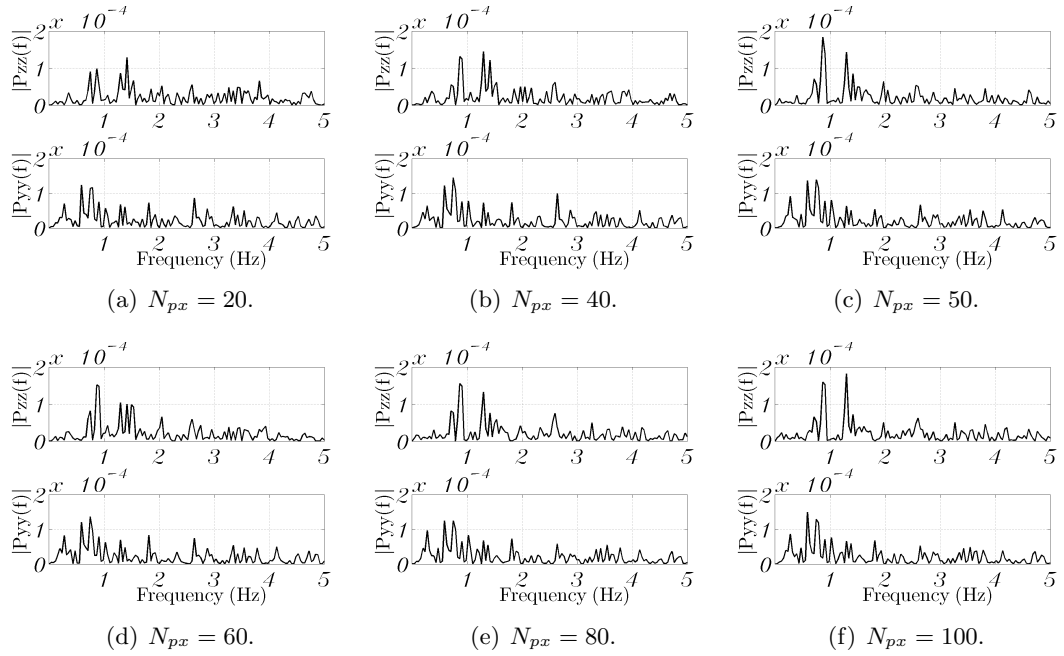


Figure B.8: GRAY method: vortex movement power spectra (rounded tip, $x_w = 1$, $\alpha = 12^\circ$, $Re = 10^6$).

Some equations relevant to vortices

If people do not believe that mathematics is simple, it is only because they do not realize how complicated life is.

JOHN VON NEUMANN

The governing equations of laminar and turbulent isolated vortices are derived after assumptions which simplify the Navier–Stokes equations. In this appendix, the governing equations are expressed in both cartesian and cylindrical coordinates in Section C.1. The vorticity form of the Navier–Stokes equations, which highlights important mechanisms especially for trailing vortices, is also given in Section C.2. Reynolds–averaged Navier–Stokes equations are presented in Section C.3 in order to highlight the role of the Reynolds stresses. Some of the fundamental relations between the cartesian and cylindrical reference frames are presented in Section C.4.

SECTION 1

Governing equations

Effects due to compressibility, heat transfer, body forces and variations in fluid properties are negligible in the present study, and thus the corresponding terms in the continuity and Navier–Stokes equations for newtonian fluids can be neglected. The vectorial form of the resulting continuity and momentum equations is:

$$\nabla \cdot \mathbf{u} = 0 \tag{C.1a}$$

$$\frac{\partial \mathbf{u}}{\partial t} + (\mathbf{u} \cdot \nabla) \mathbf{u} = -\frac{\nabla P}{\rho} + \nu \nabla^2 \mathbf{u} \tag{C.1b}$$

Writing the vector equations explicitly in cartesian coordinates leads to:

$$\frac{\partial u}{\partial x} + \frac{\partial v}{\partial y} + \frac{\partial w}{\partial z} = 0 \quad (\text{C.2a})$$

$$\frac{\partial u}{\partial t} + u \frac{\partial u}{\partial x} + v \frac{\partial u}{\partial y} + w \frac{\partial u}{\partial z} = -\frac{1}{\rho} \frac{\partial P}{\partial x} + \nu \left[\frac{\partial^2 u}{\partial x^2} + \frac{\partial^2 u}{\partial y^2} + \frac{\partial^2 u}{\partial z^2} \right] \quad (\text{C.2b})$$

$$\frac{\partial v}{\partial t} + u \frac{\partial v}{\partial x} + v \frac{\partial v}{\partial y} + w \frac{\partial v}{\partial z} = -\frac{1}{\rho} \frac{\partial P}{\partial y} + \nu \left[\frac{\partial^2 v}{\partial x^2} + \frac{\partial^2 v}{\partial y^2} + \frac{\partial^2 v}{\partial z^2} \right] \quad (\text{C.2c})$$

$$\frac{\partial w}{\partial t} + u \frac{\partial w}{\partial x} + v \frac{\partial w}{\partial y} + w \frac{\partial w}{\partial z} = -\frac{1}{\rho} \frac{\partial P}{\partial z} + \nu \left[\frac{\partial^2 w}{\partial x^2} + \frac{\partial^2 w}{\partial y^2} + \frac{\partial^2 w}{\partial z^2} \right] \quad (\text{C.2d})$$

Cylindrical coordinates are more appropriate for the study of vortex flows since important simplifications of the equations can be done. In cylindrical coordinates respectively the continuity equation and the radial, azimuthal and axial momentum equations are:

$$\frac{1}{r} \frac{\partial (ru_r)}{\partial r} + \frac{1}{r} \frac{\partial u_\theta}{\partial \theta} + \frac{\partial u_x}{\partial x} = 0 \quad (\text{C.3a})$$

$$\begin{aligned} \frac{\partial u_r}{\partial t} + u_r \frac{\partial u_r}{\partial r} + \frac{u_\theta}{r} \frac{\partial u_r}{\partial \theta} + u_x \frac{\partial u_r}{\partial x} - \frac{u_\theta^2}{r} = \\ = -\frac{1}{\rho} \frac{\partial P}{\partial r} + \nu \left[\frac{\partial^2 u_r}{\partial r^2} + \frac{1}{r} \frac{\partial u_r}{\partial r} + \frac{1}{r^2} \frac{\partial^2 u_r}{\partial \theta^2} + \frac{\partial^2 u_r}{\partial x^2} - \frac{u_r}{r^2} - \frac{2}{r^2} \frac{\partial u_\theta}{\partial \theta} \right] \end{aligned} \quad (\text{C.3b})$$

$$\begin{aligned} \frac{\partial u_\theta}{\partial t} + u_r \frac{\partial u_\theta}{\partial r} + \frac{u_\theta}{r} \frac{\partial u_\theta}{\partial \theta} + u_x \frac{\partial u_\theta}{\partial x} - \frac{u_\theta u_r}{r} = \\ = -\frac{1}{\rho r} \frac{\partial P}{\partial \theta} + \nu \left[\frac{\partial^2 u_\theta}{\partial r^2} + \frac{1}{r} \frac{\partial u_\theta}{\partial r} + \frac{1}{r^2} \frac{\partial^2 u_\theta}{\partial \theta^2} + \frac{\partial^2 u_\theta}{\partial x^2} - \frac{u_\theta}{r^2} - \frac{2}{r^2} \frac{\partial u_r}{\partial \theta} \right] \end{aligned} \quad (\text{C.3c})$$

$$\begin{aligned} \frac{\partial u_x}{\partial t} + u_r \frac{\partial u_x}{\partial r} + \frac{u_\theta}{r} \frac{\partial u_x}{\partial \theta} + u_x \frac{\partial u_x}{\partial x} = \\ = -\frac{1}{\rho} \frac{\partial P}{\partial x} + \nu \left[\frac{\partial^2 u_x}{\partial r^2} + \frac{1}{r} \frac{\partial u_x}{\partial r} + \frac{1}{r^2} \frac{\partial^2 u_x}{\partial \theta^2} + \frac{\partial^2 u_x}{\partial x^2} \right] \end{aligned} \quad (\text{C.3d})$$

For axisymmetric flows, valid for vortex flows in the mid wake, the derivatives by the azimuthal coordinate are zero:

$$\frac{\partial \cdot}{\partial \theta} = 0 \quad (\text{C.4})$$

and the Equations (C.3) become:

$$\frac{1}{r} \frac{\partial (ru_r)}{\partial r} + \frac{\partial u_x}{\partial x} = 0 \quad (\text{C.5a})$$

$$\frac{\partial u_r}{\partial t} + u_r \frac{\partial u_r}{\partial r} + u_x \frac{\partial u_r}{\partial x} - \frac{u_\theta^2}{r} = -\frac{1}{\rho} \frac{\partial P}{\partial r} + \nu \left[\frac{\partial^2 u_r}{\partial r^2} + \frac{1}{r} \frac{\partial u_r}{\partial r} + \frac{\partial^2 u_r}{\partial x^2} - \frac{u_r}{r^2} \right] \quad (\text{C.5b})$$

$$\frac{\partial u_\theta}{\partial t} + u_r \frac{\partial u_\theta}{\partial r} + u_x \frac{\partial u_\theta}{\partial x} - \frac{u_\theta u_r}{r} = -\frac{1}{\rho r} \frac{\partial P}{\partial \theta} + \nu \left[\frac{\partial^2 u_\theta}{\partial r^2} + \frac{1}{r} \frac{\partial u_\theta}{\partial r} + \frac{\partial^2 u_\theta}{\partial x^2} - \frac{u_\theta}{r^2} \right] \quad (\text{C.5c})$$

$$\frac{\partial u_x}{\partial t} + u_r \frac{\partial u_x}{\partial r} + u_x \frac{\partial u_x}{\partial x} = -\frac{1}{\rho} \frac{\partial P}{\partial x} + \nu \left[\frac{\partial^2 u_x}{\partial r^2} + \frac{1}{r} \frac{\partial u_x}{\partial r} + \frac{\partial^2 u_x}{\partial x^2} \right] \quad (\text{C.5d})$$

The boundary conditions on such flow, expressed in a plane perpendicular to the vortex axis, are the followings:

$$\text{at } r = 0, \quad u_r = 0, \quad u_\theta = 0, \quad u_x \text{ finite}, \quad \partial u_x / \partial r = 0, \quad p \text{ finite}, \quad \partial p / \partial r = 0; \quad (\text{C.6a})$$

$$\text{at } r \rightarrow \infty, \quad u_r \rightarrow 0, \quad u_\theta \rightarrow 0, \quad u_x \rightarrow 0, \quad p \rightarrow 0; \quad (\text{C.6b})$$

where p is the disturbance pressure due to the vortex flow.

Further assumptions and approximations can be applied in order to obtain analytical descriptions of vortex quantities such as swirl velocity and axial velocity profiles. The *boundary layer-type approximation* is often adopted which states that axial gradients are of small magnitude compared with radial gradients and that the radial component of the velocity is small compared to the axial and swirl components. Another assumption adopted can be the *light loading approximation* where the axial velocity perturbations are small compared to the freestream velocity, as often adopted in the theory of wakes without swirl. Moreover, *steady flow*, wing loading distribution and solution shapes are some of the other assumptions needed to obtain analytical solutions of vortex flows from Equations (C.5). See for example Batchelor (1964), Morton (1969), Moore & Saffman (1973), Phillips (1981) and Phillips & Graham (1984) for different developments of these equations.

SECTION 2

***Vorticity form of the Navier–Stokes equation
(or vorticity equation)***

An important form of the Navier–Stokes equation is found when it is expressed in terms of vorticity. The vorticity equation describes the distribution, concentration, production, transport and diffusion of such vector variable. Since vorticity is defined as the curl of the velocity,

$$\boldsymbol{\omega} = \nabla \times \mathbf{u}, \tag{C.7}$$

the vorticity equation is obtained by taking the curl of the momentum equation (C.1b). Assuming newtonian fluid and constant density, and applying some vector identities, the final form of the vorticity equation can be written as¹:

$$\frac{\partial \boldsymbol{\omega}}{\partial t} + (\mathbf{u} \cdot \nabla) \boldsymbol{\omega} = (\boldsymbol{\omega} \cdot \nabla) \mathbf{u} + \nu \nabla^2 \boldsymbol{\omega} \tag{C.8}$$

which, with Equation C.7, form the system of governing equations expressed in vorticity form. This particular form of Equation (C.8) is particularly interesting because it leads to important considerations. For instance, the equation of the vorticity component ω_x written in cartesian coordinates is:

$$\begin{aligned} \frac{\partial \omega_x}{\partial t} + \overbrace{u \frac{\partial \omega_x}{\partial x} + v \frac{\partial \omega_x}{\partial y} + w \frac{\partial \omega_x}{\partial z}}^{\text{convection}} = \\ = \underbrace{\omega_x \frac{\partial u}{\partial x}}_{\text{stretching}} + \underbrace{\left(\omega_y \frac{\partial u}{\partial y} + \omega_z \frac{\partial u}{\partial z} \right)}_{\text{tilting}} + \underbrace{\nu \left(\frac{\partial^2 \omega_x}{\partial x^2} + \frac{\partial^2 \omega_x}{\partial y^2} + \frac{\partial^2 \omega_x}{\partial z^2} \right)}_{\text{diffusion}} \end{aligned} \tag{C.9}$$

production

This equation states that in a three-dimensional and unsteady flow, the vorticity in a fixed point of the flowfield changes as effect of convection, production and diffusion. Like the classic form of the momentum equation, on the right hand side there is the rate of change expressed as time derivative and convection of vorticity.

The production term can be divided into two separate contributes: the production by stretching and the production by tilting. The latter, also called production by turning or by skewing, is the production of ω_x through the rotation of the other two

¹Different expressions of the vorticity equation can be found in the literature depending on the particular interest and focus of the author and the study.

vorticity components, namely ω_y and ω_z , by the gradients along the y and z axes of the velocity component parallel to ω_x . It can also be seen as the tilting of a vortex tube, and consequently of its vorticity vector, as effect of a background shear.

The production by stretching can be visualized taking a fluid element rotating around the x axis. If this element is stretched along the rotation axis, that is if $\frac{\partial u}{\partial x}$ is positive, the cross sectional area will decrease to satisfy the continuity equation. Also, from the angular momentum equation (which is the circulation), its angular velocity (equal to half of the vorticity) will increase being inversely proportional to the variation of the cross sectional area. This process can be particularly relevant in vortices with axial flow, which is the case for trailing vortices.

The analysis of the governing equations in the vorticity form highlights also that the production of vorticity is possible only for three-dimensional flows. For two-dimensional flows (either planar or axisymmetric flows), the vorticity vector is always perpendicular to the velocity gradient and the dot product is therefore zero. In such flows, vorticity can locally change as function of the time only as effect of transport and diffusion.

Finally, the last term represents the viscous source or sink of vorticity. Adjacent to a solid boundary, viscosity and the no-slip boundary condition, can introduce vorticity into the field. Away from solid surfaces, viscosity will generally damp any initial vorticity.

SECTION 3

Reynolds-averaged Navier-Stokes equations

For computation of time-averaged solutions of turbulent flows, the Reynolds-averaged Navier-Stokes equations (RANS) are commonly adopted. This form of the equations is obtained by separating the flow variables of Equation (C.1) into their mean and fluctuating components and then time-averaging the equations. The results in cartesian coordinates are:

$$\frac{\partial \bar{u}}{\partial x} + \frac{\partial \bar{v}}{\partial y} + \frac{\partial \bar{w}}{\partial z} = 0 \quad (\text{C.10a})$$

$$\begin{aligned}
 \bar{u} \frac{\partial \bar{u}}{\partial x} + \bar{v} \frac{\partial \bar{u}}{\partial y} + \bar{w} \frac{\partial \bar{u}}{\partial z} &= \\
 &= -\frac{1}{\rho} \frac{\partial \bar{P}}{\partial x} + \nu \left[\frac{\partial^2 \bar{u}}{\partial x^2} + \frac{\partial^2 \bar{u}}{\partial y^2} + \frac{\partial^2 \bar{u}}{\partial z^2} \right] - \underbrace{\left[\frac{\partial \overline{u'^2}}{\partial x} + \frac{\partial \overline{u'v'}}{\partial y} + \frac{\partial \overline{u'w'}}{\partial z} \right]}_{\text{Reynolds stresses}} \quad (\text{C.10b})
 \end{aligned}$$

$$\begin{aligned}
 \bar{u} \frac{\partial \bar{v}}{\partial x} + \bar{v} \frac{\partial \bar{v}}{\partial y} + \bar{w} \frac{\partial \bar{v}}{\partial z} &= \\
 &= -\frac{1}{\rho} \frac{\partial \bar{P}}{\partial y} + \nu \left[\frac{\partial^2 \bar{v}}{\partial x^2} + \frac{\partial^2 \bar{v}}{\partial y^2} + \frac{\partial^2 \bar{v}}{\partial z^2} \right] - \underbrace{\left[\frac{\partial \overline{v'u'}}{\partial x} + \frac{\partial \overline{v'^2}}{\partial y} + \frac{\partial \overline{v'w'}}{\partial z} \right]}_{\text{Reynolds stresses}} \quad (\text{C.10c})
 \end{aligned}$$

$$\begin{aligned}
 \bar{u} \frac{\partial \bar{w}}{\partial x} + \bar{v} \frac{\partial \bar{w}}{\partial y} + \bar{w} \frac{\partial \bar{w}}{\partial z} &= \\
 &= -\frac{1}{\rho} \frac{\partial \bar{P}}{\partial z} + \nu \left[\frac{\partial^2 \bar{w}}{\partial x^2} + \frac{\partial^2 \bar{w}}{\partial y^2} + \frac{\partial^2 \bar{w}}{\partial z^2} \right] - \underbrace{\left[\frac{\partial \overline{w'u'}}{\partial x} + \frac{\partial \overline{w'v'}}{\partial y} + \frac{\partial \overline{w'^2}}{\partial z} \right]}_{\text{Reynolds stresses}} \quad (\text{C.10d})
 \end{aligned}$$

where the terms in the last square brackets are known as *Reynolds stresses*. Transport equations for each one of the Reynolds stresses can be derived and they correspond to the closure equations of the RANS equations for the Reynolds stress model. Chow *et al.* (1997a) presented in their Appendix B these equations in cartesian and cylindrical reference systems and they used the equations to compare mean flow transport, generation, dissipation, pressure strain, turbulent transport and viscous transport of the Reynolds stresses in a trailing vortex.

The RANS equations expressed in cylindrical coordinates and applied to an axisymmetric flow (from Equation C.5) are:

$$\frac{1}{r} \frac{\partial (r \bar{u}_r)}{\partial r} + \frac{\partial \bar{u}_x}{\partial x} = 0 \quad (\text{C.11a})$$

$$\begin{aligned}
 \bar{u}_r \frac{\partial \bar{u}_r}{\partial r} + \bar{u}_x \frac{\partial \bar{u}_r}{\partial x} - \frac{\bar{u}_\theta^2}{r} &= \\
 &= -\frac{1}{\rho} \frac{\partial \bar{P}}{\partial r} + \nu \left[\frac{\partial^2 \bar{u}_r}{\partial r^2} + \frac{1}{r} \frac{\partial \bar{u}_r}{\partial r} + \frac{\partial^2 \bar{u}_r}{\partial x^2} \right] - \left[\frac{1}{r} \frac{\partial (r \overline{u_r'^2})}{\partial r} + \frac{\partial \overline{u_r' u_x'}}{\partial x} - \frac{\overline{u_\theta'^2}}{r} \right] \quad (\text{C.11b})
 \end{aligned}$$

$$\begin{aligned}
 \frac{\overline{u_r}}{u_r} \frac{\partial \overline{u_\theta}}{\partial r} + \frac{\overline{u_x}}{u_x} \frac{\partial \overline{u_\theta}}{\partial x} - \frac{\overline{u_\theta u_r}}{r} &= \\
 &= -\frac{1}{\rho r} \frac{\partial \overline{P}}{\partial \theta} + \nu \left[\frac{\partial^2 \overline{u_\theta}}{\partial r^2} + \frac{1}{r} \frac{\partial \overline{u_\theta}}{\partial r} + \frac{\partial^2 \overline{u_\theta}}{\partial x^2} \right] - \left[\frac{1}{r^2} \frac{\partial (r^2 \overline{u'_r u'_\theta})}{\partial r} + \frac{\partial \overline{u'_x u'_\theta}}{\partial x} \right]
 \end{aligned} \tag{C.11c}$$

$$\begin{aligned}
 \frac{\overline{u_r}}{u_r} \frac{\partial \overline{u_x}}{\partial r} + \frac{\overline{u_x}}{u_x} \frac{\partial \overline{u_x}}{\partial x} &= \\
 &= -\frac{1}{\rho} \frac{\partial \overline{P}}{\partial x} + \nu \left[\frac{\partial^2 \overline{u_x}}{\partial r^2} + \frac{1}{r} \frac{\partial \overline{u_x}}{\partial r} + \frac{\partial^2 \overline{u_x}}{\partial x^2} \right] - \left[\frac{1}{r} \frac{\partial (r \overline{u'_r u'_x})}{\partial r} + \frac{\partial \overline{u'_x{}^2}}{\partial x} \right]
 \end{aligned} \tag{C.11d}$$

SECTION 4

Conversion between cartesian and cylindrical coordinate systems

The SPIV measurements give a velocity vector field expressed in cartesian coordinates, namely the wake coordinate system. Although the vortex flow in the early wake can not be considered strictly axisymmetric, it is useful to use also a cylindrical coordinate system, called vortex reference system. The relations of the position, velocity components and Reynolds stresses expressed in the two reference frames are presented in the following equations. Both the directions of the conversions between the two coordinate systems are expressed.

Position:

$$x_w = x_v \tag{C.12a}$$

$$y_w = r \cos \theta \tag{C.12b}$$

$$z_w = r \sin \theta \tag{C.12c}$$

$$x_v = x_w \tag{C.13a}$$

$$r = \sqrt{y_w^2 + z_w^2} \tag{C.13b}$$

$$\theta = \tan^{-1} \left(\frac{z_w}{y_w} \right) \tag{C.13c}$$

Velocity:

$$\begin{Bmatrix} u \\ v \\ w \end{Bmatrix} = \begin{bmatrix} 1 & 0 & 0 \\ 0 & \cos \theta & -\sin \theta \\ 0 & \sin \theta & \cos \theta \end{bmatrix} \begin{Bmatrix} u_x \\ u_r \\ u_\theta \end{Bmatrix} \quad (\text{C.14})$$

$$\begin{Bmatrix} u_x \\ u_r \\ u_\theta \end{Bmatrix} = \begin{bmatrix} 1 & 0 & 0 \\ 0 & \cos \theta & \sin \theta \\ 0 & -\sin \theta & \cos \theta \end{bmatrix} \begin{Bmatrix} u \\ v \\ w \end{Bmatrix} \quad (\text{C.15})$$

Reynolds stresses:

$$\overline{u'^2} = \overline{u_x'^2} \quad (\text{C.16a})$$

$$\begin{Bmatrix} \overline{v'^2} \\ \overline{w'^2} \\ \overline{v'w'} \end{Bmatrix} = \begin{bmatrix} \cos^2 \theta & \sin^2 \theta & -2 \sin \theta \cos \theta \\ \sin^2 \theta & \cos^2 \theta & 2 \sin \theta \cos \theta \\ \sin \theta \cos \theta & -\sin \theta \cos \theta & \cos^2 \theta - \sin^2 \theta \end{bmatrix} \begin{Bmatrix} \overline{u_r'^2} \\ \overline{u_\theta'^2} \\ \overline{u_r' u_\theta'} \end{Bmatrix} \quad (\text{C.16b})$$

$$\begin{Bmatrix} \overline{u'v'} \\ \overline{u'w'} \end{Bmatrix} = \begin{bmatrix} \cos \theta & -\sin \theta \\ \sin \theta & \cos \theta \end{bmatrix} \begin{Bmatrix} \overline{u_x' u_r'} \\ \overline{u_x' u_\theta'} \end{Bmatrix} \quad (\text{C.16c})$$

$$\overline{u_x'^2} = \overline{u'^2} \quad (\text{C.17a})$$

$$\begin{Bmatrix} \overline{u_r'^2} \\ \overline{u_\theta'^2} \\ \overline{u_r' u_\theta'} \end{Bmatrix} = \begin{bmatrix} \cos^2 \theta & \sin^2 \theta & 2 \sin \theta \cos \theta \\ \sin^2 \theta & \cos^2 \theta & -2 \sin \theta \cos \theta \\ -\sin \theta \cos \theta & -\sin \theta \cos \theta & \cos^2 \theta - \sin^2 \theta \end{bmatrix} \begin{Bmatrix} \overline{v'^2} \\ \overline{w'^2} \\ \overline{v'w'} \end{Bmatrix} \quad (\text{C.17b})$$

$$\begin{Bmatrix} \overline{u_x' u_r'} \\ \overline{u_x' u_\theta'} \end{Bmatrix} = \begin{bmatrix} \cos \theta & \sin \theta \\ -\sin \theta & \cos \theta \end{bmatrix} \begin{Bmatrix} \overline{u'v'} \\ \overline{u'w'} \end{Bmatrix} \quad (\text{C.17c})$$